Politecnico di Torino

POLITECNICO DI TORINO

Collegio di Ingegneria Chimica e dei Materiali

Master of Science Course
in Materials Engineering for Industry 4.0

Master of Science Thesis

3D Printing of Injection Molding Inserts with Enhanced Heat Dissipation

Supervisor
Prof. Alberto Frache

Co-supervisor
Dr. Daniele Battegazzore

Candidate
Khashayar Baradaran Salmani

October 2025

Table of Contents

INTRODUCTION

Injection molding is one of the most established and widely used manufacturing processes in the plastics industry, commonly employed for the mass production of thermoplastic components that require high dimensional accuracy, repeatability, and complex geometries. Its ability to produce intricate parts in large volumes with minimal post-processing has made it indispensable across sectors such as automotive, medical devices, packaging, and consumer goods [1].

The performance of this process relies heavily on the quality of mold tooling, typically fabricated from hardened tool steels such as H13 or 1.2083, which provide excellent mechanical strength and thermal resistance [2]. However, conventional mold manufacturing involves time-consuming and expensive processes like CNC machining, electrical discharge machining (EDM), and surface treatments. These limitations become especially evident during product development, functional prototyping, or low-volume production, where the cost and lead time of traditional tooling often outweigh its benefits [3, 4].

In response to these challenges, additive manufacturing technologies have emerged as promising alternatives for producing injection mold inserts. AM allows the direct fabrication of near-net-shape parts from digital models, enabling design freedom, faster iteration, and reduced material waste [5]. For applications that demand short lead times, geometric flexibility, or temporary tooling, 3D-printed inserts offer a practical and cost-efficient solution aligned with the demands of modern, agile manufacturing [1, 3].

Nonetheless, a major limitation of polymer-based mold inserts remains their inherently low thermal conductivity, which hinders efficient heat dissipation during injection molding cycles [1, 6]. This thermal lag can lead to longer cooling times, warpage and reduced overall mold performance. To overcome this issue, recent studies have focused on enhancing thermal conductivity through the integration of conductive fillers such as copper particles and short carbon fibers [7, 8].

In this context, the use of pellet-based Fused Granular Fabrication (FGF) 3D printers, such as the Procreate G5 PRO, enables a more versatile and material-focused approach. Unlike filament-based systems, FGF allows direct printing from customized composite

formulations, by passing the filament extrusion step entirely [9]. This reduces material preparation time, minimizes thermal degradation, and broadens the scope of printable materials [5, 9].

In this work, both commercial filaments, which were manually pelletized to be used with the G5 PRO printer, and custom PLA–Copper composites with controlled copper content (60%, 80%, and 90% by weight) were processed for additive manufacturing. The composite materials were prepared in-house using a Brabender internal mixer and subsequently granulated using a PIOVAN granulator, even when the resulting granules exhibited size irregularities. This approach makes it possible to work with high filler contents and irregular feedstocks that are typically incompatible with filament-based systems, allowing the production of functional mold inserts with enhanced thermal conductivity and mechanical strength.

Beyond material development, this thesis also contributes to establishing a complete pellet-based printing workflow. For the first time within the research group, the G5 PRO printer was developed, implemented, and process-optimized in the laboratory of the Department of Applied Science and Technology (DISAT) at Politecnico di Torino, Alessandria campus, as part of the department's ongoing research in advanced manufacturing and polymer processing technologies. This machine was calibrated specifically for the additive manufacturing of thermally conductive mold inserts. The setup and operational protocols established here lay the foundation for future research on custom composite formulations and FGF technology [9, 10].

Thesis structure

The following chapters describe the background, materials, experimental procedures, and results of this research. A summary of each chapter is provided below:

Chapter 1 – STATE OF THE ART

Provides a comprehensive review of the scientific and technological background underpinning the development of 3D-printed mold inserts with enhanced thermal performance. It examines the evolution of additive manufacturing (AM) technologies, with particular emphasis on material extrusion processes such as Fused Filament Fabrication (FFF) and Fused Granular Fabrication (FGF). The chapter also explores the advantages and challenges of polymer-based inserts for injection molding, reviews recent

literature on thermally conductive composites, and highlights research gaps that motivate the present work.

Chapter 2 – MATERIALS AND METHODS

Introduces the materials used in this study, including commercial filaments (PLA, HTPLA, Carbon PA, Copper Filament) and copper powder for composite formulation. The chapter also outlines all experimental methods and equipment used, including thermal conductivity testing, dynamic mechanical analysis (DMA in tension and cantilever bending), compression testing, scanning electron microscopy (SEM), the Brabender mixer, the injection molding machine, both 3D printers (FlashForge Creator 3 Pro and Piocreat G5 PRO) , grinder (granulator), auto sputter coater, particle size distribution analysis, thermographic monitoring system, pelletizer of filaments, and filament dryer.

Chapter 3 – RESULTS AND DISCUSSION

This chapter is divided into two major sections. All printing described here was performed using the G5 PRO pellet-based 3D printer. The first section presents the characterization of samples printed from pelletized commercial filaments, including PLA, HTPLA, Carbon PA, and Copper Filament. It discusses the results obtained from thermal conductivity measurements (Hot Disk), dynamic mechanical analysis (DMA), compression testing, and scanning electron microscopy (SEM). The second section focuses on the preparation and characterization of customized PLA–Copper composites. It details the compounding process carried out using the Brabender internal mixer, the granulation step, and the subsequent characterization of the printed samples through the same series of tests.

Chapter 4 – 3D PRINTING PROCESS

This chapter is divided into two main parts. The first part provides a comparison between the two 3D printing technologies used in this study: the G5 PRO pellet-based printer and the FlashForge Creator 3 Pro filament-based printer. Key differences are analyzed in terms of extrusion mechanisms, feedstock handling, material flexibility, and process control. In addition, this section includes a direct comparison of samples printed from the same material using both systems, with an evaluation of differences in surface finish, print consistency, and performance. The second part focuses on the printing process of the mold

inserts (using the G5 PRO printer), describing the slicing settings, parameter tuning, and practical challenges encountered during fabrication with different materials.

Chapter 5 – INJECTION MOLDING PROCESS

Discusses the experimental injection molding trials performed using each type of printed insert. It includes injection parameters, thermal imaging analysis, cycle performance, post-molding observations, and comparative evaluation between materials.

Chapter 6 – SIMULATION VIA MOLDEX3D

Presents simulation studies carried out using Moldex3D software to model injection behavior, temperature distribution, heat dissipation, and pressure profile across different insert materials. Simulation results are compared to experimental findings to assess consistency and predictive accuracy.

Chapter 7 – CONCLUSION

This chapter summarizes the key findings of the study, emphasizing the outcomes achieved in the development and evaluation of thermally conductive mold inserts produced through pellet-based additive manufacturing using Fused Granular Fabrication (FGF). It discusses the limitations encountered during material preparation, processing, and testing, and outlines practical improvements to enhance both the performance of the inserts and the efficiency of the manufacturing workflow. Finally, it proposes future research directions aimed at advancing FGF technology, optimizing composite formulations, and broadening the industrial applicability of polymer-based tooling solutions.

APPENDIX

Provides practical documentation for the setup and operation of the Piocreat G5 PRO pellet-based 3D printer, including slicing software parameters, maintenance tips, and troubleshooting advice. This section is intended to support future students and researchers working with the same system.

Chapter 1

STATE OF THE ART

This chapter presents a comprehensive review of the scientific and technological background underpinning the development of 3D-printed mold inserts with enhanced thermal performance. The discussion begins by introducing the concept of mold inserts, with particular attention to the advantages offered by modular insert-based mold designs, which allow manufacturers to rapidly modify localized mold features such as logos, surface textures, or functional geometries without the need to reconstruct the entire mold assembly [2, 3]. This flexibility is particularly valuable in low-volume production, design validation, and customized manufacturing contexts.

The chapter then examines the role of additive manufacturing (AM) in tooling applications, with an emphasis on material extrusion technologies such as Fused Filament Fabrication (FFF) and Fused Granular Fabrication (FGF). While both methods enable the layer-by-layer fabrication of polymer-based inserts, they differ significantly in their compatibility with non-standard materials and in their adaptability for research-driven composite development [11]. The primary focus of this thesis is on the FGF process, which offers distinct advantages over FFF in terms of feedstock flexibility, compositional control, and processing efficiency.

Finally, the chapter explores the inherent thermal limitations of polymeric mold inserts, particularly their low thermal conductivity, which adversely affects heat transfer during the injection molding cycle. This limitation is addressed through the use of conductive fillers, such as copper particles, to enhance the thermal performance of the printed parts. The integration of such materials into printable polymer matrices, and their processing via pellet-based extrusion systems like the Piocreat G5 PRO, represents a key innovation of this research [12].

Through this framework, the chapter lays the foundation for the experimental work presented in the following chapters, situating the thesis within the broader context of

additive manufacturing, composite material engineering, and rapid tooling strategies for polymer processing.

1.1 Modular inserts in injection molding

In injection molding, the mold defines the geometry of the final part and must withstand high pressures and elevated temperatures during each cycle. Traditional molds are typically machined from hardened tool steels such as H13, which provide excellent durability and thermal stability. However, they are costly and time-consuming to fabricate, particularly when even minor changes in product geometry are required [13].

To overcome these limitations, modular mold systems based on interchangeable inserts have gained popularity. A mold insert is a detachable component that fits into a cavity of the mold base and defines part or all of the part's final shape. This design approach brings significant benefits in terms of flexibility, cost savings, and lead time reduction.

One of the most impactful advantages of using inserts is their ability to enable rapid customization. For example, if a manufacturer wants to add or modify a feature such as a logo, name, serial number, or micro-pattern on the final part, they can simply replace the insert without reworking the entire mold. This is particularly beneficial in prototyping, small batch production, and personalized manufacturing, where frequent design iterations or variant production are required. Modular inserts are a practical strategy for reducing the time and cost of mold modifications, while enabling production agility. The insert-based approach also facilitates localized maintenance or upgrades of specific mold sections without disturbing the rest of the tool, minimizing downtime and extending overall tool life.

The use of modular inserts is closely aligned with modern design for manufacturing principles, especially when integrated into digital manufacturing workflows. Through CAD-CAM integration and additive manufacturing, the design and fabrication of new inserts can be executed in a matter of hours, dramatically accelerating the development cycle.

1.2 Additive manufacturing of mold inserts

Additive manufacturing (AM), widely known as 3D printing, has become a transformative tool in the field of tooling and mold production. Traditionally, mold inserts were manufactured using subtractive techniques that are time-consuming, expensive, and poorly suited for small-scale or customized production [14]. AM offers a compelling alternative, enabling the direct fabrication of mold inserts from digital designs with significantly reduced lead time, cost, and material waste.

In the context of injection molding, 3D-printed inserts are particularly attractive for rapid prototyping, short-run production, and customization. Additive manufacturing allows manufacturers to produce inserts with tailored surface geometries, internal features, or branding elements such as patterns and part numbers without needing to redesign or refabricate the entire mold. This digital workflow supports agile product development cycles and fast design iterations [11].

Several AM technologies have been applied to mold insert fabrication. Stereolithography (SLA) has been used when high resolution and smooth surface finishes are required, while Selective Laser Sintering (SLS) offers superior mechanical properties for more demanding tooling conditions [15]. However, material extrusion techniques particularly Fused Filament Fabrication (FFF) and Fused Granular Fabrication (FGF) have become increasingly relevant due to their compatibility with a wide range of thermoplastic materials and composite formulations (Figure 2.1).

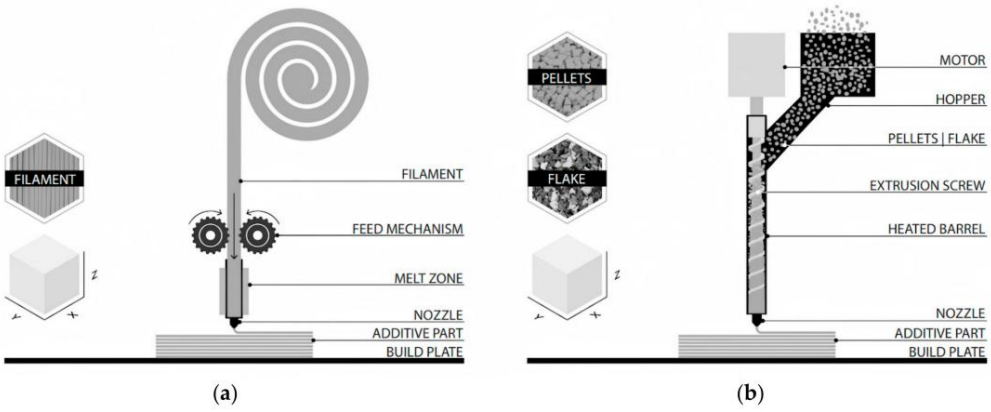

Figure 1.1. Comparison between FFF (a) and FGF (b) additive manufacturing [5]

Despite their lower mechanical and thermal resistance compared to metals, polymer-based inserts produced by AM have proven effective in numerous studies for short-run

production and prototyping purposes. Research has demonstrated that polymer inserts can withstand repeated molding cycles when appropriately designed, reinforced, or thermally optimized [1]. The possibility to quickly develop, test, and modify material compositions makes extrusion-based AM especially attractive for experimental and research-oriented applications. In this context, the present thesis explores the use and development of FGF technology to fabricate mold inserts using both commercial and customized copper-filled composites, aiming to improve thermal behavior while maintaining mechanical integrity under injection molding conditions.

Fused Granular Fabrication (FGF) also offers important environmental benefits compared to traditional FFF and injection molding approaches. Recent life cycle assessment studies have shown that pellet-based FGF systems can significantly reduce the overall climate change potential, producing less than one-fifth of the CO_2-equivalent emissions of traditional FFF and approximately one-third of those associated with conventional injection molding. This reduction is largely due to the ability of FGF to process second-use or recycled materials such as waste plastic bottles, containers, and other post-consumer discardables directly in the dryer, granulator, and printer, without the need for intermediate processing or packaging. By granting a second life to these materials, the embedded energy of the feedstock is effectively removed from the overall carbon footprint, making FGF an attractive option not only for rapid tooling applications but also for sustainable manufacturing practices [Figure 2.2].

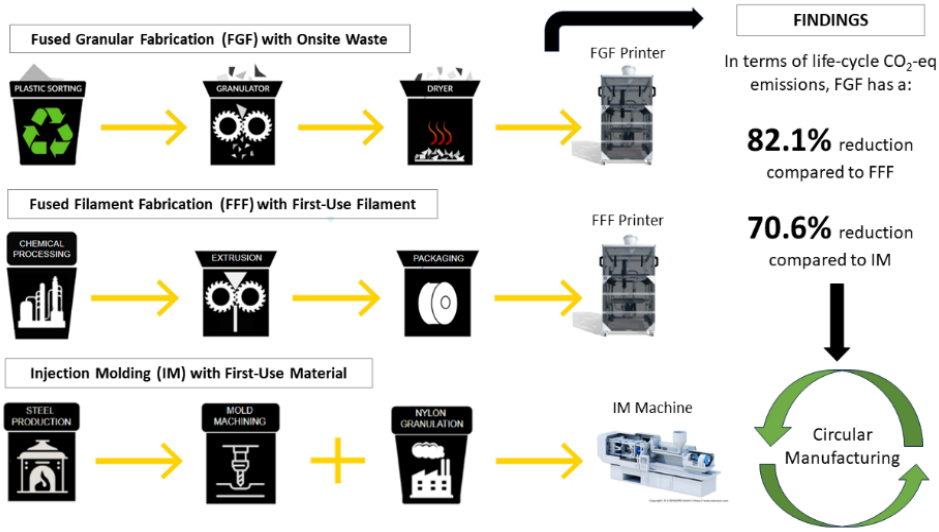

Figure 1.2. Comparative life-cycle CO_2-equivalent emissions for Fused Granular Fabrication (FGF), Fused Filament Fabrication (FFF) with, and Injection Molding (IM) [5]

1.3 Injection molding process overview

Injection molding is one of the most widely used manufacturing processes for the mass production of thermoplastic components. It involves injecting molten polymer into a mold cavity, where the material cools and solidifies to form the final part. The process is known for its high repeatability, excellent surface finish, and ability to produce complex geometries at scale.

The standard injection molding cycle can be divided into four main stages: plasticization, injection, cooling, and ejection. First, polymer granules are fed into a heated barrel, where they are melted and homogenized by a rotating screw (plasticization). Once a sufficient volume of molten material is accumulated, it is injected under high pressure into the mold cavity (injection). After the cavity is filled, the material is allowed to cool and solidify under controlled conditions (cooling), after which the mold opens and the part is ejected (ejection) [6]. The workflow of the injection molding process using 3D-printed mold inserts is illustrated in Figure 2.3.

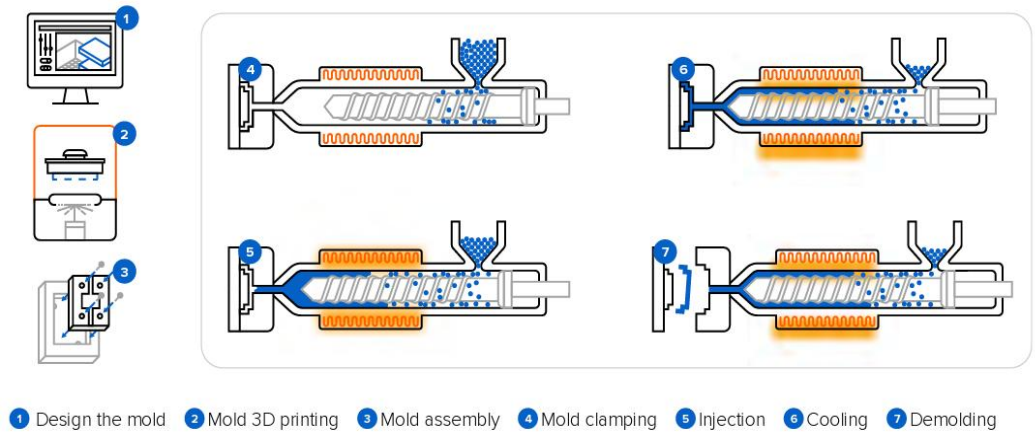

Figure 1.3. Workflow of the injection molding process using 3D-printed mold inserts [16]

Among these stages, cooling is the most time-consuming and thermally demanding phase [11]. The heat accumulated within the mold, particularly at the mold-insert interface, must be efficiently dissipated to ensure dimensional stability, reduce cycle time, and prevent defects such as warpage or incomplete solidification. In traditional steel molds, this heat is rapidly conducted through the mold body and removed using integrated cooling channels [13]. However, polymer-based inserts, which are increasingly used for rapid

tooling and prototyping, suffer from inherently low thermal conductivity and tend to retain heat for significantly longer periods.

This thermal lag can lead to several critical issues [1]:

- Increased cooling time, resulting in longer production cycles.
- Mechanical failure or deformation of the insert due to thermal fatigue.
- Surface defects and incomplete replication in the molded part caused by inadequate heat removal.

As a result, heat management becomes a key challenge when using polymeric or composite mold inserts. The main objective is to maintain a balance between customizability, material cost, and thermal performance. One promising solution is to enhance the thermal conductivity of the insert material by incorporating metallic fillers into the polymer matrix. This approach improves heat dissipation and extends the functional life of the insert while maintaining the geometric freedom offered by additive manufacturing [12].

This understanding of the injection molding cycle and the thermal stress experienced by inserts provides the necessary background for the composite material development strategies discussed in the next sections.

1.4 Thermal limitations of polymer inserts and customized composite solutions

Polymer-based inserts offer valuable advantages in terms of cost, manufacturing speed, and design flexibility. However, their limited thermal conductivity remains a critical drawback, especially in injection molding applications where rapid and uniform heat dissipation is essential. Typical thermoplastics used in additive manufacturing, such as PLA and PA, exhibit thermal conductivity values in the range of 0.1 to 0.3 W/m·K which results in poor heat dissipation during the cooling phase of the molding cycle and can negatively affect both insert durability and part quality [11].

To overcome these limitations, research has focused on modifying the thermal properties of polymers through the incorporation of conductive fillers [Figure 2.4]. Among the most

suitable fillers for improving thermal conductivity are copper particles, aluminum particles, short carbon fibers, and graphite. These additives can significantly enhance heat transfer within the polymer matrix without drastically compromising printability. Copper is of strong interest due to its exceptionally high intrinsic thermal conductivity (approximately 400 W/m·K), as well as its good compatibility with biodegradable and engineering thermoplastics when properly dispersed [7, 12].

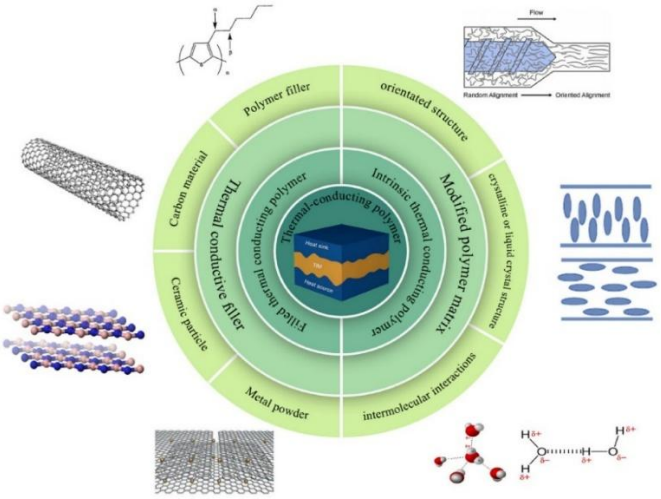

Figure 1.4. Strategies for enhancing thermal conductivity in polymers through intrinsic matrix modification and the incorporation of thermally conductive fillers [18]

The effectiveness of thermally conductive composites depends on several factors, including filler concentration, particle size and morphology, dispersion quality, and interfacial adhesion between the filler and the polymer matrix. While increasing copper content generally leads to improved thermal conductivity, high filler loadings can introduce issues such as brittleness and reduced processability, especially in filament-based systems. These limitations have increased interest in pellet-based extrusion methods like Fused Granular Fabrication (FGF), which allow for greater feedstock flexibility and the direct printing of composite materials with higher filler concentrations than those typically feasible through filament extrusion.

As shown in Figure 2.5, optimizing the filler connection mode, orientation, and distribution within the polymer matrix facilitates the formation of continuous and efficient thermal conductivity pathways. A well-connected filler network allows phonons, the primary carriers of heat in solids, to travel with minimal resistance, similar to vehicles moving smoothly along an uninterrupted highway. In contrast, poorly connected or misaligned fillers act like broken or congested roads, slowing heat transfer. By ensuring

proper filler alignment and uniform dispersion, it is possible to achieve high thermal performance even at lower filler loadings, reducing material costs and limiting negative effects on mechanical properties. This is particularly important for polymer-based mold inserts, where efficient heat dissipation directly affects cooling time, dimensional stability, and mold durability [17].

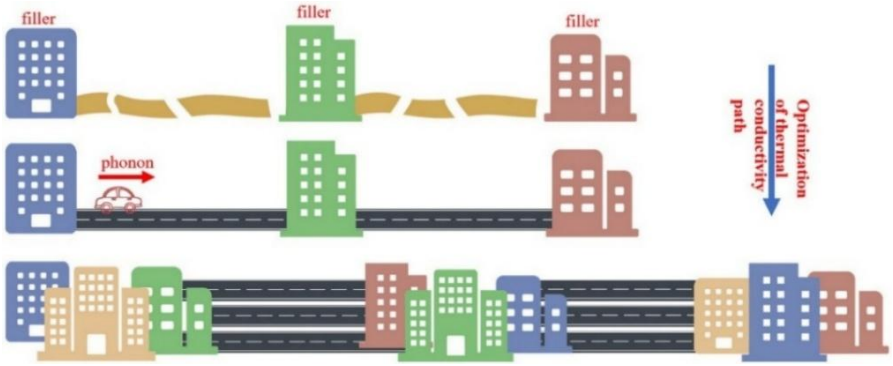

Figure 1.5. Optimization of thermal conductivity in polymer composites through filler network formation and orientation [17]

The thermal conductivity of polymer composites is strongly influenced by the quality of filler dispersion and distribution within the polymer matrix. Poor dispersion can lead to agglomerates that act as thermal barriers, while uneven distribution causes localized hotspots or low-conductivity regions. Figure 2.6 illustrates the four possible scenarios, highlighting that optimal performance is achieved with both good dispersion and good distribution.

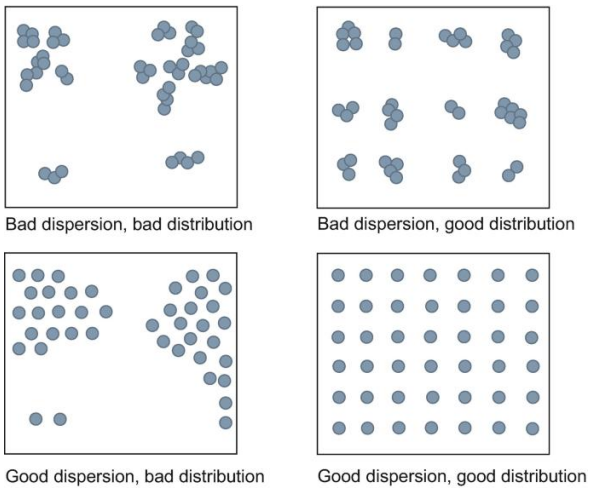

Figure 1.6. Possible combinations of filler dispersion and distribution in composites [17]

In addition to filler type and content, other microstructural and processing-related aspects also influence the thermal conductivity of polymer composites, such as filler orientation,

network connectivity, and purity, as illustrated in Figure 2.7. Understanding and controlling these parameters is essential for optimizing heat transfer in additively manufactured mold inserts [11].

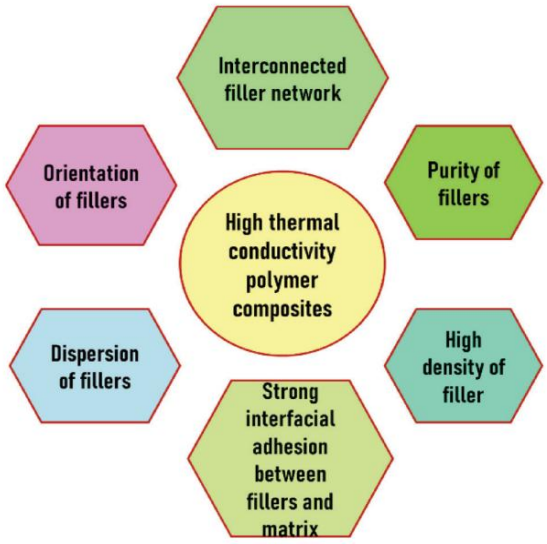

Figure 1.7. Key factors affecting the thermal conductivity of polymer composites [11]

This strategy is directly aligned with the objectives of the present research, which investigates pellet-based 3D printing as a pathway for producing injection mold inserts with enhanced thermal conductivity. The strategy combines conductive composite formulations with a flexible, research-oriented printing platform, laying the groundwork for advanced tooling solutions in low-volume, thermally demanding applications.

Chapter 2

MATERIALS AND METHODS

This chapter provides a comprehensive overview of the materials and experimental procedures used in this study. The first part presents the commercial filaments and copper powders used to produce the test samples and inserts, along with key material properties obtained from technical datasheets. It also briefly describes the two 3D printers used in the work: the FlashForge Creator 3 Pro (filament-based) and the G5 PRO Piocreat (pellet-based), both of which were utilized for sample production. A reference to the Appendix is included for detailed operation guidelines of the pellet-based G5 PRO printer.

The second part outlines the experimental techniques and instruments applied for the characterization of materials and printed components. These include thermal conductivity measurements, dynamic mechanical thermal analysis (DMTA), compression testing, morphological analysis via SEM, and other relevant laboratory equipment utilized throughout the research.

2.1 Materials

The following sections describe the materials selected for this work. This includes commercial thermoplastic filaments used in the additive manufacturing phase, as well as the copper powder incorporated into later composite formulations.

2.1.1 Commercial materials for inserts and samples fabrication

Four commercial filaments were selected for printing the test samples and mold inserts: PLA, HTPLA, Carbon PA, and Copper Filament. In addition, an insert made of AISI 1.2083 tool steel was used as a reference benchmark for comparison during injection molding.

2.1.1.1 PLA

One of the commercial filaments selected for this study was PLA (Polylactic Acid), produced by FILOALFA, a brand of Ciceri de Mondel Srl, based in Italy (Figure 2.1). PLA is a biodegradable thermoplastic derived from renewable resources such as corn

starch, and it is widely used in additive manufacturing due to its ease of printing, low thermal shrinkage, and good dimensional accuracy. It is considered an ideal material for rapid prototyping and functional parts under moderate mechanical and thermal requirements.

Figure 2.1. PLA filament spool (FILOALFA)

The filament used in this work was the blue Christmas variant with a nominal diameter of 1.75 mm and a manufacturing tolerance of ±0.05 mm. According to the technical data sheet, this PLA has a density of 1.24 g/cm³, tensile strength of 53 MPa, and a tensile modulus of 3.6 GPa. The recommended extrusion temperature ranges from 170 to 210 °C, while the glass transition temperature (Tg) is approximately 60 °C, and the melting point is around 135 °C. The heat deflection temperature (HDT) under load is also reported to be in the range of 55–60 °C (Figure 2.2).

This PLA filament was used to print test samples and mold inserts using both 3D printers, serving as a baseline reference for evaluating printability, thermal behavior, and mechanical performance in comparison to the advanced composite materials developed in the later phases of this study. Moreover, the same PLA was used as the polymeric matrix to produce customized composites loaded with copper powder (60%, 80%, and 90%), which will be discussed in the next chapter.

FILOALFA
RILIEVO AI TUOI PROGETTI
by Ciceri de Mondel

Feb, 2019

TECHNICAL DATE SHEET — **PLA**

BASE MATERIAL: Polylactic acid

PROPERTIES

	PROPERTIES	VALUE	METOD AND CONDICTION
PHYSICAL & MECHANICAL	Density	1,24 g/cm3	D792
	Hardness/ Flexure Modulus	3,8 Gpa	D790
	Tensile strength	53 Mpa	D882
	Tensile Modulus	3,6 Mpa	D882
	Tensile Elongation	6%	D882
THERMAL	Melting point	135°C	D100β
	Heat Deflection Temperature	55°C	E2092
	Viscat Softening Temperature	55-60°C	D3418
	Flammability:		
	Burging Rate	ND	
	Flame Rating	ND	

SUGGESTED PRINTER SETTING

	VALUE	UNIT
Extruder Temperature	170 – 210	°C
Print Speed	40 – 120	mm/sec
Bed Material	0 – 50	°C

PRODUCT DETAILS & CERTIFICATION

Diameter	1,75 mm 2,85 mm	Tollerance ± 0,05mm Tollerance ± 0,10mm
REACH compliant	compliant	
FDA compliant	compliant granule / raw material	
ROHS certified	compliant	

Filoalfa by Ciceri de Model Srl
Via Galvani 13, 20080
Ozzero (MI)

Figure 0.2. Technical data sheet of PLA filament (FILOALFA) [19]

2.1.1.2 HTPLA

The second commercial filament used in this work was HTPLA Copper Composite, produced by Proto pasta (Protoplant Inc., USA). This filament is based on a heat-treatable grade of PLA and is filled with approximately 60% copper alloy powder by weight, making it significantly denser and more thermally conductive than standard PLA materials (Figure 2.3). It is specifically engineered to combine aesthetic metallic appearance with improved heat resistance and stiffness after annealing.

Figure 0.3. HTPLA filament spool (Proto pasta)

The material consists of a matrix of PLA with copper metal powder as the filler, and it can undergo post-processing heat treatment to enhance its crystalline structure and dimensional stability. According to the technical data sheet, the filament has a density of approximately 2.3 g/cm³, a glass transition temperature (Tg) of about 60 °C, and a melting point onset (Tm) around 155 °C. The recommended extrusion temperature is 195 °C, with a bed temperature of around 60 °C (Figure 2.4).

Proto-pasta

Technical Data Sheet Rev .1

Brass Fill, Bronze Fill, Copper Fill HTPLA

Brass, Bronze, and Copper HTPLA print like plastic but finish like real metal for beautiful, durable parts from most standard 3D printers. These three metal composites can be heat treated to firm up parts and hold shape up to near melting (175C).

Material Properties

Properties	Value/Description
Base material	Heat treatable PLA w/ high temp resistance
Characteristics	low odor, non-toxic, renewably sourced
Molecular structure	Amorphous or partially crystalline *(Amorphous as printed, part crystalline when heat-treated) (Melting resets crystalline structure to amorphous state)*
Additives	Metal Powder
Max particle size	250 microns
Density	approx. 2.3 g/cc
Length	approx. 194 m/kg (1.75 mm) & 72 m/kg (2.85 mm)
Min bend diameter	30 mm (1.75 mm) & 55 mm (2.85 mm)
Glass transition (Tg) onset	approx. 60 deg C (140 deg F)
Melt point (Tm) onset	approx. 155 deg C (310 deg F)
Max use	Tg for amorphous, Tm for crystalline

Use limit is geometry, load & condition dependent

Print Settings

(Based on Ultimaker s5 .15mm Profile)

Setting	Value
Nozzle Temperature [°C]	195
Heated Bed Temperature [°C]	60
Print Speed [mm/s]	20-30
Flow Rate/Extrusion Multiplier [%]	100
Extrusion Width [mm]	.65 (.05mm larger than nozzle size)
Volume Flow Rate [mm³/s]	2-3

Heat Treating (for heat-treating only)

HTPLA is a semi-crystalline grade of PLA optimized for heat-treating for higher temperature use. Prior to printing, HTPLA parts should be scaled in the slicer to compensate for shrinkage when heat treating.

(Please note that all values for heat-treating are process dependent and may vary between users)

Part Axis	Percentage
Scale Values (x/y-axis)	101.5%
Scale Values (z-axis)	99%

(a large range of temperatures & times can yield acceptable results)

Typical Heat Treat Temperature	Typical Heat Treat Time
95-110 °C	10+ minutes

For a more in-depth look at brass, bronze, and copper please view proto-pasta.com/copper-alloys

Results may vary based on print settings as well as print quality

Figure 2.4. Technical data sheet of HTPLA filament (Proto pasta) [20]

This HTPLA filament was used to print test samples and mold inserts using both 3D printers. Its high copper content makes it especially interesting for thermally demanding applications such as mold inserts. However, the brittleness and printability challenges associated with such high filler loadings are key considerations in its use.

This material was selected to investigate the behavior of a commercially available conductive composite filament, serving as a point of comparison with the in-house fabricated PLA–Copper formulations produced using the Brabender mixer.

2.1.1.3 Carbon PA

The third commercial filament selected for this study was Carbon PA, developed and distributed by Roboze S.p.A., an Italian company specializing in high-performance 3D printing materials and systems (Figure 2.5). This filament is based on PA6 (polyamide) reinforced with 20% short carbon fibers, designed specifically for printing functional components with enhanced mechanical properties and high thermal resistance.

Figure 2.5. Carbon PA filament spool (Roboze S.p.A.)

Carbon PA is intended as a lightweight alternative to aluminum alloys for use in demanding environments such as automotive, aerospace, and industrial tooling. Its performance is optimized when printed on high-precision beltless printers like the Roboze Plus 400, but it can also be adapted for other professional FFF systems.

According to the technical data sheet, Carbon PA exhibits excellent mechanical properties. It has a tensile strength of 136 MPa and a tensile modulus of 15.5 GPa, with an elongation at break of 1.62%. The flexural strength is reported at 100 MPa, while the flexural modulus reaches 5 GPa. The material has a density of approximately 1.4 g/cm³. Thermally, the material shows outstanding performance, with a Heat Deflection Temperature (HDT) of 200 °C under a 1.82 MPa load, and a continuous service temperature of 150 °C, making it suitable for high-temperature applications (Figure 2.6).

In this work, the Carbon PA filament was used to print both test specimens and mold inserts using both 3D printers. Its high stiffness and thermal resistance make it a strong candidate for evaluating the performance limits of polymer-based inserts in thermally demanding injection molding scenarios.

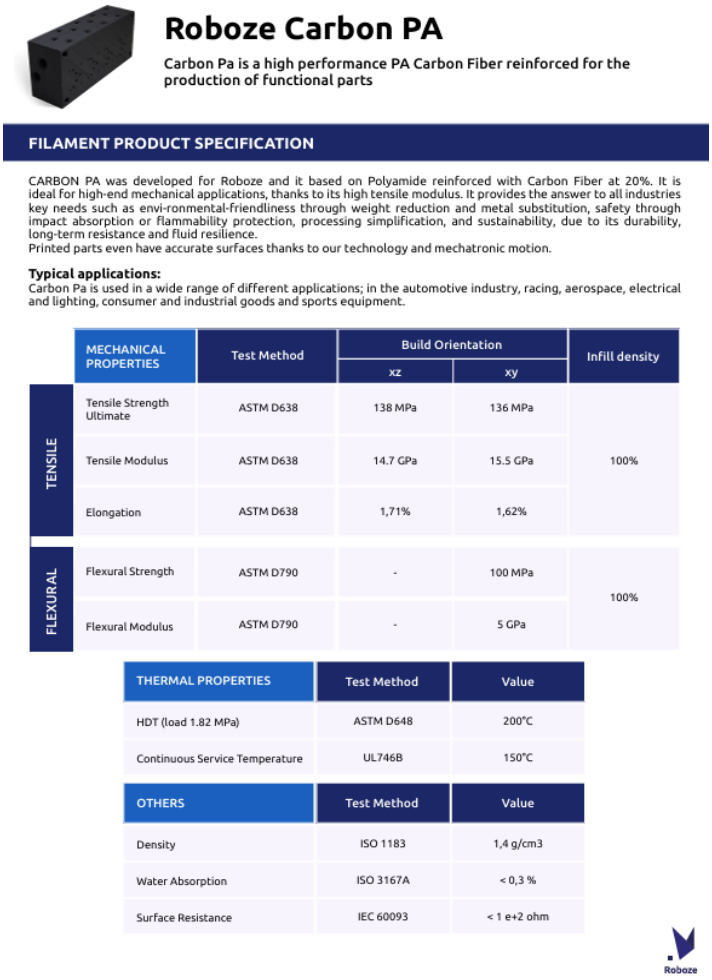

Roboze Carbon PA

Carbon Pa is a high performance PA Carbon Fiber reinforced for the production of functional parts

FILAMENT PRODUCT SPECIFICATION

CARBON PA was developed for Roboze and it based on Polyamide reinforced with Carbon Fiber at 20%. It is ideal for high-end mechanical applications, thanks to its high tensile modulus. It provides the answer to all industries key needs such as envi-ronmental-friendliness through weight reduction and metal substitution, safety through impact absorption or flammability protection, processing simplification, and sustainability, due to its durability, long-term resistance and fluid resilience.
Printed parts even have accurate surfaces thanks to our technology and mechatronic motion.

Typical applications:
Carbon Pa is used in a wide range of different applications; in the automotive industry, racing, aerospace, electrical and lighting, consumer and industrial goods and sports equipment.

	MECHANICAL PROPERTIES	Test Method	Build Orientation		Infill density
			xz	xy	
TENSILE	Tensile Strength Ultimate	ASTM D638	138 MPa	136 MPa	100%
TENSILE	Tensile Modulus	ASTM D638	14.7 GPa	15.5 GPa	
TENSILE	Elongation	ASTM D638	1,71%	1,62%	
FLEXURAL	Flexural Strength	ASTM D790	-	100 MPa	100%
FLEXURAL	Flexural Modulus	ASTM D790	-	5 GPa	

THERMAL PROPERTIES	Test Method	Value
HDT (load 1.82 MPa)	ASTM D648	200°C
Continuous Service Temperature	UL746B	150°C

OTHERS	Test Method	Value
Density	ISO 1183	1,4 g/cm3
Water Absorption	ISO 3167A	< 0,3 %
Surface Resistance	IEC 60093	< 1 e+2 ohm

Roboze

Figure 2.6. Technical data sheet of Carbon PA filament (Roboze S.p.A.) [21]

2.1.1.4 Copper Filament

The Copper Filament (Copper Filamet™) used in this study was provided by The Virtual Foundry (USA). It is a PLA-based composite filament highly loaded with copper particles, with a metal content ranging from 87% to 90% by weight and an overall density between 4.50 and 4.70 g/cm³. The filament is designed for functional prototyping and metal part fabrication via sintering, though in this thesis it was used in its unsintered form for thermal characterization and mold insert fabrication (Figure 2.7).

Figure 2.7. Copper Filament spool (The Virtual Foundry)

The recommended printing parameters for this material include a nozzle temperature between 190 °C and 230 °C, bed temperature of 40–65 °C, and a nozzle size of at least 0.6 mm. Due to the high metal content, the filament is notably abrasive and requires the use of hardened steel nozzles to avoid excessive wear during extrusion. The manufacturer highlights the need for good bed adhesion and proper cooling for small or intricate features (Figure 2.8).

In this work, the copper filament was used exclusively with the G5 PRO pellet-based 3D printer, as its high metal content made it incompatible with the FFF system due to nozzle clogging and flowability limitations. It was used to fabricate both test samples and inserts, serving as a benchmark for evaluating the thermal behavior of commercially available copper-filled filaments in comparison to the customized PLA–Copper composites developed in-house using the Brabender mixer. Its high density and enhanced thermal conductivity make it a valuable reference for assessing heat dissipation in polymer-based mold inserts under thermally demanding conditions.

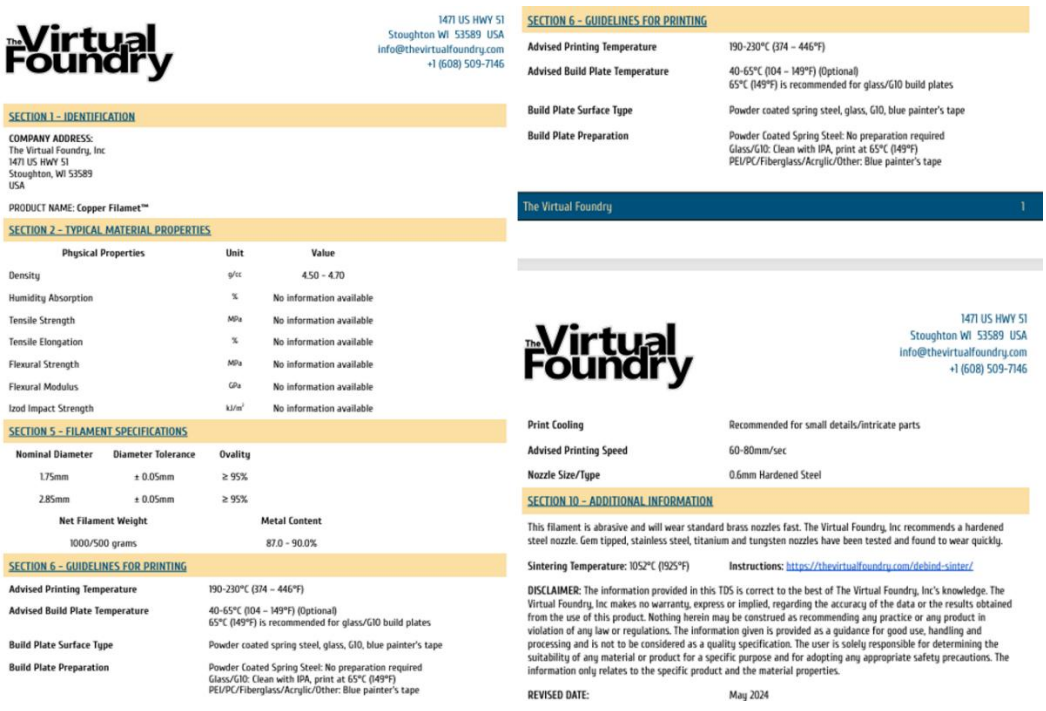

The Virtual Foundry

1471 US HWY 51
Stoughton WI 53589 USA
info@thevirtualfoundry.com
+1 (608) 509-7146

SECTION 1 - IDENTIFICATION

COMPANY ADDRESS:
The Virtual Foundry, Inc
1471 US HWY 51
Stoughton, WI 53589
USA

PRODUCT NAME: **Copper Filamet™**

SECTION 2 - TYPICAL MATERIAL PROPERTIES

Physical Properties	Unit	Value
Density	g/cc	4.50 - 4.70
Humidity Absorption	%	No information available
Tensile Strength	MPa	No information available
Tensile Elongation	%	No information available
Flexural Strength	MPa	No information available
Flexural Modulus	GPa	No information available
Izod Impact Strength	kJ/m²	No information available

SECTION 5 - FILAMENT SPECIFICATIONS

Nominal Diameter	Diameter Tolerance	Ovality
1.75mm	± 0.05mm	≥ 95%
2.85mm	± 0.05mm	≥ 95%

Net Filament Weight	Metal Content
1000/500 grams	87.0 - 90.0%

SECTION 6 - GUIDELINES FOR PRINTING

Advised Printing Temperature	190-230°C (374 - 446°F)
Advised Build Plate Temperature	40-65°C (104 - 149°F) (Optional) 65°C (149°F) is recommended for glass/G10 build plates
Build Plate Surface Type	Powder coated spring steel, glass, G10, blue painter's tape
Build Plate Preparation	Powder Coated Spring Steel: No preparation required Glass/G10: Clean with IPA, print at 65°C (149°F) PEI/PC/Fiberglass/Acrylic/Other: Blue painter's tape

SECTION 6 - GUIDELINES FOR PRINTING

Advised Printing Temperature	190-230°C (374 - 446°F)
Advised Build Plate Temperature	40-65°C (104 - 149°F) (Optional) 65°C (149°F) is recommended for glass/G10 build plates
Build Plate Surface Type	Powder coated spring steel, glass, G10, blue painter's tape
Build Plate Preparation	Powder Coated Spring Steel: No preparation required Glass/G10: Clean with IPA, print at 65°C (149°F) PEI/PC/Fiberglass/Acrylic/Other: Blue painter's tape

The Virtual Foundry

1471 US HWY 51
Stoughton WI 53589 USA
info@thevirtualfoundry.com
+1 (608) 509-7146

Print Cooling	Recommended for small details/intricate parts
Advised Printing Speed	60-80mm/sec
Nozzle Size/Type	0.6mm Hardened Steel

SECTION 10 - ADDITIONAL INFORMATION

This filament is abrasive and will wear standard brass nozzles fast. The Virtual Foundry, Inc recommends a hardened steel nozzle. Gem tipped, stainless steel, titanium and tungsten nozzles have been tested and found to wear quickly.

Sintering Temperature: 1052°C (1925°F) **Instructions:** https://thevirtualfoundry.com/debind-sinter/

DISCLAIMER: The information provided in this TDS is correct to the best of The Virtual Foundry, Inc's knowledge. The Virtual Foundry, Inc makes no warranty, express or implied, regarding the accuracy of the data or the results obtained from the use of this product. Nothing herein may be construed as recommending any practice or any product in violation of any law or regulations. The information given is provided as a guidance for good use, handling and processing and is not to be considered as a quality specification. The user is solely responsible for determining the suitability of any material or product for a specific purpose and for adopting any appropriate safety precautions. The information only relates to the specific product and the material properties.

REVISED DATE: May 2024

Figure 2.8. Technical data sheet of Copper Filament (The Virtual Foundry) [22]

2.1.1.5 AISI 1.2083 Steel

AISI 1.2083 (UNI X40Cr14) is a martensitic stainless steel with high hardenability, widely known for its excellent machinability, polishability, corrosion resistance, and

durability under thermal stress. It has a density of approximately 7.8 g/cm³ and a thermal conductivity of 16.5 W/m·K at 20 °C [23]. The typical chemical composition includes approximately 0.40% C, 0.80% Si, 0.50% Mn, 14.50% Cr, and 0.30% V.

This material is commonly used for the production of high-performance molds in plastic injection molding, especially in applications requiring prolonged durability, dimensional stability, and high surface finish quality. In this thesis, the steel insert served as a reference for comparing the thermal and mechanical performance of polymer-based mold inserts, both commercial and customized.

2.1.2 Copper Powder

The metallic filler used for the preparation of composite materials in this work was a gas atomized copper powder containing approximately 3–4% silver (Figure 2.9). The powder was produced in the laboratories of the Department of Applied Science and Technology (DISAT) of Politecnico di Torino in Alessandria campus.

Figure 2.9. Gas atomized copper powder

This copper powder was used to prepare the customized PLA–Copper composites in three different concentrations (60, 80, and 90 wt%) using the Brabender mixer and subsequent granulation, which will be described in detail in the next chapter.

2.1.3 Polypropylene – LyondellBasell Moplen HP500N

In this study, Moplen HP500N was used as the injected thermoplastic material for evaluating the functional behavior and durability of 3D-printed inserts under typical molding conditions. The main technical data are summarized in the official ISO-based datasheet provided by the manufacturer (Figure 2.10).

Moplen® HP500N, provided by LyondellBasell, is a homopolymer polypropylene widely used for injection molding applications. It is characterized by good flowability, high stiffness, and excellent moldability, making it suitable for the fabrication of thin-walled components or parts requiring dimensional stability. According to the manufacturer, this grade also complies with food contact regulations, broadening its application range beyond industrial uses.

The material is commonly adopted for producing rigid packaging, household goods, and consumer products. Its mechanical profile includes a tensile modulus of 1400 MPa, a tensile strength at yield of 35 MPa, and a Charpy notched impact strength of 4 kJ/m² at 23 °C. In terms of thermal behavior, Moplen HP500N exhibits a Vicat Softening Temperature (VST) of 153 °C and a Heat Deflection Temperature (HDT, 0.45 MPa, unannealed) of 65 °C, according to ISO standards.

Technical Data Sheet

LyondellBasell

***Moplen* HP500N**

Polypropylene, Homopolymer

Product Description

Moplen HP500N is a homopolymer used for general purpose injection moulding applications. It exhibits good flow and stiffness. *Moplen* HP500N is suitable for food contact.
Moplen HP500N is UL listed under file E31765

Regulatory Status

For regulatory compliance information, see *Moplen* HP500N Product Stewardship Bulletin (PSB) and Safety Data Sheet (SDS).

Status	Commercial: Active
Availability	Africa-Middle East; Asia-Pacific; Europe
Application	Furniture; Housewares
Market	Compounding; Consumer Products; Rigid Packaging
Processing Method	Compounding; Injection Blow Molding
Attribute	Medium Flow; Medium Stiffness

Typical Properties	Nominal Value	Units	Test Method
Physical			
Melt Flow Rate, (230 °C/2.16 kg)	12	g/10 min	ISO 1133-1
Density	0.90	g/cm³	ISO 1183-1
Mechanical			
Tensile Modulus	1400	MPa	ISO 527-1, -2
Tensile Stress at Yield	35	MPa	ISO 527-1, -2
Tensile Strain at Break	> 50	%	ISO 527-1, -2
Tensile Strain at Yield	10	%	ISO 527-1, -2
Impact			
Charpy Impact Strength - Notched, (23 °C, Type 1, Edgewise, Notch A)	4	kJ/m²	ISO 179
Thermal			
Vicat Softening Temperature			
(A/50)	153	°C	ISO 306
(B50)	85	°C	ISO 306
Heat Deflection Temperature B, (0.45 MPa, Unannealed)	95	°C	ISO 75B-1, -2

Figure 2.10. Technical data sheet of Polypropylene Moplen HP500N [24]

2.2 Methodology

The following sections describe the main equipment and instruments used throughout the experimental activities of this work, all located at the Alessandria campus of Politecnico di Torino.

2.2.1 Processing tools and production-stage equipment

During this work, various tools and machines were used for processing and production. These include two different 3D printers (FlashForge Creator 3 Pro and G5 PRO by Piocreat) used for fabricating test specimens and mold inserts. Additional equipment such as the Brabender internal mixer for composite compounding and granulation tools supported material preparation prior to printing.

2.2.1.1 FlashForge Creator 3 Pro – Filament-based FFF Printer

The FlashForge Creator 3 Pro is a professional dual-extrusion 3D printer based on FFF (Fused Filament Fabrication) technology (Figure 2.11). It features two independent nozzles, enabling printing with either two different materials (e.g., structural + support) or two colors of the same material. It supports both Mirror Mode (simultaneous printing of mirrored parts) and Duplicate Mode (simultaneous printing of identical parts), making it suitable for prototyping and small-scale production.

Figure 2.11. FlashForge Creator 3 Pro printer

This machine offers a generous build volume of 300 × 250 × 200 mm, automatic bed leveling, HEPA filtration, and a resume-print function in case of power loss. Its maximum extrusion temperature is 320 °C, while the heated bed can reach 120 °C (Figure 2.12).

In this work, the FlashForge Creator 3 Pro was primarily used to print standard test specimens. The materials processed with this printer included PLA, HTPLA, and Carbon PA, all in filament form. The slicing software used was Simplify3D (Figure 2.13), and the nozzle diameter was set at 0.6 mm, chosen to improve flow rate and reduce printing time while maintaining dimensional accuracy.

Equipment Parameter	
Printer Name	Creator 3 Pro
Number of Extruder	2, independent
Printing Technology	Fused Filament Fabrication(FFF)
Touch Screen	4.3-inch color IPS Touch Screen
Build Volume	300×250×200mm
Layer Height	0.05 - 0.4mm
Printing Accuracy	±0.2mm
Positioning Accuracy	Z axis: 0.0025mm; XY axis: 0.011mm
Printing Filament	PLA/ABS/PETG/PA/PC/HIPS/ASA/PLA-CF/ PETG-CF/PACF/WOOD filament
Filament Diameter	1.75mm (±0.07mm)
Extruder Diameter	0.4mm
Printing Speed	10~150 mm/s
Software	FlashPrint
Supported Format	Input: 3MF/STL/OBJ/FPP/BMP/PNG/JPG/JPEG Output: GX/G
Operation System	Win XP/Vista/7/8/10、Mac OS、Linux
Printer Size	627×485×615mm
Net Weight	40Kg
Connectivity	USB Stick, Wi-Fi, Ethernet

Figure 2.12. Technical specifications of the FlashForge Creator 3 Pro printer [25]

The results obtained from these specimens will later be compared with those of the same materials printed using the G5 PRO pellet-based printer, as presented in Chapter 4.

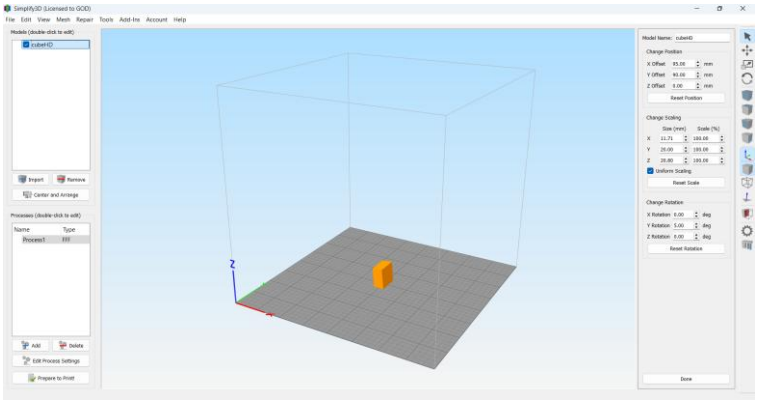

Figure 2.13. Simplify3D software

2.2.1.2 G5 PRO Piocreat – Pellet-based FGF printer

The G5 PRO Piocreat is an industrial-grade 3D printer based on Fused Granulate Fabrication (FGF) technology, used in this work to fabricate both test specimens and injection mold inserts starting from pelletized materials (Figure 2.14). A total of seven different materials were printed using this machine, including four pelletized commercial filaments (PLA, HTPLA, Carbon PA, and Copper Filament) and three customized PLA–Copper composites (60, 80, and 90 percent copper by weight), prepared using the Brabender mixer.

Figure 2.14. G5 PRO Piocreat printer

The G5 PRO features a screw-extrusion printhead capable of processing polymer pellets directly. It supports extrusion temperatures up to 400 °C and a heated bed that can reach 130 °C. The printer offers a large build volume of 500 × 500 × 500 mm, which accommodates the production of both standard samples and functional inserts (Figure 2.15). Pellets are loaded into a hopper and gravity-fed into the extruder, making the machine highly suitable for direct use with in-house formulated materials.

2. Equipment Parameters 设备参数

Basic Parameters 基本参数	
Model | 型号	G5 Pro
Printing Size | 成型尺寸	500X500X500mm
Molding Tech | 成型技术	FGF
Nozzle Number | 喷头数量	Single nozzle | 单喷头
Slice Thickness | 切片层厚	0.2-1.0mm
Nozzle Diameter | 喷嘴直径	0.4-2.0mm（可选3.0）
X-Y axis positioning accuracy | X-Y轴定位精度	±0.1mm
Filament | 打印材料	PLA/PETG/PETG+10%GF/ABS/PA6/PS/GPPS/PP/PP+30%GF/TPE/TPV/TPU/15-5PH and other composite materials | 等复合材料
Slice Software | 可兼容切片软件	Creality Print/Cura/Simplify3D
File Format | 切片支持格式	STL、OBJ、AMF、3DMF
File Transfer | 打印方式	Storage card | 存储卡脱机
Bed Temp | 热床最高温度	≤130℃
Nozzle Temp | 喷嘴最高温度	≤400℃
Resume Printing | 断电续打	YES | 支持
Auto Leveling | 自动调平	YES | 支持
AUX Leveling | 辅助调平	YES | 支持
Language | 语言	English/Chinese | 中英切换
Computer Operating System|电脑操作系统	Windows XP/7/8/10 MAC/Linux
Printing Speed | 打印速度	0~100mm/s
Power Supply | 额定电压	Input| 输入:AC100-240V 50/60Hz Output|输出:DC 24V
Nominal power | 额定功率	1.25KW

Figure 2.15. Technical specifications of the G5 PRO Piocreat printer [26]

A nozzle with a diameter of 0.8 mm was used for all prints. The printer includes both automatic and mechanical bed leveling functions and allows for manual adjustment of cooling settings. Process parameters and slicing operations were performed using the creality print software (Figure 2.16), which was specifically configured and optimized for each material used during the research.

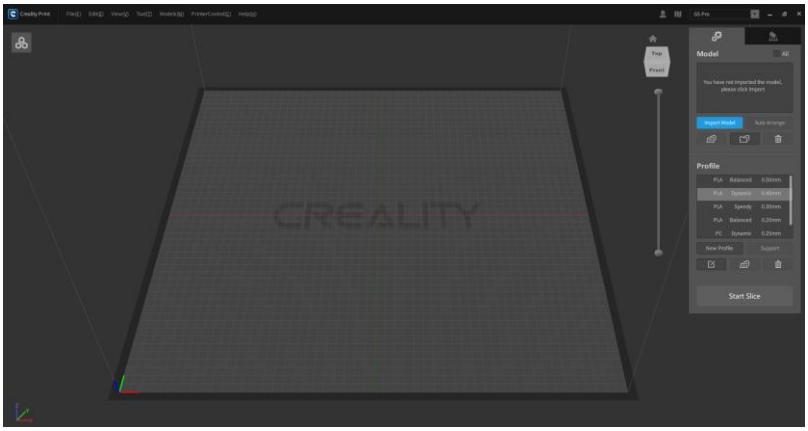

Figure 2.16. Creality Print software

The setup, calibration, and operational instructions for the G5 PRO, as well as optimization guidelines and practical troubleshooting, are described in detail in the Appendix section. The results obtained from this printer will later be compared with those of the FlashForge Creator 3 Pro, as discussed in Chapter 4.

2.2.1.3 Injection Molding Machine – Wittmann Battenfeld SmartPower 50

The injection molding phase was carried out using a Wittmann Battenfeld SmartPower 50 injection molding machine (screw diameter 25 mm). This servo-hydraulic press is characterized by a balanced four-column clamping system with a central piston transmission, ensuring uniform and symmetric force distribution across the mold (Figure 2.17). This design enhances mold protection and provides flexibility for installing a variety of molds with easy fluid connections. The plastification/injection unit is compact and accessible, allowing for quick setup and maintenance. The machine integrates a UNILOG B8 control unit, equipped with a rotatable industrial touchscreen interface and multiple user support modes for efficient parameter setup and process monitoring. The database system and integrated software library simplify repeated configurations. Additionally, the patented KERS system is implemented for energy recovery, converting kinetic energy into electric energy and storing it for reuse during subsequent phases, thereby improving the machine's energy efficiency.

Figure 2.17. Wittmann Battenfeld SmartPower 50 injection molding machine

2.2.1.4 Brabender Internal Mixer

The customized PLA–Copper composites were prepared using a Brabender internal mixer (Figure 2.18). The mixing process was carried out at 190 °C, starting with a rotation speed of 60 rpm for the first minute, followed by 95 rpm for the subsequent 2–3 minutes. This setup ensured efficient melt blending of PLA and copper powders, promoting uniform filler dispersion within the polymer matrix prior to granulation and 3D printing.

Figure 2.18. Brabender Internal Mixer

2.2.1.5 Piovan Granulator

The granulation process was performed using a piovan industrial granulator, designed for the efficient size reduction of thermoplastic materials (Figure 2.19). The composite produced via the Brabender internal mixer were introduced from the upper inlet of the granulator, where a high-speed rotating blade shredded the material into granules. These were then collected from the lower outlet chamber. The resulting pellets, suitable for further processing, were later used in 3D printing via the G5 PRO pellet-based system.

Since the granulated material exhibited some size inhomogeneity, a set of sieves with different mesh sizes was used to reduce the presence of oversized particles that could create problems such as nozzle clogging or inconsistent material flow during printing (Figure 2.20).

Figure 2.19. Piovan industrial granulator

Figure 2.20. Sieves with different mesh sizes

2.2.2 Characterization tools and analysis equipment

This subsection presents the instrumentation used to evaluate the thermal, mechanical, and morphological properties of the materials and printed samples.

2.2.2.1 Thermal Conductivity – Hot Disk TPS 2500 S

Thermal conductivity measurements were performed using the Hot Disk TPS 2500 S, shown in Figure 2.21, in accordance with ISO 22007-2. This instrument allows the evaluation of thermal transport properties, such as thermal conductivity, diffusivity, and

specific heat capacity, over a temperature range from –35 °C to 200 °C, using the transient plane source (TPS) technique.

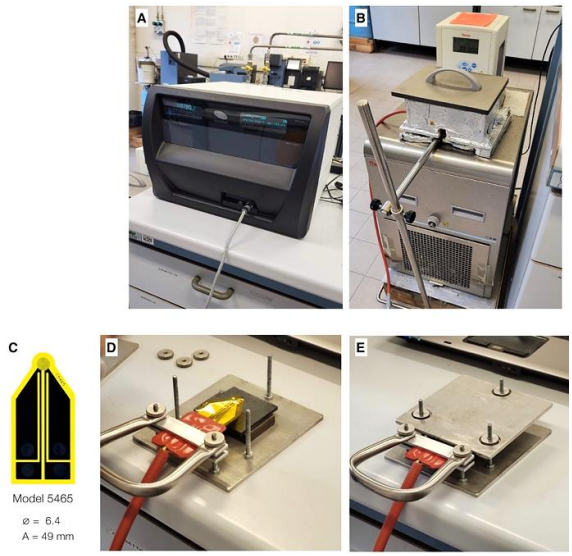

Figure 2.21. (A) Hot Disk TPS 2500 S; (B) Chiller; (C) Sensor 5465 in Kapton; (D, E) Arrangement of the specimens and the sensor between two metal plates

The system is based on a double-spiral sensor (Model 5465, radius 3.189 mm), made of nickel and laminated in Kapton, which functions simultaneously as both heating element and thermometer. The sensor is placed between two identical samples, forming a sandwich-like structure, and clamped between two metallic plates inside the apparatus to ensure optimal contact. For each measurement, two printed samples of dimensions 20 × 20 × 10 mm were used (Figure 2.22). The samples were gently polished to reduce surface roughness and improve sensor contact. Before testing, the assembled setup was thermally equilibrated in the chiller unit at 23 °C for approximately 20 minutes, to ensure thermal uniformity throughout the specimen.

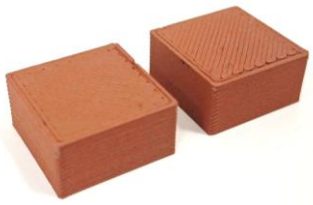

Figure 2.22. Printed samples for thermal conductivity measurement

The bulk–isotropic module was selected for all thermal conductivity measurements. Each test consisted of three scans, with a measurement time of 160 s, a power input of 30 mW, and an analysis depth of 10 mm.

2.2.2.2 Dynamic Mechanical Analysis (DMA) – TA Instruments Q800

Dynamic Mechanical Analysis (DMA) was employed to evaluate the thermo-mechanical response of the printed samples and to identify their glass transition temperature (Tg) and viscoelastic behavior. The tests were performed using TA Instruments Q800, a high precision instrument featuring a non-contact direct-drive motor, air bearing slide, and high-resolution optical encoder (Figure 2.23). These components ensure minimal mechanical compliance and allow accurate measurement of force, displacement, and viscoelastic parameters, even at very small strain amplitudes. The system is equipped with low-mass, high-stiffness clamps and an automated furnace, enabling highly stable temperature control and consistent sample handling across a wide testing range.

Figure 2.23. TA Instruments Q800

Two modes were adopted based on the geometry and mechanical properties of the specimens: single cantilever bending and controlled force tension. The printed specimens used for both configurations had dimensions of 35 × 10 × 2 mm (Figure 2.24).

Figure 2.24. Printed specimens for dynamic mechanical analysis

The tests provided key data including storage modulus (E′), loss modulus (E″), damping factor (tan δ), and displacement as functions of temperature. Figure 2.25 reports the equipment parameters.

Maximum Force		18 N
Minimum Force		0.0001 N
Force Resolution		0.00001 N
Strain Resolution		1 nanometer
Modulus Range		10^3 to $3x10^{12}$ Pa
Modulus Precision		± 1%
Tan δ Sensitivity		0.0001
Tan δ Resolution		0.00001
Frequency Range		0.01 to 200 Hz
Dynamic Sample Deformation Range		± 0.5 to 10 000 µm
Temperature Range		-150 to 600°C
Heating Rate		0.1 to 20°C/min
Cooling Rate		0.1 to 10°C/min
Isothermal Stability		± 0.1°C
Time/Temperature Superposition		Yes
RH Control		Optional
Output Values		
Storage Modulus	Complex/Dynamic Viscosity	Time
Loss Modulus	Creep Compliance	Stress/Strain
Storage/Loss Compliance	Relaxation Modulus	Frequency
Tan Delta (δ)	Static/Dynamic Force	Sample Stiffness
Complex Modulus	Temperature	Displacement
Relative Humidity (Optional)		

Figure 2.25. Technical specifications of TA Instruments Q800 [27]

2.2.2.2.1 DMA: Bending Cantilever Mode

The first DMA configuration used was the single cantilever bending mode, selected for its suitability in characterizing moderately rigid printed samples. In this mode, the specimen is clamped at one end and subjected to an oscillating force at the other, generating a bending deformation that reveals the viscoelastic behavior of the material (Figure 2.26).

The test was carried out on samples printed with dimensions of 35 × 10 × 2 mm. According to the instrument setup, the actual clamped length was 17.5 mm. The test was conducted using the following parameters:

- Mode: DMA Multi-Frequency - Strain
- Test: Temperature Ramp / Frequency Sweep
- Temperature range: from 35 °C to 150 °C
- Heating rate: 3 °C/min
- Frequency: 1 Hz
- Strain amplitude: 0.05%
- Clamp type: Single Cantilever

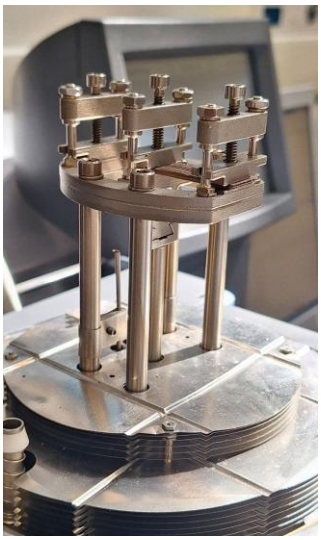

Figure 2.26. Single cantilever bending mode – DMA

The results obtained provided insight into the temperature-dependent stiffness and damping properties of the printed composites, helping to determine their performance under thermal stress. Additionally, the test conditions allowed for an approximate evaluation of the heat deflection temperature (HDT) through analysis of the storage modulus curve.

2.2.2.2.2 DMA: Controlled Force Tension Mode

A second DMA configuration was used: Controlled Force Tension, which allowed a direct analysis of dimensional stability and deformation over time. This method was introduced to evaluate the behavior of the printed samples under constant tensile load, to assess their mechanical reliability during thermal cycles typical of mold operation (Figure 2.27).

The same specimens used in the bending test were adopted, with dimensions of 35 × 10 × 2 mm, clamped in the tension film fixture. The test was conducted using the following parameters:

- Mode: DMA Controlled Force
- Test: Temperature Ramp / Controlled Force
- Temperature range: from room temperature to 120 °C
- Heating rate: 3 °C/min
- Applied force: 0.0001 N
- Clamp type: Tension Film

The goal of this test was to monitor the displacement of the material over time and temperature, providing key information about early deformation behavior, dimensional expansion, and softening. This configuration is especially relevant for printed inserts, where dimensional stability under thermal load is critical.

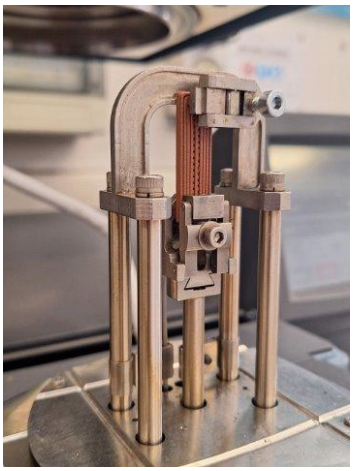

Figure 2.27. Controlled Force Tension – DMA

2.2.2.3 Compression Test – Instron 5966 Universal Testing Machine

Compression tests were carried out to assess the mechanical performance and dimensional stability of the printed specimens under load, simulating the stresses experienced by mold inserts during polymer injection cycles. The test was performed using an Instron 5966 universal testing machine, equipped with a 10 kN load cell and operated in displacement-controlled mode (Figure 2.29). The specimens were cubic blocks with dimensions of 12 × 12 × 10 mm, manufactured via 3D printing using the same formulations tested in previous sections (Figure 2.28).

Figure 2.28. Printed specimens for compression test

The test procedure included:

- Pre-load phase: displacement of 5.00 mm and trigger force of 15 N
- Test speed (Ramp 1): 1.00 mm/min (displacement-controlled)

- End criteria: The test was automatically stopped when one of the following conditions was reached:
  I. 90% force drop from peak
  II. Maximum force threshold of 10.00 kN
  III. Maximum displacement of 2.00 mm

Figure 2.29. Instron 5966 Universal Testing Machine

The purpose of this test was to evaluate the material's ability to maintain structural integrity under compression and repeated mechanical loading. The data obtained, such as compressive modulus and strain at yield or failure threshold, provide important indicators of the suitability of each formulation for tooling applications. Furthermore, understanding the early deformation response helps determine whether inserts can withstand mold closure and filling without significant distortion.

2.2.2.4 Morphological Characterization – SEM Zeiss EVO 15

Scanning Electron Microscopy (SEM) analysis was carried out using the Zeiss EVO 15 to investigate the morphology of the printed and processed materials (Figure 2.30). The SEM operates by directing a high-energy electron beam onto the specimen surface, generating signals such as secondary electrons (SE) and backscattered electrons (BSE), which provide topographical and compositional information, respectively.

Figure 2.30. SEM Zeiss EVO 15

SEM was performed on printed samples of HTPLA, Copper Filament, and PLA–Copper composites containing 60%, 80%, and 90% copper by weight, as well as on the copper powder used in the Brabender extrusion process. To examine the internal morphology of the printed specimens, DMA-tested samples were fractured in liquid nitrogen, enabling the observation of clean cross-sections ideal for morphological evaluation (Figure 2.31).

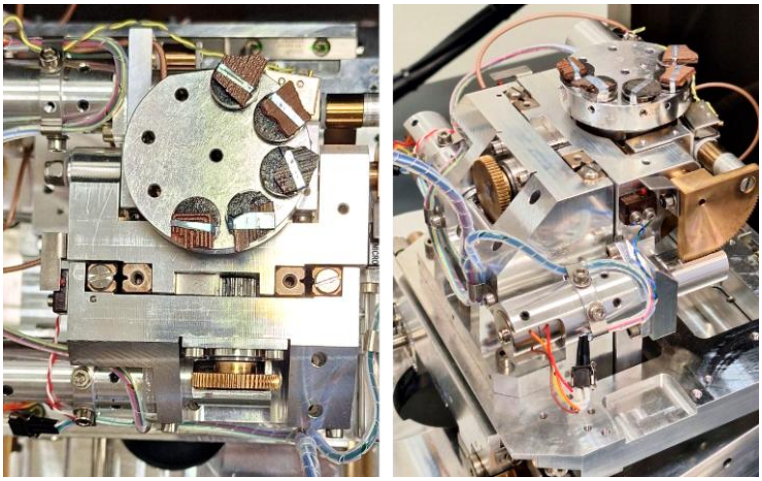

Figure 2.31. Samples mounted on the SEM sample holder

During the interaction between the electron beam and the material, different types of emission can occur. Secondary electrons are generated by inelastic collisions between the primary electrons and those in the sample; these provide primarily topographical information and are used to produce surface-detail images. Backscattered electrons, instead, are produced by elastic collisions with atomic nuclei and carry compositional contrast: the higher the atomic number of the element, the greater the intensity of

backscattered electrons. Consequently, in the resulting grayscale images, lighter areas indicate the presence of heavier elements, while darker regions correspond to lighter elements. Both SE and BSE images were collected for each material and will be analyzed in subsequent chapters to assess filler dispersion and microstructural features. Before SEM observation, all samples were coated with a thin conductive gold layer using an Agar Auto Sputter Coater, a mandatory preparation step to avoid charging effects and ensure high-quality imaging. The coating procedure is described in the following section.

2.2.2.5 Sample Coating – Agar Auto Sputter Coater

Prior to SEM analysis, all samples were coated with a thin layer of conductive gold using the Agar Auto Sputter Coater (Figure 2.32). This step is essential for non-conductive or partially conductive materials such as polymers and composites, which would otherwise accumulate surface charge under the electron beam, leading to image distortion or signal loss. The sputter coater operates under vacuum conditions and uses a low-pressure argon plasma to eject gold atoms from a target, which then deposit uniformly onto the surface of the samples mounted on the rotating holder. A visible purple plasma is generated during the process, indicating active coating. The machine allows adjustment of key parameters such as coating time, current, and vacuum level.

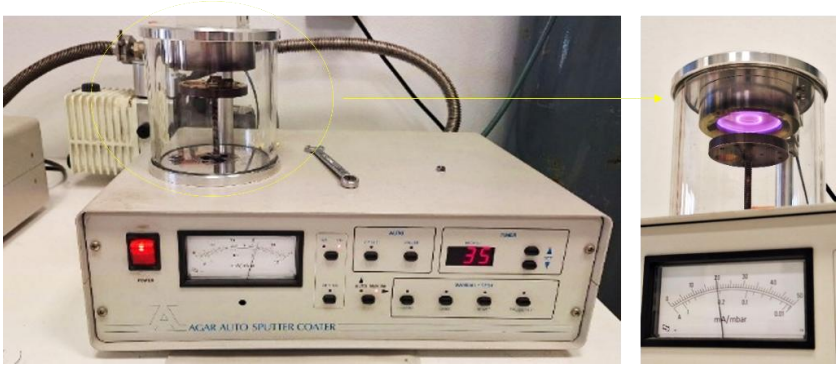

Figure 3.32. Agar Auto Sputter Coater

In this work, the coating was performed for 70 seconds at a plasma current of 30 mA. This ensured sufficient surface conductivity for high-resolution imaging, especially of internal fracture surfaces and particle distributions. The coated samples were then immediately transferred to the SEM chamber for imaging.

2.2.2.6 Particle Size Distribution Analysis – Malvern Mastersizer 3000

The particle size distribution (PSD) of the copper powder used for composite preparation was evaluated to better understand its granulometry and its potential impact on dispersion

and mechanical behavior within the polymer matrix. Measurements were performed on dry powder samples using a Malvern Mastersizer 3000 laser diffraction particle size analyzer, equipped with the Aero S dry powder dispersion unit, as shown in Figure 2.33.

Figure 2.33. Malvern Mastersizer 3000 with Aero S dry dispersion unit

In this method, the angular variation in the intensity of light scattered by the particles is measured as they pass through a laser beam, and particle size is calculated using Mie theory, assuming spherical geometry. For the present analysis, measurements were conducted with a feed rate set to 15 % and a carrier gas pressure of 3.0 bar, applying the copper reflectivity coefficient from the Malvern optical property database.

The Aero S unit ensured controlled and reproducible dispersion by accelerating the particles through a venturi using compressed air, minimizing agglomeration while avoiding excessive particle breakage. The system's wide dynamic range (0.1–3500 µm for dry mode) allowed accurate capture of the full size distribution of the powder.

This approach provided rapid and statistically reliable estimations of D10, D50, and D90 values. The data obtained from the PSD analysis were later correlated with composite processing performance and are discussed in subsequent chapters.

2.2.2.7 Thermographic Monitoring – Optris PI 640i & Optris PIX Connect

To evaluate the thermal behavior of different areas of the mold during the injection process, an infrared thermographic camera (Optris PI 640i) combined with the Optris PIX Connect software was employed. This setup enabled the observation of heat dissipation across the printed composite inserts inside the mold, as well as the cavity surface, allowing comparison with standard steel (1.2083) and highlighting the thermal response of materials reinforced with copper. The camera was mounted on the upper frame of the injection molding machine, aimed directly at the mold, to capture real-time temperature

variations during key stages of the cycle, including mold opening, polymer injection, holding, and part ejection, as shown in Figure 2.34. Representative thermal images were recorded to support later thermal and process analyses, and the Optris PIX Connect software interface used for image acquisition and temperature mapping is presented in Figure 2.35.

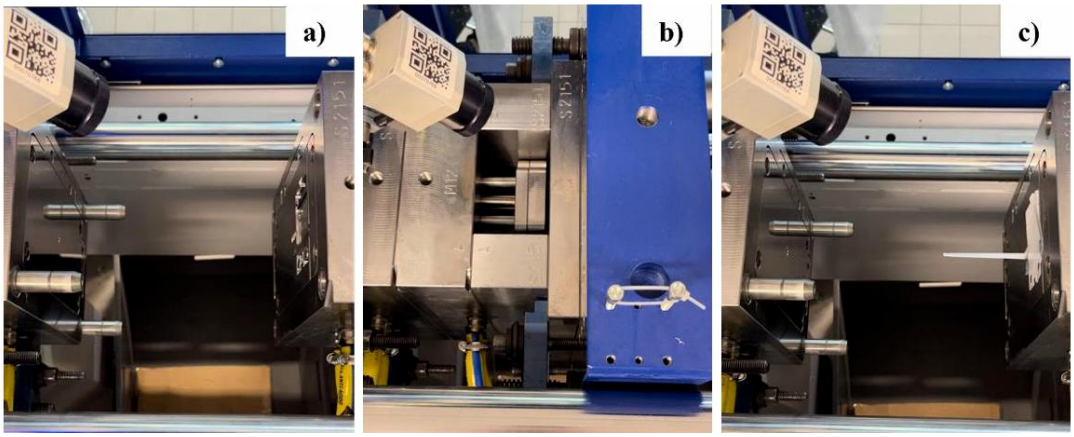

Figure 2.34. Infrared camera Optris PI 640i mounted on the upper part of the injection molding press to measure the cavity temperatures of the mold during the injection molding cycle. The images show different stages of the production cycle: (a) mold open immediately after part ejection, (b) mold closed for molten polymer injection and holding, and (c) part extraction

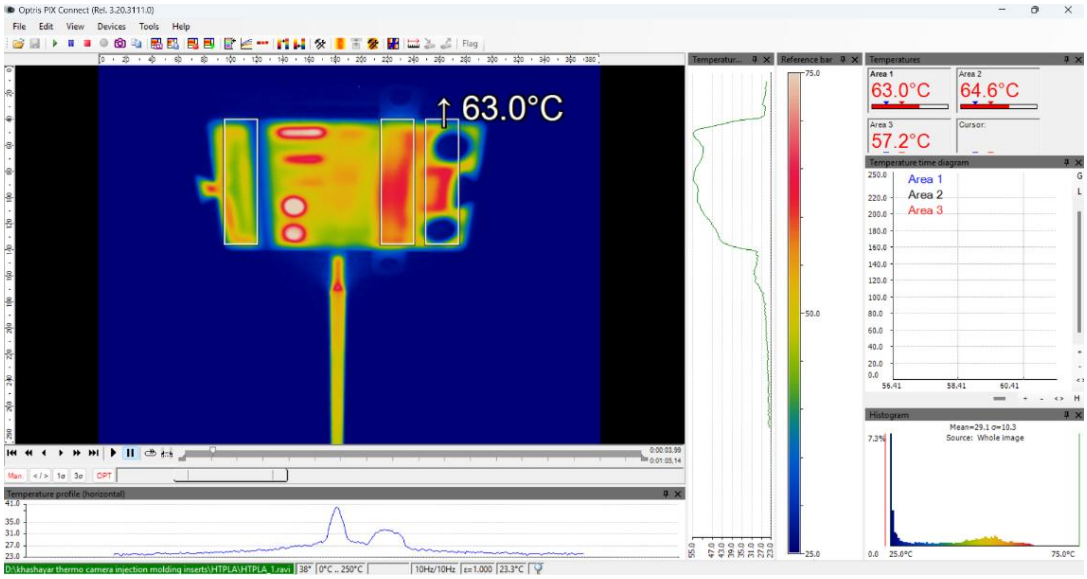

Figure 2.35. Optris PIX Connect software interface showing real-time mold temperature mapping during injection molding

The detailed technical specifications and performance characteristics of the Optris PI 640i infrared camera, including optical resolution, thermal sensitivity, spectral range, and operating temperature limits, are reported in Figure 2.36.

optris **PI 640i**
TECHNICAL DATA

optris
infrared measurements

Thermography in VGA resolution

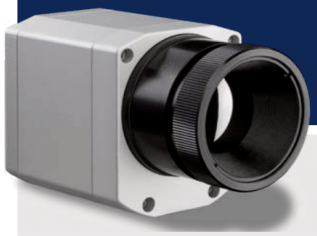

Features:

- 640 x 480 pixels
- Superb thermal sensitivity of 40 mK
- Radiometric video recording with 32 Hz / 125 Hz in subframe mode
- Interchangeable lenses: 15°, 33°, 60° and 90°
- Licence-free analysis software and complete SDK inclusive

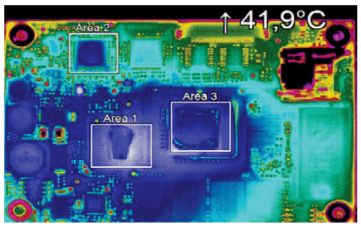

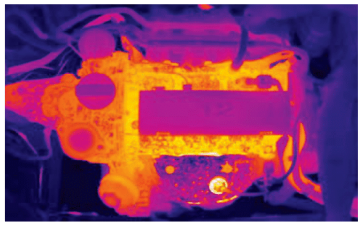

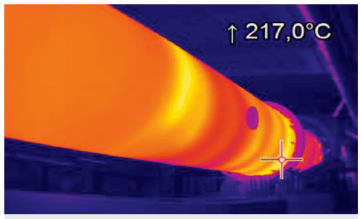

For further information as well as the product configurator, please visit:
www.optris.global/thermal-imager-optris-pi-640

Technical specifications

Optical resolution	640 x 480 pixels
Detector	FPA, uncooled (17 µm x 17 µm)
Spectral range	8 – 14 µm
Temperature ranges	–20 ... 100 °C, 0 ... 250 °C, (20) 150 ... 900 °C[1)] optional temperature range: 200 ... 1500 °C
Frame rate	32 Hz / 125 Hz @ 640 x 120 pixels
Optics (FOV)	15° x 11° FOV / f = 41.5 mm or 33° x 25° FOV / f = 18.7 mm or 60° x 45° FOV / f = 10.5 mm or 90° x 64° FOV / f = 7.7 mm
Thermal sensitivity (NETD)	40 mK
Accuracy	±2 °C or ±2 %, whichever is greater
PC interface	USB 2.0 / optional USB GigE (PoE) interface
Process interface (PIF), standard	0 – 10 V input, digital input (max. 24 V), 0 – 10 V output
Process interface (PIF), industrial	2x 0 – 10 V input, digital input (max. 24 V), 3x 0/4 – 20 mA outputs, 3x relay (0 – 30 V/ 400 mA), fail-safe relay
Cable length (USB)	1 m (standard), 5 m, 10 m, 20 m 5 m and 10 m also as high temperature USB cable (180 or 250 °C)
Ambient temperature	0 ... 50 °C
Storage temperature	– 40 ... 85 °C
Relative humidity	20 – 80 %, non-condensing
Enclosure (size / rating)	46 x 56 x 76 – 100 mm (depending on lens + focus position) / IP 67 (NEMA)
Weight	269 - 340 g (depending on lens)
Shock / Vibration [2)]	IEC 60068-2-27 (25G and 50G) / IEC 60068-2-6 (sinus shaped), IEC 60068-2-64 (broadband noise)
Tripod mount	¼ - 20 UNC
Power supply	via USB
Scope of supply	• USB camera with 1 lens • USB cable (1 m) • Table tripod • Standard PIF with cable (1 m) and terminal block • Software package optris PIX Connect • Hard transport case

[1)] Accuracy effective starting at 150 °C
[2)] For more details see operator's manual

Figure 2.36. Technical data sheet of Optris PI 640i thermographic camera [28]

2.2.2.8 Pelletizer of Filaments – Thermo Scientific™ VariCut Pelletizer

To enable pellet-based printing on the G5 PRO system, commercial filaments were pelletized using a Thermo Scientific™ VariCut Pelletizer (Figure 2.37).

Figure 2.37. Thermo Scientific™ VariCut Pelletizer

The equipment granulates the extruded strands into uniform pellets, providing a consistent feedstock for the printer's pellet extruder. In this study, PLA, HTPLA, Carbon PA, and Copper Filament were pelletized to obtain suitable feedstock for FGF printing.

2.2.2.9 Filament Dryer – PrintDry™

To minimize moisture absorption and improve extrusion quality, all hygroscopic filaments were dried prior to printing using the PrintDry™ filament dryer (Figure 2.38). Controlled heating removed absorbed water, reducing defects such as bubbling and poor adhesion. For highly hygroscopic materials, including PLA blends, Carbon PA, and composite filaments, drying was performed immediately before and during printing by feeding filament directly from the dryer into the extruder.

Figure 2.38. Filament Dryer – PrintDry™

2.2.2.10 Vacuum Induction Gas Atomization (VIGA) – PSI Hermiga 100/10

The Vacuum Induction Melting Inert Gas Atomization (VIGA) system, model PSI Hermiga 100/10, is employed to produce high-quality metallic powders. In this process, the feedstock is melted in an induction-heated crucible under vacuum, ensuring minimal contamination and accurate control of melt composition. The molten stream is then fragmented by a high-pressure jet of inert gas (argon, nitrogen, or helium), which produces fine droplets that solidify rapidly in a water-cooled atomization chamber. This method yields spherical powders with narrow particle size distributions, typically between 10 and 100 µm, with rapid solidification rates in the order of 10^5–10^6 K/s [29].

The copper powder used in this work, described in the previous section, was produced with this VIGA system at the facilities in Alessandria, ensuring the required purity and granulometry for subsequent processing and composite fabrication. Figure 2.39 shows the Gas Atomization system, PSI Hermiga 100/10, while Figure 2.40 reports the technical datasheet of the equipment.

Figure 2.39. Gas Atomization system, PSI Hermiga 100/10

Phoenix Scientific Industries

High performance process solutions

HERMIGA 100/10 VI ATOMISER

Typical system data

Crucible Type:	Induction heated crucible
Crucible Capacity:	1.5 litre (approximately 10 kg steel)
Atomisation Die Type:	Supersonic invariable type 'close-coupled' die
Atomisation Rate:	Typically 2—4 kg/minute of steel
Typical Median (d_{50}):	In range 10 to 100 µm
Melt Chamber:	Side opening, water cooled, 304L stainless steel
Atomisation Chamber:	Water cooled, 304L stainless steel
Powder Handling:	High efficiency cyclone, partial and HEPA filters
Power Requirement:	100kVA, 3 phase, 50—60 Hz
Water Requirement:	Approx. 70 litres/min, 5 bar
Gas Requirement:	Argon/Nitrogen/Helium max 6kg/min. Min pressure 20 bar.
Systems Size (L x D x H):	Dimensions of 6.0 m x 5.1 m x 5.7 m
System Weight:	5 Tonnes

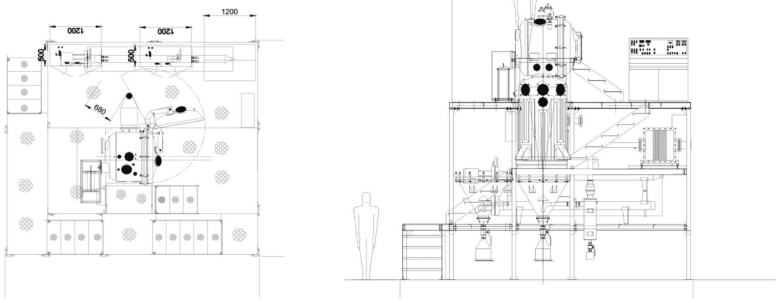

PSI Ltd - Apex Business Park - Hailsham - East Sussex BN27 3JU - United Kingdom

Phone: +44 (0)1323 449001 - Fax: +44 (0)1323 449002 - E-mail: info@psiltd.co.uk - www.psiltd.co.uk

Document Reference: Y:\MASTERS\MASTER SPECS\Hermiga 100\C1 HERMIGA 100 10 - Rev 2.pub

Figure 2.40. Technical datasheet of PSI Hermiga 100/10 [29]

Chapter 3

RESULTS AND DISCUSSION

This chapter presents the results of the experimental tests carried out during this work. All results shown refer exclusively to samples printed using the G5 PRO printer. The chapter is divided into two main sections: the first focuses on the characterization of commercial pelletized filaments, and the second on the preparation and characterization of custom-developed PLA–Copper composites.

3.1 Characterization of commercial filaments

This section is divided into five subsections, each dedicated to a specific experimental analysis performed on the four commercial filaments used in this study: PLA, HTPLA, Carbon PA, and Copper Filament. All materials were first pelletized using the instrument described in the previous chapter, to be compatible with the G5 PRO pellet-fed 3D printer. Before each test, the printed samples underwent different specific thermal treatment to ensure consistent and comparable conditions across all materials.

3.1.1 Thermal Conductivity

Thermal conductivity tests were carried out on all materials using the Hot Disk TPS 2500 S, as described in the previous chapter. The printed samples used for the measurements had dimensions of 20 × 20 × 10 mm, ensuring proper contact with the sensor for consistent readings. No thermal treatment was applied prior to testing, as previous studies have shown that such treatment does not significantly influence the thermal conductivity.

3.1.1.1 PLA

The thermal conductivity test was performed on the PLA sample using the method described in the previous chapter. The printed specimen used is shown in Figure 3.1, and the corresponding results are reported in Table 3.1.

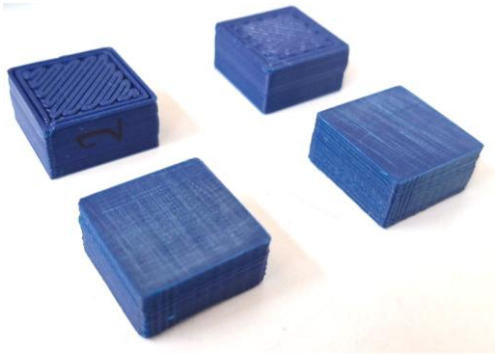

Figure 3.1. PLA samples printed for thermal conductivity measurements

And

Table 3.1. Thermal conductivity results of PLA samples

PLA	**Thermal Conductivity W/(m·K)**
Scan 1	0.164
Scan 2	0.164
Scan 3	0.164
Average	**0.164**
Standard deviation	0.000

3.1.1.2 HTPLA

The thermal conductivity test was performed on the HTPLA sample using the method described before. The printed specimen used is shown in Figure 3.2, and the corresponding results are reported in Table 3.2.

Figure 3.2. HTPLA samples printed for thermal conductivity measurements

And

Table 3.2. Thermal conductivity results of HTPLA samples

HTPLA	Thermal Conductivity W/(m·K)
Scan 1	0.530
Scan 2	0.526
Scan 3	0.531
Average	**0.529**
Standard deviation	0.002

The results indicate that the thermal conductivity of HTPLA is approximately 3.2 times higher than that of PLA, suggesting a significantly enhanced heat transfer capability. This makes HTPLA a promising option for applications such as inserts in molds, where efficient heat dissipation is critical. The improvement also highlights the effect of copper particles embedded within this commercial filament.

3.1.1.3 Carbon PA

The thermal conductivity test was performed on the Carbon PA samples. The printed specimen used is shown in Figure 3.3, and the corresponding results are reported in Table 3.3.

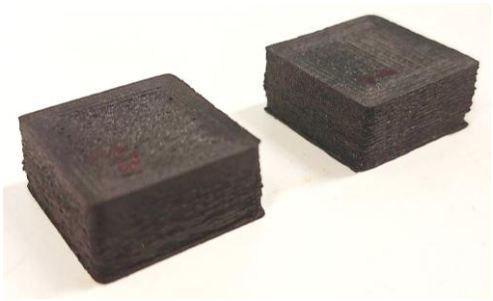

Figure 3.3. Carbon PA samples printed for thermal conductivity measurements

And

Table 3.3. Thermal conductivity results of Carbon PA samples

Carbon PA	Thermal Conductivity W/(m·K)
Scan 1	0.532
Scan 2	0.532
Scan 3	0.532
Average	**0.532**
Standard deviation	0.000

The results show that the thermal conductivity of Carbon PA is slightly higher than that of HTPLA, confirming its potential for thermal applications. However, Carbon PA has a significantly lower density (approximately 1.4 g/cm³ compared to 2.3 g/cm³ for HTPLA), which may be advantageous in applications where weight reduction is important. This balance between thermal performance and low density makes Carbon PA an interesting candidate for insert or tooling design where both thermal and mechanical constraints must be considered.

3.1.1.4 Copper Filament

The thermal conductivity test was performed on the Copper Filament samples. The printed specimen used is shown in Figure 3.4, and the corresponding results are reported in Table 3.4.

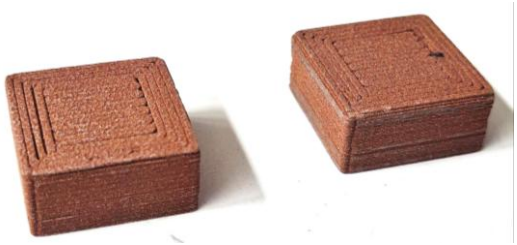

Figure 3.4. Copper Filament samples printed for thermal conductivity measurements

And

Table 3.4. Thermal conductivity results of Copper Filament samples

Copper Filament	**Thermal Conductivity W/(m·K)**
Scan 1	1.620
Scan 2	1.626
Scan 3	1.604
Average	**1.616**
Standard deviation	0.009

The results show that Copper Filament exhibits the highest thermal conductivity among all tested materials, with an average value of 1.616 W/(m·K). This represents an increase of approximately:

- 9.85 times higher than PLA
- 3.05 times higher than HTPLA
- 3.03 times higher than Carbon PA

These values suggest that Copper Filament is a very promising material for thermal applications, where efficient heat dissipation is critical. However, it should also be noted that Copper Filament has a significantly higher density compared to the other materials:

- 3.6 times heavier than PLA
- 2 times heavier than HTPLA
- 3.2 times heavier than Carbon PA

This makes Copper Filament thermally effective, but potentially less favorable in weight-sensitive applications.

3.1.2 Compression Test

Compression tests were conducted using the procedure described in the previous chapter. The printed samples used for all materials had dimensions of 12 × 12 × 10 mm, and thermal treatment was applied prior to testing to ensure consistent mechanical behavior. For each material (PLA, HTPLA, Carbon PA, and Copper Filament) the test was performed on three to four printed samples to ensure repeatability and reliability.

This test is particularly relevant because the insert inside a mold is subjected to high compressive pressures during the injection process. Therefore, the material used must be able to withstand such stresses without deformation or failure, maintaining dimensional stability and mechanical integrity under cyclic loading.

The following subsections report and analyze the results obtained for each material.

3.1.2.1 PLA

Prior to testing, the PLA samples were thermally treated at 80 °C for 1 hour. The tested specimen is shown in Figure 3.5, and the corresponding compression results are reported in Figure 3.6.

Figure 3.5. PLA samples printed for compression test

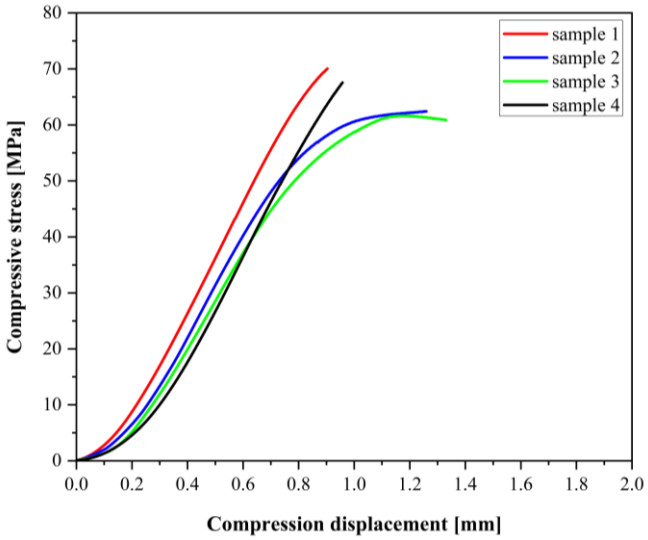

Figure 3.6. Compression test results of PLA samples

By calculating the averages from the tested specimens, the compressive modulus of PLA was found to be 892.11 ± 65.33 MPa, while the maximum compressive stress reached an average of 65.43 ± 4.05 MPa, as shown in Table 3.5.

Table 3.5. Mechanical properties of PLA specimens under compression

Sample	Young's Modulus [MPa]	Maximum Force [N]	Compressive Stress at Maximum Force [MPa]
1	941.94	10000.05	70.06
2	871.26	9005.79	62.44
3	808.82	8766.69	61.65
4	946.42	10000.01	67.57
Average	**892.11**	**9443.14**	**65.43**
Standard deviation	65.33	650.41	4.05

3.1.2.2 HTPLA

Similar to PLA, the HTPLA samples underwent thermal treatment at 80 °C for 1 hour before testing. The tested specimen is shown in Figure 3.7, and the results of the compression test are reported in Figure 3.8.

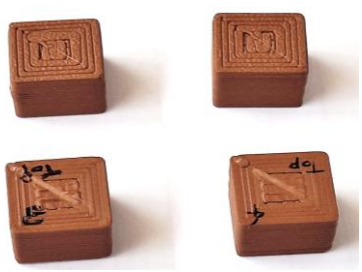

Figure 3.7. HTPLA samples printed for compression test

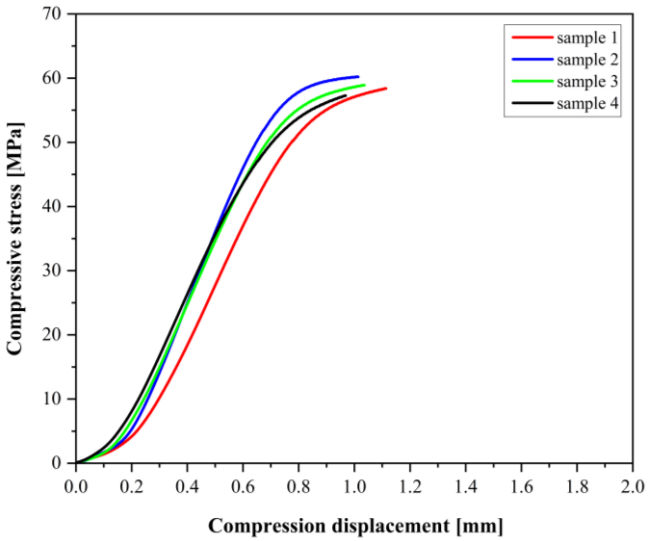

Figure 3.8. Compression test results of HTPLA samples

By calculating the averages from the tested specimens, the compressive modulus of HTPLA was found to be 908.48 ± 66.37 MPa, while the maximum compressive stress reached an average of 58.71 ± 1.22 MPa, as shown in Table 3.6.

Table 3.6. Mechanical properties of HTPLA specimens under compression

Sample	Young's Modulus [MPa]	Maximum Force [N]	Compressive Stress at Maximum Force [MPa]
1	859.77	9405.25	58.40
2	1004.23	9186.97	60.23
3	901.80	9334.36	58.94
4	868.13	9094.88	57.29
Average	**908.48**	**9255.37**	**58.71**
Standard deviation	66.37	140.40	1.22

3.1.2.3 Carbon PA

Carbon PA samples were thermally treated at 120 °C for 1 hour prior to testing. The tested specimen is shown in Figure 3.9, and the results of the compression test are presented in Figure 3.10.

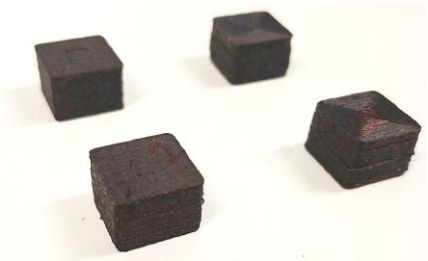

Figure 3.9. Carbon PA samples printed for compression test

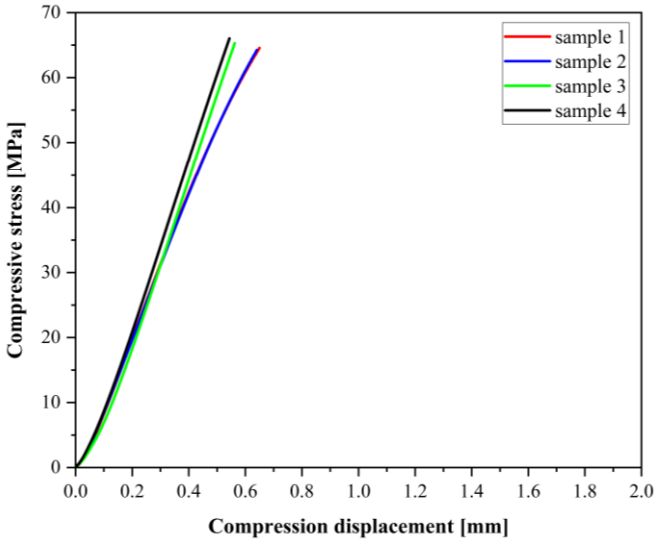

Figure 3.10. Compression test results of Carbon PA samples

By calculating the averages from the tested specimens, the compressive modulus of Carbon PA was found to be 1085.72 ± 90.46 MPa, while the maximum compressive stress reached an average of 65.05 ± 0.80 MPa, as shown in Table 3.7, which is higher than both HTPLA and PLA, a result attributed to the reinforcing effect of the carbon fibers.

Table 3.7. Mechanical properties of Carbon PA specimens under compression

Sample	Young's Modulus [MPa]	Maximum Force [N]	Compressive Stress at Maximum Force [MPa]
1	1019.58	10000.19	64.57
2	996.09	10000.02	64.26
3	1161.56	10000.01	65.30
4	1165.65	10000.23	66.05
Average	**1085.72**	**10000.11**	**65.05**
Standard deviation	90.46	0.11	0.80

3.1.2.4 Copper Filament

Copper Filament samples underwent thermal treatment at 80 °C for 1 hour before testing. The specimen used is shown in Figure 3.11, and the results of the compression test are presented in Figure 3.12.

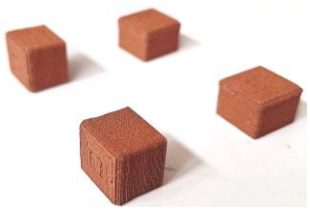

Figure 3.11. Copper Filament samples printed for compression test

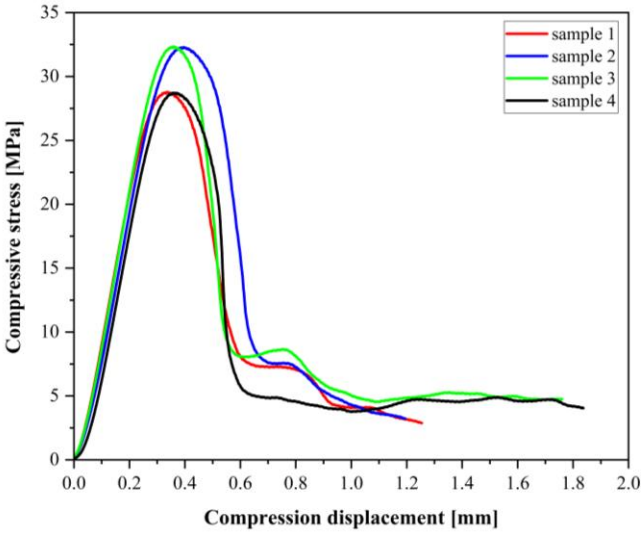

Figure 3.12. Compression test results of Copper Filament samples

By calculating the averages from the tested specimens, the compressive modulus of Copper Filament was found to be 1182.15 ± 25.89 MPa, while the maximum compressive stress reached an average of 30.54 ± 2.06 MPa, as shown in Table 3.8. Although Copper Filament exhibits the highest compressive modulus among the commercial filaments, this stiffness comes at the cost of ductility. The high copper content increases rigidity, resulting in a steeper elastic response; however, the same filler concentration also disrupts matrix continuity and reduces the material's ability to undergo plastic deformation. As a result, despite its superior stiffness, Copper Filament demonstrates brittle behavior under compression. This represents a critical trade-off to consider in applications requiring both thermal conductivity and mechanical resilience, especially for insert components used in molds.

Table 3.8. Mechanical properties of Copper Filament specimens under compression

Sample	Young's Modulus [MPa]	Maximum Force [N]	Compressive Stress at Maximum Force [MPa]
1	1190.37	4144.63	28.78
2	1164.39	4787.60	32.30
3	1215.05	4762.51	32.34
4	1158.78	4194.01	28.72
Average	**1182.15**	**4472.19**	**30.54**
Standard deviation	25.89	350.45	2.06

Unlike the other materials, Copper Filament exhibited a markedly non-linear stress–strain behavior under compression. Some specimens began to crack during the test (as shown in Figure 3.13), indicating brittle failure and a sudden drop in load-bearing capacity after

reaching peak stress. This mechanical response is attributed to the high copper content in the composite. While copper significantly enhances thermal conductivity, it also compromises the ductility of the polymer matrix.

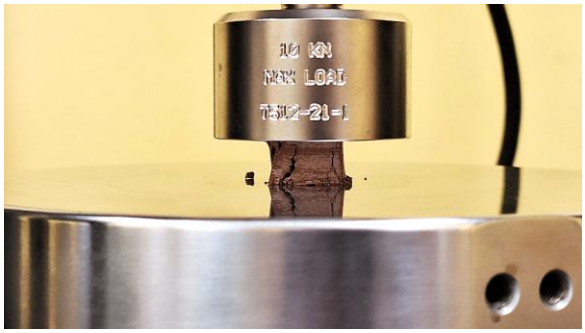

Figure 3.13. Crack propagation during compression testing of Copper Filament specimens

The high filler content (in this case, 90% copper for Copper Filament) interrupts the continuity of the polymer structure, facilitating crack initiation and propagation. Moreover, if the interfacial adhesion between copper particles and the PLA matrix is not strong enough, it further limits stress transfer efficiency and exacerbates brittleness. Therefore, although copper-rich composites like Copper Filament offer significant thermal advantages, their mechanical brittleness under compressive loads must be carefully considered for structural applications such as mold inserts.

3.1.3 Dynamic Mechanical Analysis – Bending Mode

This analysis was carried out using the method previously described. The printed specimens had dimensions of 35 × 10 × 2 mm and were subjected to thermal treatment prior to testing. One of the main goals of this test was to evaluate the storage modulus (E′) and determine the Heat Deflection Temperature (HDT) of each material. Understanding the HDT is essential for evaluating the suitability of each material for use in mold inserts. If the HDT is lower than the EOF temperature predicted by Moldex3D simulations, the material is unsuitable for use as an insert, as demonstrated in the case of PLA.

3.1.3.1 PLA

The DMA test in bending mode (single cantilever) was performed on PLA samples after thermal treatment at 80 °C for 1 hour. The sample used is shown in Figure 3.14, and the results of the test are illustrated in Figure 3.15.

Figure 3.14. PLA samples printed for DMA test

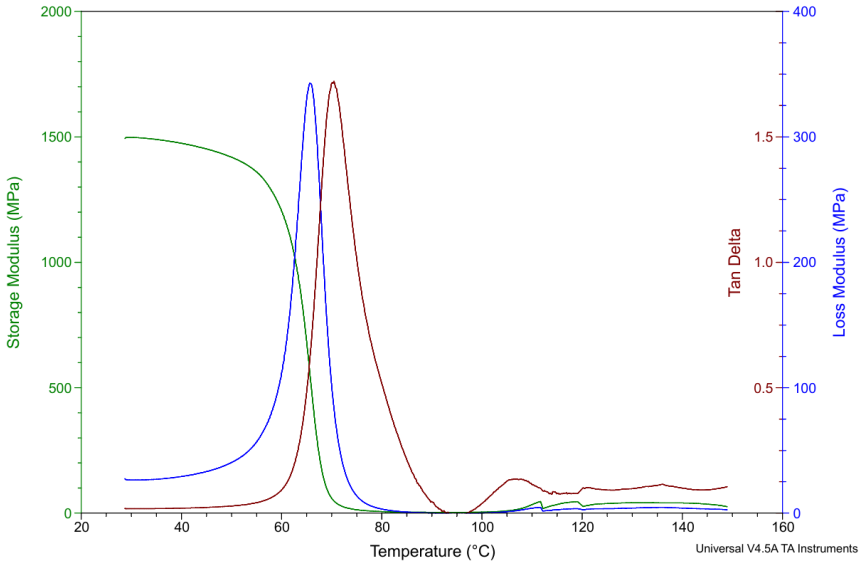

Figure 3.15. DMA (bending mode) test results of PLA samples

The storage modulus decreases with temperature, and the HDT is identified at approximately 64°C, where the storage modulus drops below 800 MPa [30].

3.1.3.2 HTPLA

The printed HTPLA samples underwent a thermal treatment of 1 hour at 80 °C before testing. The test was performed following the method described in the previous chapter. The sample is shown in Figure 3.16, and the results are presented in Figure 3.17.

Figure 3.16. HTPLA samples printed for DMA test

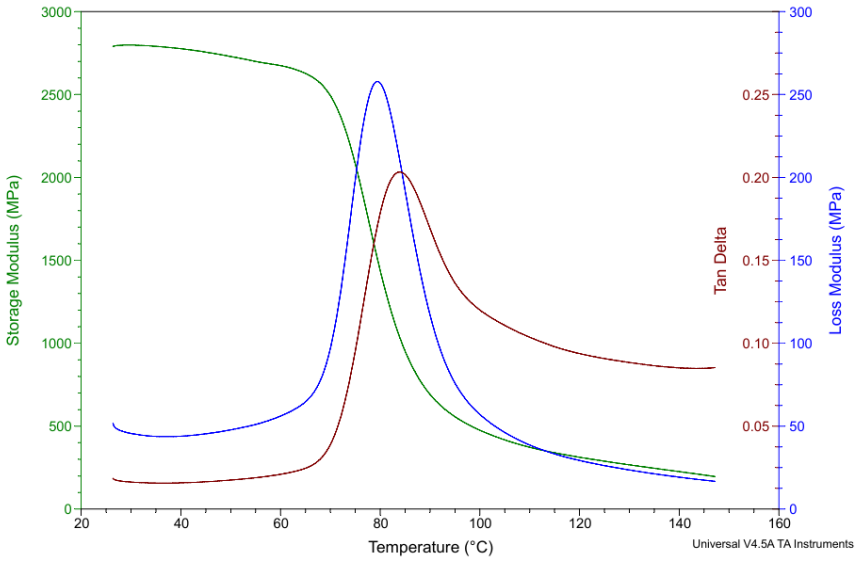

Figure 3.17. DMA (bending mode) test results of HTPLA samples

From the storage modulus curve, the HDT (defined as the temperature where the modulus drops below 800 MPa) was found to be approximately 87.5°C. This is significantly higher than the value observed for PLA, due to the different PLA matrix nature and the presence of copper in the formulation.

3.1.3.3 Carbon PA

The Carbon PA sample was subjected to a thermal treatment of 1 hour at 120 °C prior to testing. The test followed the previously described method, with the sample and results shown in Figure 3.18 and Figure 3.19, respectively.

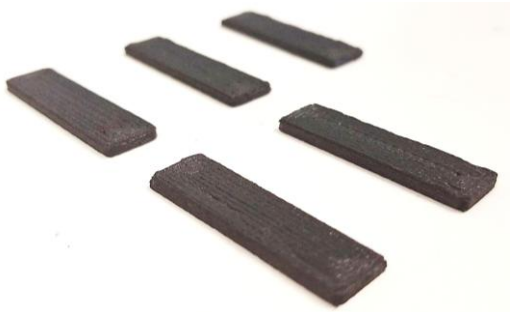

Figure 3.18. Carbon PA samples printed for DMA test

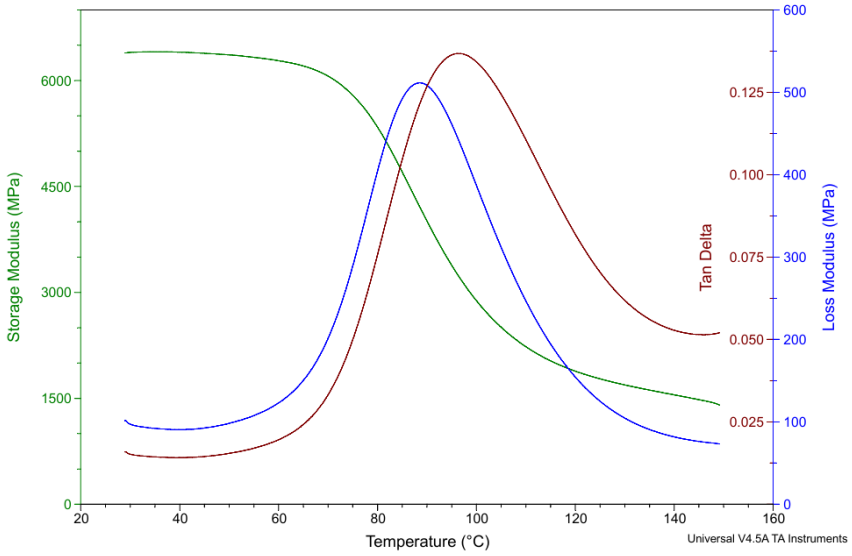

Figure 3.19. DMA (bending mode) test results of Carbon PA samples

From the storage modulus curve, it is evident that the material maintains a modulus above 800 MPa throughout the entire temperature range analyzed. Therefore, its HDT exceeds 150 °C, making Carbon PA the most thermally stable option among the commercial filaments tested. This confirms its suitability for demanding thermal applications such as mold inserts.

3.1.3.4 Copper Filament

The Copper Filament sample underwent a thermal treatment of 1 hour at 80 °C before testing. The test method followed the procedure described previously. The tested specimen and the results are shown in Figure 3.20 and Figure 3.21.

Figure 3.20. Copper Filament samples printed for DMA test

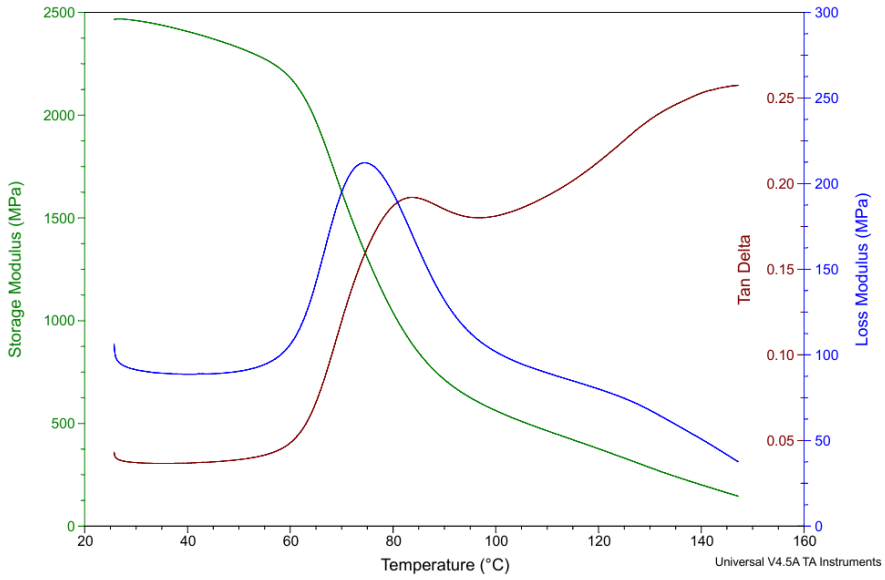

Figure 3.21. DMA (bending mode) test results of Copper Filament samples

From the storage modulus curve, the HDT is approximately 86.5 °C. Its HDT is lower than Carbon PA, which may influence its performance under extreme thermal loads. Additionally, Figure 3.22 presents the DMA (bending mode) test results for all samples, including PLA, HTPLA, Carbon PA, and Copper Filament, with particular focus on the storage modulus (E′).

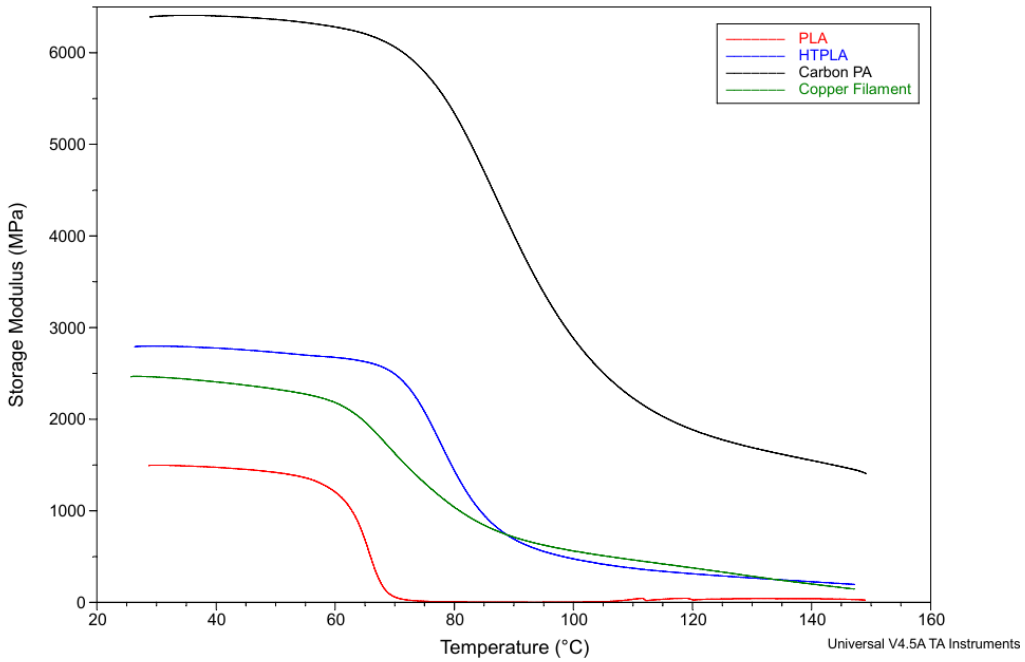

Figure 3.22. DMA (bending mode) test results for all commercial samples

3.1.4 Dynamic Mechanical Analysis – Tension Mode

This section presents the results of the DMA tests conducted in tension mode on commercial pelletized filament samples. The same thermal treatment was applied as before, and specimens were prepared with dimensions of 35 × 10 × 2 mm, identical to those used in the bending mode analysis. This test measures the displacement behavior of materials under thermal loading, which is particularly relevant for mold inserts, as they must withstand both elevated temperatures and mechanical stress during injection molding.

3.1.4.1 PLA

The DMA test in tension mode was performed on PLA samples after thermal treatment at 80 °C for 1 hour. The sample used is shown in Figure 3.23, and the results of the test are illustrated in Figure 3.24.

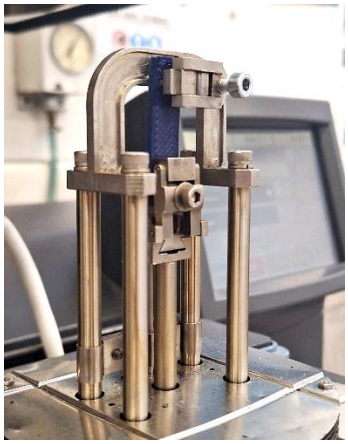

Figure 3.23. PLA sample printed for DMA test

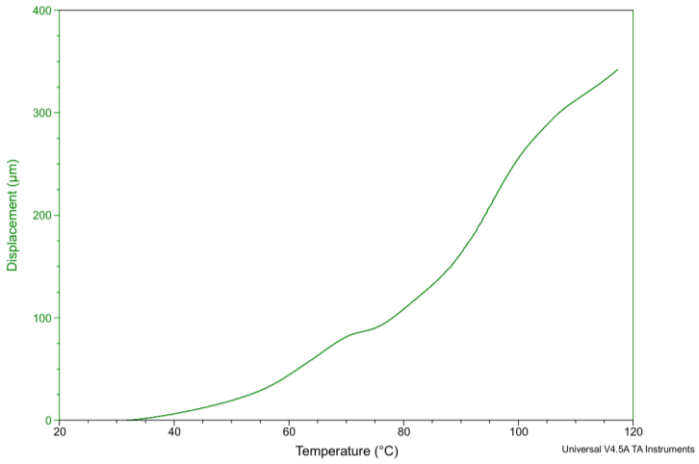

Figure 3.24. DMA (tension mode) test results of PLA samples

The maximum displacement observed during the test was approximately 360 µm.

3.1.4.2 HTPLA

The DMA test in tension mode was performed on HTPLA samples after thermal treatment at 80 °C for 1 hour. The sample used is shown in Figure 3.25, and the results of the test are illustrated in Figure 3.26.

Figure 3.25. HTPLA sample printed for DMA test

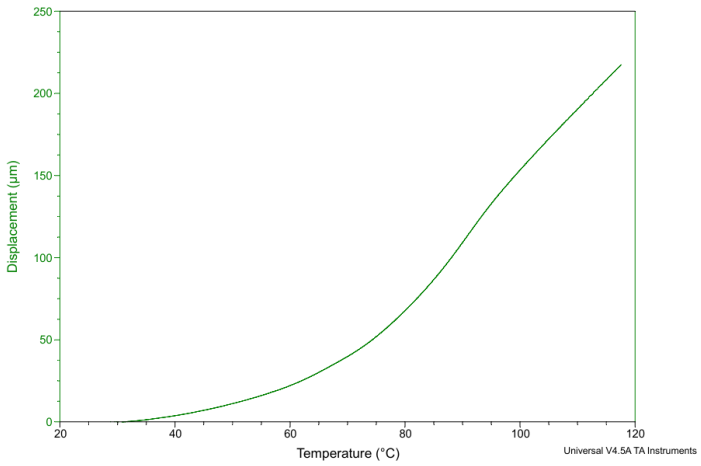

Figure 3.26. DMA (tension mode) test results of HTPLA samples

The maximum displacement observed during the test was approximately 217 µm, confirming better thermal dimensional stability than PLA.

3.1.4.3 Carbon PA

The DMA test in tension mode was performed on Carbon PA samples after thermal treatment at 120 °C for 1 hour. The sample used is shown in Figure 3.27, and the results of the test are presented in Figure 3.28.

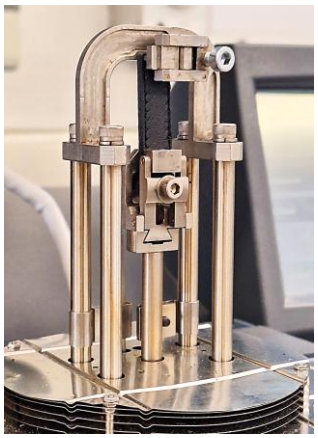

Figure 3.27. Carbon PA sample printed for DMA test

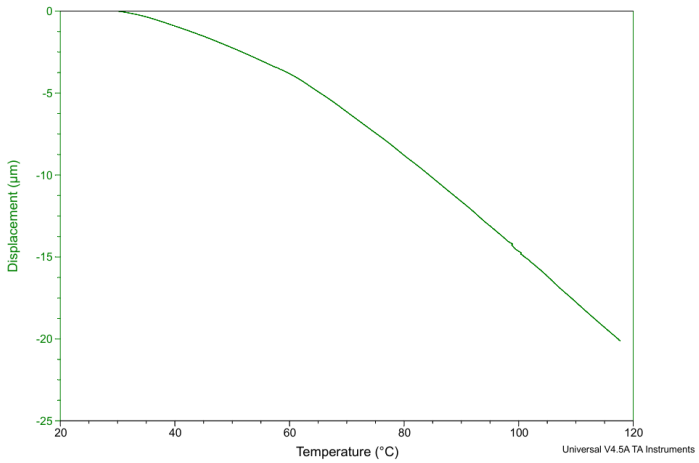

Figure 3.28. DMA (tension mode) test results of Carbon PA samples

Unlike the other tested materials, the Carbon PA sample exhibited a negative displacement trend, with a maximum contraction of approximately −22 µm over the temperature range investigated. This indicates slight shrinkage rather than expansion with increasing temperature. It can be hypothesized that this effect is attributable to the reinforcing carbon fibers within the polymer matrix. The fibers may restrict the overall thermal expansion of the PA matrix and, due to anisotropic stress distribution, induce a net contraction under thermal load. This dimensional stability could be particularly advantageous for insert applications, where preservation of geometry under thermal cycling is critical.

3.1.4.4 Copper Filament

The DMA test in tension mode was performed on Copper Filament samples after thermal treatment at 80 °C for 1 hour. The sample used is shown in Figure 3.29, and the results are illustrated in Figure 3.30.

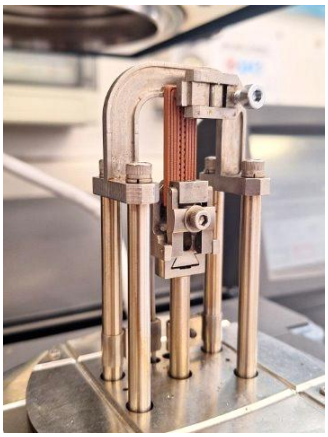

Figure 3.29. Copper Filament sample printed for DMA test

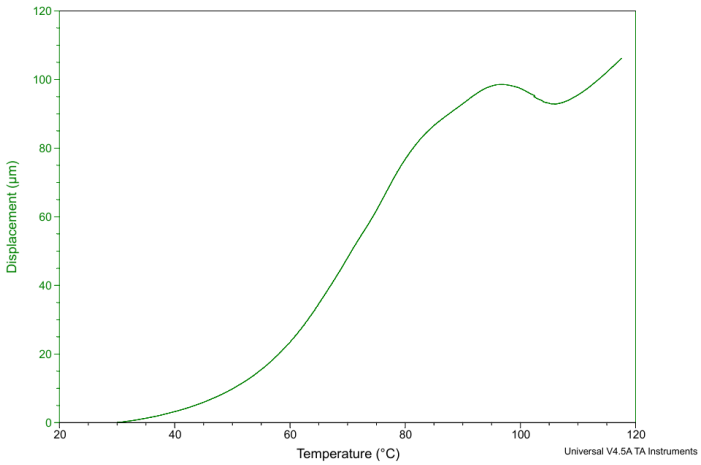

Figure 3.30. DMA (tension mode) test results of Copper Filament samples

Copper Filament showed a steady displacement increase with temperature, with a maximum displacement of approximately 106 µm. This relatively low expansion, compared to PLA and HTPLA, reflects the dimensional stability introduced by the high copper filler content, which helps reduce thermal elongation. Notably, the maximum displacement observed for PLA and HTPLA was approximately 3.4 times and 2 times higher than Copper Filament, respectively.

Although Copper Filament showed greater brittleness and lower compressive strength compared to HTPLA, its behavior under thermal tensile loading reveals a different characteristic. Despite being mechanically more fragile, Copper Filament exhibited significantly lower displacement, which is not contradictory but rather indicative of its composition. The high copper filler content in Copper Filament, being rigid and thermally stable, effectively suppresses thermal expansion. In contrast, HTPLA, with a more ductile polymer matrix and lower filler content, allows for greater elongation. Therefore, while

HTPLA performs better mechanically, Copper Filament demonstrates superior dimensional stability and higher thermal conductivity under thermal stress, thanks to the dominant influence of copper particles in both constraining deformation and enhancing heat dissipation.

Additionally, Figure 3.31 compares the DMA results in tension mode for all samples (PLA, HTPLA, Carbon PA, and Copper Filament), providing a direct overview of the displacement behavior across the different materials.

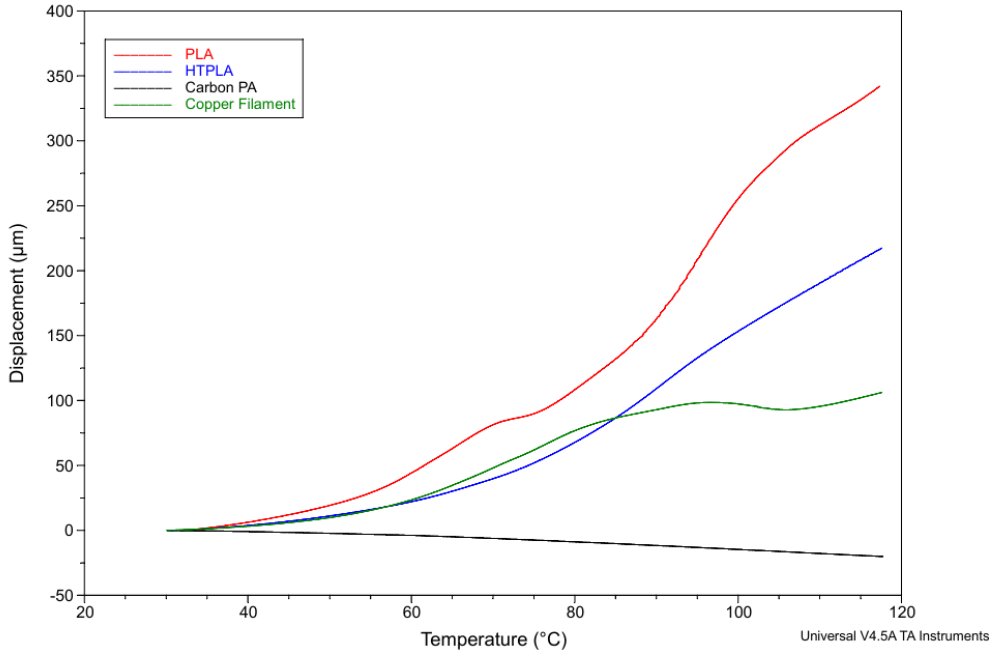

Figure 3.31. DMA (tension mode) test results for all commercial samples

3.1.5 Scanning Electron Microscopy (SEM) Analysis

As described in the previous chapter, morphological analysis was performed using the SEM Zeiss EVO 15. Before imaging, all specimens were coated using the Agar Auto Sputter Coater, a mandatory step to ensure proper surface conductivity. For each sample, two types of SEM images were acquired: Secondary Electron (SE) mode for surface morphology and High Definition Backscattered Electron (HDBSD) mode for compositional contrast.

SEM analysis was conducted only on HTPLA and Copper Filament to compare the size and distribution of copper particles, their adhesion to the PLA matrix, and other morphological aspects with those of the PLA–Copper composites produced via

Brabender. The SEM analysis of the PLA–Copper composites and the copper powder used for their formulation will be presented at the end of this chapter.

3.1.5.1 HTPLA

To understand the internal morphology of the HTPLA filament reinforced with copper, Scanning Electron Microscopy (SEM) was carried out. This analysis is essential to assess the shape, size, and distribution of copper particles within the polymer matrix, as well as their interaction with the PLA structure. A well-dispersed and homogeneous copper distribution is crucial for ensuring effective thermal conductivity, as localized agglomerations or voids can reduce heat dissipation efficiency and compromise mechanical stability.

As shown in Figure 3.32, the cross-section of the filament reveals a generally uniform distribution of copper particles, visible as bright spots throughout the matrix. The SEM image was acquired in HDBSD mode and highlights how the particles are well dispersed, with only minimal signs of agglomeration.

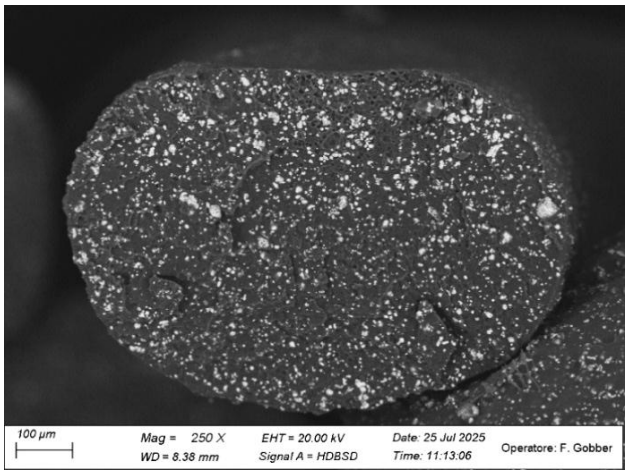

Figure 3.32. SEM cross-section of HTPLA at 250× (HDBSD mode)

As shown in Figure 3.33, the panel displays SEM images of HTPLA at two magnifications (150× and 65×) and under both HDBSD and SE detection modes. At 150×, the cross-sectional views of individual filaments confirm uniform filament geometry and a consistent filler distribution. The HDBSD mode (top left) highlights the presence of copper particles embedded within the matrix, while the SE mode (top right) better reveals surface morphology and extrusion quality. At the lower magnification (65×, bottom row), the printed structure is clearly visible. The width and length of the extruded layers can be distinctly observed, reflecting the geometry maintained during the printing process. While

some voids are visible between the layers, they are not significant and do not indicate major interfacial defects.

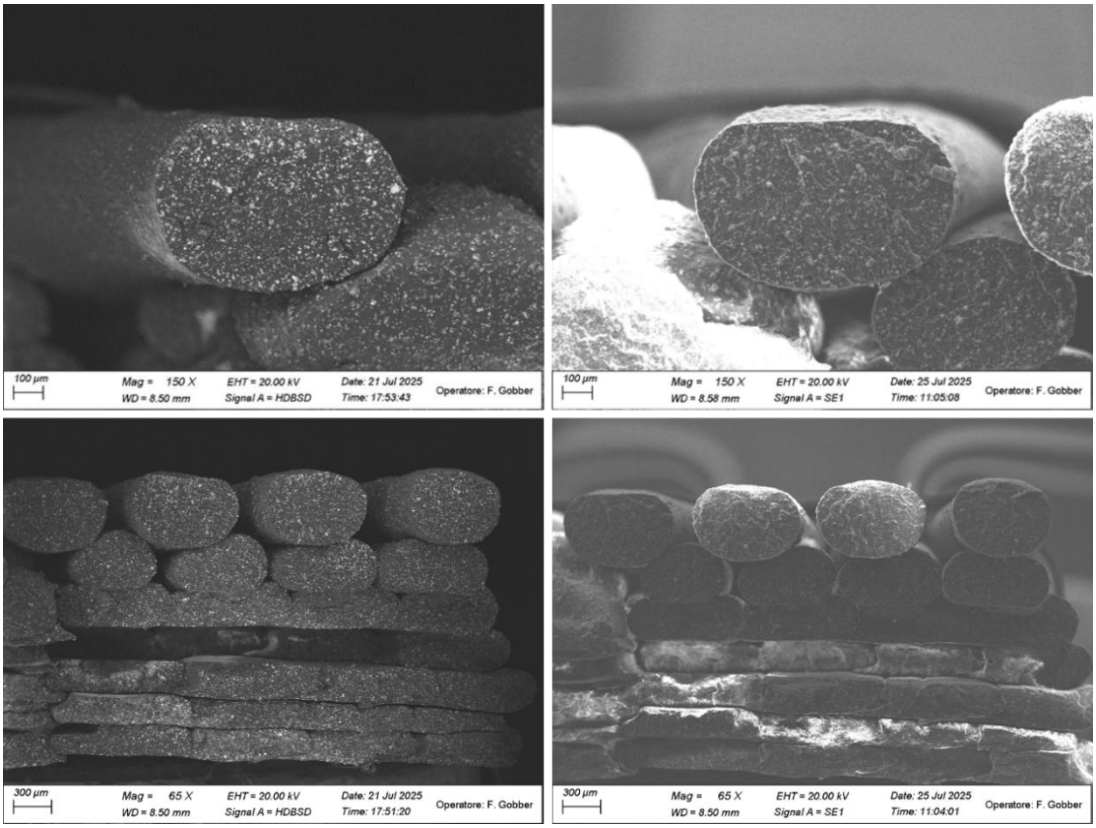

Figure 3.33. SEM images of HTPLA at 150× and 65× magnifications in HDBSD and SE modes

As shown in Figure 3.34, a deeper investigation of the copper particles embedded within the HTPLA matrix reveals a heterogeneous distribution of particle sizes, ranging approximately from 7 µm to over 45 µm. The particles exhibit irregular shapes and a rough surface morphology, strongly indicating that they are water atomized rather than gas atomized. This irregularity results from the rapid solidification characteristic of water atomization processes.

The rough surface texture and non-spherical geometry may improve mechanical interlocking between the copper particles and the polymer matrix, which could contribute to increased stiffness. However, such irregularities might also introduce local stress concentrations that could influence the ductility of the composite. The morphology of HTPLA will be compared with that of PLA–Copper composites produced using the Brabender system in future sections.

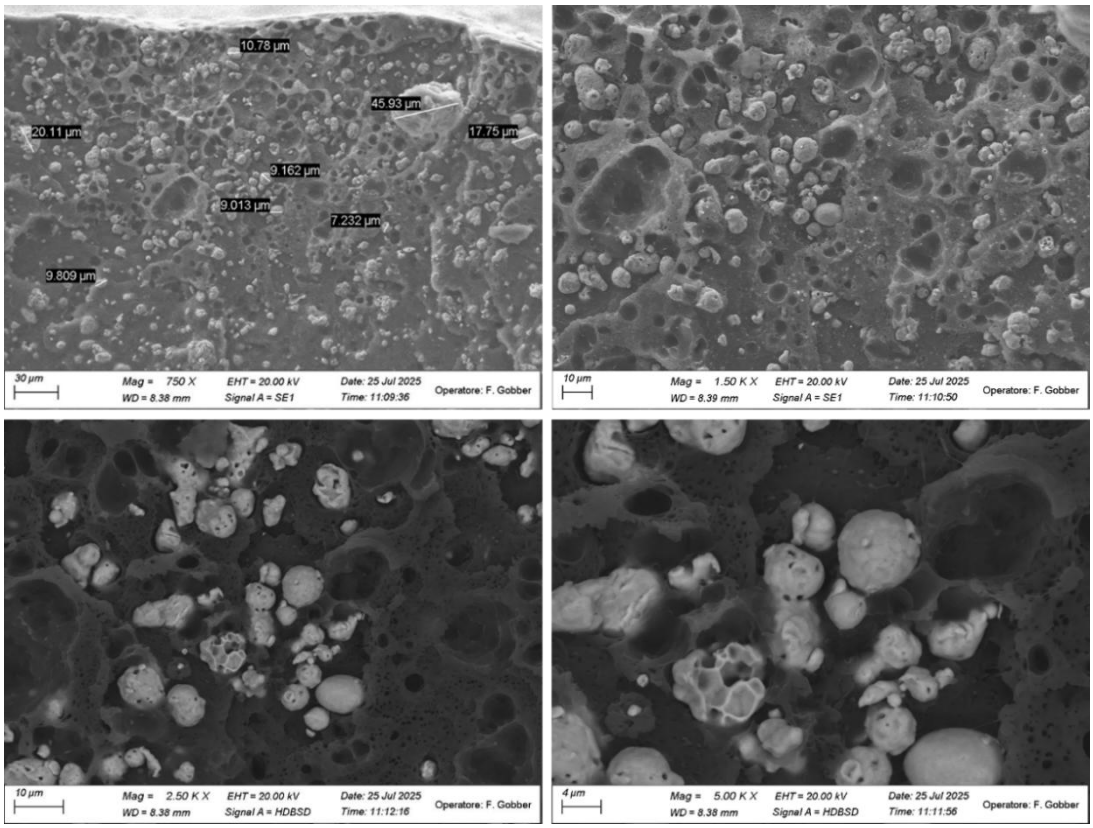

Figure 3.34. SEM images of HTPLA at different magnifications in SE and HDBSD modes

3.1.5.2 Copper Filament

The SEM images in Figure 3.35 show the microstructure of the Copper Filament material, characterized by an extremely high concentration of copper filler. Compared to HTPLA, the copper particles in Copper Filament appear much more densely packed and uniformly distributed, creating a nearly continuous metallic phase within the polymer matrix.

The particles are predominantly spherical, smooth, and fine, which strongly suggests the use of gas atomized copper powder rather than water atomized. Gas atomization typically results in more uniform particle sizes and better flowability, which aids in consistent dispersion during compounding.

The HDBSD images highlight the distinct brightness of copper, making it easy to distinguish the metallic phase. The matrix shows good embedding around the particles; however, the high filler load may compromise toughness, as reflected in the compression tests. This densely packed microstructure supports the very high thermal conductivity measured for Copper Filament, while also explaining its brittle mechanical behavior, due to the reduced polymer volume fraction and limited matrix continuity.

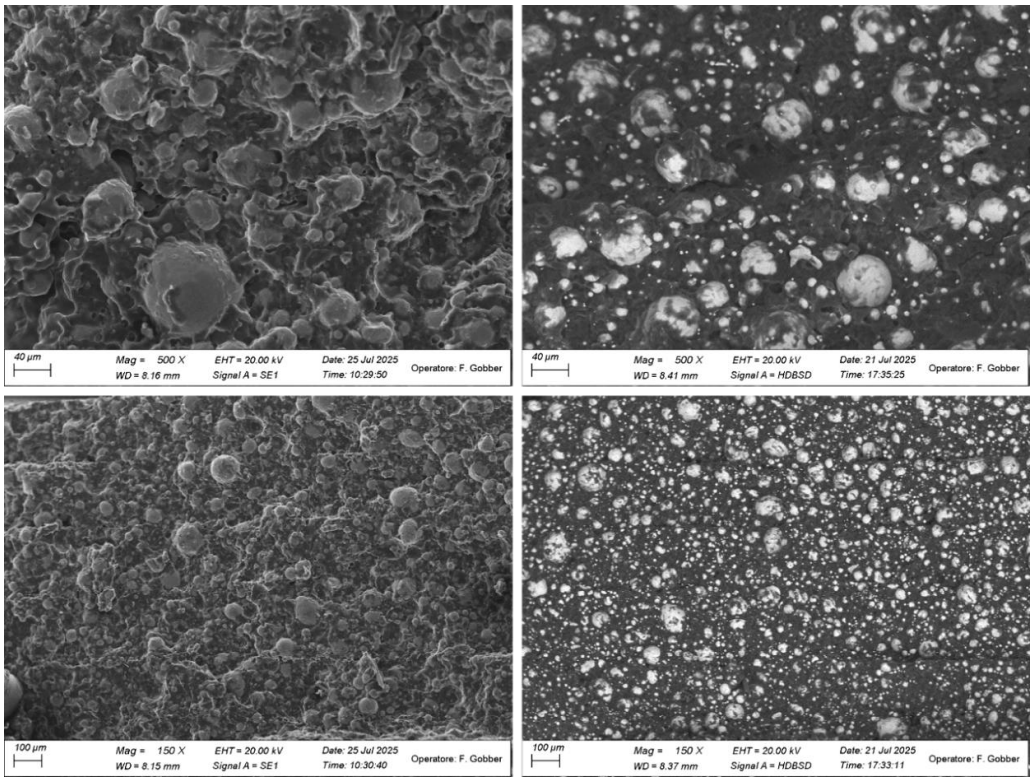

Figure 3.35. SEM images of Copper Filament at 500× and 150× magnifications in HDBSD and SE modes

Figure 3.36 shows copper particles with diameters ranging from ~20 µm to over 100 µm, indicating a broad size distribution with noticeable heterogeneity.

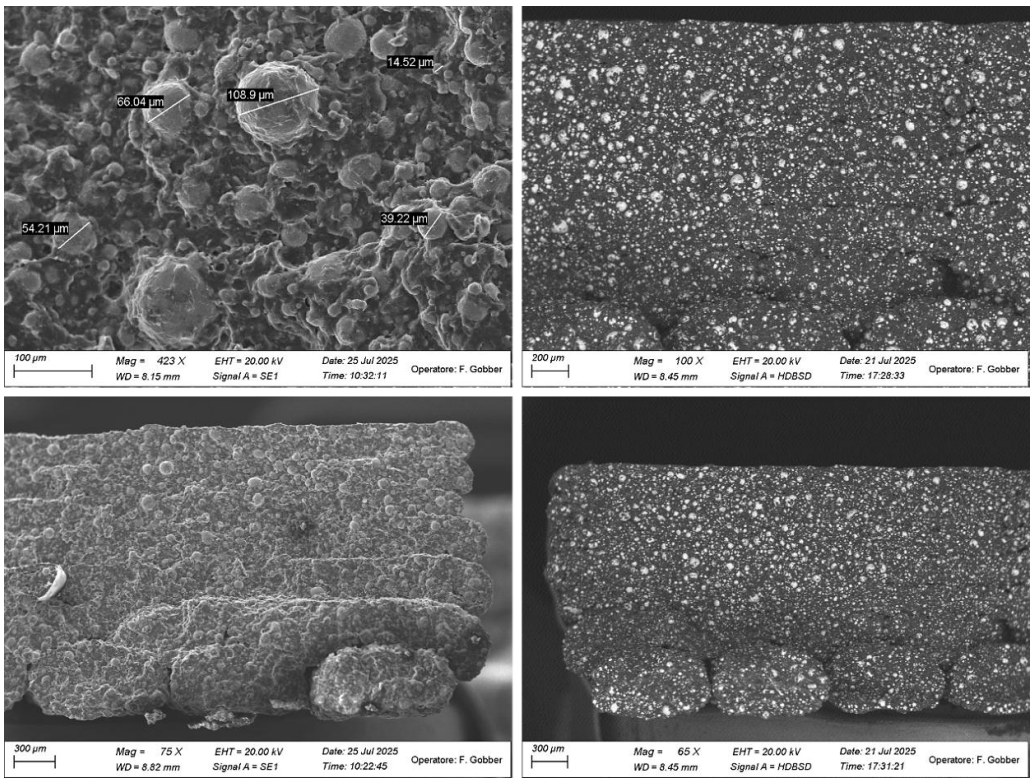

Figure 3.36. SEM images of Copper Filament at different magnifications in SE and HDBSD modes

Additionally, in one of the cross-sectional SEM images (Figure 3.37), the presence of elongated, fiber-like structures is observed within the matrix. These could be residual fibers from the production process and merit further investigation. Their orientation and integration may play a role in the mechanical performance and structural integrity of the printed parts.

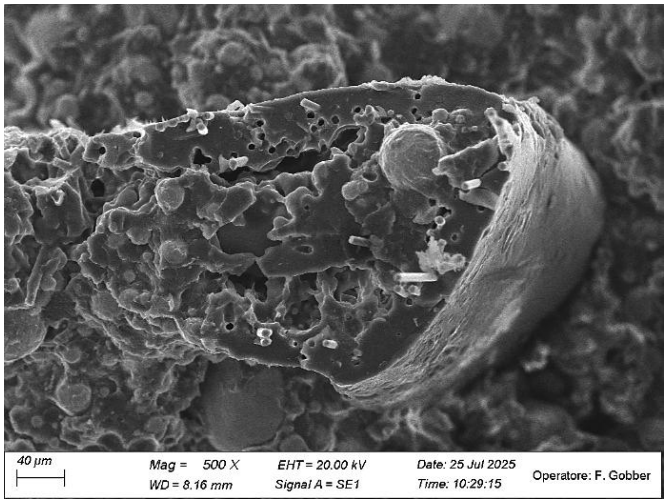

Figure 3.37. SEM image of Copper Filament cross-section highlighting elongated fiber-like structures embedded in the matrix

Overall, the SEM analysis of Copper Filament confirms a highly engineered filament structure with excellent copper dispersion, spherical particle morphology. The microstructural observations presented here will later be compared with those of the custom PLA–Copper composites developed via Brabender mixer, to better understand how particle morphology, size distribution, and processing techniques influence the final performance of printed inserts.

3.2 Preparation and characterization of PLA–Copper composites

To ensure independence from commercial filaments and to access specific material formulations that are not always commercially available, it was necessary to develop custom feedstock materials compatible with the G5 PRO printer. In many cases, commercial filaments can be costly, limited in availability, or lack the desired composition for targeted applications. Therefore, the production of PLA–Copper composites was carried out in-house using the Brabender twin-screw extruder.

This section outlines the preparation and characterization of PLA–Copper composites with three different copper weight fractions: 60%, 80%, and 90%. The PLA used as the polymer matrix corresponds to the blue-colored PLA described in the previous chapter, while the copper powder, previously introduced, is a gas-atomized metal powder developed by Professor Federico Simone Gobber and collaborators at Politecnico di Torino.

3.2.1 Characterization of copper powder

The copper powder used to produce the customized composites was first analyzed using the Malvern Mastersizer 3000 for particle size distribution (PSD). After drying, the sample exhibited Dx(10) = 9.89 µm, Dx(50) = 36 µm, and Dx(90) = 117 µm, as shown in Figure 3.38.

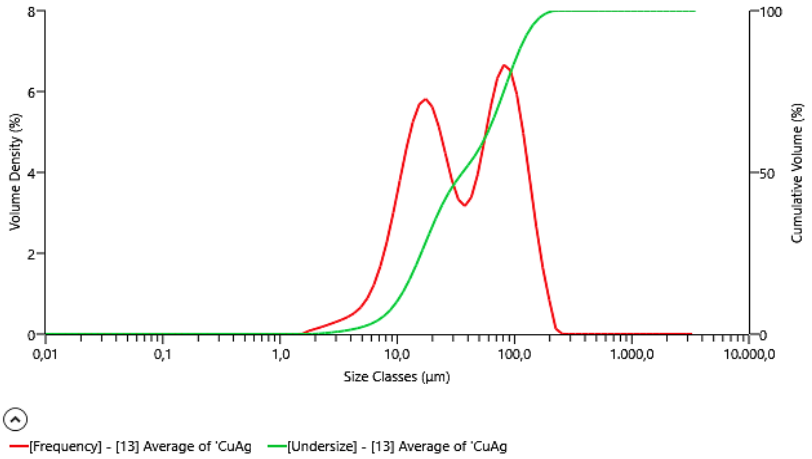

Figure 3.38. Particle size distribution (PSD) curve of the copper powder

The volume-based distribution reveals a relatively broad particle size range, with a fine fraction (< 10 µm) coexisting alongside a substantial medium-to-large particle population (> 100 µm). This bimodal tendency can improve powder packing efficiency by allowing fine particles to fill interstitial voids between larger ones, leading to higher bulk density and reduced porosity.

Morphological examination was conducted by scanning electron microscopy (SEM) at different magnifications and detector modes. Figure 3.39 presents four images acquired at 1.50 kX magnification, which the powder shows a predominantly spherical to near-spherical morphology, characteristic of gas-atomized copper. The spherical shape is associated with rapid solidification of molten droplets, while the small fraction of

irregular grains likely originates from incomplete spheroidization or mechanical fragmentation during atomization. Higher magnification views reveal smooth to slightly textured surfaces, with shallow dimples and fine asperities. Numerous satellite particles, in the form of smaller spheres attached to the surface of larger ones, are evident. These satellites form through in flight collisions between semi solid droplets and, while they can reduce flowability, they may enhance interfacial mechanical interlocking within the composite.

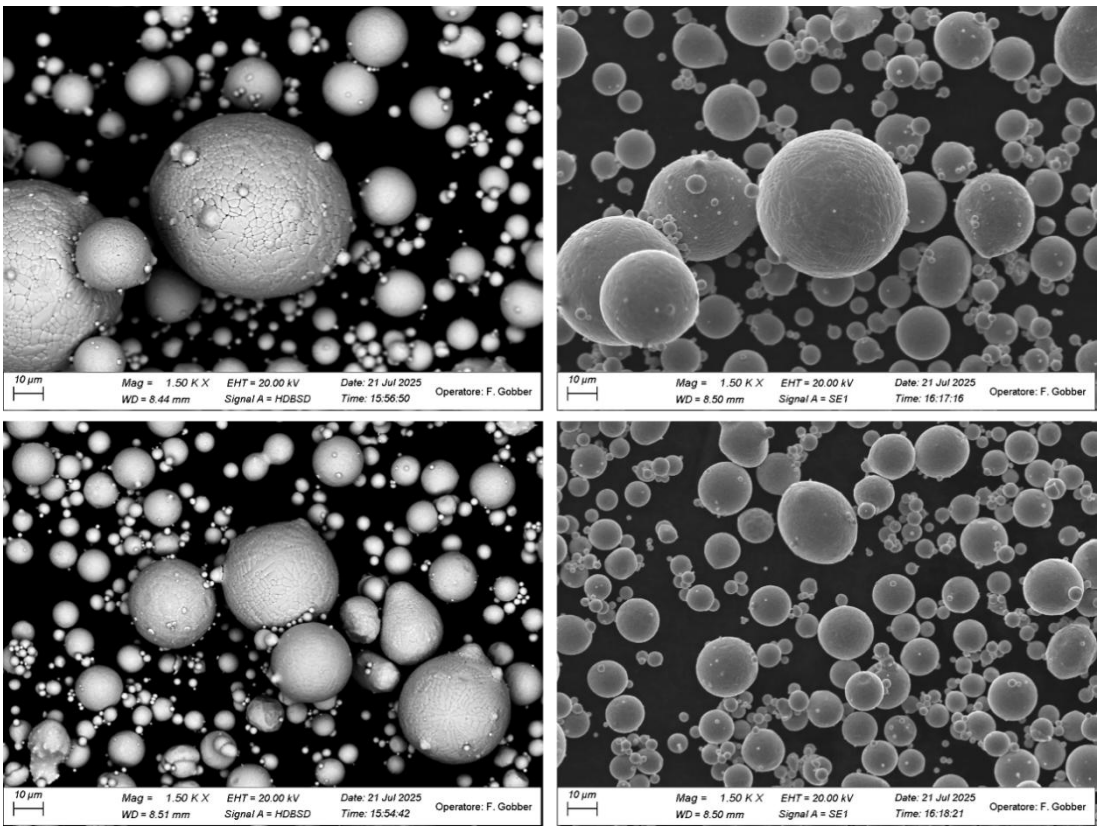

Figure 3.39. SEM images of copper powder in SE and HDBSD modes

Figure 3.40 shows low-magnification SEM images of the copper powder, providing an overview of the size distribution. Fine particles are dispersed among the larger spheres, visually confirming the broad PSD. The relatively homogeneous distribution at these scales supports uniform blending during composite preparation. In addition, the clean metallic surface and the absence of extensive oxidation or porosity indicate that the powder was well-protected during production and storage, ensuring a high-quality feedstock.

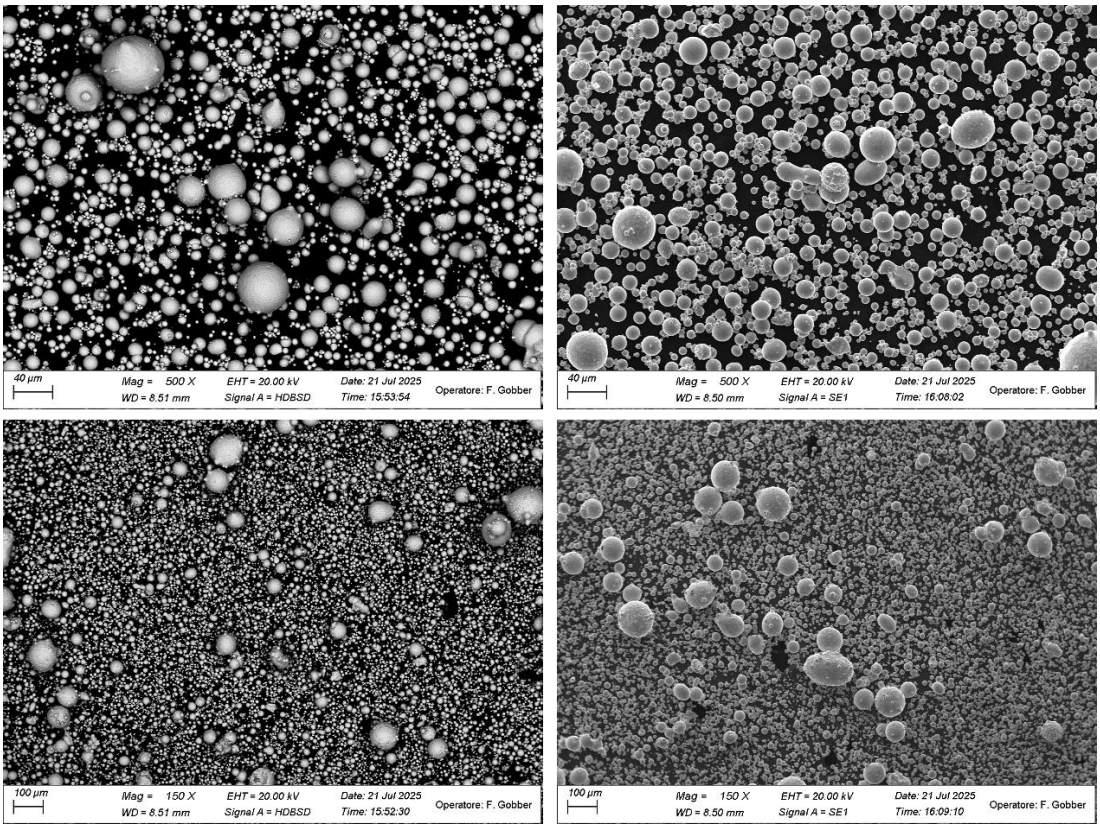

Figure 3.40. SEM images of copper powder at different magnifications in SE and HDBSD modes

3.2.2 Preparation of PLA–Copper Composites

To produce PLA–Copper composites optimized for pellet-based 3D printing with the G5 PRO printer, a complete material formulation and processing route was developed. This approach allowed for full independence from commercial filaments and enabled the creation of custom formulations.

The procedure commenced with a pre-drying step to eliminate residual moisture from both the polymer and the metal powder. Pelletized PLA and copper powder were placed in a vacuum oven at 50 °C for two hours. This step was essential to improve the quality of dispersion during melt compounding and to avoid moisture-related defects in the final printed parts.

Once dried, the amounts of PLA and copper required to achieve the desired 60 wt% copper composition were calculated based on their known densities (1.4 g/cm³ for PLA and approximately 8.9–9.0 g/cm³ for copper). The materials were weighed accordingly and manually premixed in a clean container (Figure 3.41, left). This manual blending step, though simple, was carried out thoroughly to initiate the distribution of copper particles

throughout the PLA matrix and improve dispersion efficiency during compounding (Figure 3.41, right).

Figure 3.41. Preparation and manual mixing of PLA with copper powder

The manually blended mixture was then gradually introduced into the chamber of a Brabender internal mixer, initially operating at 30 rpm. After complete loading (Figure 3.42), the mixing speed was increased to 60 rpm for one minute to enhance blending, and subsequently to 95 rpm for approximately three minutes to apply sufficient forces to promote uniform distribution of copper within the molten PLA.

Figure 3.42. Compounding of PLA and copper using the Brabender mixer

After mixing, the material was removed from the chamber (Figure 3.43), and the procedure was repeated multiple times to accumulate enough composite material for the next stages of processing. This was also necessary due to the limited capacity of the Brabender internal mixer, which allows a maximum batch volume of approximately 45 cm^3. The mixed product was then granulated using the Piovan industrial granulator (Figure 3.44) to produce pellets of smaller and more manageable dimensions.

Figure 3.43. Material removed from the Brabender after compounding

Figure 3.44. Piovan industrial granulator

However, since the granules obtained exhibited a broad particle size distribution, they were passed through a set of sieves with different mesh sizes to remove oversized particles and improve uniformity. This sieving step was essential to ensure consistent feeding during printing, as large or irregular particles can adversely affect flow and printing stability.

Finally, the sieved composite granules were subjected to a second drying cycle at 70 °C for two hours in a vacuum oven set to 210 mbar. This final drying ensured that the pellets were fully moisture-free and ready for 3D printing. The resulting material (Figure 3.45) was then stored under dry conditions and used in the subsequent characterization and printing steps.

Figure 3.45. Sieved PLA–Copper composite granules

The same procedure was followed to prepare PLA–Copper composites with 80 wt% and 90 wt% copper content, using adjusted mass ratios while keeping all processing parameters consistent across batches.

3.2.3 Characterization of PLA–Copper Composites

This section presents the experimental characterization of the three custom PLA–Copper composites prepared using the Brabender internal mixer: PLA–Copper 60%, PLA–Copper 80%, and PLA–Copper 90%. Each composite was designed with a specific objective; PLA–Copper 60% to allow direct comparison with HTPLA, PLA–Copper 90% to benchmark against Copper Filament filaments, and PLA–Copper 80% to explore an intermediate formulation with no direct commercial equivalent.

All samples were printed using the G5 PRO printer and subjected to appropriate thermal treatments prior to testing. The results of the following analyses provide insight into the thermal, mechanical, and morphological behavior of the developed materials.

3.2.3.1 Thermal Conductivity

Thermal conductivity tests were carried out on all materials using the Hot Disk TPS 2500 S, as described in the previous chapter. The printed samples used for the measurements had dimensions of 20 × 20 × 10 mm, ensuring proper contact with the sensor for consistent readings. No thermal treatment was applied prior to testing, as previous studies have shown that such treatment does not significantly influence the thermal conductivity.

3.2.3.1.1 PLA–Copper 60%

The thermal conductivity test was performed on the PLA–Copper 60% sample using the method described in the previous chapter. The printed specimen used is shown in Figure 3.46, and the corresponding results are reported in Table 3.9.

Figure 3.46. *PLA–Copper 60% samples printed for thermal conductivity measurements*

And

Table 3.9. Thermal conductivity results of PLA–Copper 60% samples

PLA–Copper 60%	**Thermal Conductivity W/(m·K)**
Scan 1	0.403
Scan 2	0.401
Scan 3	0.400
Average	**0.401**
Standard deviation	0.001

Although PLA–Copper 60% has the same nominal copper content as the commercial HTPLA material (60 wt%), it exhibited a lower average thermal conductivity of 0.401 $W \cdot m^{-1} \cdot K^{-1}$, compared to 0.529 $W \cdot m^{-1} \cdot K^{-1}$ for HTPLA. This result may appear unexpected given the comparable filler content, but it can be explained by considering differences in microstructure and processing.

In PLA–Copper 60%, the copper particles are dispersed within the PLA matrix but do not form a continuous thermally conductive network. As a result, heat transfer remains limited by the polymer phase and interfacial resistance between the copper and PLA. In contrast, HTPLA benefits from industrial-scale processing conditions that enhance particle dispersion, interface contact, and possibly polymer crystallinity, all of which contribute to more efficient thermal transport.

These findings demonstrate that achieving high thermal conductivity in metal–polymer composites depends not only on filler content, but also on particle distribution, interfacial bonding, and processing quality.

3.2.3.1.2 PLA–Copper 80%

The thermal conductivity test was performed on the PLA–Copper 80% sample using the method described in the previous chapter. The printed specimen used is shown in Figure 3.47, and the corresponding results are reported in Table 3.10.

Figure 3.47. PLA–Copper 80% samples printed for thermal conductivity measurements

And

Table 3.10. Thermal conductivity results of PLA–Copper 80% samples

PLA–Copper 80%	**Thermal Conductivity W/(m·K)**
Scan 1	0.828
Scan 2	0.828
Scan 3	0.830
Average	**0.829**
Standard deviation	0.001

The average thermal conductivity measured for PLA–Copper 80% was 0.829 $W \cdot m^{-1} \cdot K^{-1}$, which represents a clear improvement compared to both PLA–Copper 60% (0.401 $W \cdot m^{-1} \cdot K^{-1}$) and commercial HTPLA (0.529 $W \cdot m^{-1} \cdot K^{-1}$). At 80 wt% copper loading, the copper particles are likely near the percolation threshold, enabling more effective heat transfer through improved interparticle contact and reduced influence from the insulating PLA matrix.

3.2.3.1.3 PLA–Copper 90%

The thermal conductivity test was performed on the PLA–Copper 90% sample using the method described in the previous chapter. The printed specimen used is shown in Figure 3.48, and the corresponding results are reported in Table 3.11.

Figure 3.48. PLA–Copper 90% samples printed for thermal conductivity measurements

And

Table 3.11. Thermal conductivity results of PLA–Copper 90% samples

PLA–Copper 90%	**Thermal Conductivity W/(m·K)**
Scan 1	1.647
Scan 2	1.561
Scan 3	1.500
Average	**1.569**
Standard deviation	0.060

An average thermal conductivity of 1.569 $W \cdot m^{-1} \cdot K^{-1}$ was recorded, marking a substantial increase over both PLA–Copper 60% (0.401 $W \cdot m^{-1} \cdot K^{-1}$) and PLA–Copper 80% (0.829 $W \cdot m^{-1} \cdot K^{-1}$). At this high filler loading, a dense metallic network is more likely to form, significantly enhancing heat transfer throughout the composite.

The measured value is also closely aligned with that of the commercial Copper Filament, which exhibited an average thermal conductivity of 1.616 $W \cdot m^{-1} \cdot K^{-1}$. This result suggests that the PLA–Copper 90% composite effectively replicates the thermal performance of high-conductivity commercial alternatives. The results confirm that increasing copper content is a key factor in improving thermal conductivity, but careful control over dispersion and processing remains essential to ensure consistency.

3.2.3.2 Compression Test

Compression tests were conducted following the procedure described in the previous chapter. All printed samples had dimensions of 12 × 12 × 10 mm, and underwent the same thermal treatment (1 hour at 80 °C) prior to testing to ensure consistent mechanical behavior. For each material, PLA–Copper 60%, PLA–Copper 80%, and PLA–Copper 90%, the test was performed on three to four samples to verify repeatability and reliability.

This test is particularly relevant because the insert inside a mold is subjected to high compressive pressures during the injection process. Therefore, the material used must be able to withstand such stresses without deformation or failure, maintaining dimensional stability and mechanical integrity under cyclic loading.

The following subsections report and analyze the results obtained for each composite.

3.2.3.2.1 PLA–Copper 60%

The tested specimen is shown in Figure 3.49, and the corresponding compression results are reported in Figure 3.50. Sample 3 was discarded because the results were inconsistent and deemed unreasonable.

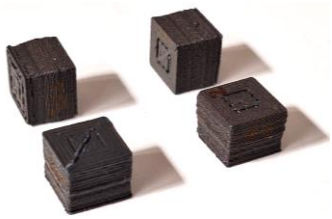

Figure 3.49. PLA–Copper 60% samples printed for compression test

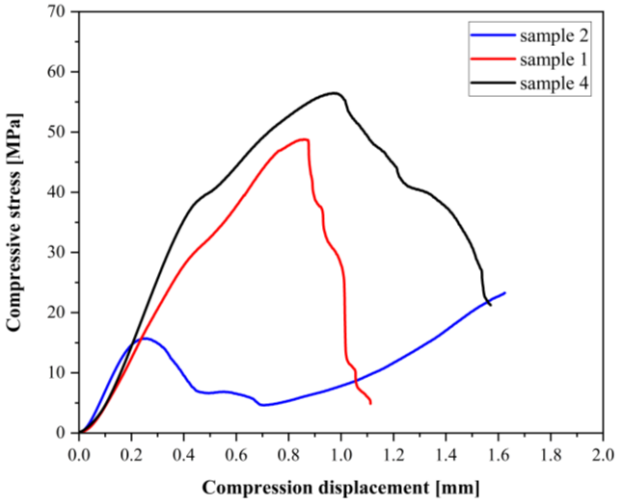

Figure 3.50. Compression test results of PLA–Copper 60% samples

The average compressive modulus was calculated to be 935.84 ± 117.41 MPa, and the maximum compressive stress reached an average of 42.84 ± 17.37 MPa, as shown in Table 3.12.

Table 3.12. Mechanical properties of PLA–Copper 60% specimens under compression

Sample	Young's Modulus [MPa]	Maximum Force [N]	Compressive Stress at Maximum Force [MPa]
1	828.96	7237.24	48.78
2	917.04	3501.36	23.28
4	1061.52	8343.57	56.47
Average	**935.84**	**6360.72**	**42.84**
Standard deviation	117.41	2537.31	17.37

Fracture occurred gradually, as shown in Figure 3.51, without abrupt failure, indicating relatively ductile behavior.

Figure 3.51. Crack propagation and fracture during compression testing of PLA–Copper 60% specimens

Compared to HTPLA, which also contains approximately 60 wt% copper, PLA–Copper 60% exhibited lower stiffness and strength. HTPLA showed an average compressive modulus of 908.48 ± 66.37 MPa and a maximum compressive stress of 58.71 ± 1.22 MPa, along with a more linear stress–strain response that reflects a stiffer mechanical behavior.

These differences are likely due to variations in the PLA matrix composition, the degree of crystallinity, the type of copper powder used, and the homogeneity of filler distribution within the matrix. All these factors significantly influence the mechanical properties under compression.

3.2.3.2.2 PLA–Copper 80%

The tested specimen is shown in Figure 3.52, and the corresponding compression results are reported in Figure 3.53. Four specimens were evaluated, and the results demonstrate an overall increase in both stiffness and strength compared to PLA–Copper 60%. Sample 2 was discarded because the results were inconsistent and deemed unreasonable.

Figure 3.52. PLA–Copper 80% samples printed for compression test

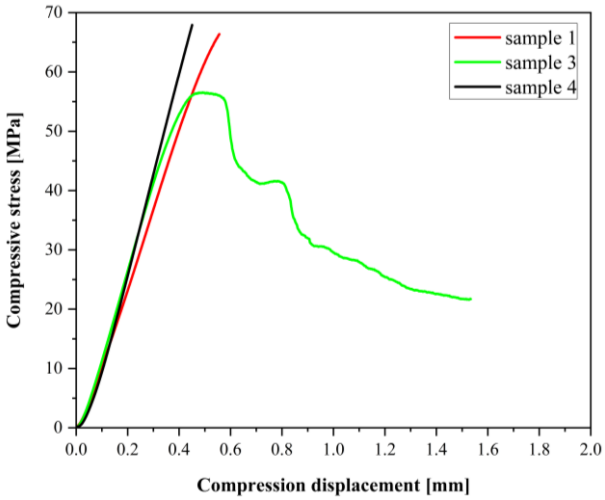

Figure 3.53. Compression test results of PLA–Copper 80% samples

The average compressive modulus was calculated to be 1480.76 ± 168.58 MPa, while the maximum compressive stress reached 63.60 ± 6.17 MPa (Table 3.13). This represents a significant increase compared to PLA–Copper 60%, which showed 935.84 ± 117.41 MPa and 42.84 ± 17.37 MPa, respectively.

Table 3.13. Mechanical properties of PLA–Copper 80% specimens under compression

Sample	Young's Modulus [MPa]	Maximum Force [N]	Compressive Stress at Maximum Force [MPa]
1	1321.99	10000.11	66.37
3	1462.62	8325.02	56.53
4	1657.68	10000.44	67.91
Average	**1480.76**	**9441.86**	**63.60**
Standard deviation	168.58	967.21	6.17

The failure mode remained brittle in most cases, with sharp cracking observed post-yield, as shown in Figure 3.54.

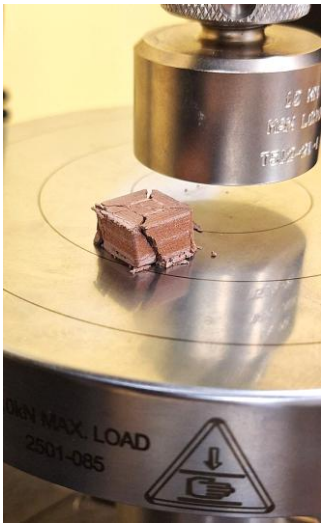

Figure 3.54. Crack propagation and fracture during compression testing of PLA–Copper 80% specimens

Compared to HTPLA, PLA–Copper 80% also exhibits higher stiffness and slightly higher compressive strength. While HTPLA averaged a compressive modulus of 908.48 ± 66.37 MPa and stress of 58.71 ± 1.22 MPa, PLA–Copper 80% surpassed these values, especially in modulus, indicating a more rigid composite structure.

3.2.3.2.3 PLA–Copper 90%

The tested specimen is shown in Figure 3.55, and the corresponding compression results are reported in Figure 3.56. Four specimens were tested; however, Sample 4 was excluded from the analysis due to inconsistent and unreliable results.

Figure 3.55. PLA–Copper 90% samples printed for compression test

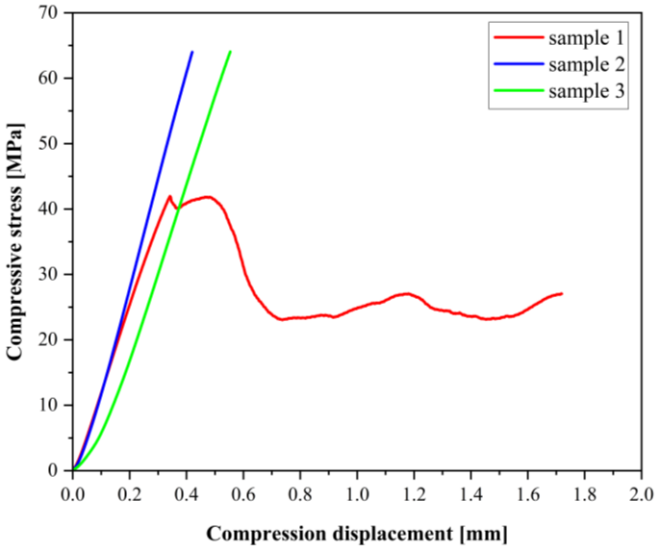

Figure 3.56. Compression test results of PLA–Copper 90% samples

The average compressive modulus was calculated to be 1445.60 ± 176.30 MPa, while the maximum compressive stress reached 56.67 ± 12.75 MPa, as shown in Table 3.14.

Table 3.14. Mechanical properties of PLA–Copper 90% specimens under compression

Sample	Young's Modulus [MPa]	Maximum Force [N]	Compressive Stress at Maximum Force [MPa]
1	1329.00	6450.12	41.95
2	1648.42	10000.18	64.00
3	1359.39	10000.14	64.05
Average	**1445.60**	**8816.81**	**56.67**
Standard deviation	176.30	2049.62	12.75

As shown in Figure 3.57, the samples exhibited clear brittle fracture, breaking into multiple fragments upon failure.

Figure 3.57. Brittle fracture during compression testing of PLA–Copper 90% specimens

Commercial Copper Filament exhibited an average compressive modulus of 1182.15 ± 25.89 MPa and a compressive strength of 30.54 ± 2.06 MPa. While PLA–Copper 90% exceeds Copper Filament in both modulus and strength, it also shows greater variability between specimens. The improved mechanical properties may be attributed to the specific PLA grade and the copper particle morphology used, as well as to the presence of fibers within the Copper Filament, as demonstrated in Section 3.1.5.2, while the higher variation could stem from microstructural inconsistencies or reduced interfacial adhesion at such a high filler content. As with Copper Filament, the high copper loading in PLA–Copper 90% leads to a brittle response, with limited plastic deformation prior to failure.

3.2.3.3 Dynamic Mechanical Analysis – Bending Mode

This analysis was performed following the procedure described earlier. Printed specimens with dimensions of 35 × 10 × 2 mm were used, and all samples underwent same thermal treatment (1 hour at 80 °C) prior to testing. The objective of this test was to evaluate the storage modulus (E′) and determine the Heat Deflection Temperature (HDT) of the PLA–Copper composites. Assessing the HDT is particularly important for mold insert applications, as the material must maintain mechanical stability at elevated temperatures. If the HDT is lower than the EOF temperature predicted by Moldex3D simulations, the material is unsuitable for use as an insert.

3.2.3.3.1 PLA–Copper 60%

The test was performed for printed PLA–Copper 60% samples after thermal treatment following the method described in the previous chapter. The sample is shown in Figure 3.58, and the results are presented in Figure 3.59.

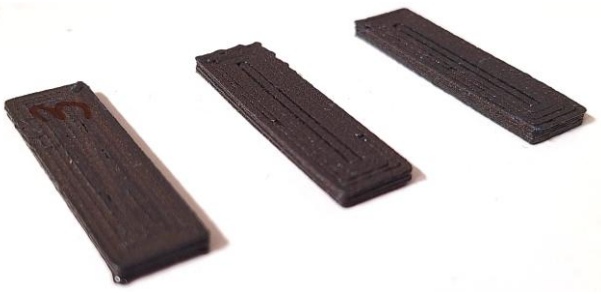

Figure 3.58. PLA–Copper 60% samples printed for DMA test

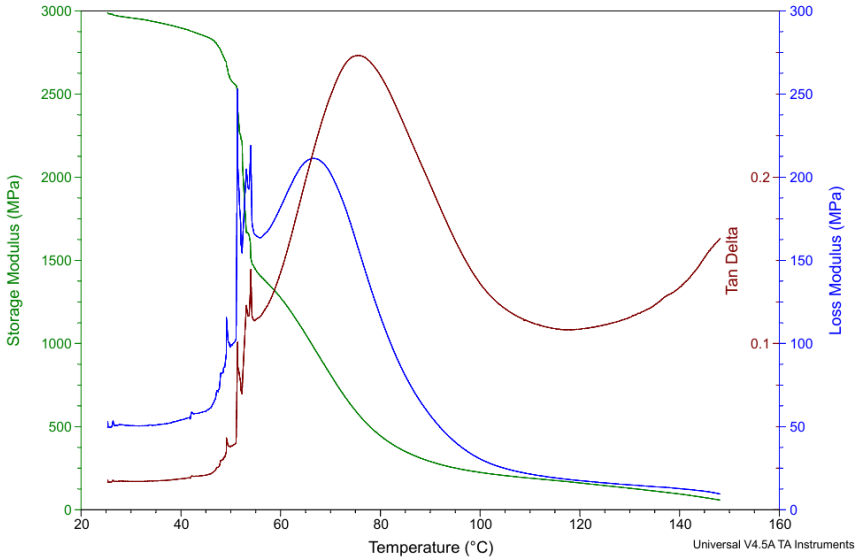

Figure 3.59. DMA (bending mode) test results of PLA–Copper 60% samples

From the storage modulus curve, the HDT (defined as the temperature at which the modulus drops below 800 MPa) was found to be approximately 70 °C. The material maintained a relatively high modulus up to this point, after which a sharp decline was observed.

Compared to HTPLA, which exhibited an HDT of approximately 87.5 °C, PLA–Copper 60% shows lower thermal stability under bending. Although both materials contain approximately the same amount of copper, this difference is likely due to variations in the PLA matrix composition and degree of crystallinity. During thermal treatment, HTPLA appears to crystallize more effectively, which contributes to its superior resistance to softening under load. In contrast, the customized PLA–Copper composites do not exhibit the same level of crystallization efficiency. This could be attributed to the intrinsic nature of the PLA used, the absence of specific nucleating additives, or other formulation differences that are typically optimized in commercial filaments.

This result highlights the importance of not only filler content, but also matrix formulation and microstructure in determining the thermo-mechanical performance of composites.

3.2.3.3.2 PLA–Copper 80%

The test was performed for printed PLA–Copper 80% samples after thermal treatment. The sample is shown in Figure 3.60, and the results are presented in Figure 3.61.

Figure 3.60. PLA–Copper 80% samples printed for DMA test

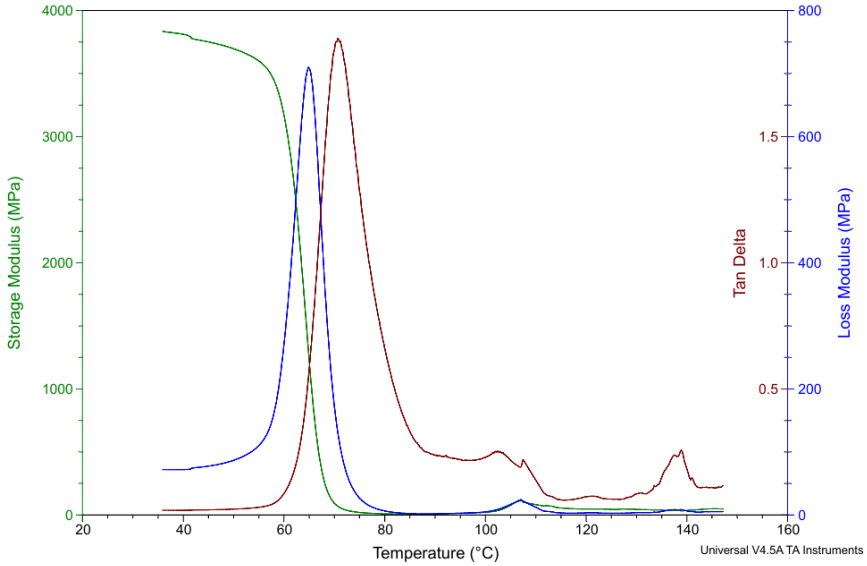

Figure 3.61. DMA (bending mode) test results of PLA–Copper 80% samples

From the storage modulus curve, the HDT (determined as the temperature at which the modulus drops below 800 MPa) was found to be approximately 66 °C. This is unexpectedly low, especially considering that neat PLA typically exhibits an HDT of around 64 °C. The result suggests that the copper filler did not contribute to improving thermal stability under flexural load, and that crystallization during thermal treatment was largely ineffective.

Moreover, a comparison with HTPLA highlights the extent of this limitation. HTPLA reached an HDT of 87.5 °C, and even beyond that temperature, the modulus declined more gradually. In contrast, PLA–Copper 80% experienced a very steep modulus drop, and after the transition point, the storage modulus remained consistently below 100 MPa.z

These results suggest that despite the high copper content, the matrix structure of PLA–Copper 80% lacks the crystalline reinforcement observed in commercial filaments like HTPLA. The poor crystallization behavior may be linked to the nature of the PLA used, absence of nucleating agents, or incompatibility between filler and polymer, all of which limit the material's resistance to thermal softening under load.

3.2.3.3.3 PLA–Copper 90%

The test was performed on printed PLA–Copper 90% specimens after thermal treatment using the procedure described earlier. The sample used is shown in Figure 3.62, and the results are presented in Figure 3.63.

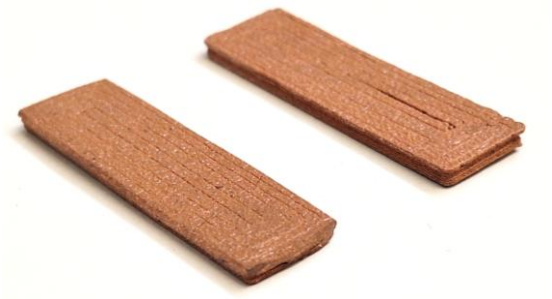

Figure 3.62. PLA–Copper 90% samples printed for DMA test

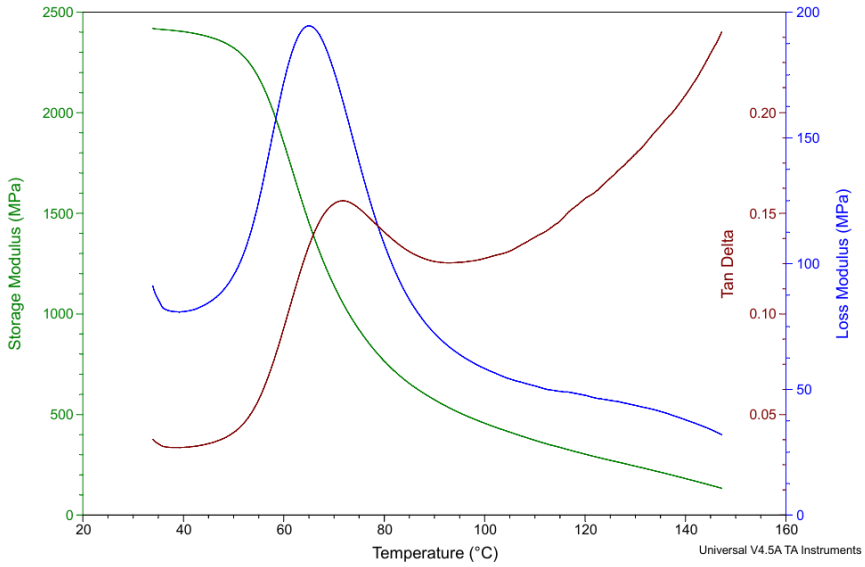

Figure 3.63. DMA (bending mode) test results of PLA–Copper 90% samples

From the storage modulus curve, the HDT (defined as the temperature where the modulus drops below 800 MPa) was found to be approximately 78.7 °C. This represents a clear improvement over PLA–Copper 60% (70 °C) and PLA–Copper 80% (66 °C). However,

the HDT is still lower than that of Copper Filament, which reached approximately 86.5 °C.

While PLA–Copper 90% retains stiffness better than the other custom formulations, its thermal performance remains slightly inferior to the commercial filament. This may again be attributed to differences in matrix crystallinity or additive content, both of which influence the formation of thermally stable structures during heat treatment.

Figure 3.64 presents the DMA (bending mode) test results for all samples, including HTPLA, Copper Filament, PLA–Copper 60%, PLA–Copper 80% and PLA–Copper 90% with particular focus on the storage modulus (E′). Compared to PLA–Copper 80%, PLA–Copper 90% shows a much less aggressive decline in modulus beyond the HDT, maintaining a gradual slope in the post-transition region. This behavior is more comparable to Copper Filament and reflects better resistance to softening, though still limited by the formulation's thermal development.

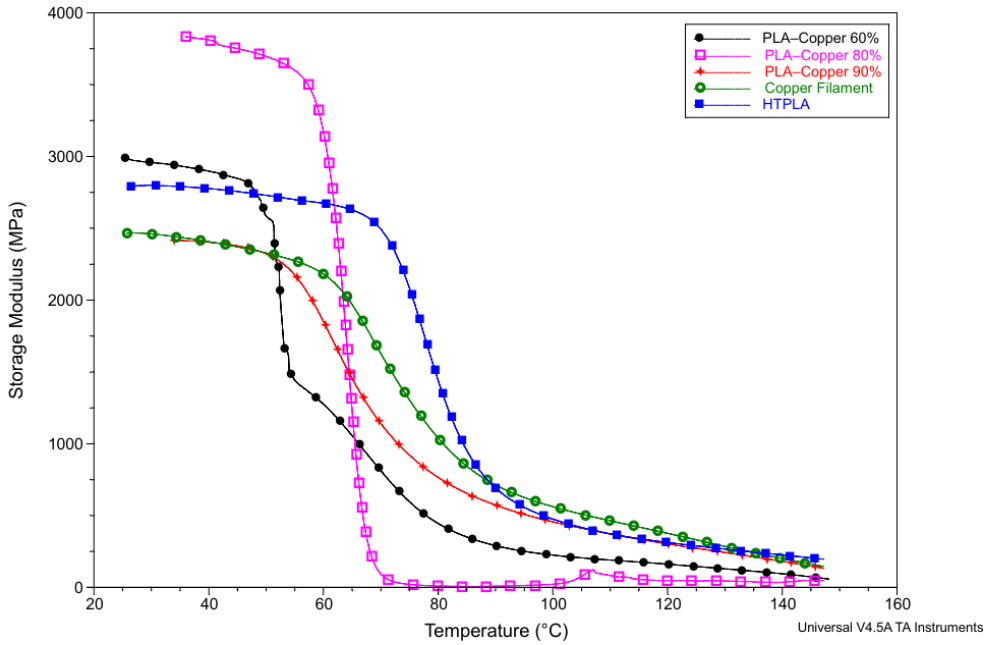

Figure 3.64. DMA (bending mode) test results for all samples

3.2.3.4 Dynamic Mechanical Analysis – Tension Mode

This section presents the results of the DMA tests conducted in tension mode on the customized PLA–Copper composite samples. All specimens underwent the same thermal treatment applied in previous analyses (1 hour at 80 °C), and were prepared with dimensions of 35 × 10 × 2 mm, identical to those used in the bending mode tests.

This analysis evaluates the deformation behavior of the materials under thermal and tensile loading, which is particularly relevant for mold insert applications. During the injection molding process, inserts are exposed not only to elevated temperatures but also to mechanical stresses that can lead to deformation or failure.

3.2.3.4.1 PLA–Copper 60%

The DMA test in tension mode was performed on PLA–Copper 60% samples. The sample used is shown in Figure 3.65, and the results of the test are illustrated in Figure 3.66.

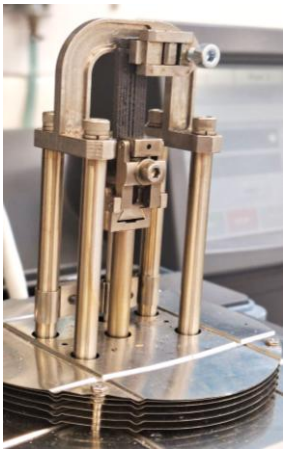

Figure 3.65. PLA–Copper 60% sample printed for DMA test

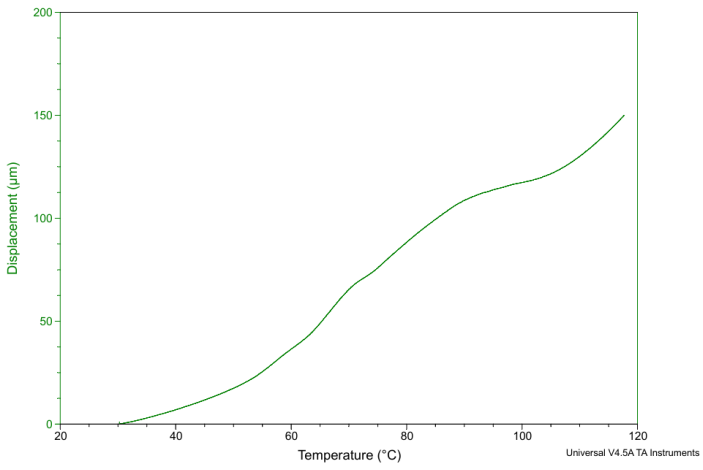

Figure 3.66. DMA (tension mode) test results of PLA–Copper 60% samples

The maximum displacement observed during the test was approximately 150 µm.

3.2.3.4.2 PLA–Copper 80%

The DMA test in tension mode was conducted on PLA–Copper 80% samples. The specimen is shown in Figure 3.67, and the displacement curve is presented in Figure 3.68.

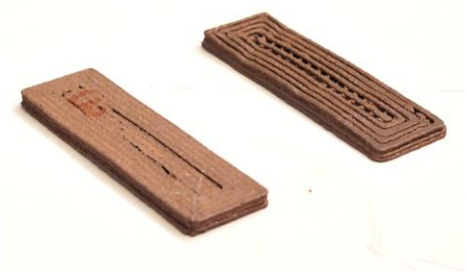

Figure 3.67. PLA–Copper 80% sample printed for DMA test

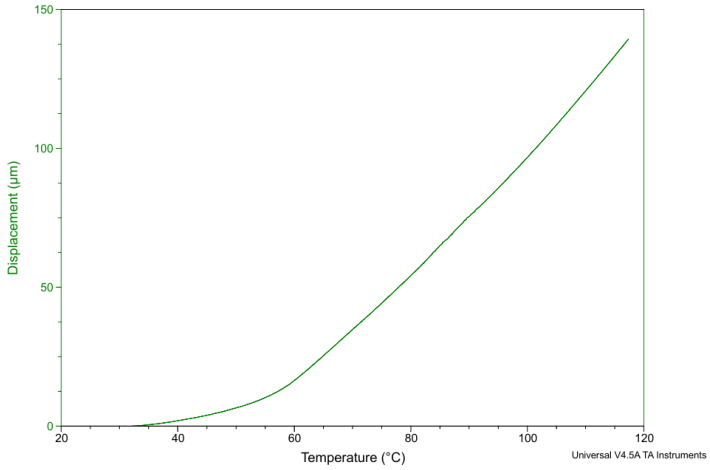

Figure 3.68. DMA (tension mode) test results of PLA–Copper 80% samples

The maximum displacement recorded was approximately 139 µm. The displacement increased steadily with temperature, indicating stable but gradual softening under tensile loading. Compared to PLA–Copper 60% and HTPLA, the displacement remained slightly lower, suggesting better dimensional stability at elevated temperatures, though the difference is not significant.

3.2.3.4.3 PLA–Copper 90%

The DMA test in tension mode was conducted on PLA–Copper 90% samples. The tested specimen is shown in Figure 3.69, and the results are presented in Figure 3.70.

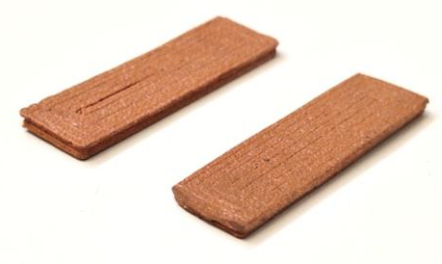

Figure 3.69. PLA–Copper 90% sample printed for DMA test

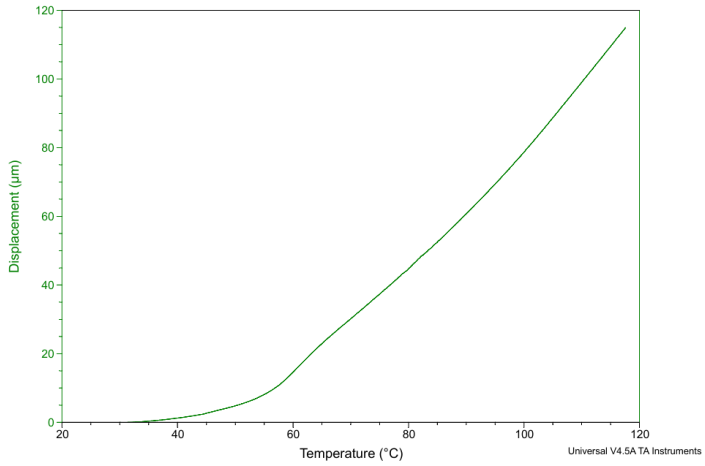

Figure 3.70. DMA (tension mode) test results of PLA–Copper 90% samples

The maximum displacement recorded was approximately 115 µm. When compared to Copper Filament, which showed a maximum displacement of 106 µm, the behavior is highly similar. This suggests that at high copper content, both materials exhibit reduced thermal elongation due to the rigidity imparted by the metallic filler network. Additionally, Figure 3.71 compares the DMA results in tension mode for all samples providing a direct overview of the displacement behavior across the different materials.

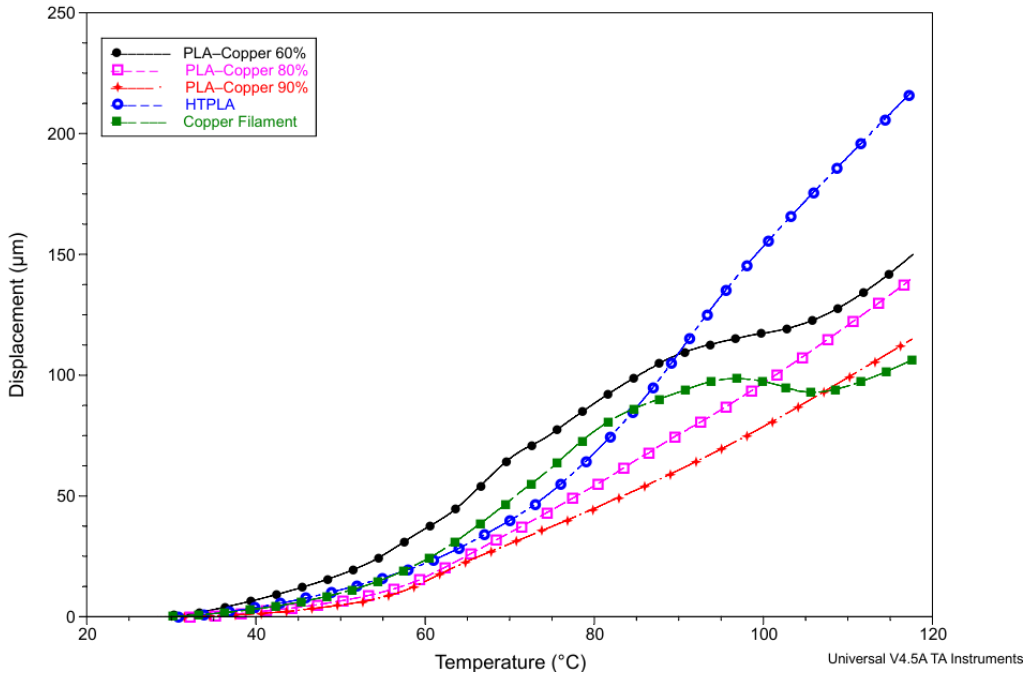

Figure 3.71. DMA (tension mode) test results for all samples

3.2.3.5 Scanning Electron Microscopy (SEM) Analysis

As described in the previous chapter, morphological analysis was performed using a Zeiss EVO 15 Scanning Electron Microscope. Prior to imaging, all samples were coated with a thin conductive layer using the Agar Auto Sputter Coater.

For each composite, two types of SEM images were acquired: Secondary Electron (SE) mode, used to examine surface morphology and fracture features, and High Definition Backscattered Electron (HDBSD) mode, employed to assess compositional contrast, particularly the distribution and visibility of copper particles within the PLA matrix.

The analysis aims to highlight differences in particle dispersion, copper–matrix interaction, and microstructural characteristics that may influence the thermal and mechanical behavior of the composites.

3.2.3.5.1 PLA–Copper 60%

Figure 3.72 presents SEM micrographs of the PLA–Copper 60% composite acquired in both SE and HDBSD modes at a magnification of 150×. In SE mode, the fracture surface appears relatively rough and heterogeneous, with visible spherical inclusions embedded within the matrix. These inclusions correspond to the copper particles, which are more clearly distinguished in HDBSD mode due to their higher atomic number, resulting in bright contrast against the darker PLA background.

The dispersion of copper particles appears generally uniform across the examined areas, though some regions exhibit mild agglomeration or voids, likely due to imperfect interfacial bonding or microstructural inconsistencies during compounding. The particle sizes vary from a few microns up to tens of microns, and several cavities around larger particles suggest possible debonding or poor adhesion at the filler–matrix interface, potentially affecting mechanical performance under load.

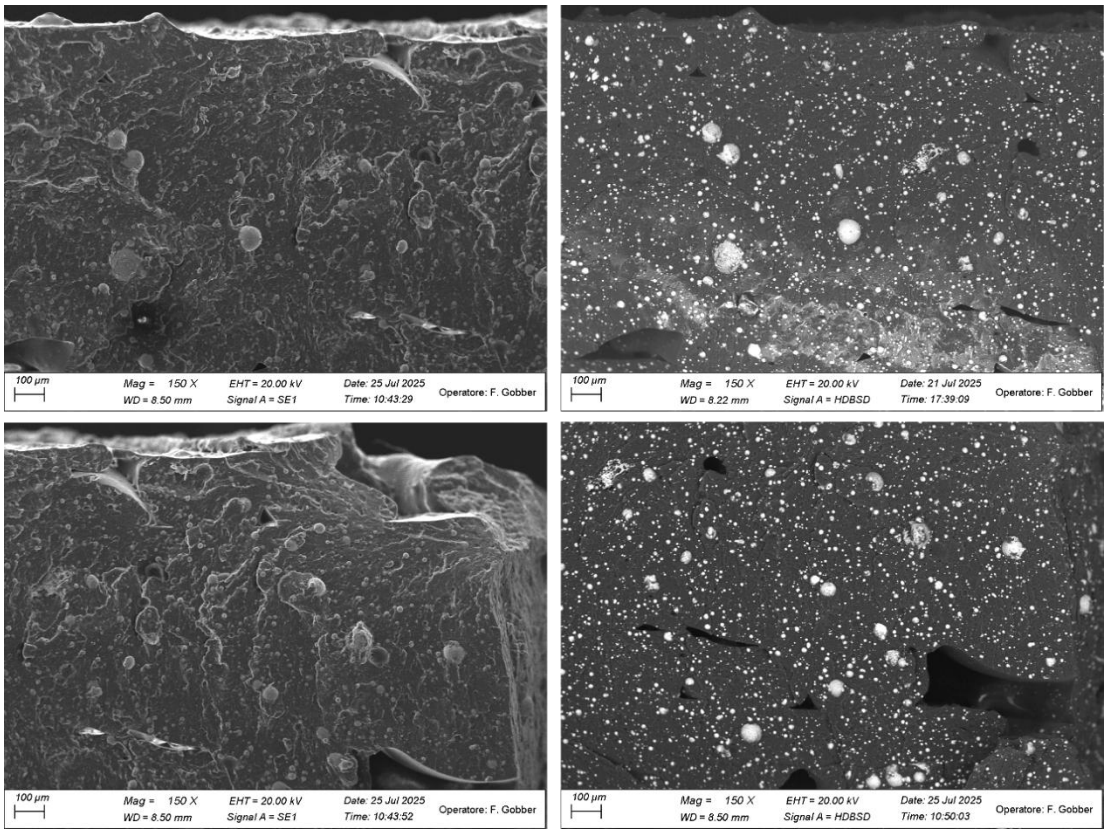

Figure 3.72. SEM images of PLA–Copper 60% at 150× magnification in HDBSD and SE modes

The high-magnification SE image in Figure 3.73 reveals a broad distribution of copper particle sizes, ranging from approximately 10 µm to over 75 µm, with some particles embedded cleanly and others partially detached from the PLA matrix. These larger voids surrounding specific particles indicate poor local adhesion or possible debonding during fracture, which may negatively affect mechanical integrity.

Compared with the pristine copper powder characterized in Section 3.2.1 (Dx10 ≈ 9.9 µm, Dx50 ≈ 36 µm, Dx90 ≈ 117 µm), the particle sizes visible in the PLA–Copper 60% composite (~10–75 µm) are consistent with the native distribution but skewed toward the mid-size fraction. The lower apparent maximum size compared to the pristine Dx90 value can be partly explained by the stereological bias of cross-sectional SEM imaging, which tends to underestimate the true particle diameter unless the particle is sectioned through its equator. In addition, some clustering and partial embedding of particles in the polymer matrix may have influenced the observed size distribution.

The corresponding HDBSD image shows a high density of smaller copper particles distributed throughout the matrix, with occasional localized clustering. While the overall

filler dispersion is fairly homogeneous, this clustering highlights the incomplete distribution efficiency achieved during Brabender mixing.

At low magnification (bottom row), the SEM images show the bulk cross-section of specimens printed using the G5 PRO pellet-fed printer. The layered structure from the printing process is visible, and several interlayer gaps and microvoids appear near larger copper inclusions. These may act as stress concentrators under mechanical loading or thermal cycling, potentially reducing part reliability.

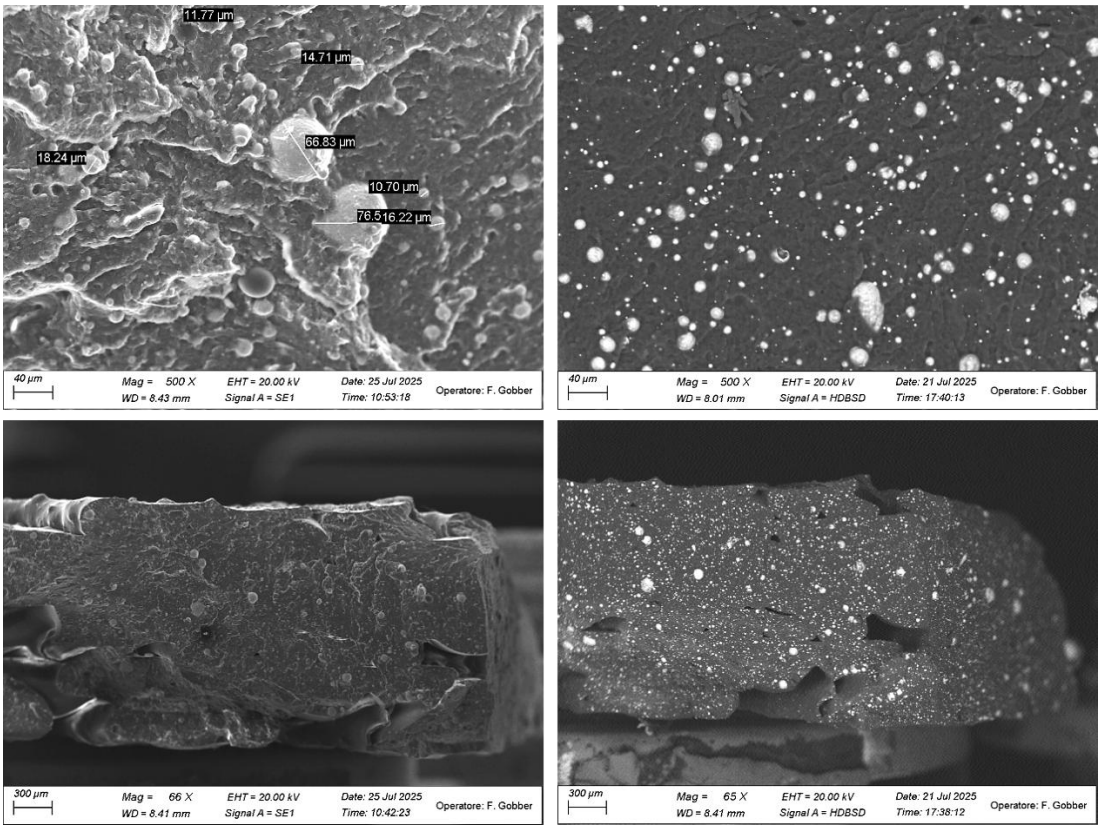

Figure 3.73. SEM images of PLA–Copper 60% at different magnifications in SE and HDBSD modes

As shown in Figure 3.74, the copper particles are predominantly spherical, confirming their gas atomized origin, unlike the irregularly shaped particles observed in HTPLA.

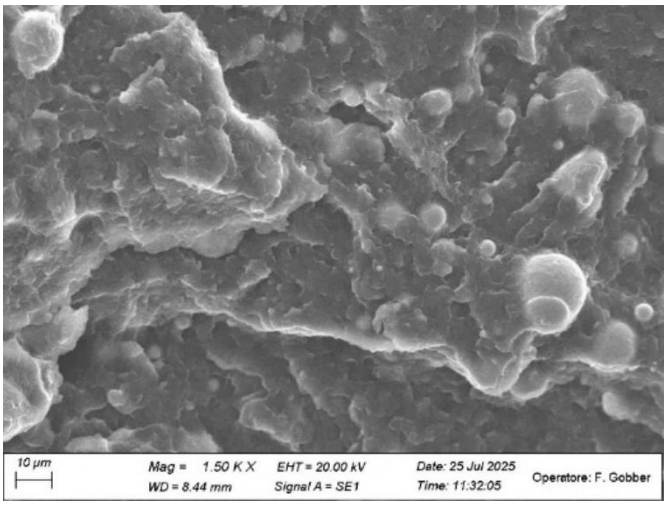

Figure 3.74. SEM image of PLA–Copper 60% at 1500× magnification in SE mode

3.2.3.5.2 PLA–Copper 80%

In Figure 3.75, SE-mode SEM images of the PLA–Copper 80% composite reveal a denser population of copper particles embedded within the PLA matrix, as expected with increased filler content. The low-magnification image shows a relatively consistent dispersion across the cross-section, while higher-magnification views highlight significant variations in particle size. Measurements indicate a wide particle size distribution, with diameters ranging from below 10 µm up to approximately 78 µm. Some particles are well integrated within the matrix, but others display signs of debonding or are surrounded by voids, indicating interfacial detachment.

As shown in Figure 3.76, the copper particles exhibit spherical morphology consistent with gas atomization. Their close packing and occasional clustering at this concentration reinforce the importance of optimizing interfacial adhesion and particle distribution to avoid structural weaknesses.

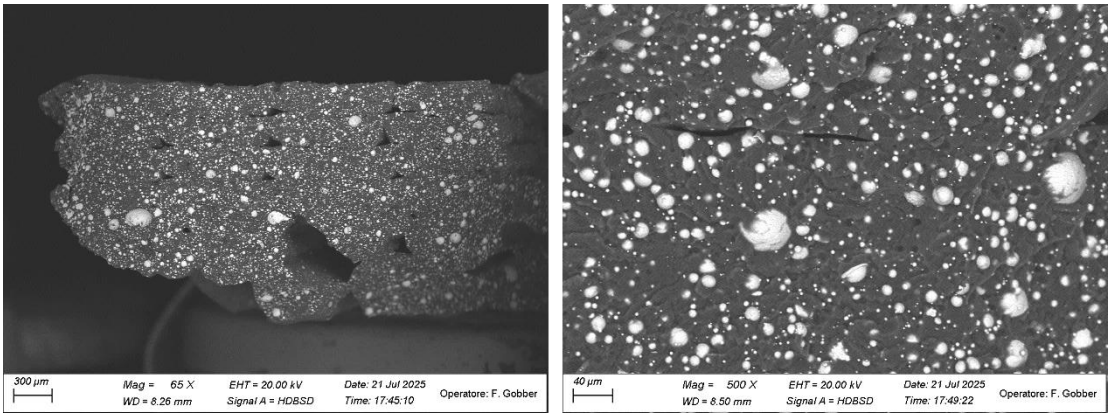

Figure 3.76. SEM images of PLA–Copper 80% at different magnifications in HDBSD mode

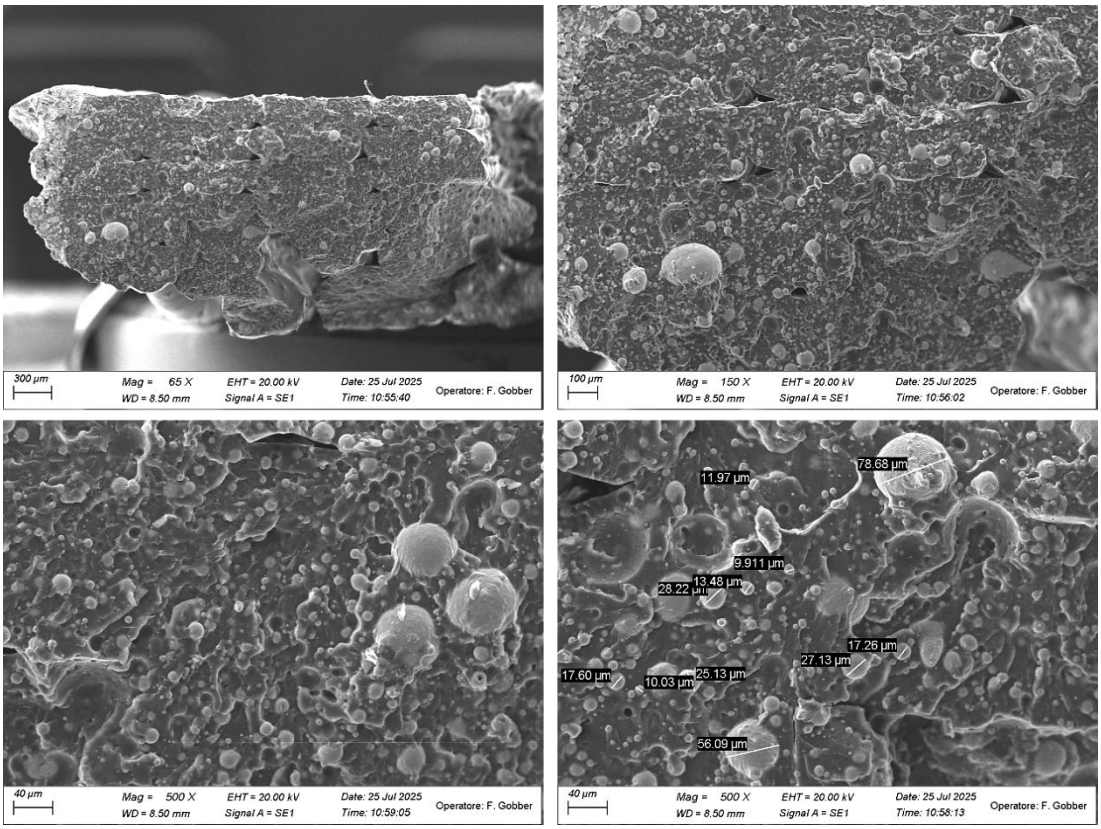

Figure 3.75. SEM images of PLA–Copper 80% at different magnifications in SE and HDBSD modes

At this filler level, particle-to-particle spacing is significantly reduced, increasing the risk of localized clustering, which can negatively affect both mechanical integrity and thermal homogeneity. These observations confirm that although dispersion remains largely effective, the elevated copper content in PLA–Copper 80% challenges the interfacial compatibility and morphological uniformity of the composite.

3.2.3.5.3 PLA–Copper 90%

In Figure 3.77, SEM micrographs of PLA–Copper 90% reveal an extremely high filler concentration, with copper particles densely packed throughout the PLA matrix. The distribution is generally homogeneous, though interparticle spacing is minimal, approaching a quasi-continuous phase in several regions.

Different images in Figure 3.78 provide further insights. Particle diameters range from as small as 6.5 µm up to over 60 µm, and most particles maintain a spherical morphology. Compared to the PLA–Copper 60% and 80% composites, the 90% formulation shows tighter packing and significantly reduced polymer matrix volume, like the microstructure observed in Copper Filament. However, while Copper Filament's structure presents a more uniform and compact metallic phase, the PLA–Copper 90% samples exhibit slightly

greater variation in particle size, and more frequent micro-voids and debonding zones, particularly around larger particles.

Additionally, the images show a distinct layered morphology, with some layer separation and voids that could contribute to mechanical brittleness. In contrast, Copper Filament, as a commercial filament, exhibits a more compact extrusion profile (Figure 3.78, top row). Despite these differences, the overall morphological structure of PLA–Copper 90% is still notably close to Copper Filament in terms of particle shape, packing density, and metallic continuity. These similarities support the comparable thermal conductivity measured experimentally. However, minor structural discontinuities and non-uniformities in the PLA–Copper 90% composite may explain the slightly lower performance metrics compared to Copper Filament, particularly in compressive behavior.

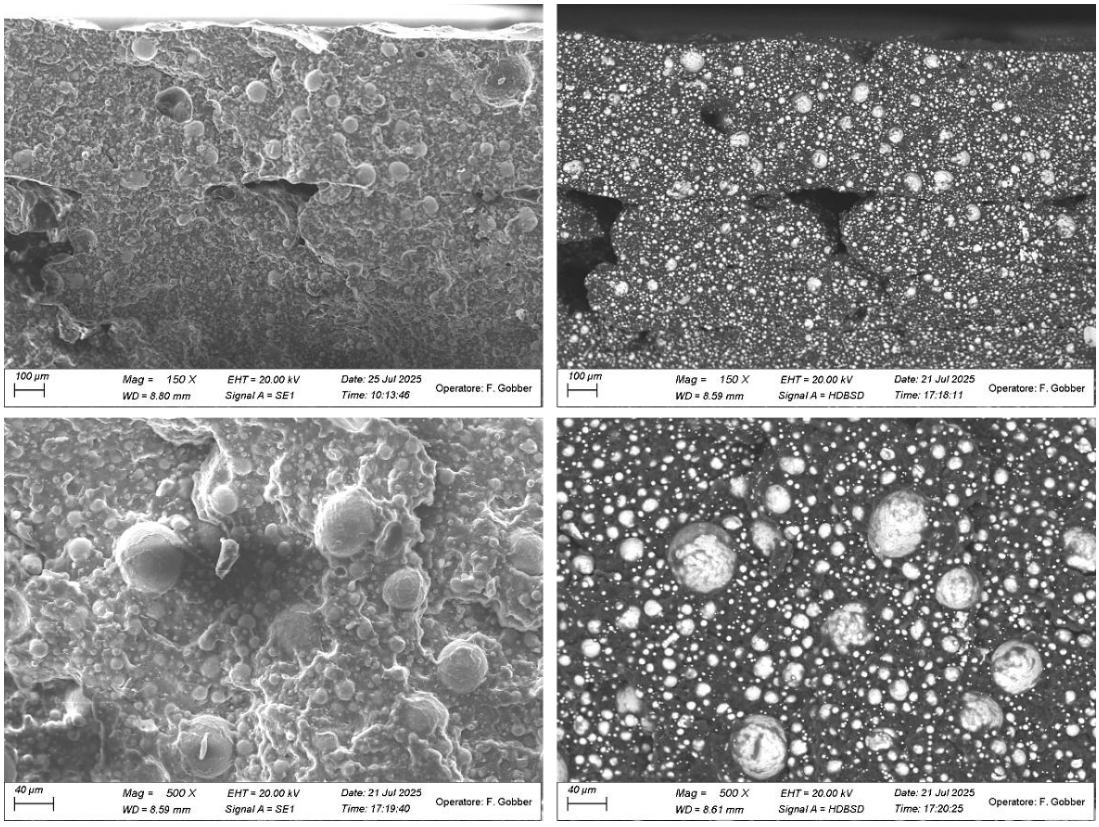

Figure 3.77. SEM images of PLA–Copper 90% at 500× and 150× magnifications in HDBSD and SE modes

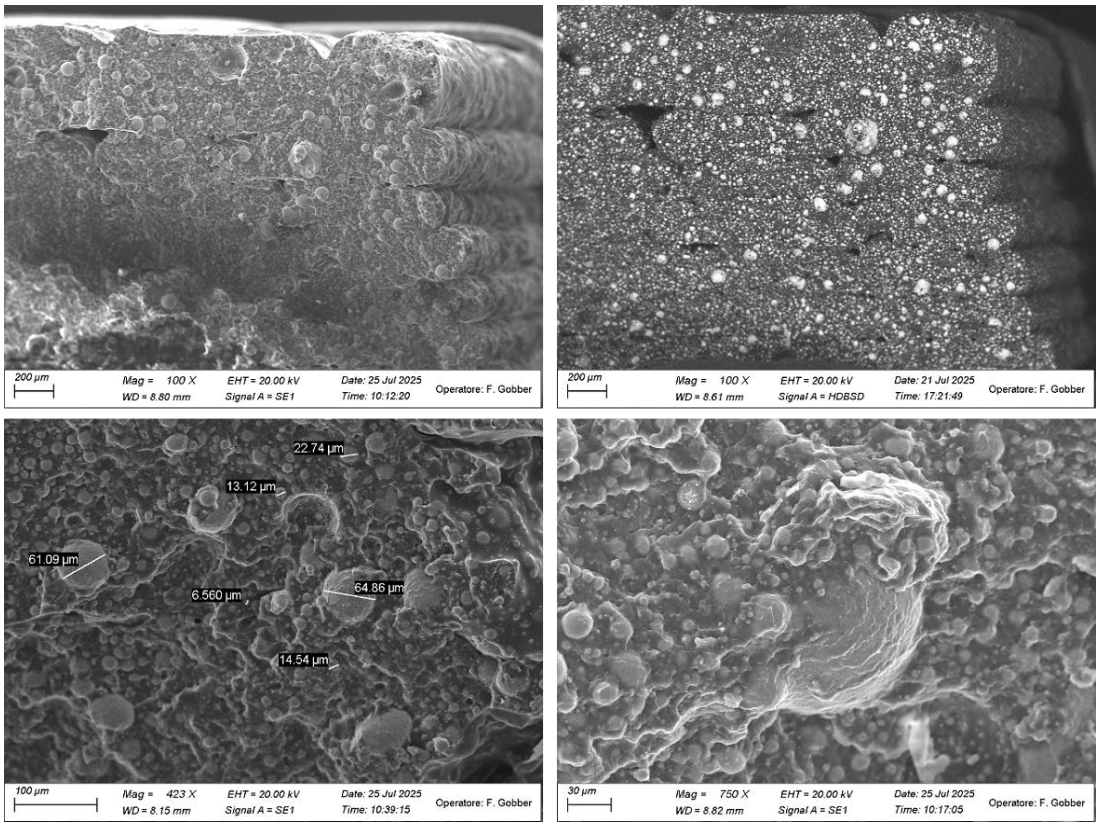

Figure 3.78. SEM images of PLA–Copper 90% at different magnifications in SE and HDBSD modes

Chapter 4

3D PRINTING PROCESS

This chapter focuses on the 3D printing processes adopted throughout the study, with particular attention to the influence of printer type and process parameters on the performance of printed parts. It is divided into two main sections.

Section 4.1 presents a comparative study between two different 3D printers: the G5 PRO pellet-based printer and the FlashForge Creator 3 Pro filament-based printer. The comparison is based on the mechanical and thermal characterization of samples produced using the same commercial filaments (PLA, HTPLA, and Carbon PA), and includes compression testing, thermal conductivity measurements, and dynamic mechanical analysis in both bending and tension modes. Copper Filament was excluded from this comparison, as previous studies have shown that it is not compatible with the FlashForge printer. Key process parameters used for sample fabrication on both machines are also reported.

Section 4.2 is dedicated to the printing of functional mold inserts using the G5 PRO, covering all printed inserts made from both commercial filaments and the customized PLA–Copper composites. It outlines the full set of printing parameters applied for each material, describes the observations made during the printing process, and discusses any challenges encountered related to material flow, print quality, or geometry stability.

4.1 FGF vs FFF: Process Parameters and Printed Part Characterization

This section is divided into two main parts. First, it discusses the printing process parameters and the optimization strategies applied to produce high-quality specimens using both the G5 PRO (FGF) and FlashForge (FFF) printers. Particular attention is given to the challenges and adjustments required for each material and system. In the second part, the performance of the printed samples is analyzed and compared based on results from thermal conductivity, compression testing, and dynamic mechanical analysis (DMA) in both bending and tension modes.

4.1.1 Printing Process Parameters

This subsection outlines the key process parameters used for printing test specimens on both the G5 PRO (FGF) and FlashForge (FFF) printers. For each material (PLA, HTPLA, and Carbon PA) parameters such as nozzle temperature, bed temperature, printing speed, layer height, and cooling settings are listed to highlight the differences in process setup between the two machines. In addition to these filaments, two other materials were also evaluated: Copper Filament and the customized PLA–Copper composites (with 60%, 80%, and 90% copper content) developed for this study. However, these high-metal-content filaments were only processed using the G5 PRO, as they are not compatible with the FlashForge printer due to hardware limitations such as insufficient nozzle torque and material feeding capability.

One of the main goals was to maintain as similar process parameters as possible across both printers, to ensure a fair comparison and isolate the influence of the printing technology itself (FGF vs FFF). However, a 100% match was not achievable due to fundamental differences between the machines. For example, the FlashForge printer features a closed chamber, while the G5 PRO operates in an open environment, leading to different cooling and solidification rates. Additionally, the nozzle diameter differed between the two systems (0.6 mm for FlashForge and 0.8 mm for G5 PRO), which also impacts extrusion flow and layer bonding. Other design and hardware differences further limited the ability to fully align all parameters, but values were carefully selected to achieve comparable extrusion conditions and print quality wherever possible.

These process settings can significantly affect material flow, interlayer adhesion, crystallinity development, and ultimately the thermal and mechanical performance of the printed samples.

4.1.1.1 PLA

To print PLA filaments using the FlashForge printer, the material was pre-dried in a vacuum oven at 50 °C for 2 hours. The use of a filament dryer during printing was also recommended to prevent moisture absorption from the environment and to ensure continuous drying, thereby maintaining stable extrusion. For the G5 PRO, the filaments were first pelletized and then dried under the same conditions, followed by immediate printing. The main process parameters used for HTPLA printing with both the G5 PRO and FlashForge printers are in Table 4.1.

Table 4.1. PLA printing parameters on FlashForge and G5 PRO

Parameter	FlashForge	G5 PRO
Nozzle Diameter	0.60 mm	0.80 mm
Line Width	0.72 mm	1.20 mm
Layer Height	0.20	0.25 mm
Wall Line Count	2	2
Top/Bottom Layers	3 / 3	3 / 3
Infill Density	100%	100%
Infill Pattern	Rectilinear	Zigzag
Infill Angles	±45°	[0°, 90°]
Printing Temperature	220 °C	210 °C
Build Plate Temperature	50 °C	65 °C
Print Speed	50 mm/s	20 mm/s
Retraction Distance	1.0 mm	1.0 mm
Retraction Speed	30 mm/s	25 mm/s
Cooling Fan	0% (Layer 1), 50% (≥ 2nd layer)	75% constant
Adhesion Type	Skirt	Skirt
Extrusion Multiplier / Flow	90%	105–110%

For both printers, the printing process followed the same sequence: first, samples for thermal conductivity testing (Hot Disk), followed by DMA specimens, then compression test samples. However, mold inserts were printed only using the G5 PRO, and this step was performed after printing all test samples and completing process optimization.

4.1.1.2 HTPLA

Before printing, HTPLA filaments were dried in a vacuum oven for 3 hours at 50 °C to minimize moisture-related defects and ensure stable extrusion. For the FlashForge printer, filaments were kept in a filament dryer during printing to prevent moisture reabsorption from the environment. In the case of G5 PRO, the dried filaments were immediately pelletized and printed to preserve their dry state and improve flow consistency.

The main process parameters used for HTPLA printing with both the G5 PRO (FGF) and FlashForge (FFF) printers are summarized in Table 4.2.

Table 4.2. HTPLA printing parameters on FlashForge and G5 PRO

Parameter	FlashForge	G5 PRO
Nozzle Diameter	0.60 mm	0.80 mm
Line Width	0.65 mm	0.85 mm
Layer Height	0.20	0.25 mm
Wall Line Count	2	3
Top/Bottom Layers	3 / 3	0 / 0
Infill Density	100%	100%
Infill Pattern	Rectilinear	Zigzag
Infill Angles	[±45°]	[0°, +45°, –45°]
Printing Temperature	220 °C (Layer 1), 200 °C (≥ 2nd layer)	205–215 °C
Build Plate Temperature	60 °C	65 °C
Print Speed	20 mm/s	15 mm/s
Retraction Distance	1.0 mm	1.0 mm
Retraction Speed	30 mm/s	10 mm/s
Cooling Fan	0% (Layer 1), 60% (≥ 2nd layer)	55% constant
Adhesion Type	Skirt	Brim
Extrusion Multiplier / Flow	100%	85–90%

4.1.1.3 Carbon PA

To prepare Carbon PA for printing, the filament was dried in a vacuum oven at 70 °C for 5 hours. Due to the highly hygroscopic nature of polyamides, the use of a filament dryer during printing was mandatory to prevent moisture-related extrusion issues and to ensure dimensional stability.

As with previous materials, the same printing sequence was followed for both printers. The process parameters used for Carbon PA printing on both printers are summarized in Table 4.3.

Table 4.3. Carbon PA printing parameters on FlashForge and G5 PRO

Parameter	FlashForge	G5 PRO
Nozzle Diameter	0.60 mm	0.80 mm
Line Width	0.72 mm	0.85 mm
Layer Height	0.20	0.25 mm
Wall Line Count	2	10
Top/Bottom Layers	3 / 3	0 / 0
Infill Density	100%	100%
Infill Pattern	Rectilinear	Zigzag
Infill Angles	[±45°]	[0°, 90°]
Printing Temperature	260 °C (Layer 1), 200 °C (≥ 2nd layer)	262 °C
Build Plate Temperature	70 °C	96 °C
Print Speed	50 mm/s	15 mm/s
Retraction Distance	1.0 mm	1.0 mm
Retraction Speed	30 mm/s	10 mm/s
Cooling Fan	0% (Layer 1), 60% (≥ 2nd layer)	Disabled
Adhesion Type	Skirt	Brim
Extrusion Multiplier / Flow	100%	90%

4.1.1.4 Copper Filament

Copper Filament, due to its extremely high copper content, could not be printed using the FlashForge printer, as previously demonstrated by other researchers. Therefore, all Copper Filament samples and inserts were fabricated exclusively using the G5 PRO printer. Copper Filament was printed using the same G-code and base settings as HTPLA; however, real-time manual control during printing was essential to ensure successful results. One of the key advantages of the G5 PRO system is its ability to dynamically tune critical parameters during printing, including nozzle and bed temperatures, Z-offset, flow rate, and cooling fan settings. This manual control was crucial for achieving proper flow, bed adhesion, and dimensional stability with Copper Filament.

The following parameter ranges were commonly applied during Copper Filament printing:

- Nozzle Temperature: 199–205 °C
- Bed Temperature: 65–70 °C

- Flow Rate: 85–95% (but increased to 120–140% during the initial layers)
- Print Speed: 75–85%
- Z-offset: –2.54 to –2.60 mm
- Cooling Fan: On

These adjustments significantly improved print consistency and reduced the risk of delamination or under-extrusion caused by the high metal content and reduced polymer fraction of the Copper Filament. The flexibility offered by the G5 PRO enabled successful printing of this highly filled material, which would otherwise be unprintable on the FlashForge printer due to limitations in extrusion force and hardware constraints.

4.1.1.5 PLA–Copper composites (60 %, 80 %, 90 %)

PLA–Copper composite pellets containing 60 %, 80 % and 90 % by weight of copper powder were processed using the Piocreat G5 PRO printer. The copper powder used for compounding was the gas atomized grade described in Section 3.2.1 As the feedstock was prepared in-house and exhibited a heterogeneous granule size distribution, thorough drying prior to printing was essential. All material was dried at 65 °C for 3 hours to minimize moisture-related defects and improve extrusion consistency.

Initial printing trials demonstrated that the HTPLA G-code and base settings could be used as a starting point; however, real-time manual control during fabrication was necessary to achieve consistent results. The G5 PRO's capability to dynamically adjust nozzle temperature, bed temperature, Z-offset, flow rate, and cooling settings during the print was critical for accommodating the higher viscosity and melt lag behavior of the copper-filled PLA.

The printing parameters were adapted to account for the higher density and more viscous flow behavior of the copper-filled PLA. Across the three compositions, the general settings were:

- Nozzle Temperature: 235–250 °C
- Bed Temperature: 70 °C
- Flow Rate: 120–130 % (temporarily increased to 210 % during initial layers to ensure adequate melt flow and full bead formation)
- Print Speed: 80–90 %
- Z-offset: –2.59 mm
- Cooling Fan: On

During printing, the inhomogeneous nature of the compounded granules caused intermittent variations in extrusion rate, particularly when coarse particles reached the melt zone. Melt lag was a frequent occurrence, leading to delayed flow response after retraction or acceleration events. To compensate, the first layers were often printed at a manually increased flow rate of 210 % before reducing to the target range once a stable melt pool was established.

These adjustments helped maintain bed adhesion, prevent under-extrusion, and improve dimensional stability. Despite the challenges inherent to printing highly filled composites, the G5 PRO's ability to adjust parameters in real time enabled the successful production of test geometries and functional components across all three filler loadings.

4.1.2 Comparative Analysis of Fused Granular and Fused Filament Fabrication

This part presents the experimental results of mechanical and thermal tests performed on specimens printed using both the G5 PRO (FGF) and FlashForge (FFF) systems. The goal is to assess the effect of the printing method on the final properties of parts fabricated with identical commercial materials (PLA, HTPLA, and Carbon PA).

For each material, test results from both printers are grouped within the same figure to enable a direct and meaningful comparison. These comparisons provide insight into how the printing strategy (pellet-based vs filament-based) affects sample quality, consistency, and functional performance.

The results showed that both systems were capable of producing parts with comparable overall performance. FlashForge offered slightly better dimensional precision and more consistent results in thermal testing, while the G5 PRO demonstrated competitive mechanical properties and significantly greater material flexibility. These findings confirm that the G5 PRO, despite its larger nozzle and open-chamber configuration, can produce functional parts with mechanical and thermal properties similar to, and in some cases better than those made by the FlashForge printer. Furthermore, the G5 PRO presents notable advantages in terms of lower material costs and a more affordable machine price. Its ability to process customized formulations not available in the commercial filament

market makes it a more versatile and cost-effective solution for research, development, and application-specific manufacturing.

4.1.2.1 Thermal Conductivity Comparison

Figure 4.1 shows the PLA, HTPLA, and Carbon PA specimens produced using the FlashForge Creator 3 Pro and the PIOCREAT G5 PRO, while Table 4.4 reports the corresponding thermal conductivity values. Identical filament materials were used to isolate the influence of the printing system on thermal performance.

For PLA, the FlashForge sample exhibited a slightly higher thermal conductivity than the G5 PRO. Conversely, for HTPLA the G5 PRO produced a marginally higher value compared to the FlashForge. Carbon PA displayed the highest conductivity among the three materials, yet the results from both printers were practically identical.

Overall, these results indicate that the type of printer (FlashForge vs. G5 PRO) had little influence on the measured thermal conductivity of the tested materials. The variations observed are within narrow margins, suggesting that the intrinsic properties of the materials dominate thermal performance, while the printing system contributes only a minimal effect under the selected process parameters.

Table 4.4. Thermal conductivity of samples printed with FlashForge and G5 PRO

Material	FlashForge Creator 3 Pro (W/m·K)	PIOCREAT G5 PRO (W/m·K)
PLA	0.175 ± 0.005	0.164 ± 0.004
HTPLA	0.483 ± 0.003	0.529 ± 0.009
Carbon PA	0.533 ± 0.003	0.532 ± 0.002

Material	FlashForge Creator 3 Pro	PIOCREAT G5 PRO
PLA	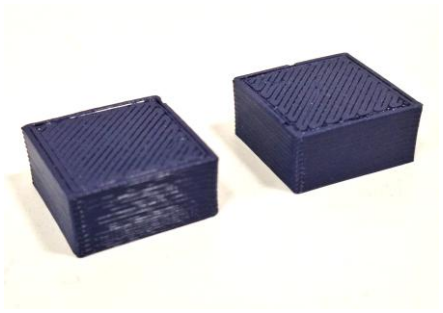	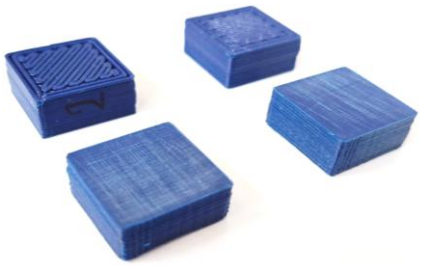
HTPLA	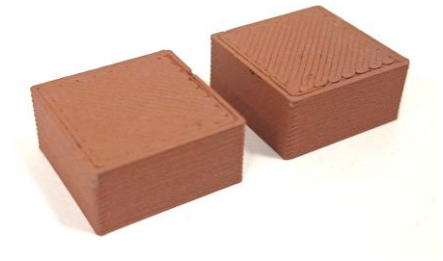	
Carbon PA	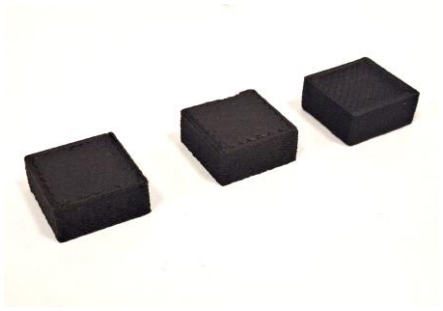	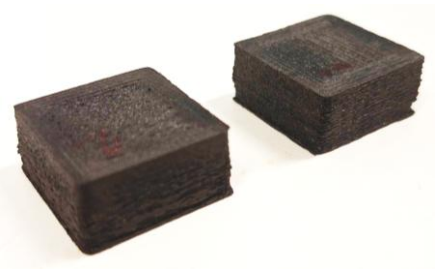

Figure 4.1. Printed specimens for thermal conductivity analysis using FlashForge and G5 PRO

4.1.2.2 Compression Test Comparison

Figure 4.2 shows representative images of the compression specimens, while Figure 4.3 illustrates the compressive stress–displacement curves for all materials printed with the two systems. Table 4.5 reports the corresponding average compressive properties obtained from three to four specimens per condition. The values are expressed as mean ± standard deviation, which provides an indication of both the central tendency and the variability of the measurements.

For PLA the FlashForge samples showed slightly higher stiffness and strength compared to those produced with the G5 PRO. This difference can be explained by process characteristics such as nozzle resolution, extrusion accuracy and cooling profiles that may favor more uniform interlayer bonding in FFF printing.

In the case of HTPLA the same trend was observed, with FlashForge parts exhibiting somewhat higher modulus and compressive strength than their G5 PRO counterparts. The differences remain small, which suggests that both printers deliver consistent mechanical performance for this material.

For Carbon PA the trend was reversed. The G5 PRO samples achieved a clearly higher modulus compared to FlashForge, while the compressive stress values were similar. The improvement in stiffness with the G5 PRO can be associated with its pellet-based feeding system and higher extrusion throughput, which are more suitable for processing fiber-reinforced polymers.

In spite of these differences, the compressive stress values showed only limited variation, suggesting that both printers provide mechanically reliable parts within the tested conditions.

Table 4.5. Compression mechanical properties of specimens printed with FlashForge and G5 PRO

Sample	Young's Modulus [MPa]	Maximum Force [N]	Compressive Stress at Maximum Force [MPa]
PLA – G5 PRO	892.11 ± 65.33	9443.14 ± 650.41	65.43 ± 4.05
PLA - FlashForge	1024.15 ± 25.93	10000.09 ± 0.06	69.97 ± 0.56
HTPLA - G5 PRO	908.48 ± 66.37	9255.37 ± 140.40	58.71 ± 1.22
HTPLA - FlashForge	1004.89 ± 35.58	8988.48 ± 482.30	63.57 ± 3.60
Carbon PA - G5 PRO	1085.72 ± 90.46	10000.11 ± 0.11	65.05 ± 0.80
Carbon PA - FlashForge	759.51 ± 12.34	10000.07 ± 0.04	63.18 ± 0.44

Material	FlashForge Creator 3 Pro	PIOCREAT G5 PRO
PLA	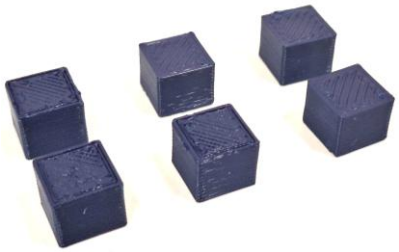	
HTPLA	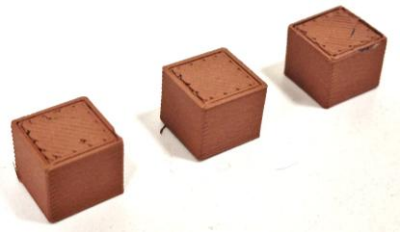	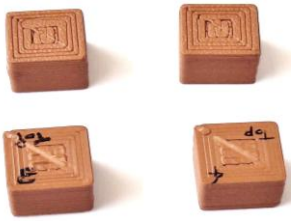
Carbon PA	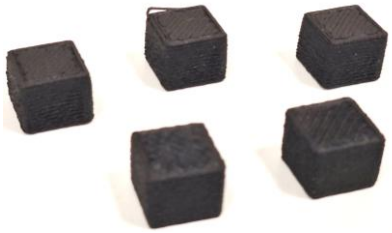	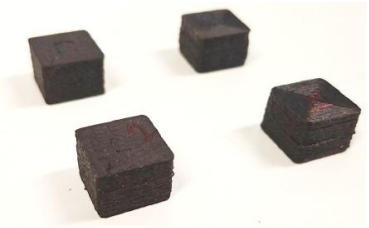

Figure 4.2. Printed specimens for compression analysis with FlashForge and G5 PRO

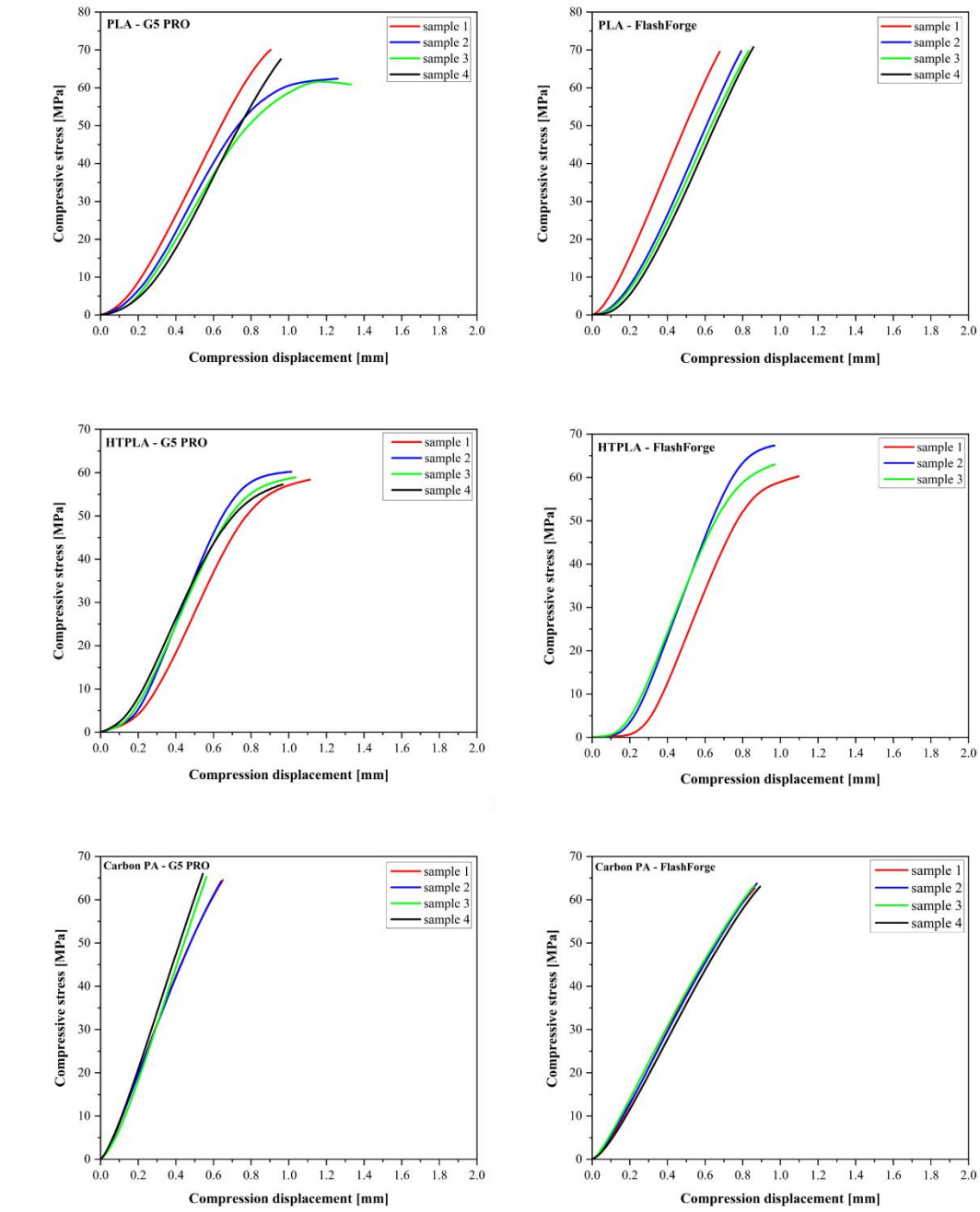

Figure 4.3. Compression test results of specimens printed with FlashForge and G5 PRO

4.1.2.3 Dynamic Mechanical Analysis (Bending Mode) Comparison

Figure 4.4 shows the specimens tested in bending mode, while Figure 4.5 presents the storage modulus (E′) as a function of temperature for PLA, HTPLA, and Carbon PA printed with both the FlashForge Creator 3 Pro and the PIOCREAT G5 PRO. This comparison allows an assessment of both stiffness and thermal stability, with particular

attention to the heat deflection temperature (HDT), defined here as the temperature at which the storage modulus decreases below 800 MPa.

Material	FlashForge Creator 3 Pro	PIOCREAT G5 PRO
PLA		
HTPLA	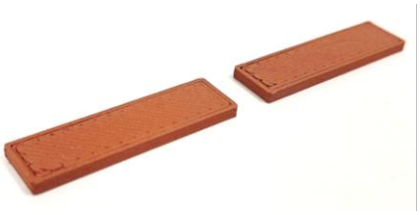	
Carbon PA		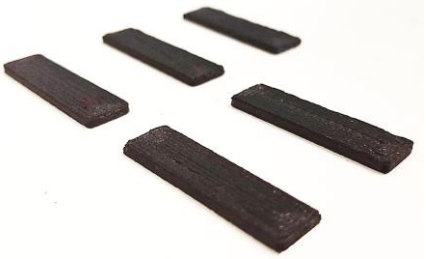

Figure 4.4. Printed specimens for dynamic mechanical analysis with FlashForge and G5 PRO

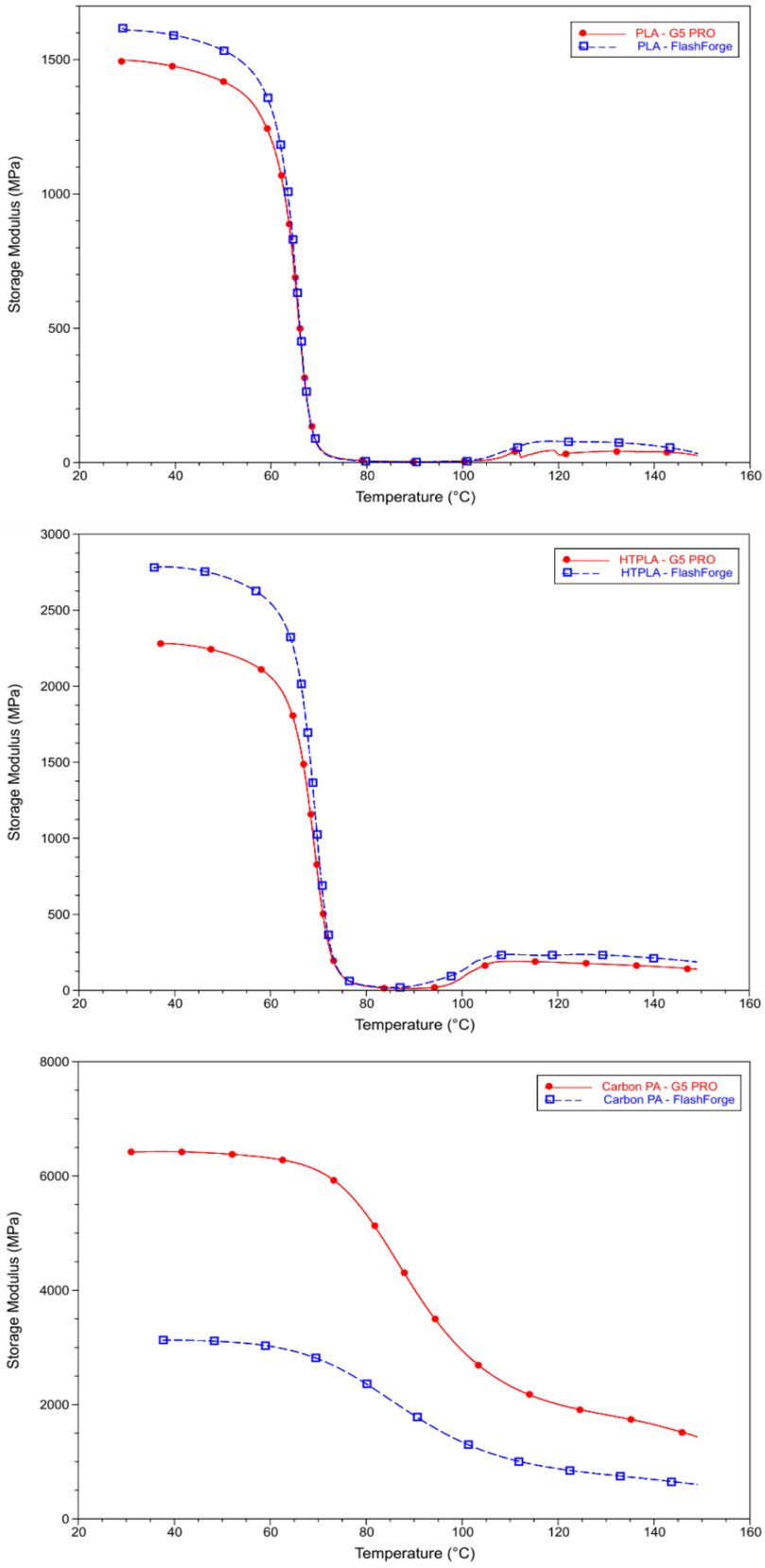

Figure 4.5. DMA (bending mode) results of specimens printed with FlashForge and G5 PRO

For PLA and HTPLA, FlashForge specimens started with slightly higher stiffness. These differences were limited, suggesting that the two systems delivered comparable thermo-mechanical behavior for these materials.

For Carbon PA, the difference between the two printers was more evident. The G5 PRO samples exhibited significantly higher modulus values across the entire temperature range and also achieved a higher HDT compared to the FlashForge specimens. This suggests that the pellet-fed G5 PRO process provided improved interlayer bonding and resistance to softening. These findings highlight the role of printer configuration and feeding technology in determining the thermo-mechanical behavior of printed parts.

4.1.2.4 Dynamic Mechanical Analysis (Tension Mode) Comparison

The images of the tested samples are the same as those already presented in Figure 4.4 for the DMA bending mode analysis. Figure 4.6 shows the displacement–temperature curves for PLA, HTPLA, and Carbon PA printed using the FlashForge Creator 3 Pro and the PIOCREAT G5 PRO. All tests were conducted following the same thermal treatment protocol to ensure consistent baseline conditions across materials and printers.

For PLA and HTPLA, both printers showed similar displacement trends with temperature, with G5 PRO specimens reaching slightly higher values at elevated temperatures. The differences were minor, indicating comparable thermo-mechanical behavior.

Carbon PA behaved differently, exhibiting negative displacement that indicates contraction under heating. This effect was stronger in the G5 PRO samples, while the FlashForge samples showed only slight contraction. Overall, both systems produced stable and reproducible thermo-mechanical behavior.

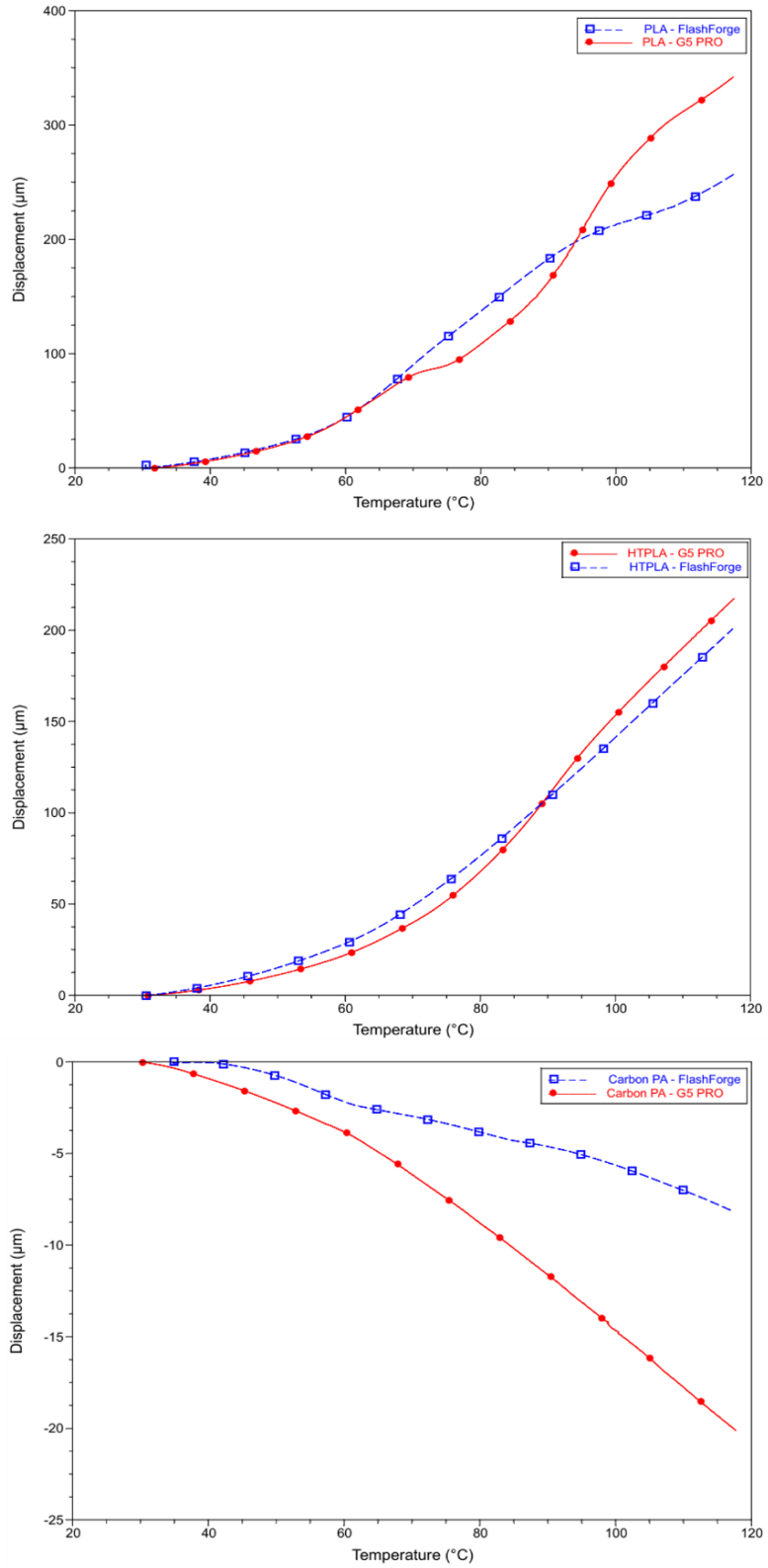

Figure 4.6. DMA (tension mode) results of specimens printed with FlashForge and G5 PRO

4.2 Printing Process of Inserts with G5 PRO

The mold inserts were manufactured using the G5 PRO pellet-based 3D printer, following a defined sequence based on material type: PLA, HTPLA, Carbon PA, and Copper Filament, followed by three custom PLA–Copper composite formulations. The initial four materials were commercially available as standard filaments and were pelletized to enable compatibility with the G5 PRO's fused granular fabrication system. The copper-filled composites, in contrast, were developed and compounded specifically for this study.

Each insert was printed only after completing the production and characterization of mechanical and thermal test specimens for the corresponding material. This ensured that the process parameters were fully optimized and that the performance of each formulation was well understood prior to its application in mold tooling. As shown in Figure 4.7, the geometry and dimensions of the mold inserts are detailed.

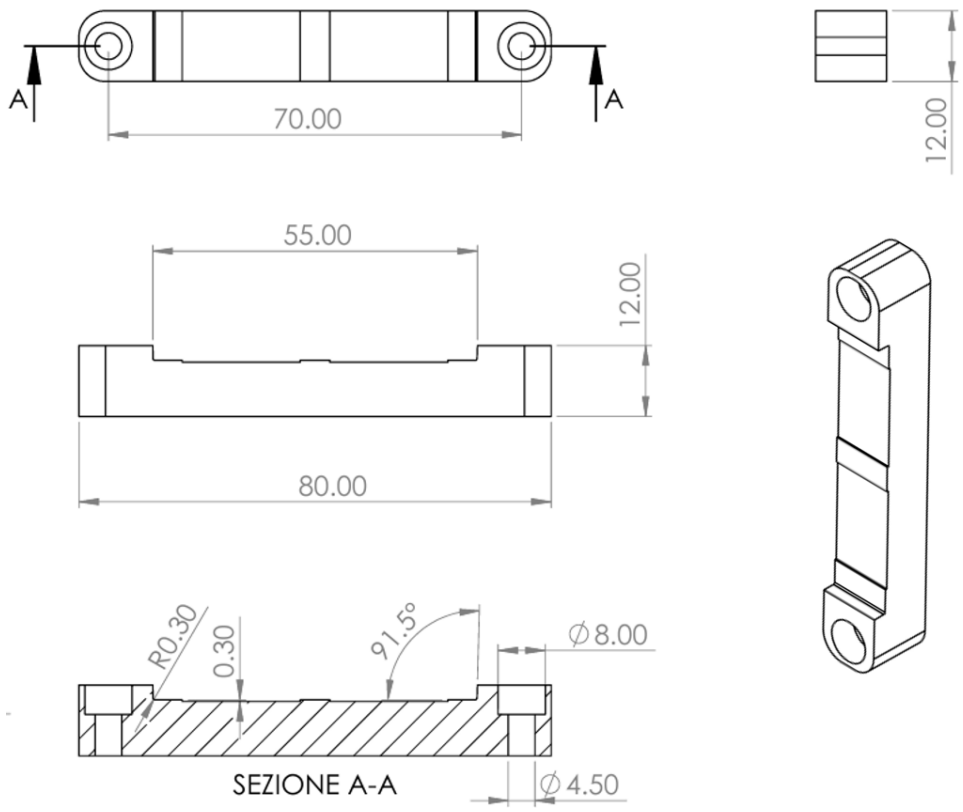

Figure 4.7. Schematic of insert geometry

All inserts had the same geometry, specifically designed to fit into the standard mold cavity. Post-processing by surface finishing (manual polishing) was performed to

eliminate surface irregularities, compensate for any warping induced during printing, and achieve dimensional tolerances suitable for precise alignment within the mold assembly.

Dimensional measurements were taken before and after polishing to quantify surface adjustments. Specifically, insert dimensions A, B, C, D, and E (as shown in Figure 4.8) were monitored to evaluate geometric stability and dimensional consistency across the insert's critical sections.

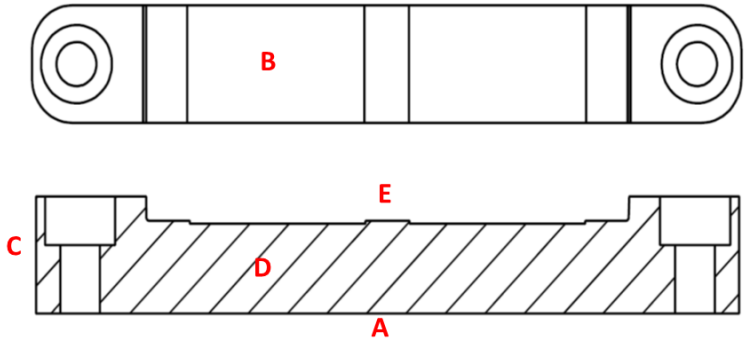

Figure 4.8. Insert geometry with labeled dimensions (A–E)

Also, after printing and before injection molding, all inserts underwent thermal treatment in the oven to improve crystallinity and overall performance. Each insert was weighed and its density calculated to assess the presence of internal voids or inconsistencies. These issues may arise from material shrinkage, under-extrusion, or inadequate layer bonding; factors that are especially important in fused granular fabrication due to the high viscosity of molten pellets and the large nozzle diameters commonly used in this process.

The following subsections present the evaluation of the additive manufacturing process, addressing key factors such as printability, warping, nozzle clogging, cooling behavior, build platform adhesion, and the impact of copper loading on both thermal and mechanical performance. Additionally, the discussion highlights critical considerations related to print setup and extrusion, particularly for composites with high metal content.

4.2.1 PLA Insert

The PLA insert was fabricated using the Piocreat G5 PRO FGF 3D printer, utilizing FILOALFA® PLA as the feedstock. The general process parameters adopted for this fabrication were previously detailed in Section 4.1.1.

One critical aspect in the successful printing of functional inserts (regardless of the material used) is the orientation of the part on the build platform. For the G5 PRO system

specifically, the optimal positioning is with the longest axis of the insert aligned perpendicular to the Y-axis, as shown in Figure 4.9.

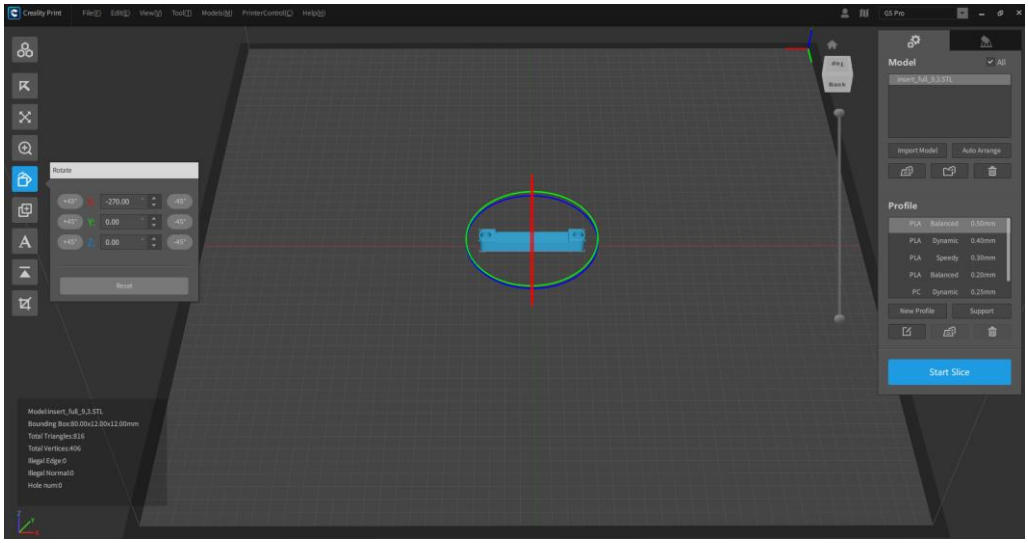

Figure 4.9. Orientation of inserts during printing.

This orientation is dictated by the kinematic constraints of the G5 PRO: the build plate is limited to movement solely along the Y-axis, while the nozzle can travel along the X and Z axes. If the insert is oriented parallel to the Y-axis, the platform must execute the majority of movement, which increases mechanical stress and the risk of detachment, especially for long and narrow geometries. Conversely, aligning the insert along the X-axis ensures that most of the movement burden is handled by the nozzle (specifically through its X-axis translation) which provides better print stability and accuracy.

Experimental trials confirmed that minimizing motion from the build plate, and instead relying on the more stable and precise nozzle system for positional changes, significantly improved print success. This approach not only reduced the likelihood of layer shift or adhesion failure but also allowed for smoother deposition and better overall quality of the insert.

To optimize the mechanical integrity and reduce internal voids, a specific infill pattern was adopted during the printing of the PLA insert. The first three and last three layers were printed using a ±45° infill orientation, while the intermediate layers followed an alternating 0°/90° pattern (Figure 4.10). This strategy was implemented to ensure effective overlap between adjacent filament paths, thereby minimizing the presence of unfilled gaps and enhancing the structural cohesion of the part.

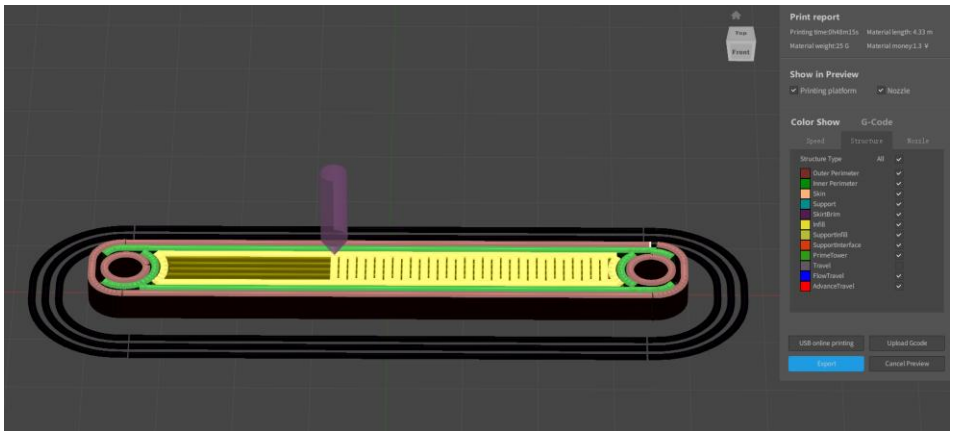

Figure 4.10. Printing pattern of the PLA insert

Finally, after printing the PLA insert (Figure 4.11), the part was weighed and found to have a mass of approximately 10.15 grams. The volume of the insert, 8.804 cm^3, was extracted directly from the STL file generated in SolidWorks during the CAD modeling phase. Based on this volume and the measured mass, the actual density of the printed insert was calculated to be approximately 1.15 g/cm^3.

This measured density is lower than the theoretical density of the PLA material, which is specified as 1.24 g/cm^3 by the manufacturer. The discrepancy is due to internal voids and micro-defects resulting from the FGF printing process. Such porosity typically arises from incomplete layer bonding or fluctuations in extrusion flow. In this case, the estimated void content was approximately 7.01%, a value in line with expectations for pellet-based additive manufacturing systems.

Figure 4.11. PLA insert

Table 4.6 reports the dimensional measurements of the PLA insert in the as-printed state and after polishing and thermal treatment (TT).

Table 4.6. Dimensional measurements of PLA insert

	AP (as printed) [mm]	After TT and Polishing [mm]
A	79.99	79.81
E	54.84	54.82
C	12.20	12.03
D	10.03	9.91
B	12.02	11.99

4.2.2 HTPAL Insert

The HTPLA insert was fabricated using the Piocreat G5 PRO 3D printer, utilizing Proto pasta® HTPLA as the feedstock. The general process parameters followed those outlined in Section 4.1.1, with specific adjustments tailored to this material. In particular, the Z-offset was set to –2.60 mm to position the nozzle closer to the bed, improving first-layer adhesion. Additionally, the part cooling fan was kept off for most of the print duration to maintain uniform temperature distribution and reduce the risk of warping.

The infill strategy combined zigzag [±45°, 0°] patterns to maximize interlayer bonding and minimize voids. It was also observed that pre-drying the pellets was essential to ensure proper adhesion and surface quality. Without drying, frequent detachment and delamination occurred. A drying step of 2 hours at 50 °C significantly improved print consistency and overall part integrity.

The orientation of the part on the build platform was kept consistent with the previous case, with the insert aligned perpendicular to the Y-axis. This configuration minimized the required movement of the G5 PRO's bed and improved print stability by leveraging the more controlled motion of the nozzle in the X and Z axes.

After fabrication (Figure 4.12), the same procedure used for the PLA insert was applied to estimate the void content. Using the part's CAD-derived volume and measured mass, and referencing a theoretical density of approximately 2.30 g/cm³ (as specified in the HTPLA datasheet), the void content was estimated to fall within the range of 1.5–2.1%. This low porosity indicates effective material consolidation and a high-quality result for pellet-based HTPLA printing.

Figure 4.12. HTPLA insert

Table 4.7 reports the dimensional measurements of the HTPLA insert in the as-printed state and after polishing and thermal treatment (TT).

Table 4.7. Dimensional measurements of HTPLA insert

	AP (as printed) [mm]	After TT and Polishing [mm]
A	80.25	79.75
E	54.24	54.21
C	12.06	11.88
D	9.66	9.44
B	12.46	11.94

4.2.3 Carbon PA Insert

The Carbon PA insert was fabricated using the Piocreat G5 PRO FGF 3D printer, utilizing Roboze® carbon-fiber-reinforced polyamide pellets. The general process parameters were based on those described in Section 4.1.1, with specific adjustments required due to the different material characteristics. Notably, a Z-offset of –2.60 mm was applied manually to improve first-layer adhesion, as the part was prone to detachment during early prints.

Due to the presence of 20% carbon fibers and the change in matrix from PLA to PA, it was necessary to closely monitor the printing process. Adjustments to flow rate and print speed were often required to maintain dimensional consistency and minimize extrusion instability. The use of a 0°/90° pattern was found to be more effective in reducing warping and detachment compared to ±45° configurations. Additionally, pre-drying was critical; pellets were dried for 5 hours at 70 °C, which significantly improved bonding.

The orientation of the insert on the build platform followed the same approach as in previous cases, with the part aligned perpendicular to the Y-axis, optimizing print stability by minimizing build plate movement and relying on controlled nozzle motion.

After fabrication (Figure 4.13), the same methodology used in previous sections was applied to evaluate the void content. Using the insert's CAD-derived volume and the measured mass, and referencing the theoretical density of 1.40 g/cm³ (as reported in the Roboze datasheet), the actual density was calculated to be approximately 1.23 g/cm³. This corresponds to an estimated void content of 12.14%. While higher than the PLA and HTPLA inserts, this level of porosity remains acceptable for functional prototyping and short-run molding applications.

Figure 4.13. Carbon PA insert

Table 4.8 reports the dimensional measurements of the Carbon PA insert in the as-printed state and after polishing and thermal treatment (TT).

Table 4.8. Dimensional measurements of Carbon PA insert

	AP (as printed) [mm]	**After TT and Polishing [mm]**
A	81.53	79.87
E	54.56	54.51
C	11.91	11.77
D	9.52	9.38
B	12.65	11.91

4.2.4 Copper Filament Insert

The Copper Filament insert was fabricated using the Piocreat G5 PRO printer, employing Filamet™ copper-filled PLA pellets produced by Virtual Foundry. The orientation of the

insert on the build platform followed the same convention as previous cases, with the longest axis positioned perpendicular to the Y-axis. In Figure 4.14, the printing of the Copper Filament insert with the G5 PRO is shown.

Figure 4.14. Copper Filament insert during printing with G5 PRO

After fabrication (Figure 4.15), the same method applied to previous inserts was used to estimate the void content. Using the CAD-derived volume and measured mass, and comparing against the theoretical density range of 4.50–4.70 g/cm³ (as provided in the datasheet), the actual density was found to be in the range of 4.3–4.4 g/cm³. This corresponds to an estimated void content between 2.1% and 8.5%, with an average of approximately 5.3%.

Figure 4.15. Copper Filament insert

Table 4.9 reports the dimensional measurements of the Copper Filament insert in the as-printed state and after polishing and thermal treatment (TT).

Table 4.9. Dimensional measurements of Copper Filament insert

	AP (as printed) [mm]	After TT and Polishing [mm]
A	80.54	79.73
E	54.48	54.10
C	12.22	12.20
D	9.69	9.68
B	12.58	11.93

4.2.5 PLA–Copper composites (60 %, 80 %, 90 %) Inserts

The PLA–Copper composite inserts were fabricated using the Piocreat G5 PRO (FGF) 3D printer, employing custom-compounded PLA pellets containing 60 %, 80 % and 90 % by weight of copper powder. Prior to printing, all feedstock was dried at 65 °C for 3 hours in a vacuum oven to improve extrusion consistency.

Printing trials were first performed using the HTPLA G-code as a baseline, confirming that simple geometry samples could be successfully produced without major modifications. However, the fabrication of full-size mold inserts required active manual control during the print process. The orientation of the insert on the build platform followed the same convention as previous cases, with the longest axis positioned perpendicular to the Y-axis. While a 0°/±45° pattern was initially tested, it was found to be less suitable for these high-metal-load composites. A 90° orientation was adopted for improved dimensional stability and reduced risk of delamination, as shown in figure 4.16.

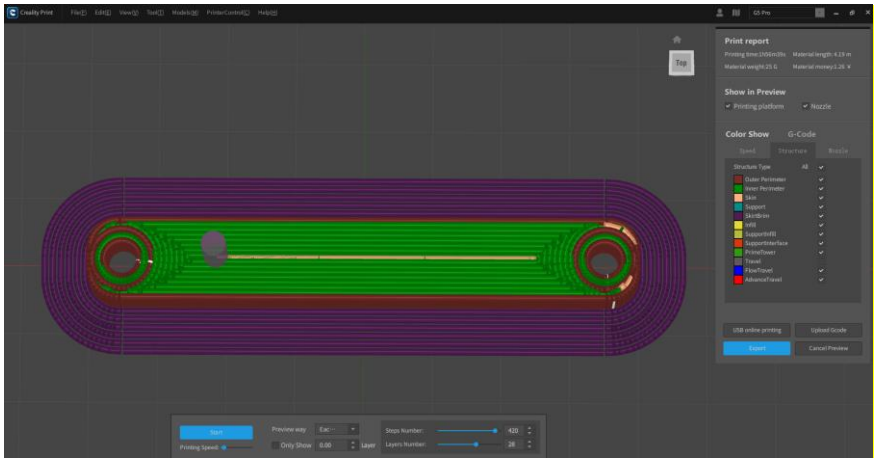

Figure 4.16. Printing orientation and pattern of the PLA–Copper insert

A brim was employed in all cases to improve bed adhesion and minimize the risk of edge lifting during the initial layers (Figure 4.17). This was particularly important for the high-metal-content formulations, where reduced polymer fraction can decrease adhesion strength and increase warping tendencies.

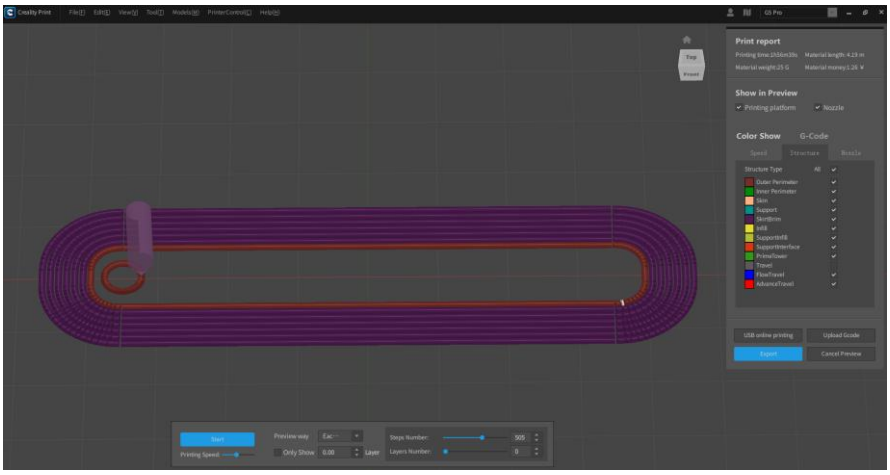

Figure 4.17. Brim configuration during printing

Due to the heterogeneous nature of the compounded granules, which were less uniform than commercial-grade pellets, print quality exhibited more variability. Occasional coarse granules arriving at the nozzle altered extrusion behavior compared to periods when finer particles were fed, leading to short-term changes in deposition rate. Melt lag was a recurrent issue, particularly in the first layers. To mitigate under-extrusion at the start of the print, the flow rate was manually increased to 210 % for the initial layers, ensuring sufficient material delivery and complete track fusion. After this initial phase, the flow was reduced to around 130 % to prevent overflow and excessive bead size.

The overall printing process for the three compositions followed similar procedures, although the 90 % copper formulation required more aggressive compensation due to its extremely high filler content. For copper 90 % composition, the first 25 % of the build was printed with the flow manually set at 230 % and the nozzle temperature elevated to 260 °C to promote complete melting. Under these conditions, a typical insert required 2.5 to 3 hours to fabricate.

The printed inserts for each composition are shown in Figure 4.18 (PLA–Copper 60 %), Figure 4.19 (PLA–Copper 80 %), and Figure 4.20 (PLA–Copper 90 %).

Figure 4.18. PLA–Copper 60 % insert

Figure 4.19. PLA–Copper 80 % insert

Figure 4.20. PLA–Copper 90 % insert

Tables 4.10, 4.11, and 4.12 report the dimensional measurements of the PLA–Copper inserts with 60%, 80%, and 90% copper content, respectively. For each composition, the values are presented in the as-printed state and after polishing and thermal treatment (TT).

Table 4.10. Dimensional measurements of PLA–Copper 60 % insert

	AP (as printed) [mm]	**After TT and Polishing [mm]**
A	79.75	79.32
E	54.44	53.99
C	12.02	11.97
D	9.58	9.52
B	12.25	11.87

Table 4.11. Dimensional measurements of PLA–Copper 80 % insert

	AP (as printed) [mm]	After TT and Polishing [mm]
A	79.95	79.47
E	54.45	54.41
C	11.86	11.81
D	9.38	9.34
B	12.22	11.72

Table 4.12. Dimensional measurements of PLA–Copper 90 % insert

	AP (as printed) [mm]	After TT and Polishing [mm]
A	79.91	79.58
E	54.38	54.20
C	11.96	11.89
D	9.54	9.47
B	12.46	11.93

Table 4.13 summarizes the dimensional measurements of all inserts after thermal treatment (TT) and polishing, reported in millimeters. The comparison includes PLA, HTPLA, Carbon PA, Copper Filament, and PLA–Copper composites at different filler loadings, with the corresponding reference values of the steel insert also reported. This provides a direct evaluation of dimensional stability with respect to the reference geometry defined by the steel insert.

It can be observed that all polymer-based inserts exhibit small dimensional deviations compared to steel, generally within a few tenths of a millimeter. When expressed as percentage differences, the deviations of dimensions A–E typically fall below 2–3% for most materials, with the PLA–Copper 90% insert showing the closest match to steel. Overall, the differences remain limited, indicating that all tested materials retained a geometry comparable to the reference steel insert after TT and polishing.

Table 4.13. Dimensional comparison (A, B, C, D, E) of all inserts after thermal treatment and polishing

	A [mm]	E [mm]	C [mm]	D [mm]	B [mm]
PLA	79.81	54.82	12.03	9.91	11.99
HTPLA	79.75	54.21	11.88	9.44	11.94
Carbon PA	79.87	54.51	11.77	9.38	11.91
Copper Filament	79.73	54.10	12.20	9.68	11.93
PLA–Copper 60%	79.32	53.99	11.97	9.52	11.87
PLA–Copper 80%	79.47	54.41	11.81	9.34	11.72
PLA–Copper 90%	79.58	54.20	11.89	9.47	11.93
Steel	79.97	54.83	12.04	9.27	11.95

4.2.5.1 Porosity evaluation of PLA–Copper 60 % composite

The PLA–Copper 60 % insert and corresponding test samples were fabricated from custom-compounded pellets containing a nominal copper mass fraction of 60 % and a PLA mass fraction of 40 %. As this formulation is not commercially standardized, the theoretical density was calculated using the rule of mixtures (Equation 4.1), with the density of PLA taken as 1.24 g/cm³ and that of copper as 8.90 g/cm³:

$$\text{Theoretical density} = \frac{1}{\frac{0.40}{1.24} + \frac{0.60}{8.90}} = 2.564\ \text{g/cm}^3$$

Equation 4.1. Theoretical density of the PLA–Copper 60 % composite calculated using the rule of mixtures

The actual density (Equation 4.2) was obtained by measuring the mass of the printed insert and dividing by volume, yielding an average value of 2.226 ± 0.118 g/cm³. The porosity (void fraction) was calculated as:

$$\text{Porosity} = \frac{\text{theoretical density} - \text{actual density}}{\text{theoretical density}} \times 100 = \frac{2.564 - 2.226}{2.564} \times 100 = 13.2\ \%$$

Equation 4.2. Porosity calculation for the PLA–Copper 60 % composite

This relatively high porosity level is consistent with prior studies on highly filled metal–polymer composites fabricated by fused granular fabrication, where incomplete inter-bead fusion, irregular particle packing, and local melt-flow instabilities can contribute to void formation.

4.2.5.2 Porosity evaluation of PLA–Copper 80 % composite

The PLA–Copper 80 % insert and corresponding test samples were fabricated from custom-compounded pellets containing a nominal copper mass fraction of 80 % and a PLA mass fraction of 20 %. As this formulation is not commercially standardized, the theoretical density was calculated using the rule of mixtures (Equation 4.3), with the density of PLA taken as 1.24 g/cm³ and that of copper as 8.90 g/cm³:

$$\text{Theoretical density} = \frac{1}{\frac{0.20}{1.24} + \frac{0.80}{8.90}} = 3.981\ \text{g/cm}^3$$

Equation 4.3. Theoretical density of the PLA–Copper 80 % composite calculated using the rule of mixtures

The actual density (Equation 4.4) was obtained by measuring the mass of the printed insert and dividing by its CAD-derived volume, yielding an average value of 3.790 ± 0.005 g/cm³.

The void fraction was then calculated as:

$$\text{Porosity} = \frac{\text{theoretical density} - \text{actual density}}{\text{theoretical density}} \times 100 = \frac{3.981 - 3.790}{3.981} \times 100 = 4.79\ \%$$

Equation 4.4. Porosity calculation for the PLA–Copper 80 % composite

Compared with the 60 % Cu formulation, the porosity level here is lower, suggesting improved inter-bead fusion and particle packing at higher copper loading. As also observed in the SEM micrographs for the PLA–Copper 80 % composition, fewer and smaller voids are visible within the printed structure.

4.2.5.3 Porosity evaluation of PLA–Copper 90 % composite

The PLA–Copper 90 % insert and corresponding test samples were fabricated from custom-compounded pellets containing a nominal copper mass fraction of 90 % and a PLA mass fraction of 10 %. As this formulation is not commercially standardized, the theoretical density was calculated using the rule of mixtures (Equation 4.5), with the density of PLA taken as 1.24 g/cm³ and that of copper as 8.90 g/cm³:

$$\text{Theoretical density} = \frac{1}{\frac{0.10}{1.24} + \frac{0.90}{8.90}} = 5.498\ \text{g/cm}^3$$

Equation 4.5. Theoretical density of the PLA–Copper 90 % composite calculated using the rule of mixtures

The actual density (Equation 4.6) was obtained by measuring the mass of the printed insert and dividing by its CAD-derived volume, yielding an average value of 5.317±0.008 g/cm³. The porosity (void fraction) was then calculated as:

$$\text{Porosity} = \frac{\text{theoretical density} - \text{actual density}}{\text{theoretical density}} \times 100 = \frac{5.498 - 5.317}{5.498} \times 100 = 3.29\ \%$$

Equation 4.6. Porosity calculation for the PLA–Copper 90 % composite

This porosity level is the lowest among the three tested formulations, indicating that at very high copper loading the composite achieves high packing density and minimal void content, as also observed in the SEM micrographs.

Chapter 5

INJECTION MOLDING PROCESS

5.1 Materials and Methods of the Injection Molding Process

All injection molding trials were performed using the Wittmann Battenfeld SmartPower 50 injection molding machine (complete description in chapter 2). The same cycle parameters were applied for all inserts to ensure a consistent basis for comparison. For the purposes of this study, the steel insert cavity was replaced with additively manufactured inserts of the same nominal geometry, produced from different commercial composite feedstocks.

The mold used in this work (Figure 5.1) was manufactured from Steel 1.2083, a martensitic stainless steel with high hardenability, good resistance to corrosion, and excellent resistance to hot oxidation, commonly used for hot-work molds in plastic processing.

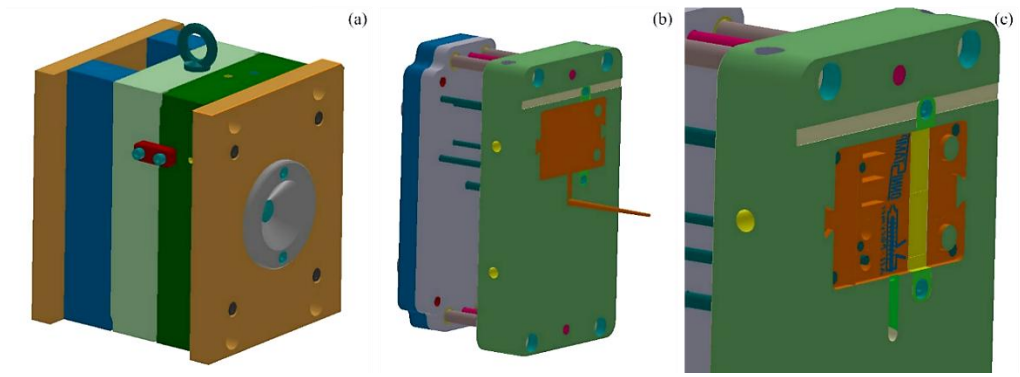

Figure 5.1. Mold used in this thesis: (a) closed mold configuration, (b) open mold showing the filled cavity with the sprue still attached, and (c) detail of the mold cavity highlighting the replaced insert portion in yellow and light green

The mold includes an interchangeable insert plate measuring 230 × 130 × 40 mm. Internal cooling channels with a 6 mm diameter are positioned 24 mm below the mold surface, and a water flow rate of 10 L/min was maintained during all tests, as shown in Figure 5.2.

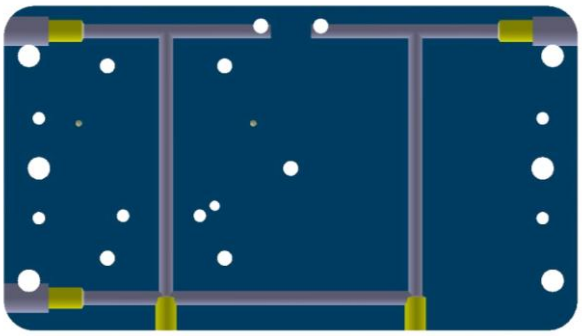

Figure 5.2. Internal layout of the mold's cooling system

In addition, a cross-sectional view of the mold is presented in Figure 5.3, where the yellow-highlighted area indicates the cavity designed to accommodate the interchangeable insert.

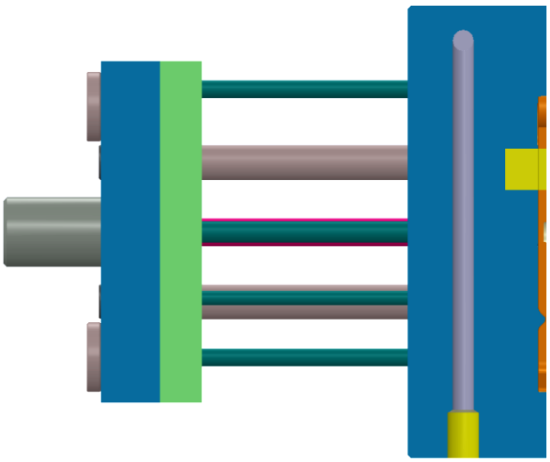

Figure 5.3. Cross-section of the mold and insert cavity

For all experimental trials, the injection molding parameters were maintained constant to ensure direct comparability of results across the different inserts. The melt temperature was set to 180 °C, while the mold temperature was regulated at 25 °C. Each cycle incorporated a packing time of 10 s, followed by a cooling time of 15 s prior to part ejection. The plasticized shot volume was fixed at 25 cm^3. The processed material was polypropylene (LyondellBasell Moplen HP500N), whose properties and characteristics are described in detail in chapter 2.

For each insert, ten consecutive injection cycles were carried out under identical processing conditions, without altering the set parameters. The applied holding pressure profile for these cycles is reported in Table 5.1, while the subsequent subsections present the specific observations and results for each insert. During the trials, infrared

thermography (Optris PI 640i) was employed to monitor the in-mold surface temperature of the insert at key points in the cycle, as shown in Figure 5.4. Additionally, all molded parts were weighed immediately after ejection using a precision balance to record any variation in part mass across cycles. The corresponding mass–cycle graphs for each insert are presented in the subsequent subsections, together with a quality evaluation in which the results are compared against those obtained with the steel insert.

Table 5.1. Pressure profile during injection

Cycle	Pressure [bar]
1	50
2	50
3	100
4	200
5	400
6	600
7–10	600

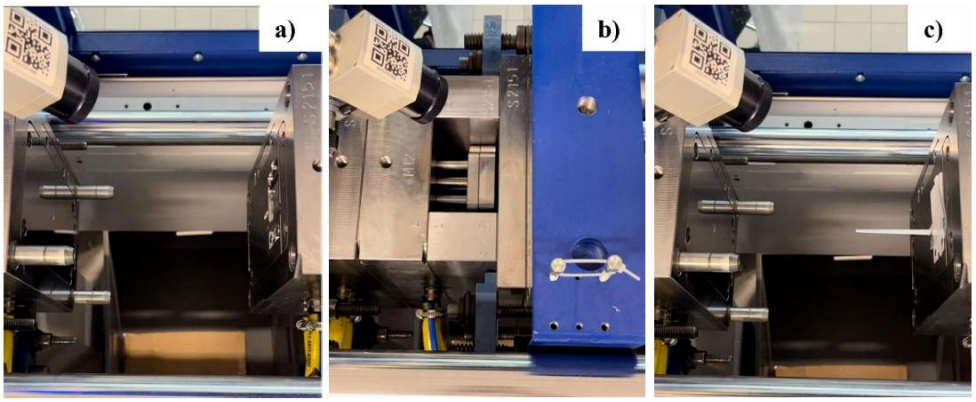

Figure 5.4. Infrared thermal camera mounted above the injection molding press to monitor the surface temperature of the insert during the cycle: (a) mold open immediately after part ejection, (b) mold closed during polymer injection and, (c) mold opening for part removal

5.2 Analysis of Insert Performance During Injection molding

In the following subsections, the performance of seven different inserts is analyzed in the order: Steel, Carbon PA, HTPLA, Copper Filament, PLA–Copper 60%, PLA–Copper 80%, and PLA–Copper 90%. Although the PLA insert was available, it was not tested due to its low thermal conductivity, which would significantly limit its in-mold performance.

5.2.1 Steel Insert

During the ten consecutive injection cycles performed with the steel insert, no issues were encountered regarding part ejection. All molded parts were released smoothly by the ejector system without the need for manual removal, as expected for steel.

Figure 5.5 shows six representative parts (out of ten) produced with the steel insert, arranged in sequence. The corresponding masses, measured immediately after ejection, are reported in Table 5.2.

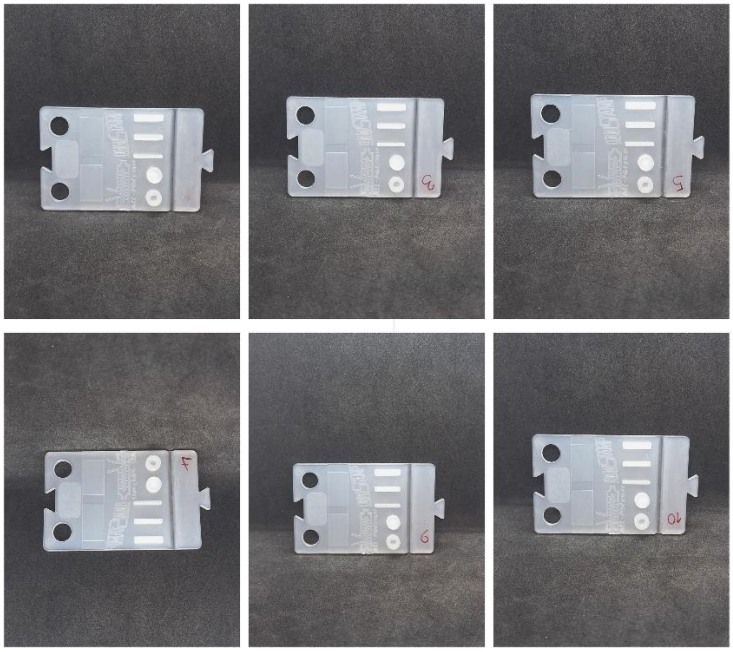

Figure 5.5. Molded parts using the steel insert

Table 5.2. Weights of injection-molded parts produced with the steel insert

Cycle	Weight [g]
1	9.7825
2	9.7822
3	10.0686
4	10.1763
5	10.2915
6	10.4287
7	10.4364
8	10.4302
9	10.4267
10	10.4338

In the case of the steel insert, the high heat dissipation caused the surface temperature to return to room level in less than 2 seconds after mold opening, as illustrated in Figure 5.6 (b). Figure 5.6 (a) corresponds to the mold opening and part ejection, while Figure 5.6 (b) was captured immediately afterward.

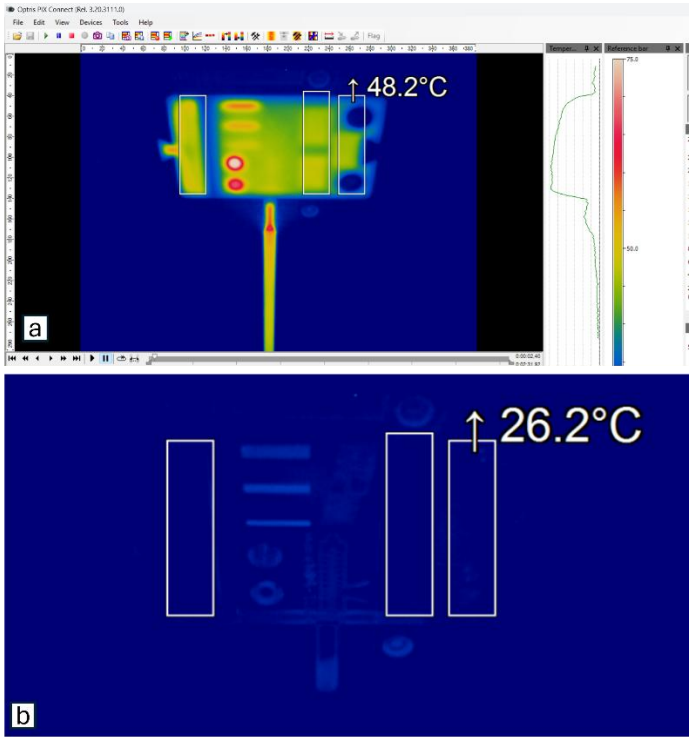

Figure 5.6. Infrared thermography of the steel insert during the tenth cycle: (a) mold opening and part ejection, (b) immediately after mold opening

5.2.2 Carbon PA Insert

During the ten consecutive injection cycles performed with the Carbon PA insert, the ejection performance changed notably over time. In the first five cycles, the ejector system was able to remove the parts smoothly without manual intervention. However, from the sixth cycle onward, the ejectors alone were not sufficient, and the parts had to be removed manually due to partial adhesion to the mold surface.

Figure 5.7 shows six representative parts (out of ten) produced with the Carbon PA insert, arranged in sequence. Their corresponding masses, measured immediately after ejection, are listed in Table 5.3.

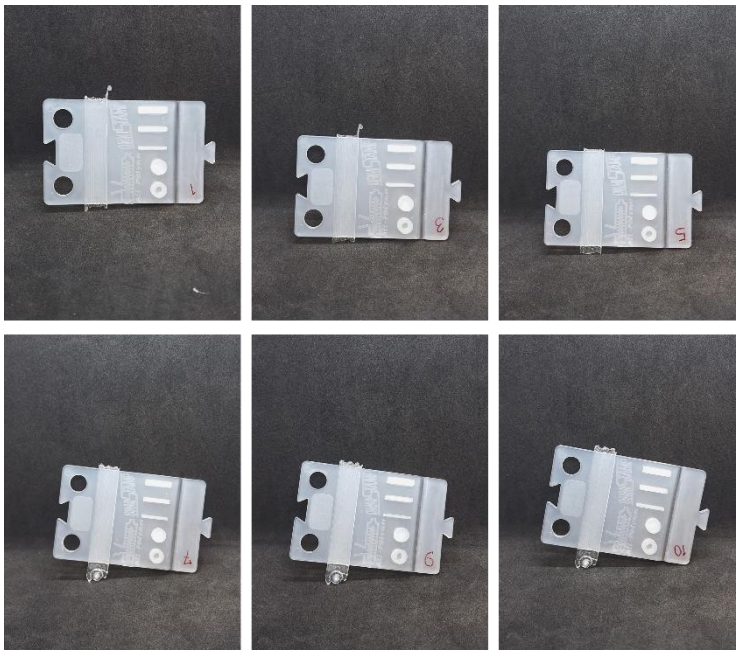

Figure 5.7. Molded parts using the Carbon PA insert

Table 5.3. Weights of injection-molded parts produced with the Carbon PA insert

Cycle	Weight [g]
1	9.7680
2	9.7297
3	10.0221
4	10.1571
5	10.3186
6	10.5688
7	10.5745
8	10.5838
9	10.5805
10	10.5867

In Figure 5.8, the Carbon PA insert is shown mounted inside the mold both before injection (a) and immediately after the last injection cycle (b). Figure 5.9 presents the insert after removal from the mold, highlighting the surface details and defects that developed over the course of the ten cycles.

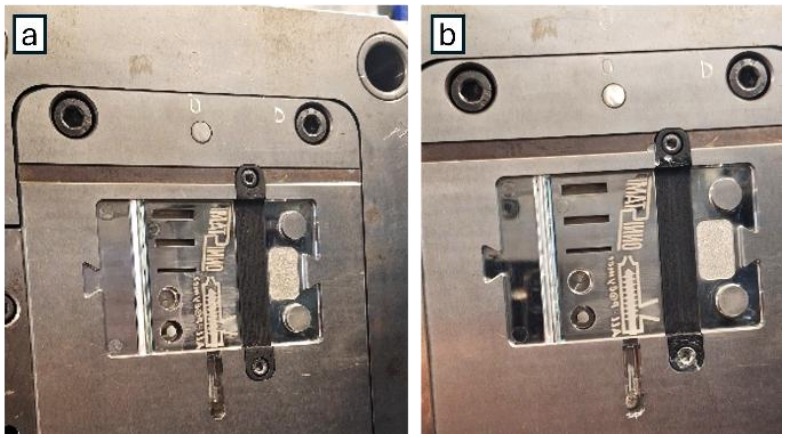

Figure 5.8. Carbon PA insert mounted inside the mold both before injection (a) and after injection (b)

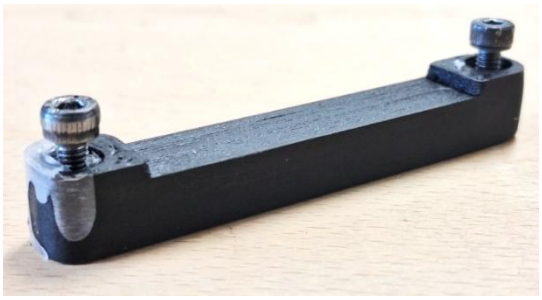

Figure 5.9. Carbon PA insert after removal from the mold

Thermal monitoring of the insert surface was conducted throughout the trials. Figure 5.10 presents the temperature maps obtained via infrared thermography for the first cycle (top row) and the tenth cycle (bottom row), with measurements at 1 s, 20 s, 40 s, and 60 s after mold opening.

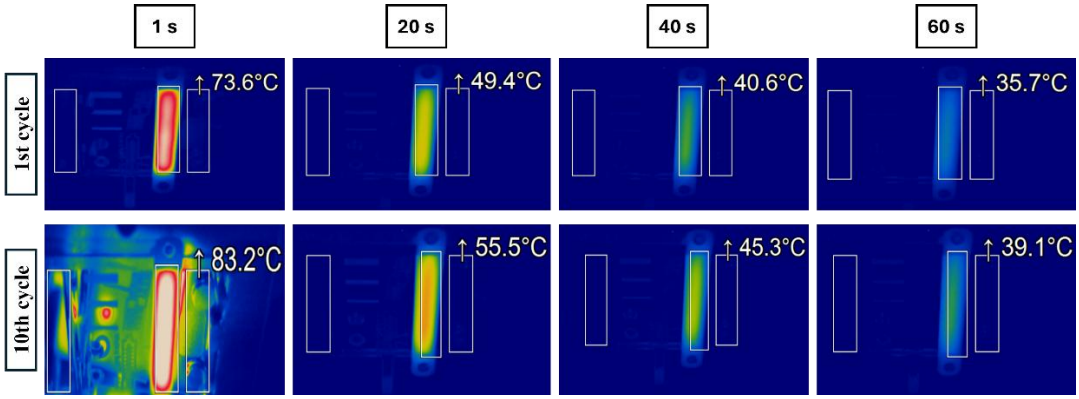

Figure 5.10. Infrared thermography of the Carbon PA insert during the first (top row) and tenth (bottom row) cycles at 1, 20, 40, and 60 seconds after mold opening

5.2.3 HTPLA Insert

During the ten consecutive injection cycles with the HTPLA insert, the ejector system was sufficient to remove all molded parts without the need for manual assistance. However, removing the insert itself from the mold after completing the tests was slightly difficult. The height and surface of the HTPLA insert were perfectly aligned with the surrounding mold surface, which is a positive outcome from a dimensional and fit perspective.

Figure 5.11 shows six representative parts (out of ten) produced with the HTPLA insert, arranged in sequence. Their corresponding masses, measured immediately after ejection, are listed in Table 5.4.

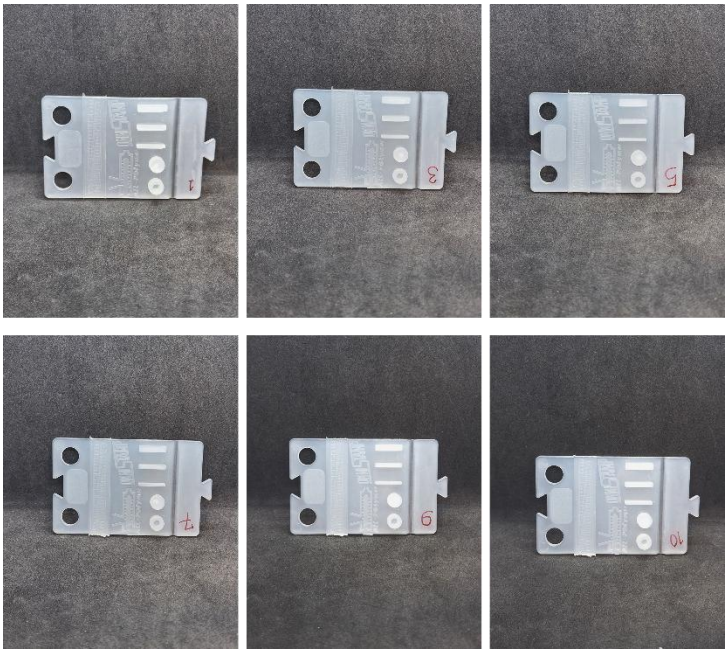

Figure 5.11. Molded parts using the HTPLA insert

Table 5.4. Weights of injection-molded parts produced with the HTPLA insert

Cycle	Weight [g]
1	9.7680
2	9.7297
3	10.0221
4	10.1571
5	10.3186
6	10.5688
7	10.5745

8	10.5838
9	10.5805
10	10.5867

Figure 5.12 presents the HTPLA insert inside the mold before injection (a) and immediately after the last injection cycle (b). Figure 5.13 shows the insert after removal from the mold, with details of the surface condition and any defects resulting from the ten-cycle trial.

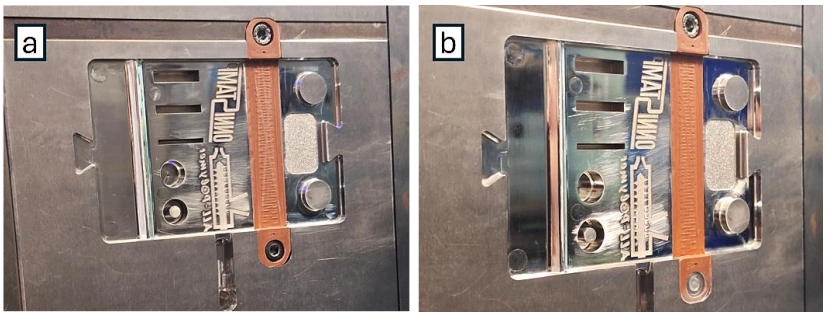

Figure 5.12. HTPLA insert mounted inside the mold both before injection (a) and after injection (b)

Figure 5.13. HTPLA insert after removal from the mold

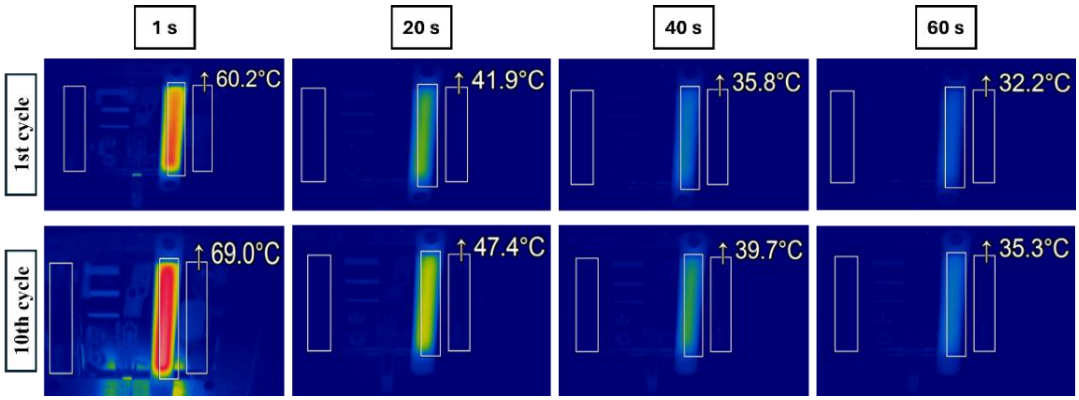

Figure 5.14. Infrared thermography of the HTPLA insert during the first (top row) and tenth (bottom row) cycles at 1, 20, 40, and 60 seconds after mold opening

Thermal monitoring of the HTPLA insert surface was conducted throughout the trials. Figure 5.14 presents the temperature maps obtained via infrared thermography for the first cycle (top row) and the tenth cycle (bottom row), with measurements at 1 s, 20 s, 40 s, and 60 s after mold opening.

5.2.4 Copper Filament Insert

During the injection molding with the Copper Filament insert, performance remained stable for the first five cycles, with no issues in part ejection or process stability. However, at the sixth cycle the insert fractured during mold opening. In this event, when the mold opened for part ejection, the insert was also removed from its seat and broke. This failure is attributed to the high rigidity and extreme brittleness of the material. While Copper Filament offers excellent thermal conductivity, its mechanical fragility severely limits its suitability for repeated injection molding operations. Consequently, only six cycles were completed instead of the planned ten.

Figure 5.15 shows the molded parts obtained with the Copper Filament insert, arranged in sequence from the first to the sixth cycle. The corresponding part masses, measured immediately after ejection, are reported in Table 5.5.

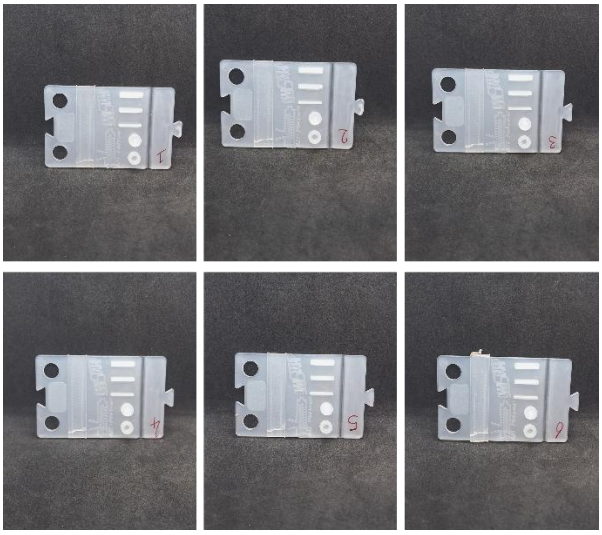

Figure 5.15. Molded parts using the Copper Filament insert

Table 5.5. Weights of injection-molded parts produced with the Copper Filament insert

Cycle	Weight [g]
1	9.5893
2	9.5772

3	9.9073
4	10.0430
5	10.2198
6	10.4886

Figure 5.16 presents the Copper Filament insert positioned inside the mold prior to injection. A small crack is already visible on the insert at this stage, likely resulting from its high fragility. Figure 5.17 shows the insert after removal from the mold, highlighting the surface condition and the damage resulting from the trial.

Figure 5.16. Copper Filament insert positioned inside the mold

Figure 5.17. Copper Filament insert after removal from the mold

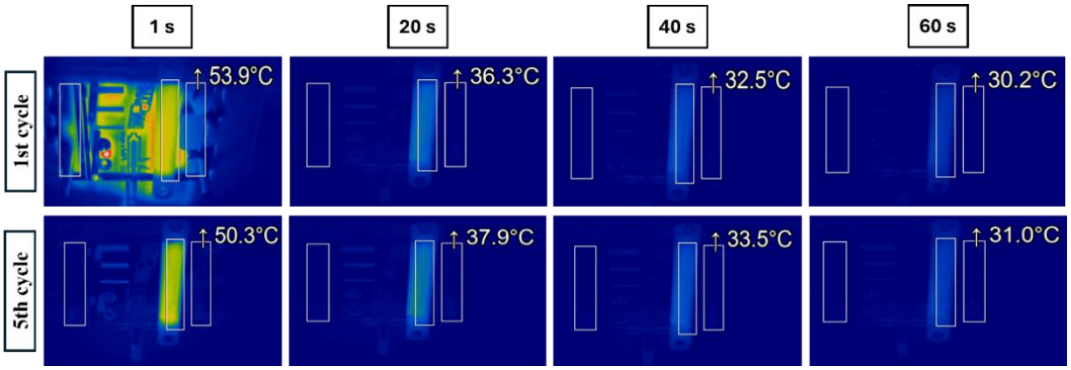

Figure 5.18. Infrared thermography of the Copper Filament insert during the first (top row) and fifth (bottom row) cycles at 1, 20, 40, and 60 seconds after mold opening

Thermal monitoring of the Copper Filament insert surface was conducted throughout the trials. Figure 5.18 presents temperature maps obtained via infrared thermography for the first cycle (top row) and the fifth cycle (bottom row), with measurements taken at 1 s, 20 s, 40 s, and 60 s after mold opening.

5.2.5 PLA–Copper 60% Insert

During the ten consecutive injection cycles performed with the PLA–Copper 60% insert, ejection of the molded parts was generally smooth, except for cycles 5 and 7, where the ejector system alone was insufficient and manual removal was required. In these two cases, partial adhesion of the part to the insert surface was observed. Removal of the insert from the mold after the trials was slightly difficult due to minor attachment between the insert and the mold cavity.

Figure 5.19 shows six representative parts (out of ten) produced with the PLA–Copper 60% insert, arranged in sequence. Their corresponding masses, measured immediately after ejection, are listed in Table 5.6.

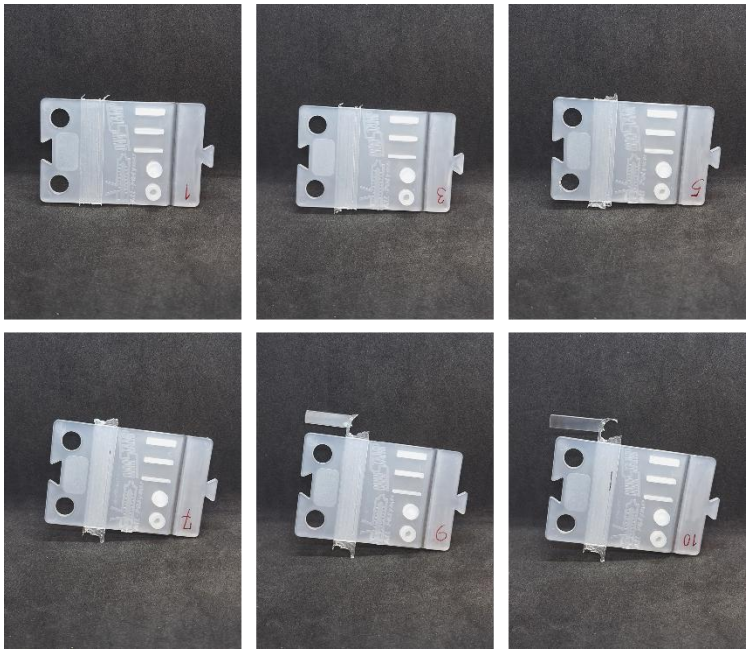

Figure 5.19. Molded parts using the PLA–Copper 60% insert

Table 5.6. Weights of injection-molded parts produced with the PLA–Copper 60% insert

Cycle	Weight [g]
1	9.7133
2	9.6134

3	9.9934
4	10.1643
5	10.3759
6	10.6527
7	10.6583
8	10.7552
9	10.7660
10	10.7786

Figure 5.20 shows the PLA–Copper 60% insert inside the mold before injection (a) and immediately after the last injection cycle (b). Figure 5.21 depicts the insert after removal from the mold, highlighting its surface condition and any defects that developed during the process.

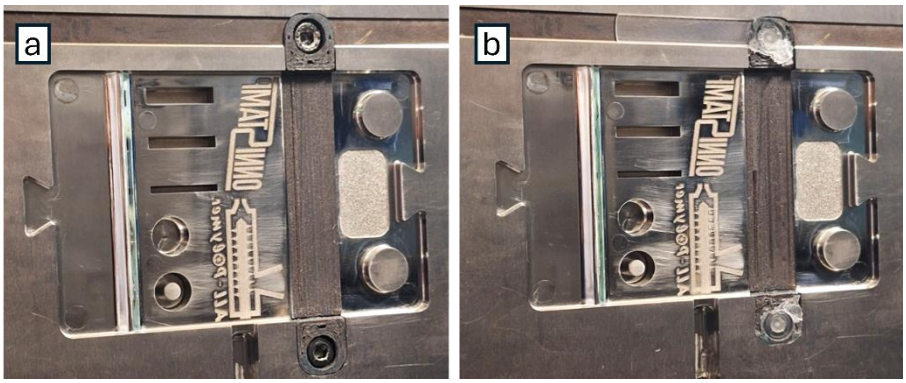

Figure 5.20. PLA–Copper 60% insert mounted inside the mold both before injection (a) and after injection (b)

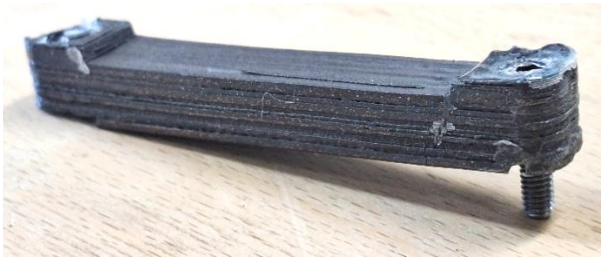

Figure 5.21. PLA–Copper 60% insert after removal from the mold

Thermal monitoring of the PLA–Copper 60% insert surface was conducted throughout the trials. Figure 5.22 presents the temperature maps obtained via infrared thermography for the first cycle (top row) and the tenth cycle (bottom row), with measurements at 1 s, 20 s, 40 s, and 60 s after mold opening.

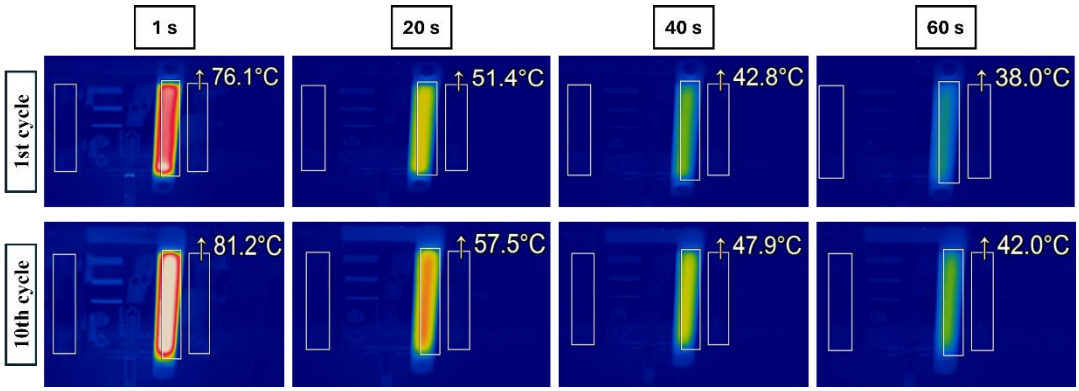

Figure 5.22. Infrared thermography of the PLA–Copper 60% insert during the first (top row) and tenth (bottom row) cycles at 1, 20, 40, and 60 seconds after mold opening

5.2.6 PLA–Copper 80% Insert

During the ten consecutive injection cycles performed with the PLA–Copper 80% insert, the ejection of molded parts was consistently efficient, with the exception of cycles 1 and 6, where manual assistance was required to remove the part. Overall, this insert demonstrated one of the best performances among all tested materials, combining mechanical stability with effective heat dissipation and consistent dimensional integrity.

Figure 5.23 shows six representative parts (out of ten) produced with the PLA–Copper 80% insert, arranged in sequence. Their corresponding masses, measured immediately after ejection, are listed in Table 5.7.

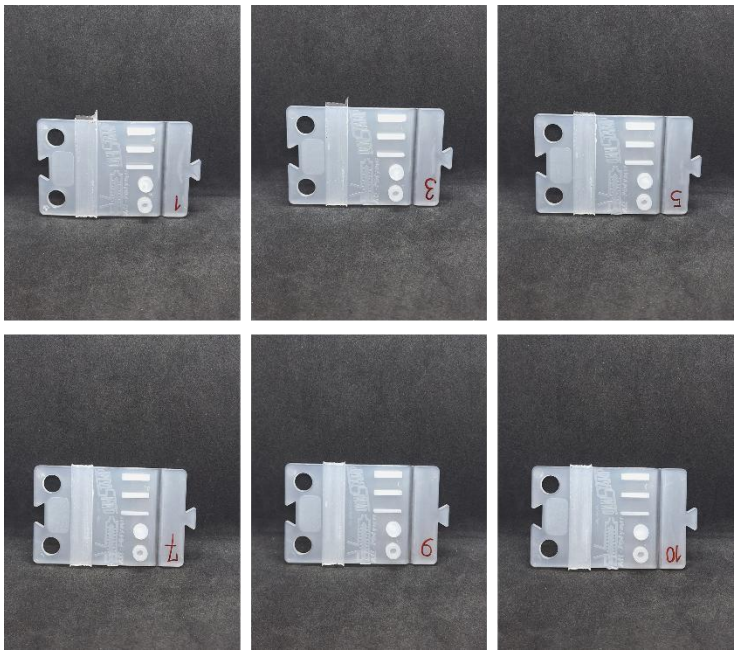

Figure 5.23. Molded parts using the PLA–Copper 80% insert

Table 5.7. Weights of injection-molded parts produced with the PLA–Copper 80% insert

Cycle	Weight [g]
1	9.8421
2	9.7971
3	10.1004
4	10.2259
5	10.4234
6	10.6907
7	10.7610
8	10.7804
9	10.7812
10	10.7874

Figure 5.24 shows the PLA–Copper 80% insert inside the mold before injection (a) and immediately after the last injection cycle (b). Figure 5.25 depicts the insert after removal from the mold, highlighting its surface condition and any defects observed after the ten-cycle test.

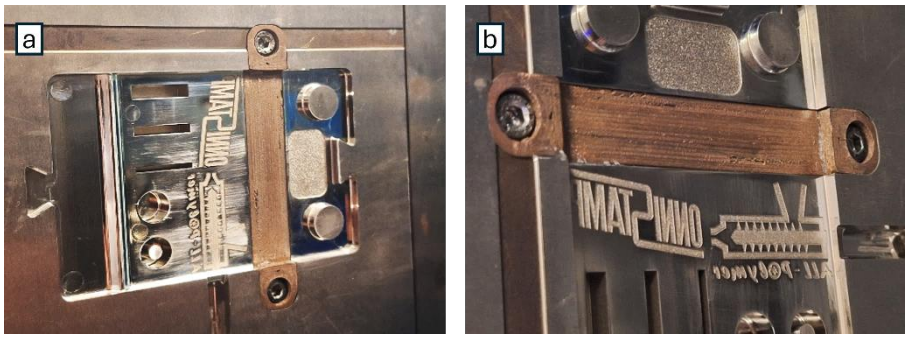

Figure 5.24. PLA–Copper 80% insert mounted inside the mold both before injection (a) and after injection (b)

Figure 5.25. PLA–Copper 80% insert after removal from the mold

Thermal monitoring of the PLA–Copper 80% insert surface was conducted throughout the trials. Figure 5.26 presents the temperature maps obtained via infrared thermography for the second cycle (top row) and the tenth cycle (bottom row), with measurements at 1 s, 20 s, 40 s, and 60 s after mold opening. The first cycle is not reported here because the temperature capture was affected by manual part removal; however, the pressure profile of the first and second cycle is the same (50 bar).

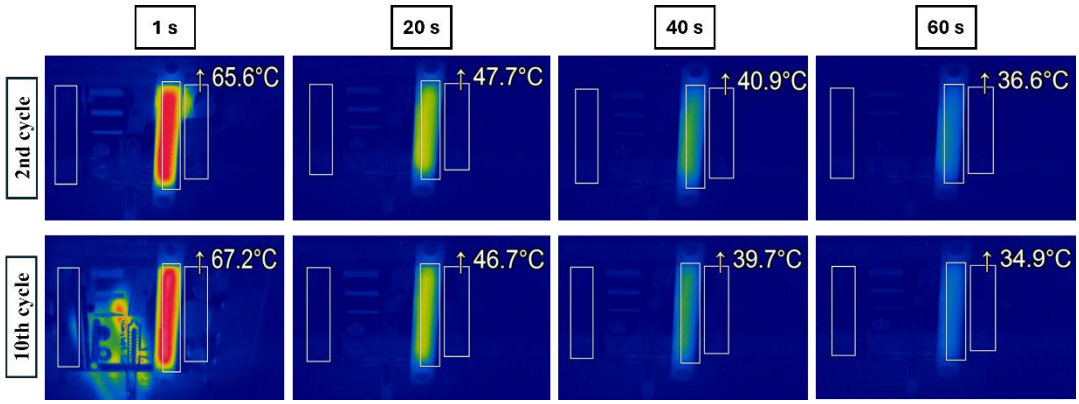

Figure 5.26. Infrared thermography of the PLA–Copper 80% insert during the second (top row) and tenth (bottom row) cycles at 1, 20, 40, and 60 seconds after mold opening

5.2.7 PLA–Copper 90% Insert

During the ten consecutive injection cycles with the PLA–Copper 90% insert, the ejection performance declined notably after the fifth cycle. From the sixth cycle onward, attachment between the molded part and the insert surface occurred, preventing the ejector system from fully releasing the part and necessitating manual removal from the mold. A small crack was already present in the middle of the insert prior to the start of injection, reflecting its high fragility, similar to the behavior observed with the Copper Filament insert.

Figure 5.27 shows six representative parts (out of ten) produced with the PLA–Copper 90% insert, arranged in sequence. Their corresponding masses, measured immediately after ejection, are listed in Table 5.8.

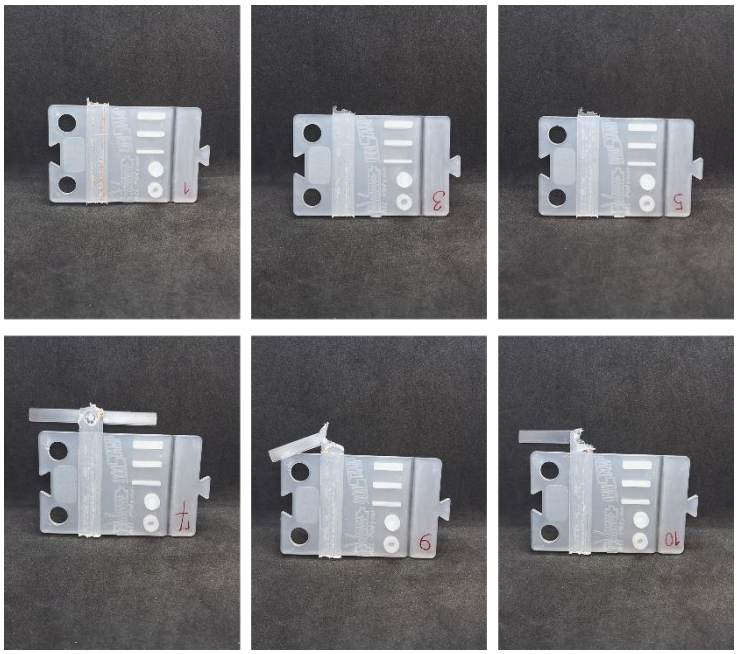

Figure 5.27. Molded parts using the PLA–Copper 90% insert

Table 5.8. Weights of injection-molded parts produced with the PLA–Copper 90% insert

Cycle	Weight [g]
1	9.8251
2	9.7671
3	10.0766
4	10.1975
5	10.3503
6	10.5605
7	11.0477
8	11.0499
9	10.8004
10	10.8483

Figure 5.28 shows the PLA–Copper 90% insert positioned in the mold before injection (a) and immediately after the last injection cycle (b). Figure 5.29 depicts the insert after removal from the mold, highlighting its surface condition and the damage sustained during the trial.

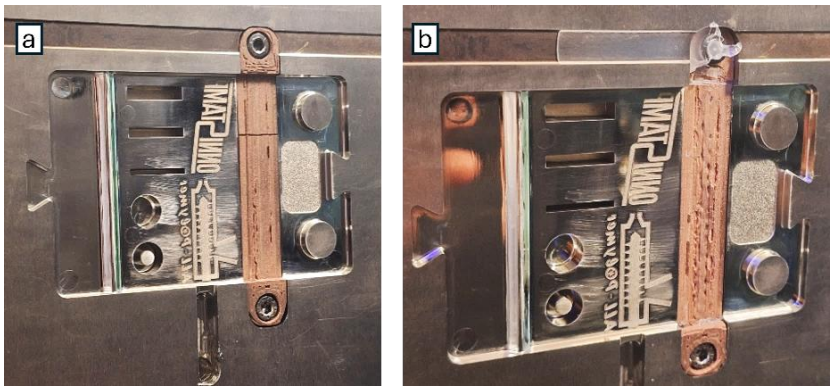

Figure 5.28. PLA–Copper 90% insert mounted inside the mold both before injection (a) and after injection (b)

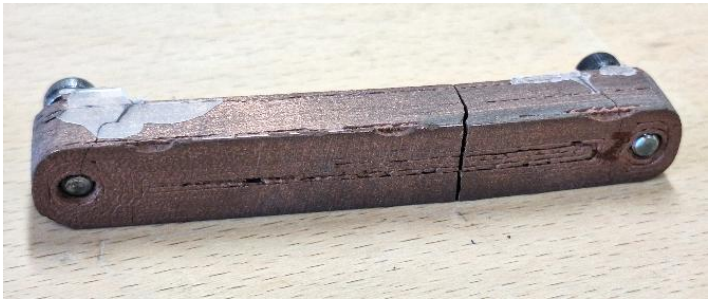

Figure 5.29. PLA–Copper 90% insert after removal from the mold

Thermal monitoring of the PLA–Copper 90% insert surface was conducted throughout the trials. Figure 5.29 presents the temperature maps obtained via infrared thermography for the first cycle (top row) and the tenth cycle (bottom row), with measurements at 1 s, 20 s, 40 s, and 60 s after mold opening.

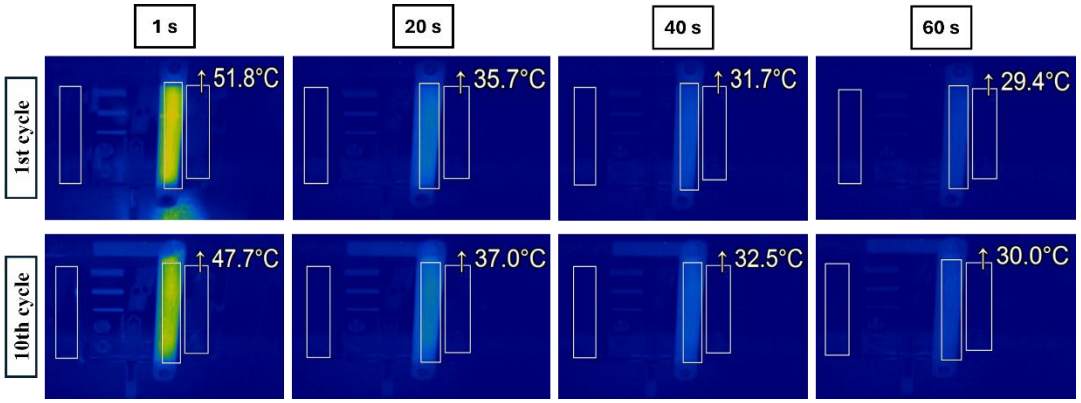

Figure 5.29. Infrared thermography of the PLA–Copper 90% insert during the first (top row) and tenth (bottom row) cycles at 1, 20, 40, and 60 seconds after mold opening

Figure 5.30 shows representative parts from the 10th injection molding cycle produced using PLA–Copper 60%, PLA–Copper 80%, and PLA–Copper 90% inserts. While high thermal conductivity is crucial for reducing cycle times and improving cooling efficiency, the overall quality of molded parts also depends on additional factors such as the printability of the insert material and its mechanical stability during processing. In this respect, the PLA–Copper 80% insert provided the most consistent part quality, highlighting the importance of balancing thermal performance with structural rigidity and fabrication quality when selecting materials for polymer–metal composite inserts.

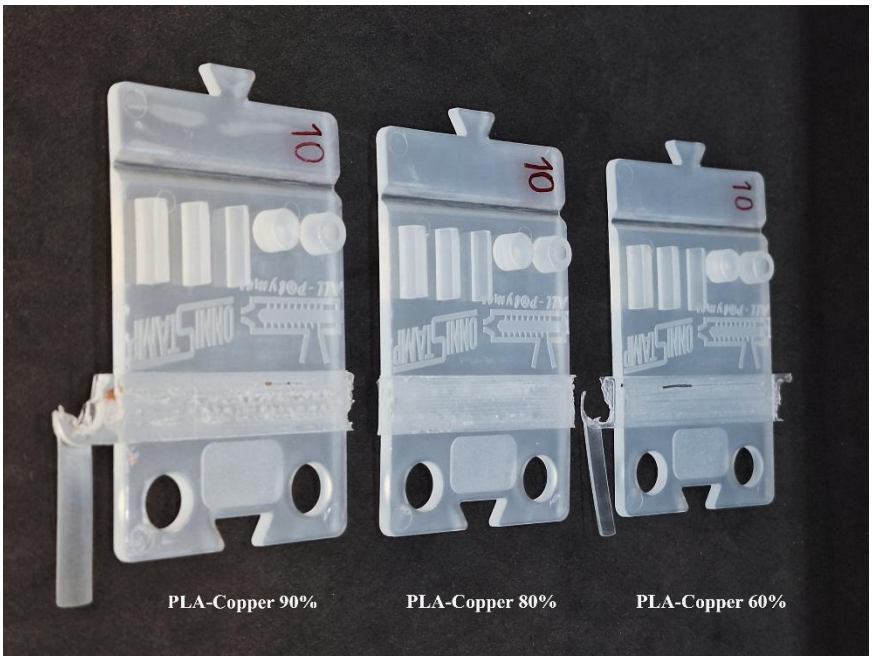

Figure 5.30. Parts molded in the 10th cycle using PLA–Copper 60%, 80%, and 90% inserts

Figure 5.31 presents the weights of the parts produced over ten injection cycles using seven different inserts. The yellow line, corresponding to the steel insert, is used as the reference across all datasets. The results show a progressive increase in weight from the first to the sixth cycle, consistent with the rise in injection pressure. Beyond the sixth cycle, a stable trend would be expected under constant pressure; however, the experimental data still shows a slight increase despite the constant pressure. Among the PLA–Copper inserts, PLA–Copper 80% exhibited the most stable behavior, with smaller variations in weight compared to PLA–Copper 60% and PLA–Copper 90%, further confirming its balanced thermal and mechanical performance.

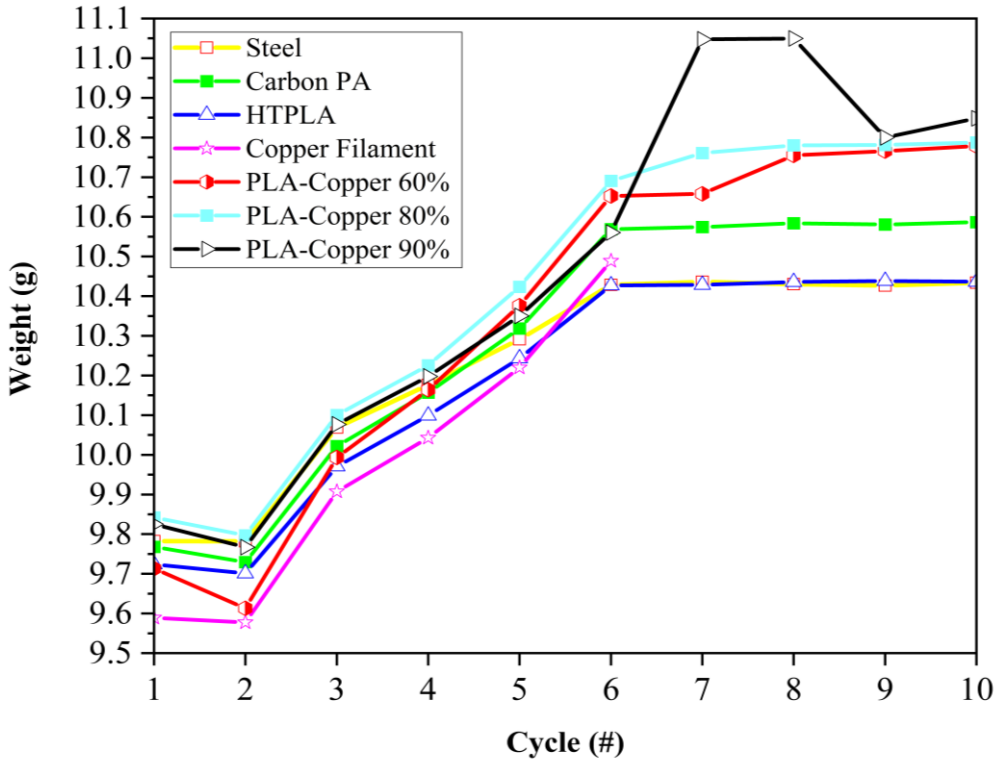

Figure 5.31. Evolution of part weights over ten injection cycles for various inserts

Chapter 6

SIMULATION VIA Moldex3D

Injection molding remains one of the most versatile and high-throughput manufacturing routes for polymer parts, yet the presence of inserts with different thermal and mechanical properties significantly alters the evolution of temperature, pressure, and solidification during processing. Insert molding technologies are increasingly applied not only for functional assemblies but also for rapid tooling solutions, where polymer-based or composite inserts replace conventional steel tooling to reduce cost and lead time. However, the adoption of polymer or polymer–metal composite inserts requires a detailed understanding of their thermo-mechanical behavior under the cyclic loading of injection molding, since reduced thermal conductivity and lower stiffness may induce defects, shorten insert life, or affect part quality.

Advanced numerical tools, such as Moldex3D, enable the prediction of the entire molding cycle (including filling, packing, cooling, and warpage) by accounting for three-dimensional heat transfer, pressure distribution, and material–mold interactions. Compared with traditional 2.5D analyses, true 3D simulation is essential when heterogeneous inserts are involved, since differences in thermal conductivity and density strongly influence melt front advancement and local solidification.

In this work, simulations were conducted for commercially available materials (Carbon PA, HTPLA, and Copper Filament) together with non-commercial PLA–Copper composites produced with copper loadings of 60%, 80%, and 90% by weight. This material set covers a wide conductivity spectrum, from low-conductivity inserts to highly conductive polymer–metal composites. By integrating experimentally measured properties such as density, elastic modulus, and thermal conductivity into the Moldex3D database, the simulations reflect the realistic performance of printed inserts.

The aim of this chapter is to investigate how the different materials influence the thermal and pressure fields inside the mold, with particular focus on the effect of increasing copper content on cooling rates, temperature uniformity, and cycle efficiency. The results provide a comparative framework between readily available commercial filaments and

novel high-conductivity composites, offering practical guidance for the design and application of 3D-printed inserts in injection molding.

6.1 Moldex3D Simulation Setup

6.1.1 Insert Material Properties

To perform the simulations, Moldex3D requires the definition of the main thermo-physical and mechanical properties of the mold inserts. Table 6.1 reports the material properties that were implemented in the software for each insert type, both for the commercial filaments (Carbon PA, HTPLA, and Copper Filament) and for the developed PLA–Copper composites. In addition, a reference simulation was also performed with a conventional steel 1.2083 insert, to provide a direct comparison between polymer-based solutions and a standard metallic mold insert.

Table 6.1. Material properties assigned to Moldex3D for the definition of mold inserts

Insert	Density ($kg \cdot m^{-3}$)	Thermal Conductivity ($W \cdot m^{-1} \cdot K^{-1}$)	Elastic Modulus (MPa)
Carbon PA	1400	0.532	1085.72
HTPLA	2300	0.529	908.48
Copper Filament	4500	1.616	1181
PLA–Copper 60%	2226	0.401	936
PLA–Copper 80%	3790	0.829	1480.76
PLA–Copper 90%	5317	1.569	1445.6
Steel 1.2083	7800	16.5	2.1×10^5

6.1.2 Processing Conditions

All simulations were carried out considering the injection of polypropylene (Moplen HP500N) into the cavity. The same processing conditions were applied across all insert materials to ensure that any observed differences in temperature distribution, cooling efficiency, and pressure profile could be attributed exclusively to the thermal and mechanical properties of the inserts.

As shown in Figure 6.1, the project settings include the definition of the injection machine and the polymer selected for the simulations.

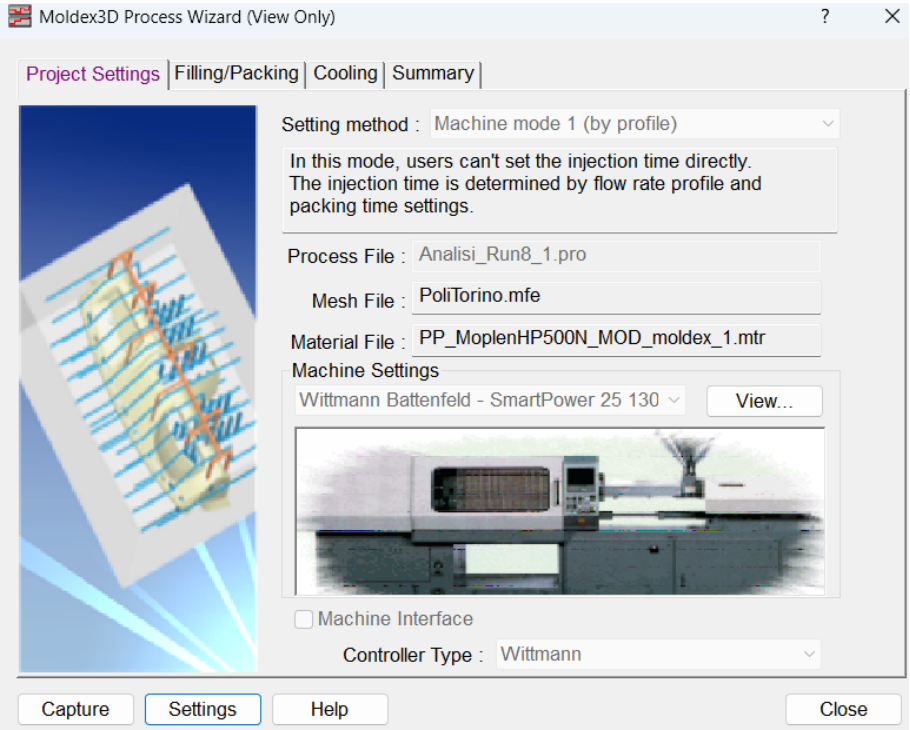

Figure 6.1. Project settings in Moldex3D

As illustrated in Figure 6.2, the filling and packing settings were defined, including the melt and mold temperatures as well as the packing parameters applied in all simulations.

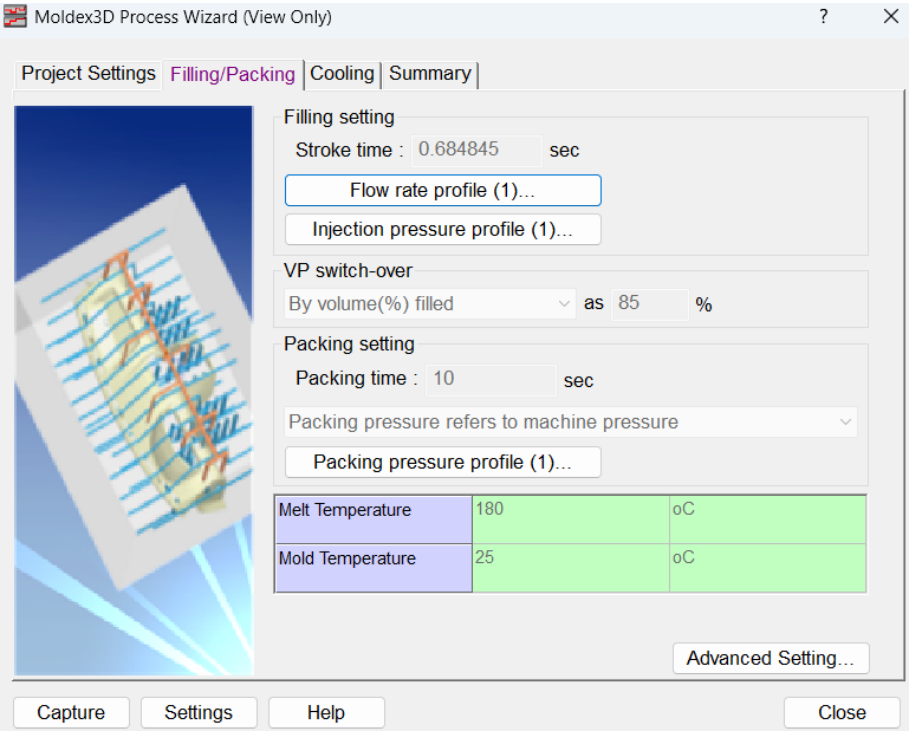

Figure 6.2. Filling and packing settings defined in Moldex3D

Figure 6.3 summarizes the detailed machine parameters into Moldex3D, including injection unit, clamp unit, general specifications, and screw information.

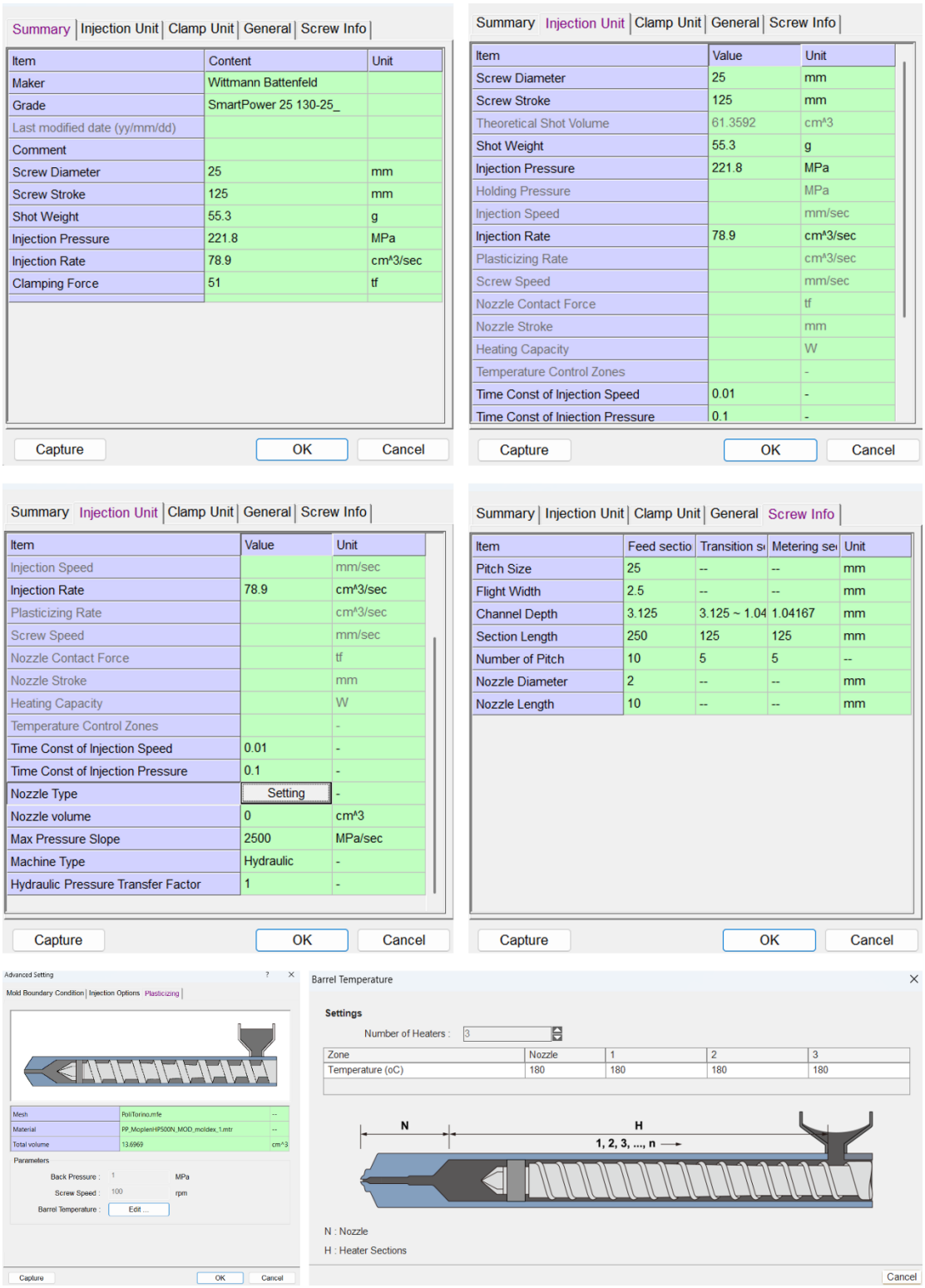

Figure 6.3. Injection molding machine parameters

Figure 6.4 shows the injection pressure and flow rate profiles applied in the simulations, which were defined according to the machine setup.

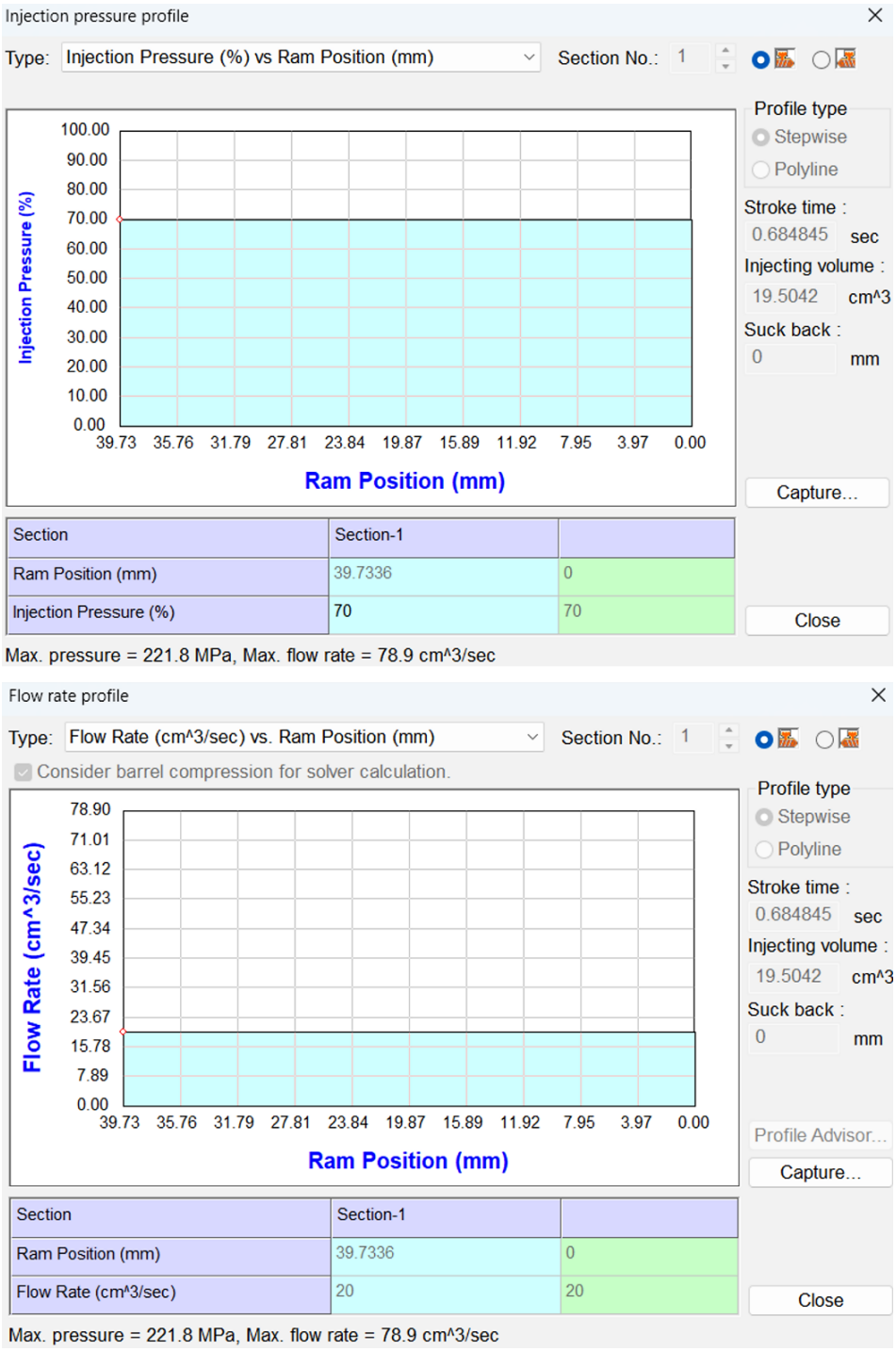

Figure 6.4. Injection pressure and flow rate profiles in Moldex3D

The cooling stage configuration, including mold temperature, coolant flow conditions, and ejection criteria, is reported in Figure 6.5.

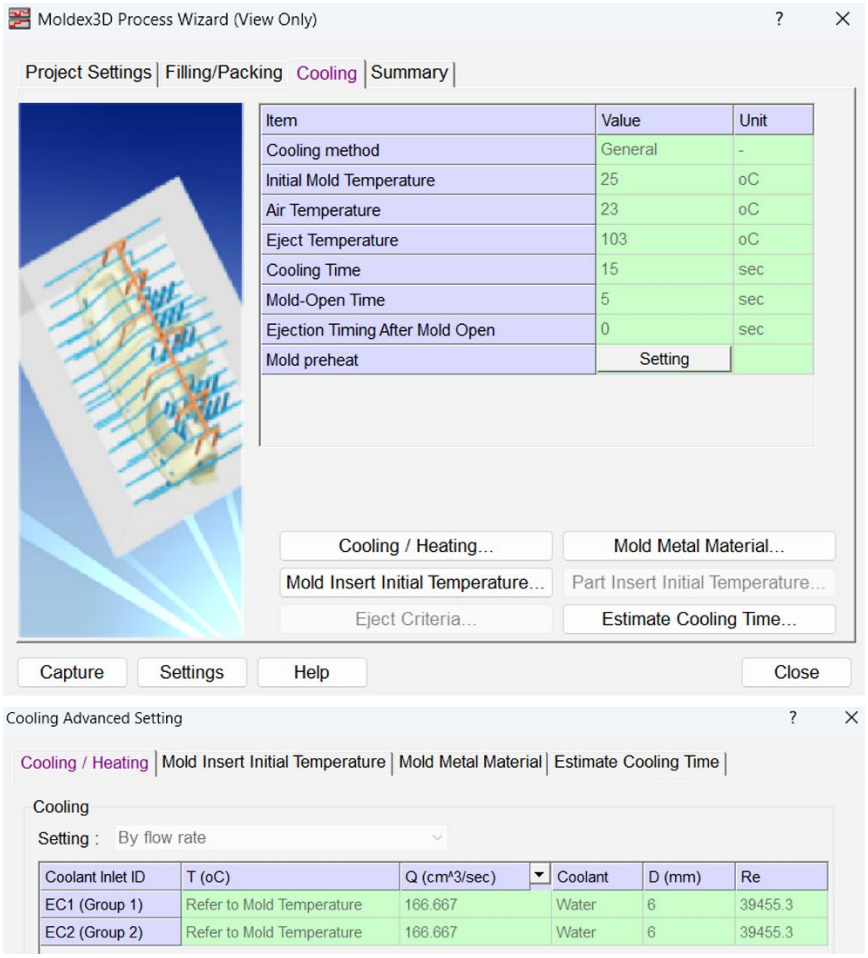

Figure 6.5. Coolant settings defined in Moldex3D

Figure 6.6 provides a summary of all process conditions applied in the simulations, including filling, packing, cooling, and overall cycle time.

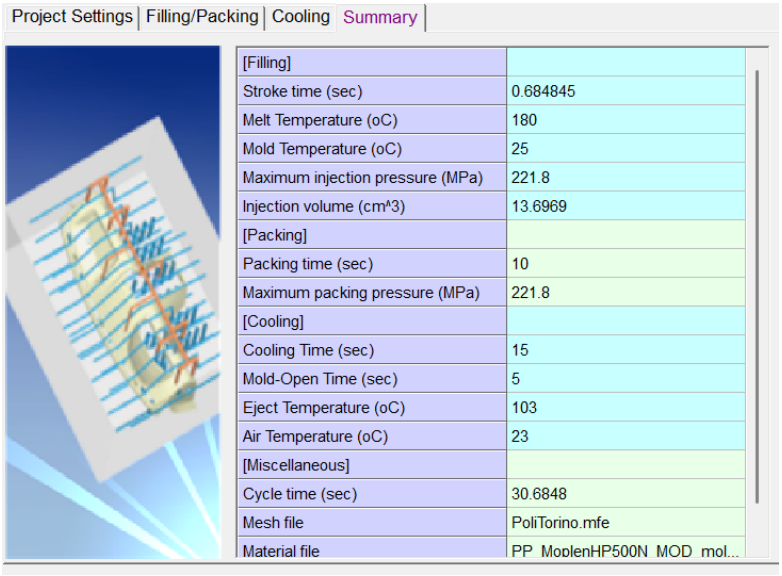

Figure 6.6. Summary of processing conditions defined in Moldex3D

6.1.3 Geometry Configuration

Figure 6.7 presents four orthogonal views of the model, with the runner highlighted in blue and the insert in purple. This configuration was applied consistently in all simulations, with only the insert material being varied.

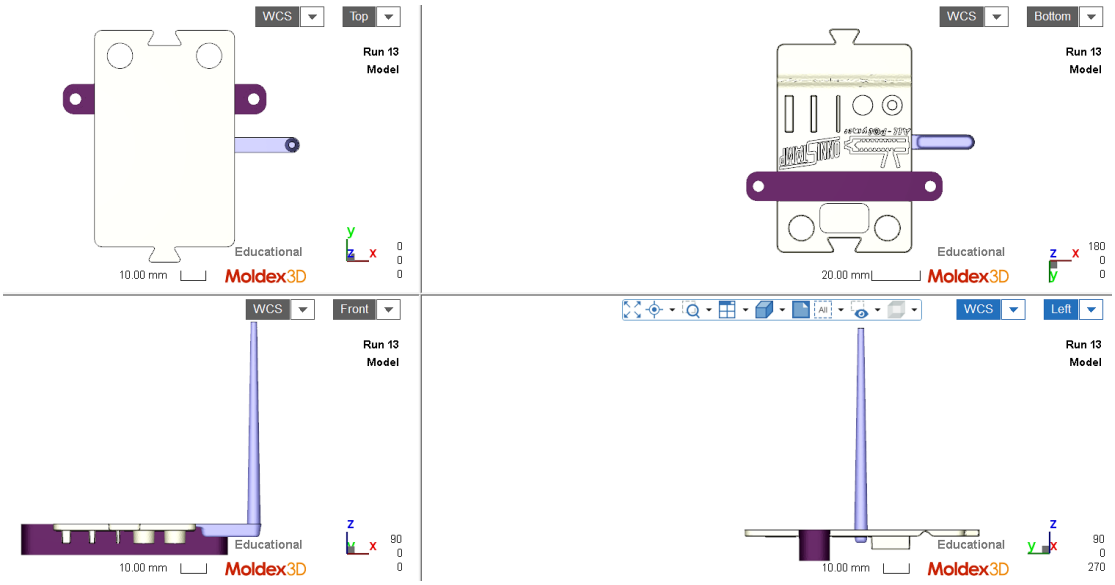

Figure 6.7. Molded part (white) geometry with runner (blue) and insert (purple) shown in four orthogonal views

Figure 6.8 illustrates the complete mold configuration, including the cooling channel layout and the cavity geometry. The cooling channels, highlighted in blue, were arranged symmetrically around the insert to ensure uniform heat extraction. This configuration was applied in all simulations to maintain consistent boundary conditions.

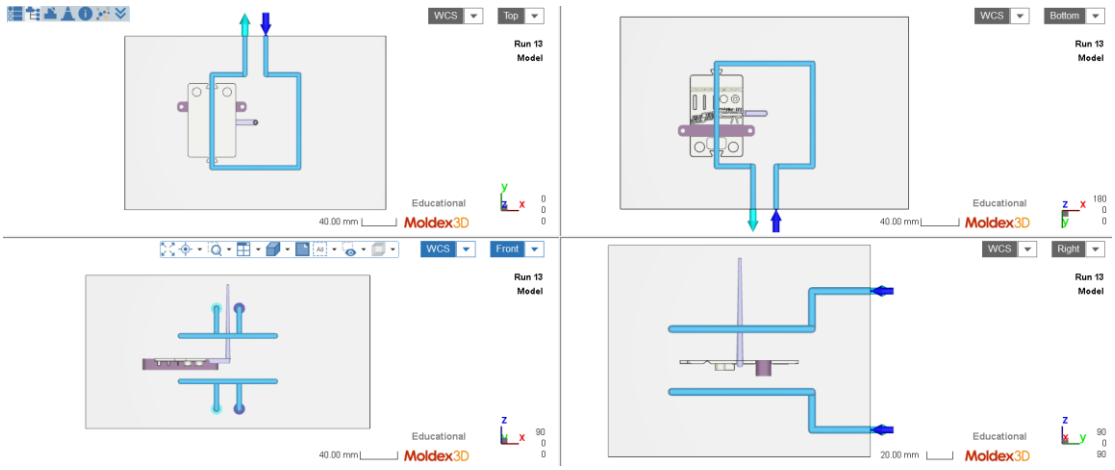

Figure 6.8. Mold geometry showing cavity and cooling channel layout

Figure 6.9 provides a closer view of the mold configuration, highlighting the relative positions of the molded part, the insert, the runner system, and the cooling channels. The coolant inlets and outlets are also indicated, allowing a clear representation of the boundary conditions applied in the simulations.

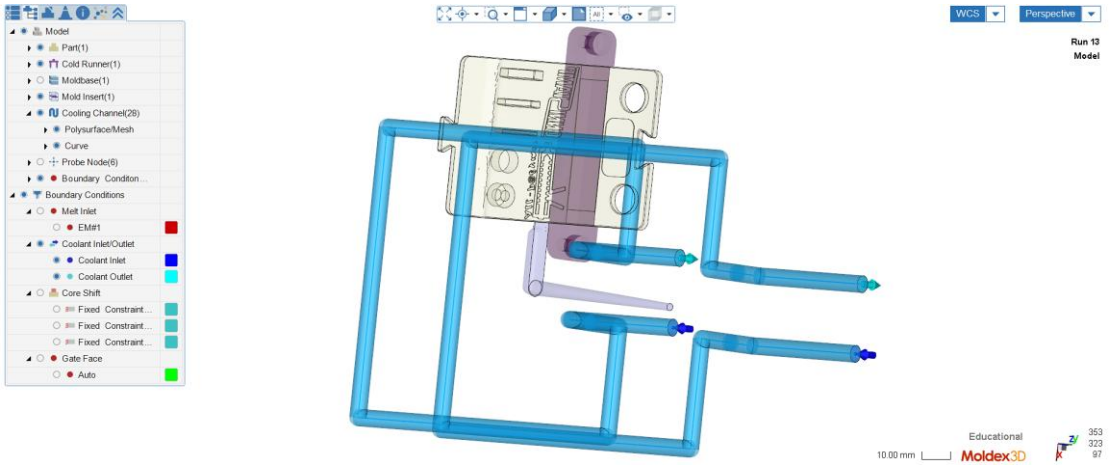

Figure 6.9. Detailed view of the mold assembly

Figure 6.10 shows the meshed model of the part, insert, and runner used in Moldex3D. A sufficiently refined and well-structured mesh is essential to obtain accurate results, particularly in regions of high thermal and flow gradients.

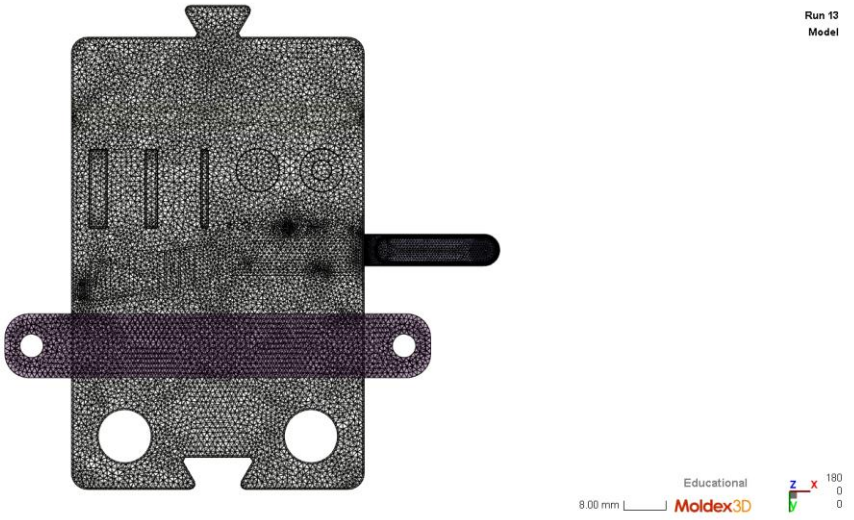

Figure 6.10. Meshed model of the part, insert, and runner in Moldex3D

Figure 6.11 presents multiple views of the meshed insert geometry, highlighting the refinement applied to critical features. The local mesh density was increased in regions

of high thermal and flow gradients to improve accuracy while maintaining computational efficiency.

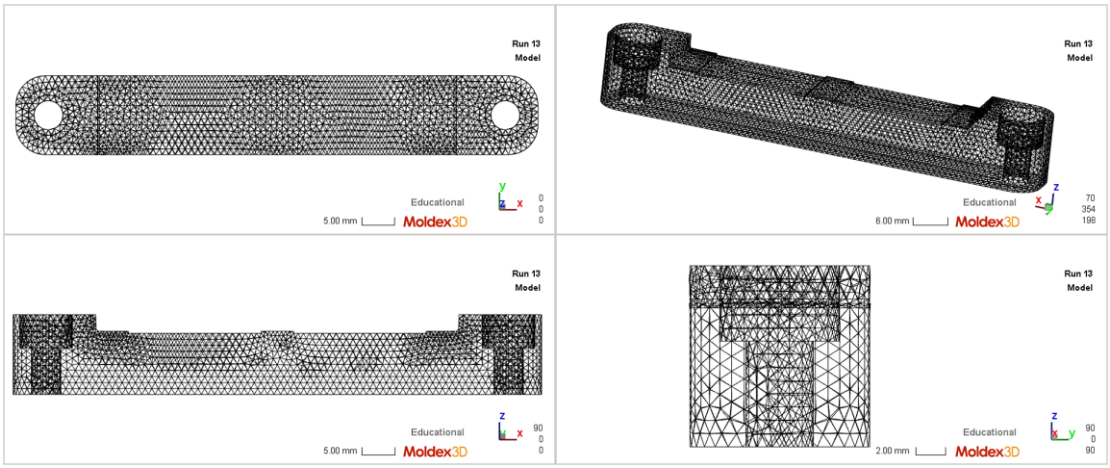

Figure 6.11. Detailed mesh views of the insert geometry in Moldex3D

6.2 Simulation Results

Since all molding parameters and geometrical conditions were kept constant, the analysis of simulation results focuses primarily on the influence of the insert material. The evaluation is divided into two parts: (i) insert-related performance, including temperature evolution, heat dissipation, applied pressure, and displacements, and (ii) part-related outcomes, such as temperature distribution, pressure, warpage, and dimensional stability.

6.2.1 Analysis of Insert Behavior

Since the geometry of the mold, the injected polymer (PP Moplen HP500N), and the processing conditions were identical across all cases, the key variable was the material of the insert. This subsection therefore presents the results related directly to the thermal and mechanical response of the inserts, which represent the main objective of this study.

6.2.1.1 Temperature Profile of Inserts

The thermal behavior of the inserts was analyzed at four key stages of the injection molding cycle: end of filling (EOF), end of packing (EOP), end of cooling (EOC), and mold opening. These snapshots allow a comprehensive assessment of the heat transfer capability of each insert material.

The reference case with a steel 1.2083 insert is shown in Figure 6.12. The figure includes four snapshots corresponding to the end of filling (EOF), end of packing (EOP), end of cooling (EOC), and mold opening. These results collectively illustrate the characteristic thermal response of a conventional metallic insert.

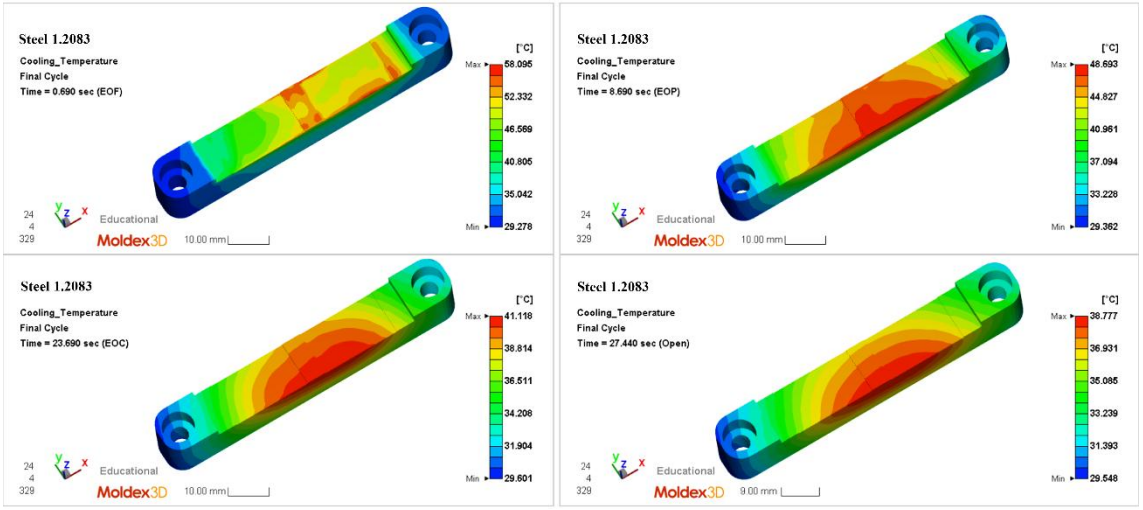

Figure 6.12. Temperature distribution in steel 1.2083 insert at four stages of the molding cycle: EOF, EOP, EOC, and mold opening

As expected, the high thermal conductivity of steel promotes rapid heat removal from the polymer melt and results in a uniform temperature distribution throughout the insert. Localized hot spots are quickly dissipated between EOF and EOP, while by the end of cooling and mold opening stages, the overall temperature field is stable and homogeneous. This behavior establishes a benchmark condition against which the performance of polymer-based inserts can be evaluated. In particular, the steel insert demonstrates the ideal scenario of fast heat extraction and minimal temperature gradients, thereby providing favorable conditions for consistent part quality and dimensional stability.

The corresponding EOF temperature distributions for the polymer-based inserts are reported in Figure 6.13, covering Carbon PA, HTPLA, Copper Filament, PLA–Copper 60%, PLA–Copper 80%, and PLA–Copper 90%. Neat PLA was excluded from this analysis, as previous studies have already demonstrated its poor thermal performance in mold applications due to inadequate heat dissipation and excessive temperature retention.

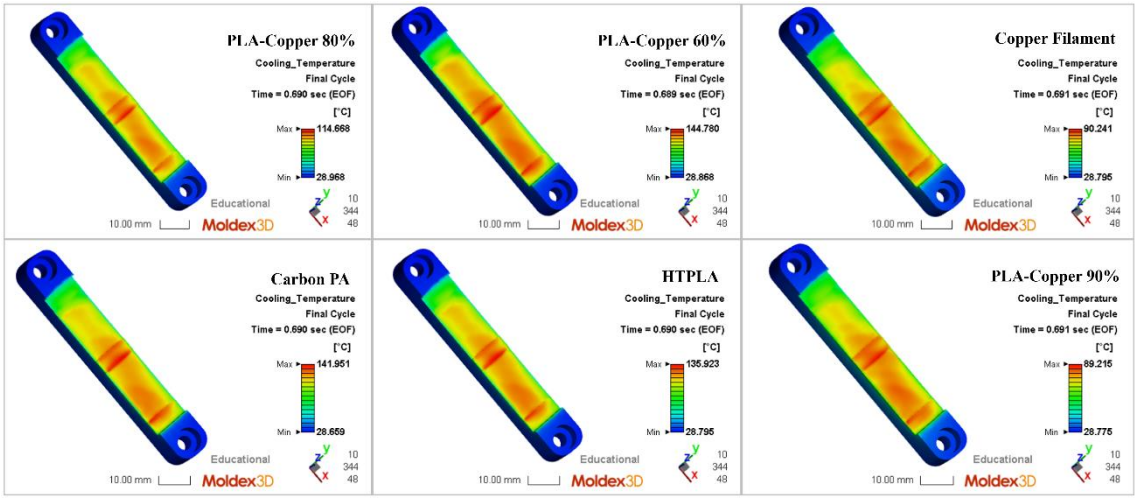

Figure 6.13. EOF temperature distribution in alternative inserts: Carbon PA, HTPLA, Copper Filament, PLA–Copper 60%, PLA–Copper 80%, and PLA–Copper 90%

Compared with the steel reference, all polymeric inserts exhibit higher surface temperatures at EOF, reflecting their lower thermal conductivity. Among the commercial filaments, Carbon PA and HTPLA retain significant hot spots, with maximum temperatures exceeding 130 °C, indicating limited heat extraction during the filling stage. The Copper Filament performs slightly better, achieving the best performance among the commercial materials and showing results that are already comparable with those obtained for PLA–Copper 90%.

In contrast, the PLA–Copper composites demonstrate a clear improvement in thermal behavior. With increasing copper content, the maximum EOF temperature decreases, and the temperature field becomes more uniform. PLA–Copper 60% still retains localized hot regions similar to Carbon PA and HTPLA, while PLA–Copper 80% shows intermediate behavior. The best performance is achieved with PLA–Copper 90%, which approaches the uniformity of the steel insert and shows significantly reduced peak temperatures compared with the other polymeric materials.

These results highlight the strong influence of filler content on the early cooling dynamics of polymer-based inserts. The addition of copper not only reduces maximum surface temperatures but also improves temperature uniformity, thereby enhancing the thermal stability of the insert during the critical filling stage.

The thermal state of the inserts at the end of packing (EOP) is shown in Figure 6.14. In this representation, the inserts were sectioned to expose the internal temperature distribution, providing a clearer view of heat transfer within the bulk material.

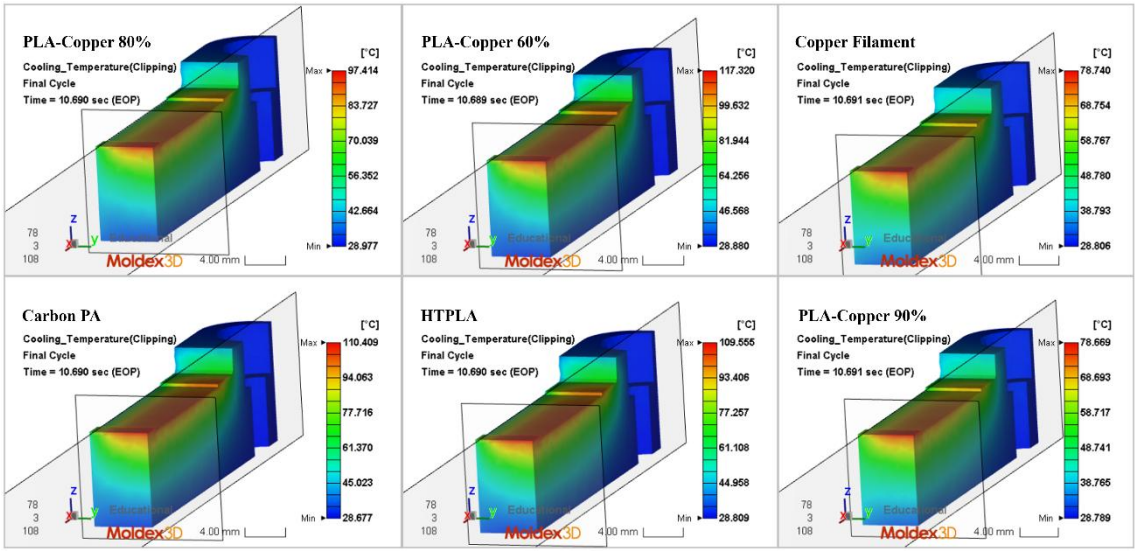

Figure 6.14. Sectional view of temperature distribution at the end of packing (EOP) for different inserts

The results confirm the trends already observed at EOF. Carbon PA and HTPLA still retain the highest internal temperatures, exceeding 110 °C in localized regions, which demonstrates their limited ability to dissipate heat even after the additional packing stage. The temperature gradient between the cavity-facing surface and the insert interior remains pronounced, reflecting low thermal conductivity.

The Copper Filament again exhibits superior performance among the commercial materials, with maximum EOP temperatures below 80 °C and a more uniform profile across the insert thickness. Its behavior is already comparable to that of PLA–Copper 90%, which shows the lowest overall temperatures and the most effective heat transfer of all the tested composites.

For the PLA–Copper composites, the effect of filler content is evident. PLA–Copper 60% still maintains high internal temperatures (>115 °C), close to those of Carbon PA and HTPLA, while PLA–Copper 80% demonstrates a moderate reduction. The best performance is achieved by PLA–Copper 90%, where internal temperatures remain below 80 °C and the distribution is nearly homogeneous across the section, approaching the benchmark set by the steel insert.

These observations underline the importance of thermal conductivity in stabilizing the insert during packing. Materials with higher copper loading promote not only faster surface cooling but also more efficient bulk heat dissipation, which directly impacts dimensional stability and reduces the risk of localized thermal stresses.

At the end of cooling (EOC), the differences between the investigated inserts become even more evident (Figure 6.15). The sectioned views highlight the internal temperature distribution, showing how effectively each material dissipates the heat accumulated during filling and packing.

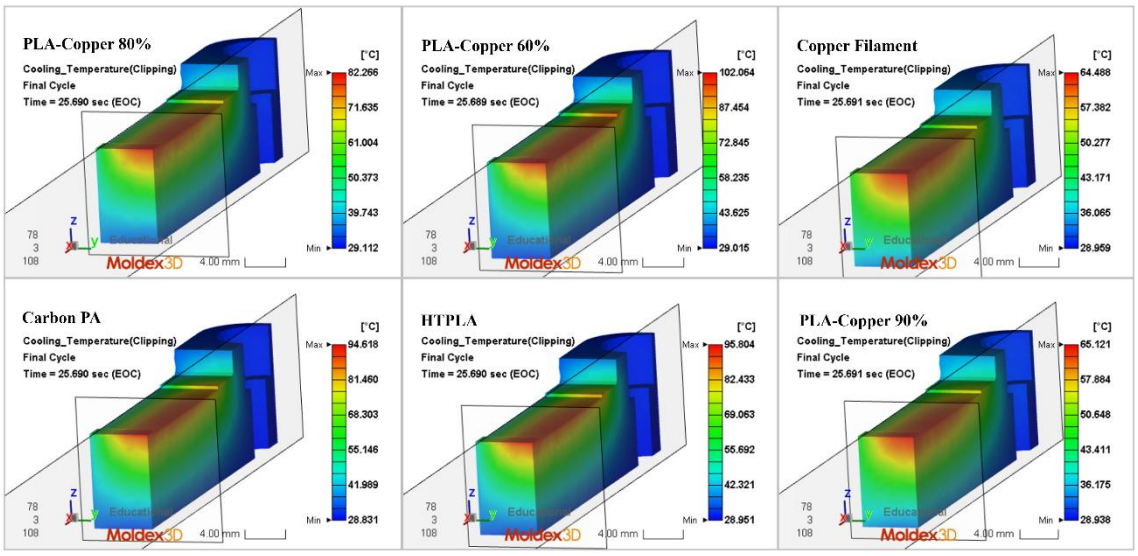

Figure 6.15. Sectional view of temperature distribution at the end of cooling (EOC) for different inserts

Carbon PA and HTPLA still retain the highest temperatures, with localized values close to or above 95 °C. This indicates that, even after the full cooling stage, these materials are not able to efficiently transfer heat away from the cavity surface, leaving considerable thermal gradients within the insert. Such behavior would negatively influence dimensional stability and could accelerate thermal fatigue in real molding conditions.

The Copper Filament continues to perform as the best of the commercial materials, with maximum EOC temperatures of ~65 °C and a relatively uniform internal profile. The thermal field shows limited gradients across the insert thickness, which demonstrates its effectiveness in dissipating heat compared with standard polymers.

PLA–Copper 60% still maintains higher temperatures (~102 °C) more than Carbon PA and HTPLA. PLA–Copper 80% reduces the peak to ~82 °C, while PLA–Copper 90% achieves a performance nearly identical to the Copper Filament, with maximum temperatures around 65 °C. These results indicate that increasing copper fraction significantly enhances cooling efficiency, and at high loading levels, the thermal performance approaches that of the benchmark metallic insert.

Overall, the EOC analysis demonstrates that materials with low conductivity (Carbon PA, HTPLA, PLA–Copper 60%) accumulate heat and retain higher internal temperatures, whereas inserts with enhanced conductivity (Copper Filament, PLA–Copper 90%) achieve rapid and uniform dissipation, ensuring more favorable thermal stability for repeated injection cycles.

At the mold opening stage, the inserts reach their final thermal state before ejection, as shown in Figure 6.16. This stage is particularly important since it determines the residual heat within the mold assembly and directly influences both dimensional stability of the molded part and the thermal load experienced by the inserts during cyclic operation.

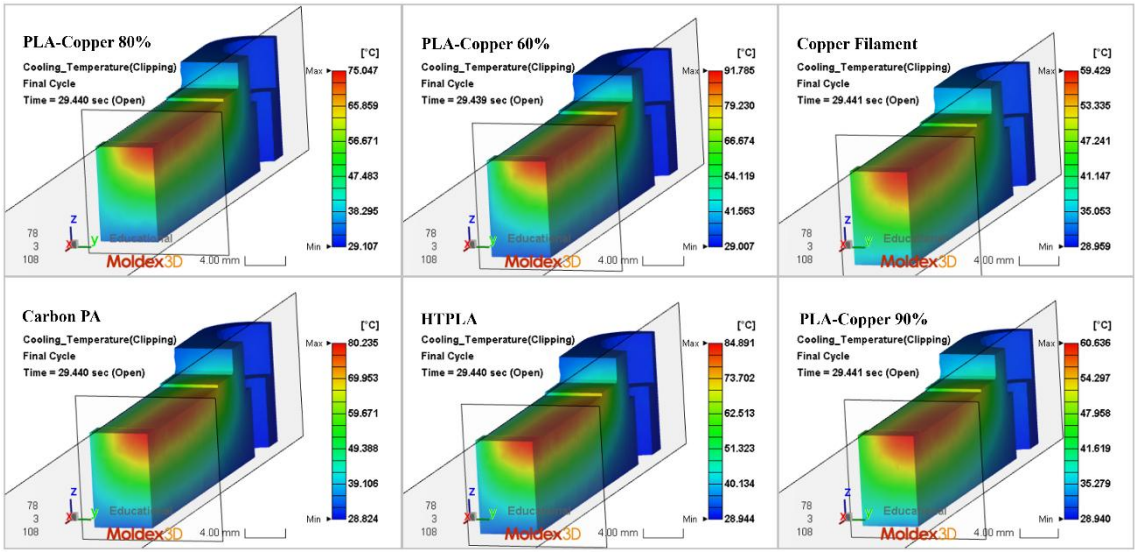

Figure 6.16. Sectional view of temperature distribution at mold opening for different inserts

The results confirm the consistent differences observed in earlier stages. Carbon PA and HTPLA still retain the highest temperatures, with peak values above 80 °C. Their internal regions remain considerably warmer than the cavity surface, indicating inefficient bulk heat dissipation. This behavior would likely increase the risk of dimensional variation and may shorten insert life under repeated molding cycles.

The Copper Filament again demonstrates the most favorable performance among the commercial materials, with maximum temperatures of ~59 °C and a uniform distribution across the insert. Its cooling efficiency is nearly identical to that of PLA–Copper 90%, which also stabilizes around ~60 °C. Both materials therefore approach the performance of metallic inserts, providing efficient heat removal and uniformity by the time of mold opening.

The intermediate cases, PLA–Copper 60% and PLA–Copper 80%, show a clear gradient in performance. PLA–Copper 60% still records higher internal temperatures (>90 °C), more than HTPLA and Carbon PA, while PLA–Copper 80% reduces these values to ~75 °C, demonstrating noticeable improvement but not yet achieving the efficiency of Copper Filament or PLA–Copper 90%.

The results from EOF to mold opening (Figures 6.12–6.16) confirm that insert performance is strongly governed by thermal conductivity. Carbon PA (0.532 W/m·K), HTPLA (0.529 W/m·K), and PLA–Copper 60% (0.401 W/m·K) retained the highest internal temperatures, while and PLA–Copper 80% (0.829 W/m·K) showed intermediate behavior. The best performance was achieved by PLA–Copper 90% (1.569 W/m·K) and Copper Filament (1.616 W/m·K), which approached the uniform cooling of the steel reference. This close agreement between measured conductivity values and simulation trends confirms that thermal conductivity is the dominant parameter.

6.2.1.2 Pressure Profile of Inserts

Besides thermal behavior, the pressure acting on the inserts during injection is another critical factor influencing their structural stability and lifetime. The reference case with the steel 1.2083 insert is presented in Figure 6.17. The contour plots illustrate the pressure distribution, highlighting localized peaks around the gate and flow entrance regions. The maximum pressure reached values slightly above 10 MPa, which are well within the capacity of steel inserts, given their high stiffness and negligible deformation under these conditions.

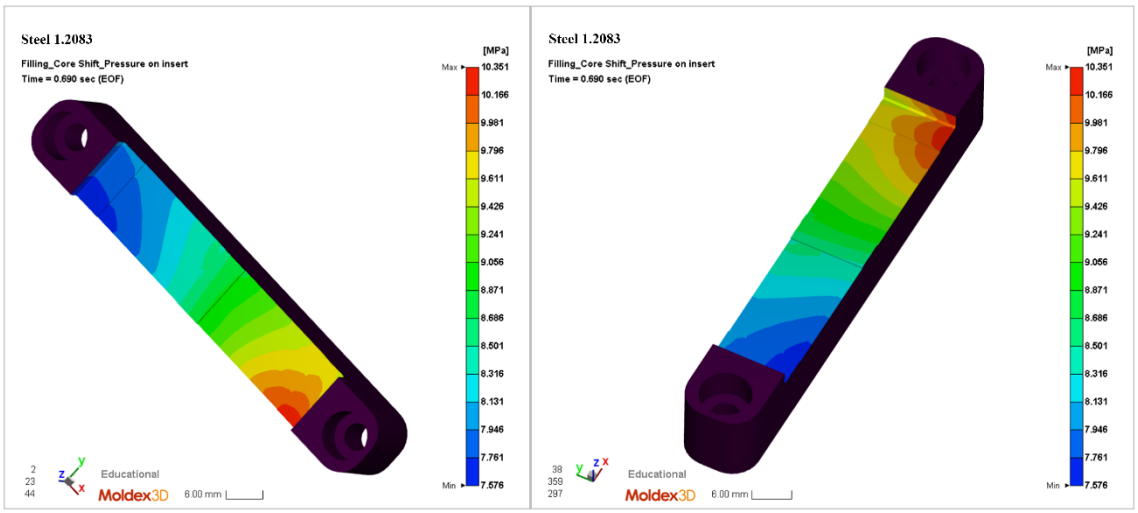

Figure 6.17. Pressure distribution on the steel 1.2083 insert

Figure 6.18 shows the corresponding pressure distributions for the polymeric and composite inserts. The results indicate that the applied cavity pressure is essentially the same for all cases, ranging between 7.4 MPa (min) and 10.2 MPa (max), with only small local variations. This confirms that the difference in insert performance is not related to the applied pressure itself, but rather to the mechanical response of the materials.

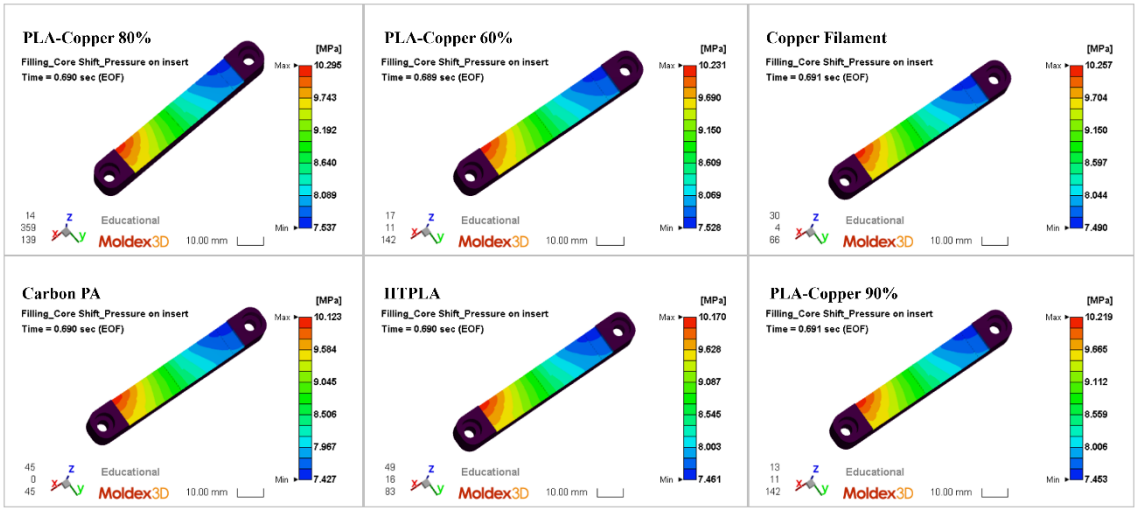

Figure 6.18. Pressure distribution for different inserts

Considering the maximum pressure of ~10 MPa obtained in the simulations, the compression tests (Figure 6.19) indicate that the inserts undergo a deformation in the range of 0.1–0.3 mm, corresponding to approximately 1–3% strain. This confirms that, although the applied pressure is essentially the same for all inserts (7.4–10.2 MPa), the resulting displacement remains within acceptable limits for all materials tested.

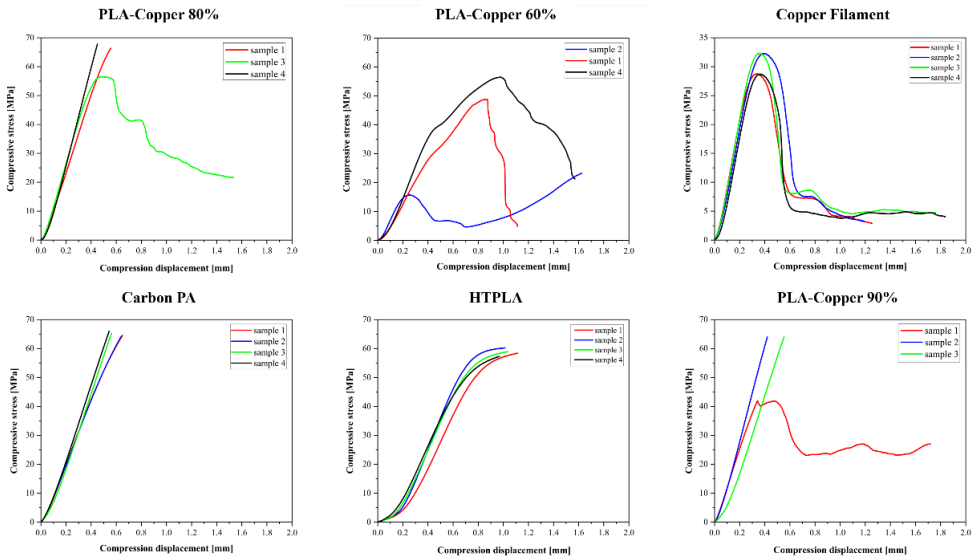

Figure 6.19. Experimental compression test results for different samples

6.2.1.3 Insert Displacement

In addition to temperature and pressure, the structural response of the inserts was analyzed in terms of displacement under injection loading. The reference case with the steel 1.2083 insert is reported in Figure 6.20. As expected, the total displacement is negligible, with maximum values in the order of 4.8×10^{-4} mm, confirming the dimensional stability of metallic inserts even under the highest cavity pressures.

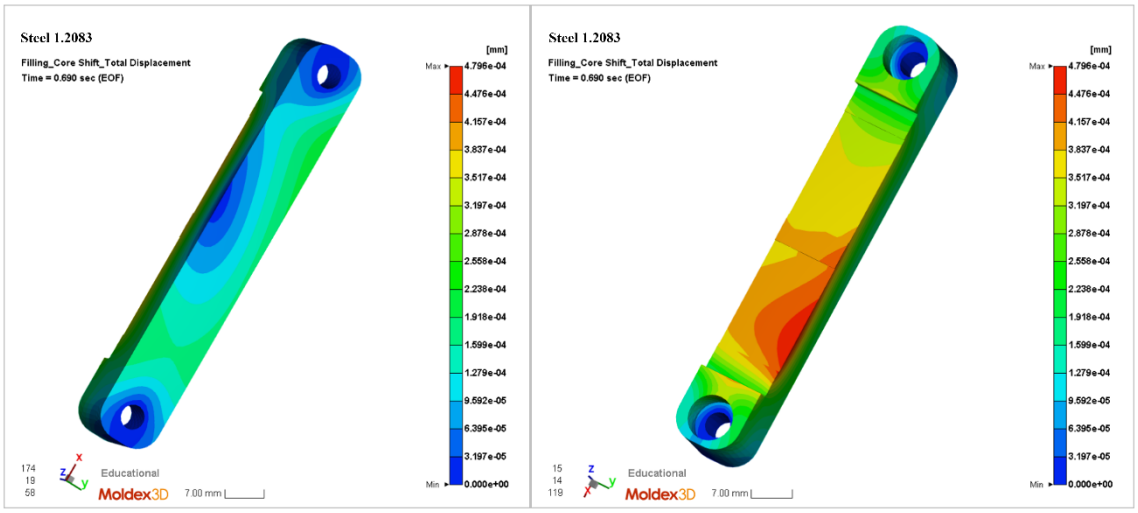

Figure 6.20. Total displacement distribution of steel 1.2083 insert

The corresponding displacement maps for the polymeric and composite inserts are shown in Figure 6.21. In this case, displacements are several orders of magnitude higher than for steel. The maximum values range approximately between 0.06 mm and 0.10 mm, depending on the insert material. This trend is consistent with the lower elastic modulus of polymer-based materials compared with steel.

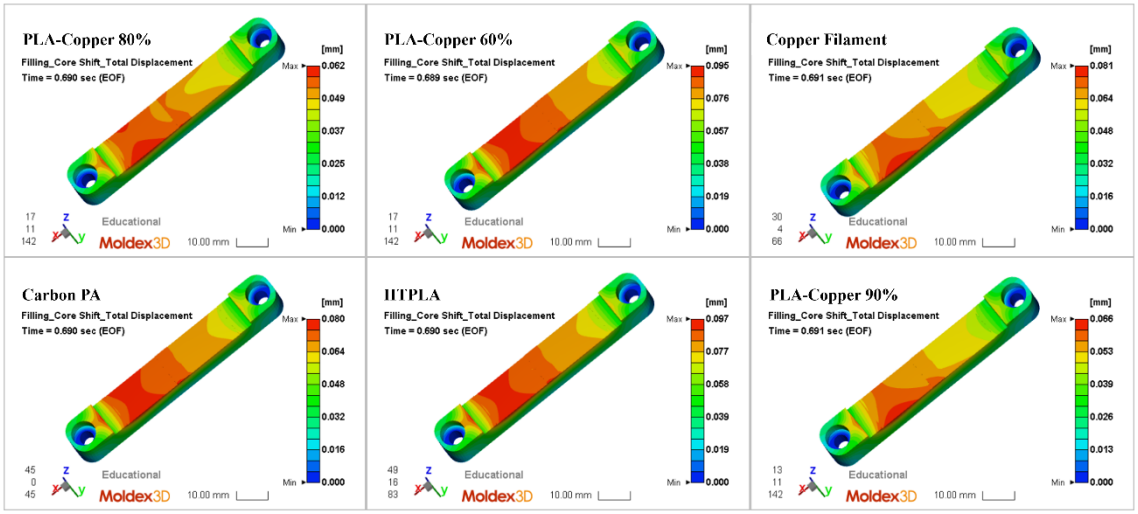

Figure 6.21. Total displacement distribution of different inserts

Among the tested materials, HTPLA and PLA–Copper 60% exhibited the highest displacements (~0.09–0.10 mm), while the PLA–Copper 90% and 80% composites showed improved resistance with the lowest displacement (~0.06 mm).

6.2.2 Analysis of Molded Part Behavior

After analyzing the thermal and mechanical response of the inserts, the attention is shifted to the behavior of the molded part itself. Since geometry, polymer, and processing conditions were kept constant across all simulations, any influence of the insert material is expected to manifest primarily during cooling, with consequences for dimensional stability. To structure this analysis, the molded part is first evaluated in terms of filling behavior through the melt front time, followed by temperature and pressure profiles, displacement, and volumetric shrinkage.

6.2.2.1 Melt Front Time

Figure 6.22 shows the melt front time distribution obtained for the reference case with the steel 1.2083 insert, while Figure 6.23 presents the corresponding results for the polymeric inserts. In all cases, the melt front advances uniformly from the gate through the cavity until complete filling at ~0.69 s.

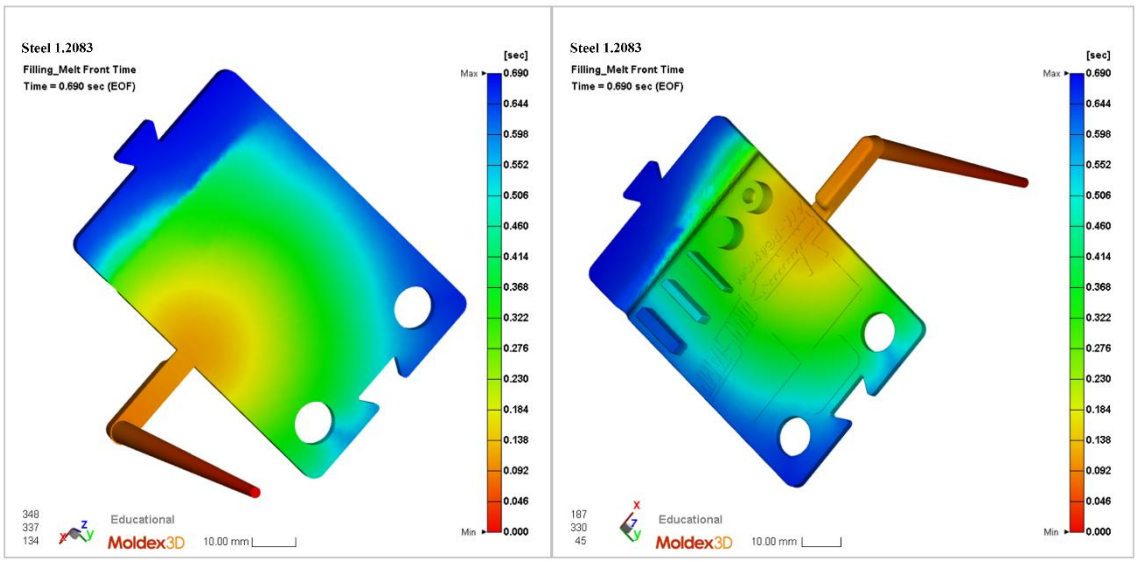

Figure 6.22. Melt front time distribution of the part with steel 1.2083 insert

The filling pattern and total filling time are essentially identical for all inserts, since the part geometry, gate design, polymer, and injection conditions were kept constant.

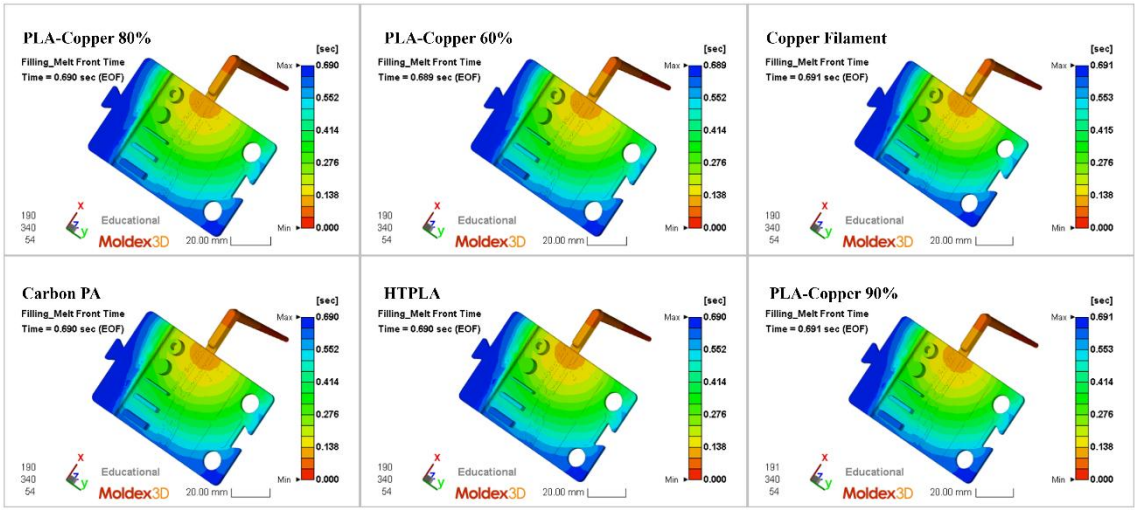

Figure 6.23. Melt front time distribution of the part with different insert

6.2.2.2 Temperature Profile of Part

Figure 6.24 shows the temperature distribution of the molded part at the end of filling (EOF) and end of packing (EOP) in the reference case with a steel 1.2083 insert. During filling, the highest temperatures are concentrated near the gate and flow path, while by the end of packing, the overall distribution becomes more uniform due to the progressive cooling at the mold walls.

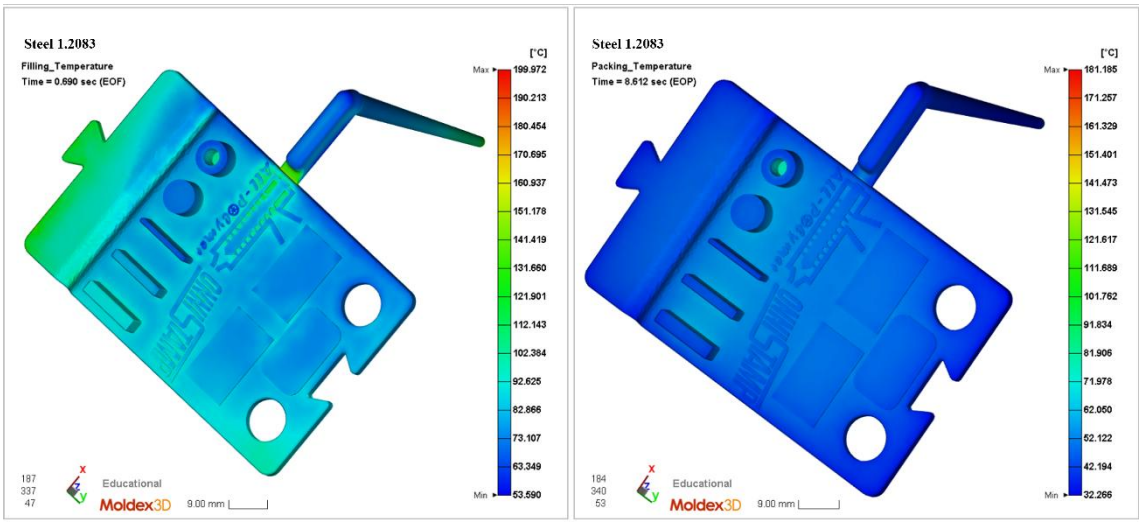

Figure 6.24. Temperature distribution of the part with steel insert at EOF and EOP

Figure 6.25 reports the temperature fields at the end of filling, while Figure 6.26 shows the distributions at the end of packing. The results confirm that the overall filling temperature pattern of the part is essentially the same across all cases, since the polymer, geometry, and injection conditions were fixed. However, localized differences can be

observed near the cavity surface: inserts with higher conductivity, such as PLA–Copper 90% and Copper Filament, show slightly reduced surface temperatures, whereas HTPLA and Carbon PA retain more heat at the polymer–insert interface.

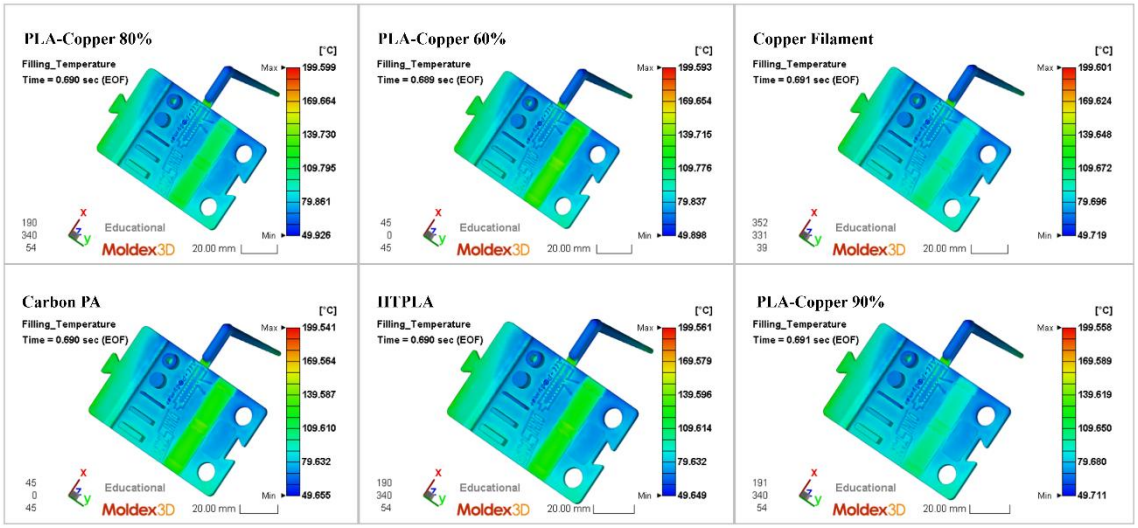

Figure 6.25. Temperature distribution of the part at EOF with different inserts

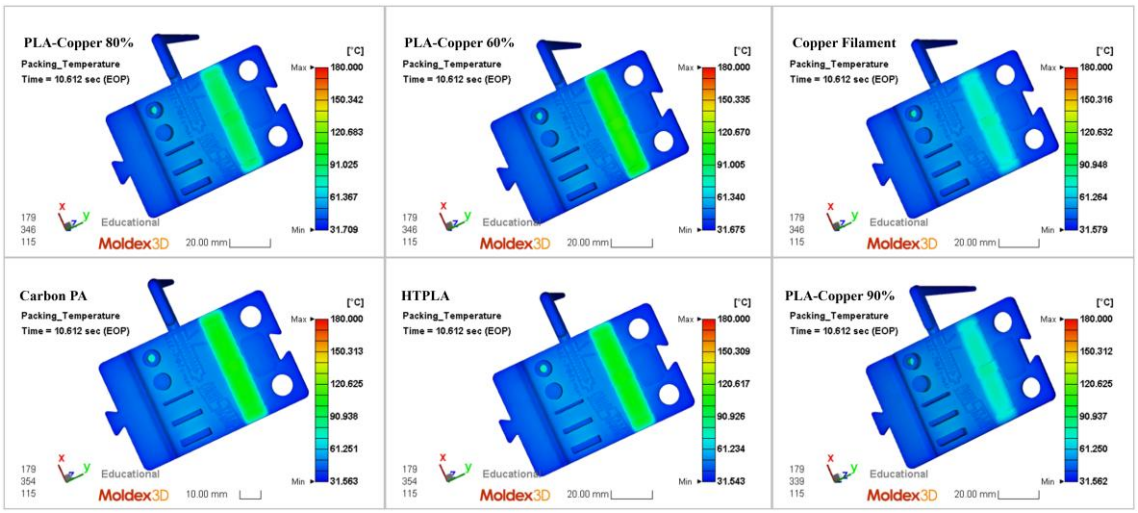

Figure 6.26. Temperature distribution of the part at EOP with different inserts

Although these differences remain modest at this stage, they play an important role in the cooling efficiency and final warpage of the part.

6.2.2.3 Pressure Profile of Part

Figure 6.27 shows the pressure distribution of the molded part at the end of filling (EOF) and end of packing (EOP) for the reference case with a steel 1.2083 insert. During filling, the pressure is highest near the gate and gradually decreases along the flow path.

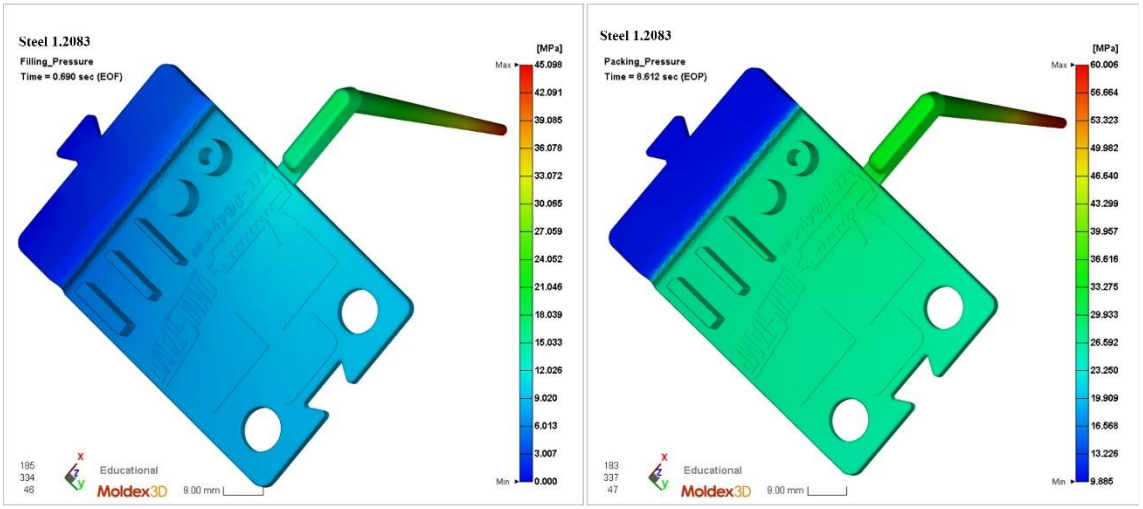

Figure 6.27. Pressure distribution of the part at EOF and EOP with steel insert

Figure 6.28 shows the pressure maps during filling, while Figure 6.29 illustrates the pressure distribution at the end of packing. The maximum cavity pressures were found to be in the range of 45–60 MPa, which is consistent across all simulations.

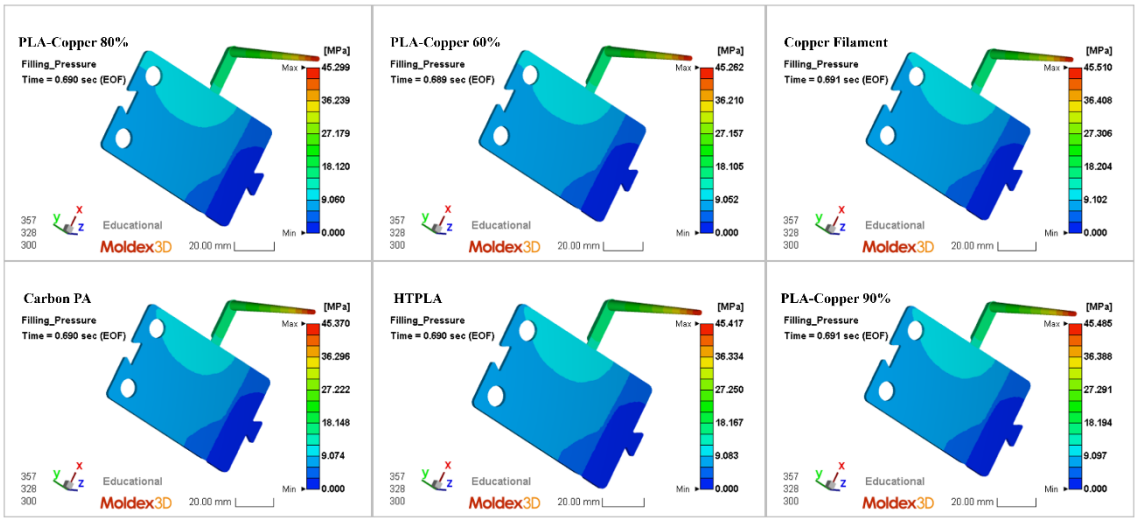

Figure 6.28. Pressure distribution of the part at EOF with different insert

The pressure fields reveal no significant differences between inserts, since the process parameters, part geometry, and polymer were kept constant. However, when combined with the insert-specific thermal and mechanical responses presented earlier, these pressure conditions provide a basis for evaluating potential deformation or warpage.

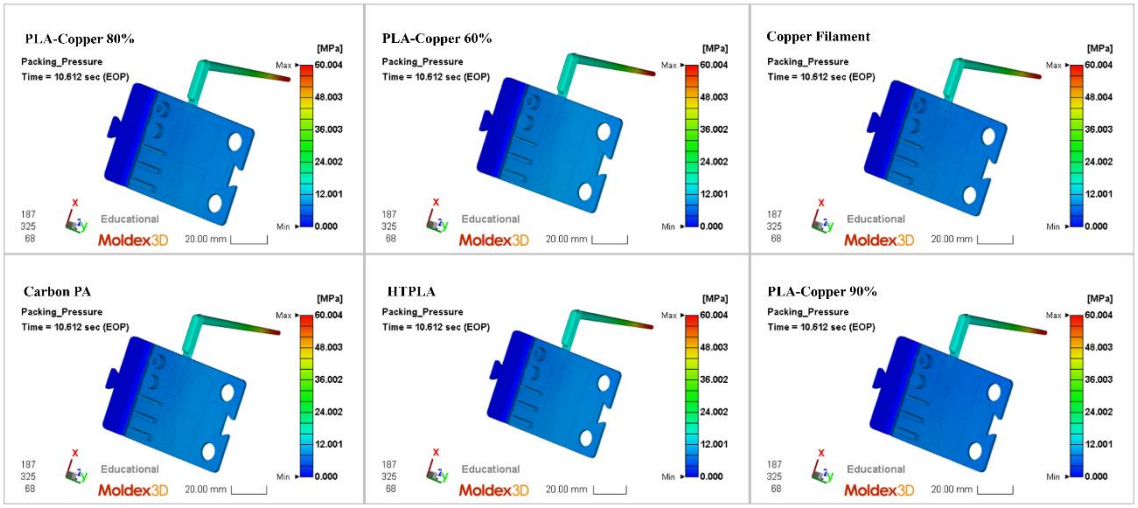

Figure 6.29. Pressure distribution of the part at EOP with different insert

6.2.2.4 Part Displacement

Figure 6.30 shows the predicted warpage of the molded part with the steel 1.2083 insert, while Figure 6.31 compares the results for the polymeric inserts. The displacement maps indicate that deformation is most pronounced near the edges and corners of the part, while the central region remains relatively stable with minimal displacement.

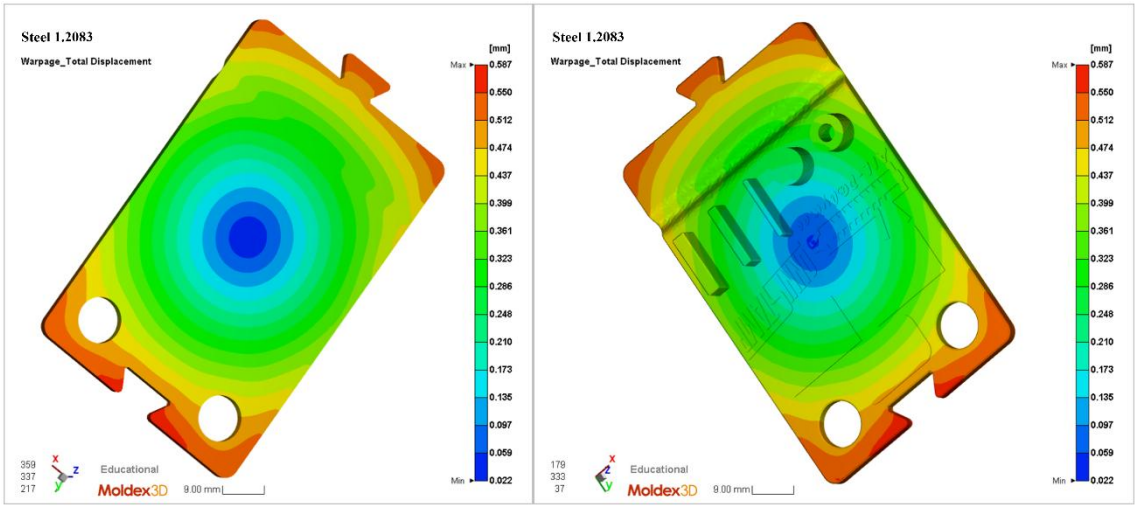

Figure 6.30. Total displacement of the part with steel insert

The maximum displacement values are of similar magnitude across all cases, typically ranging between 0.58 and 0.64 mm. Inserts with lower thermal conductivity, such as HTPLA, Carbon PA, and PLA–Copper 60%, tend to produce slightly higher warpage, while Copper Filament and PLA–Copper 90% achieve marginally lower values, consistent with their enhanced heat dissipation.

Overall, while differences between materials are not dramatic, inserts with higher conductivity show a modest improvement in reducing warpage, which correlates with the more uniform cooling behavior observed in previous sections.

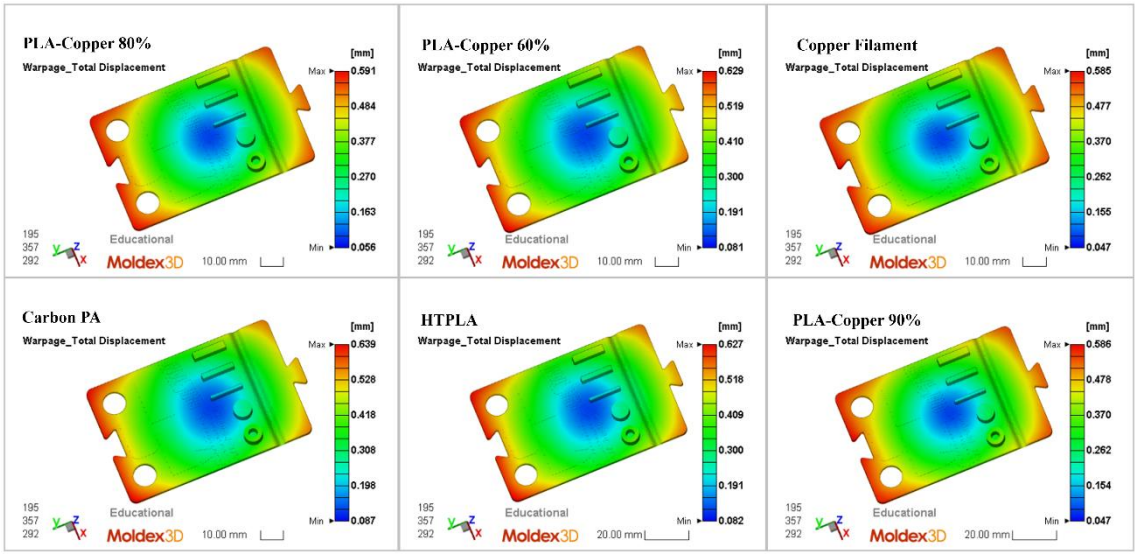

Figure 6.31. Total displacement of the part with different inserts

6.2.2.5 Volumetric Shrinkage of Part

Volumetric shrinkage is a critical parameter in injection molding, as it directly affects dimensional accuracy and the likelihood of defects such as voids or sink marks. Figure 6.32 illustrates the volumetric shrinkage distribution of the part molded with a steel 1.2083 insert, evaluated at three key stages of the molding cycle: end of filling (EOF), end of packing (EOP), and extended packing (representative of the end of cooling and mold opening).

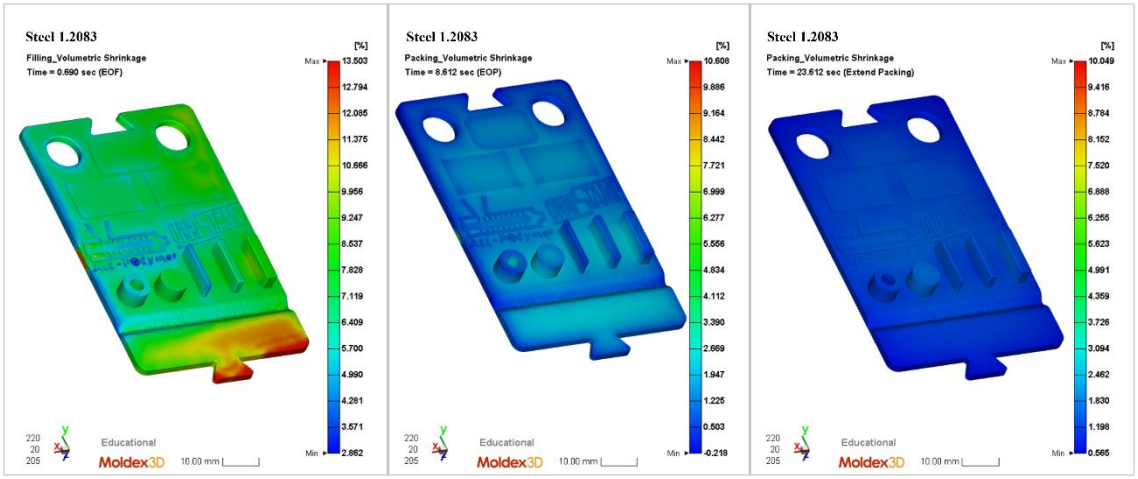

Figure 6.32. Volumetric shrinkage of the part with steel insert at EOF, EOP, and extended Packing

At EOF, shrinkage reaches its highest level since the cavity is only filled but not yet compensated by holding pressure. During the packing stage, shrinkage decreases significantly due to the compensating effect of the applied pressure, highlighting the stabilizing role of this phase in achieving dimensional consistency. At extended packing, shrinkage stabilizes further and reflects the final condition of the part at mold opening.

The influence of different polymer-based inserts is shown in Figures 6.33–6.35, corresponding to EOF, EOP, and extended packing, respectively. At EOF, shrinkage values are generally higher across all materials compared to the steel reference.

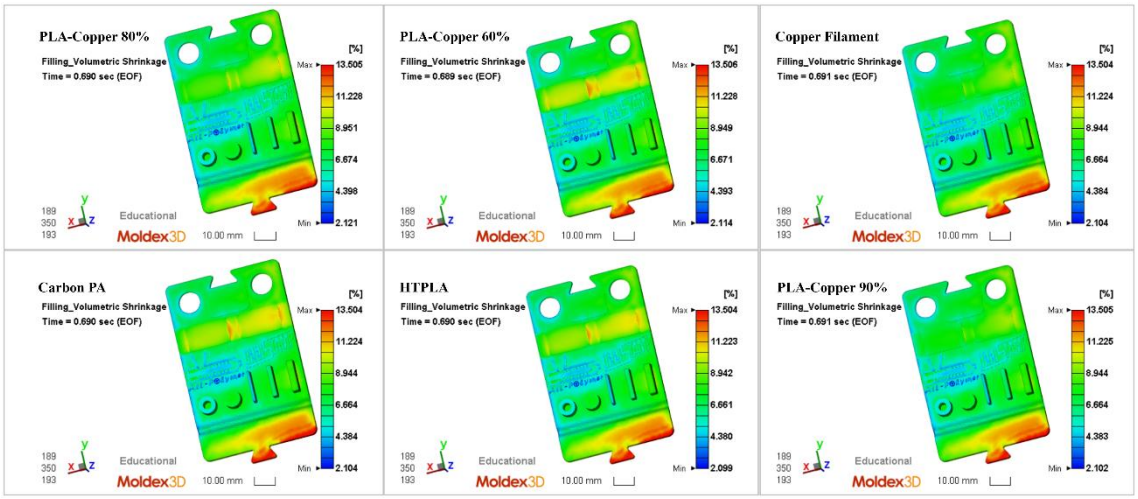

Figure 6.33. Volumetric shrinkage of the part at EOF with different inserts

By EOP, maximum shrinkage values converge to a similar range (≈0.5–12%), but clear differences emerge in the spatial distribution of shrinkage. Inserts with lower thermal conductivity, such as HTPLA, Carbon PA, and PLA–Copper 60%, exhibit wider yellow/green regions located at the part surface in direct contact with the insert. This indicates slower heat extraction and locally elevated shrinkage in those areas. In contrast, inserts with higher thermal conductivity, namely PLA–Copper 90% and Copper Filament, promote more efficient heat dissipation. As a result, the shrinkage field is more uniform, with reduced localized gradients, approaching the behavior observed with the steel insert.

At extended packing, these trends become more representative of the final part geometry. All polymer-based inserts still show slightly higher shrinkage compared to steel, but the difference between low- and high-conductivity materials remains evident. High-conductivity inserts (PLA–Copper 90% and Copper Filament) consistently yield a more homogeneous shrinkage distribution, minimizing localized dimensional variations. This

confirms that the thermal properties of the insert directly govern the local cooling rate at the insert–part interface and, consequently, the final shrinkage behavior and dimensional stability of the molded component.

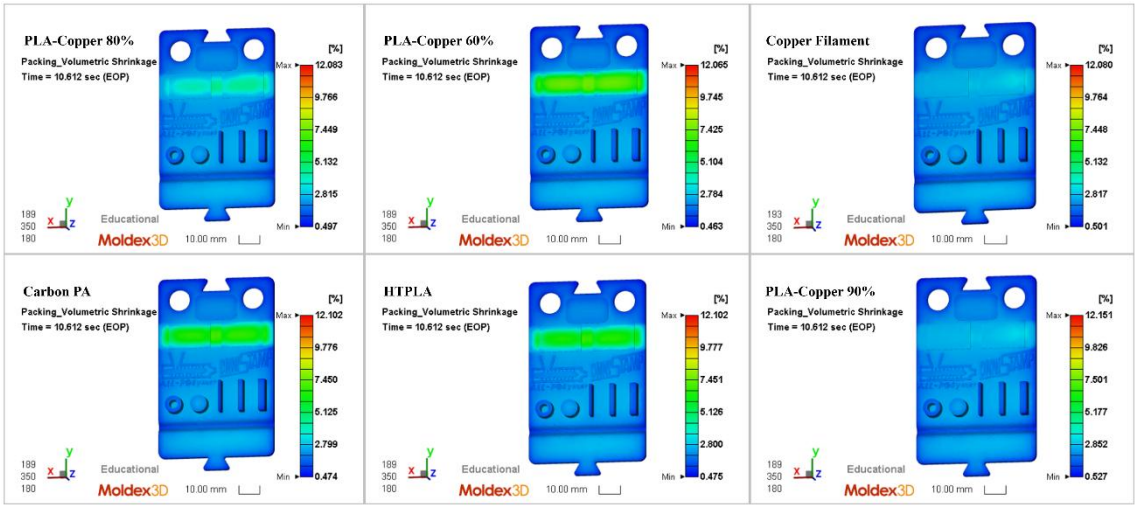

Figure 6.34. Volumetric shrinkage of the part at EOP with different inserts

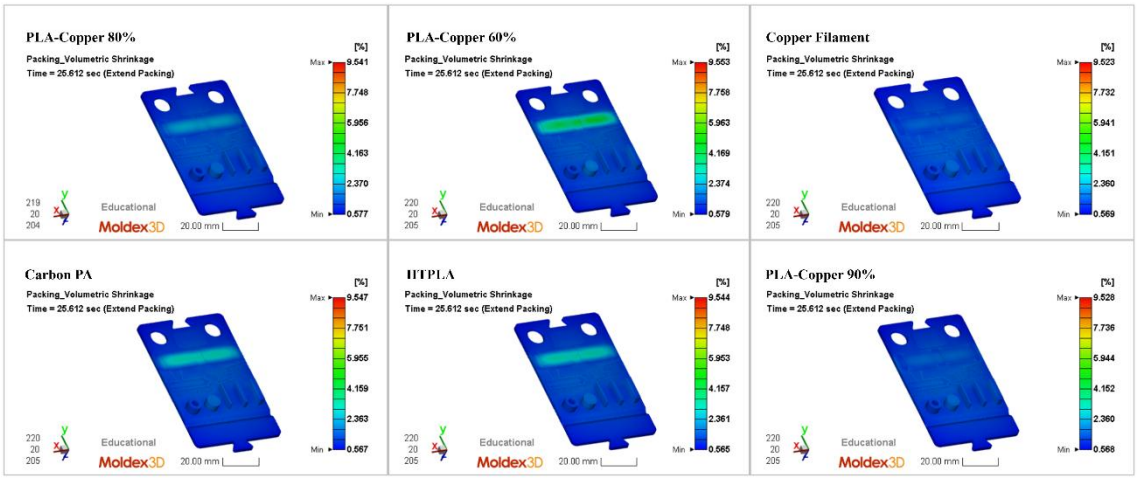

Figure 6.35. Volumetric shrinkage of the part at extended packing with different inserts

These results confirm the strong link between insert thermal properties and the volumetric shrinkage behavior of the molded part. High-conductivity inserts not only accelerate cooling but also enhance packing efficiency, thereby minimizing shrinkage-related defects.

The Moldex3D simulations provided a detailed understanding of the thermal and mechanical response of the different inserts during the injection molding cycle. Across all cases, thermal conductivity emerged as the dominant parameter, strongly influencing both the temperature distribution within the insert and the cooling efficiency of the

molded part. Inserts with higher conductivity, namely PLA–Copper 90% and Copper Filament, demonstrated rapid heat dissipation and lower temperature gradients, approaching the performance of the steel reference. In contrast, inserts with lower conductivity, such as HTPLA and PLA–Copper 60%, retained higher internal temperatures and showed reduced thermal stability.

The pressure and displacement analyses confirmed that all inserts were subjected to comparable cavity pressures in the range of 7.4 to 10.2 MPa, well within the structural limits of both steel and polymer-based inserts. However, displacement predictions highlighted differences in stiffness: while steel inserts exhibited negligible deformation, polymer-based inserts showed measurable displacements in the order of 0.06–0.10 mm. Among them, PLA–Copper 90% and PLA–Copper 80% composites displayed the lowest displacements, whereas HTPLA and PLA–Copper 60% were less resistant to warpage.

Although identical packing and cooling times were imposed in Moldex3D, the practical cycle time would not be the same for all inserts. High-conductivity inserts (PLA–Copper 90%, Copper Filament, and steel) would reach the eject temperature (103 °C) more quickly, enabling shorter cycles, whereas low-conductivity inserts (HTPLA, PLA–Copper 60%) would require extended cooling to achieve the same condition, effectively lengthening the cycle time.

Comparison with experimental injection molding trials (Chapter 5) showed that simulations and experiments were in very close agreement. The trends predicted by Moldex3D, such as the improved thermal response of high-conductivity inserts and the greater susceptibility to deformation of low-stiffness composites, were consistent with real process behavior. For example, the prolonged cooling times and higher part temperatures observed experimentally with PLA-based inserts were reproduced by Moldex3D, while the improved cycle stability of PLA–Copper composites and Copper Filament was also captured. Minor deviations between simulation and experiment may arise from machine-related variations and measurement uncertainties. Nevertheless, since the Moldex3D analysis was performed in transient mode, the simulations account for the evolution of multiple cycles and therefore reproduce the real process behavior very closely. The strong agreement obtained confirms the reliability of Moldex3D for predicting insert performance.

Taken together, the Moldex3D simulations not only validate the experimental findings but also extend them by providing detailed insight into temperature fields, pressure distributions, and local deformations within the inserts. These combined results demonstrate that polymer–copper composites, with PLA–Copper 90% showing superior thermal performance and PLA–Copper 80% offering a balanced thermal–mechanical behavior, represent the most promising candidates for replacing steel inserts in selected applications.

Chapter 7

CONCLUSION

The present work explored the potential of additive manufacturing for the production of injection molding inserts, focusing on the transition from filament-based FFF systems to pellet-based fused granular fabrication (FGF) technology. While polymeric inserts inherently present lower thermal conductivity and mechanical robustness than steel, they offer substantial benefits in terms of cost reduction, design freedom, and time savings, especially for prototyping and small-batch production. The main objective of this thesis was to develop and evaluate a novel approach for rapid tooling using the Piocreat G5 PRO pellet printer, thereby eliminating the intermediate step of filament extrusion and enabling the direct use of compounded or recycled feedstocks.

This work contributes a novel FGF-based workflow for rapid tooling on the G5 PRO platform, demonstrates the feasibility of processing pelletized commercial filaments, and introduces new PLA–Copper composites (60, 80, and 90 wt%) specifically tailored for improving heat dissipation in mold inserts. Furthermore, by integrating experimental injection molding trials with Moldex3D simulations, the thesis establishes a validated framework for predicting and optimizing the thermal performance of polymer–metal composite inserts. These contributions advance pellet-based additive manufacturing from a prototyping tool toward a credible rapid tooling methodology for functional injection molding applications.

Four commercial filaments were first pelletized and successfully printed into test specimens and inserts, validating the capability of the G5 PRO system to process standard polymeric grades within controlled conditions. Among the various performance factors investigated, heat dissipation proved to be the most critical, in agreement with recent literature on polymer-based injection tooling. To address this limitation, new PLA–Copper compounds with different filler loadings (60, 80, and 90 wt%) were prepared, characterized, and tested against reference materials (Carbon PA, HTPLA, Copper Filament) and a steel insert.

The characterization results highlighted the dual role of copper; while increasing thermal conductivity and improving heat dissipation during molding, higher filler contents also reduced toughness and increased brittleness, potentially limiting insert durability. Moving from neat PLA to PLA–Copper clearly improved the thermal performance of the inserts, but at the same time it confirmed that excessively high copper content, although excellent for conductivity, compromises mechanical stability. Thus, the best-performing inserts were those where a balance between thermal and mechanical properties was achieved.

Injection molding trials performed over ten cycles per insert demonstrated that PLA–Copper 90% and the commercial Copper Filament delivered the highest thermal performance, achieving the fastest cooling and the most accurate part replication, approaching the response of the steel reference. At the same time, PLA–Copper 80% proved to be the most balanced option, combining strong heat dissipation with greater mechanical stability and durability under molding conditions. By contrast, PLA–Copper 60% showed only limited improvements, confirming that lower copper contents provide reduced benefits for rapid tooling applications.

Moldex3D simulations were also carried out and confirmed the results obtained from the injection molding experiments, showing consistent trends in heat dissipation and cycle performance across the different inserts.

This research demonstrates that FGF technology, combined with polymer–metal composites, can extend the practical use of additively manufactured inserts in injection molding. The PLA–Copper 90% and Copper Filament inserts achieved the most promising results for thermal management, while PLA–Copper 80% offered a favorable compromise between conductivity and mechanical integrity. The study confirms that pellet-based 3D printing not only broadens material flexibility but also reduces cost and time, positioning FGF as a viable alternative to filament-based approaches for rapid tooling.

While polymer inserts cannot yet replace steel for long production runs, their performance is sufficiently close for low-volume or pilot-scale applications. Looking ahead, several avenues of development appear particularly promising. First, mechanical reinforcement of copper-rich composites is needed to counteract the brittleness introduced by very high copper loadings. This could be achieved by surface-treating the copper particles to improve adhesion with the PLA matrix, blending PLA with tougher polymers, or

introducing secondary reinforcements such as short fibers or nanofillers to share stresses and delay crack initiation. Such strategies would preserve the benefits of high thermal conductivity while enhancing structural stability under repeated molding cycles.

Second, refinement of FGF printing parameters can reduce porosity and improve consistency in insert fabrication. Because pellet extrusion is inherently less precise than filament-based FFF, careful tuning of temperature profiles, extrusion flow, and bead compaction is critical to ensure dense, well-fused structures. The adoption of optimized process settings, combined with post-processing techniques such as annealing, could significantly improve the dimensional stability and mechanical performance of FGF-printed inserts.

Third, hybrid design strategies represent a pathway to extend tool life and approach the robustness of metallic inserts. For example, polymer inserts could be enhanced with metallic surface coatings (e.g., nickel or copper plating) to improve wear resistance and reduce direct polymer–melt interaction. Alternatively, conformal cooling features or embedded conductive channels could be integrated into the printed geometry to accelerate heat extraction and improve part repeatability. Even combinations of polymer cores with thin metallic skins could merge the cost and weight advantages of polymers with the durability of metals.

Ultimately, the combination of FGF processing and tailored composite or hybrid solutions offers a strong foundation for sustainable, fast, and cost-effective rapid tooling. By addressing brittleness, porosity, and wear resistance through these future developments, polymer-based inserts can be advanced from their current role in prototyping and pilot production toward wider adoption in functional, small-series injection molding applications.

BIBLIOGRAPHY

[1] V. Moritz and e. al., "Heat Dissipation Plays Critical Role for Longevity of Polymer-Based 3D-Printed Inserts for Plastics Injection Molding," *Journal of Manufacturing and Materials Processing*, vol. 6, no. 117, 2022.

[2] A. Maggio, "Progettazione e sviluppo tramite stampa 3D di inserti di stampi per Injection Molding," Politecnico di Torino, 2024.

[3] A. Bagalkot and e. al., "A Methodology for Setting the Injection Molding Process Parameters for Polymer Rapid Tooling Inserts," *Rapid Prototyping Journal*, 2019.

[4] J. Qayyum and e. al., "Performance of 3D Printed Polymer Mold for Metal Injection Molding Process," *Rapid Prototyping Journal*, vol. 23, no. 3, 2017.

[5] E. Bilal and e. al., "Circularity: Understanding the Environmental Tradeoffs of Additive Manufacturing with Waste Plastics," *Recycling*, vol. 9, no. 72, 2024.

[6] R. Chang and e. al., "Three-Dimensional Insert Molding Simulation in Injection Molding," in *ANTEC 2004 Conference Proceedings*, 2024.

[7] M. Moradi and e. al., "Enhancing 3D Printing Copper-PLA Composite Fabrication via Fused Deposition Modeling through Statistical Process Parameter Study," *Micromachines*, vol. 15, no. 1082, 2024.

[8] S. Dehghan-Toranposhti and e. al., "Fabrication, Characterization and Evaluating Properties of 3D Printed PLA-Mn Scaffolds," *Scientific Reports*, vol. 14, no. 16592, 2024.

[9] A. Woern and e. al., "Fused Particle Fabrication 3-D Printing: Recycled Materials' Optimization and Mechanical Properties," *Materials*, vol. 11, no. 1413, 2018.

[10] PIOCREAT, "Tips for using 3D G5 PRO Piocreat," 2023.

[11] M. Pérez and e. al., "Development of High Thermal Conductivity Polymer Composites for Injection Molding Inserts," *Polymers*, vol. 15, no. 4518, 2023.

[12] S. Siengchin and e. al., "A Review of Polymer Composites with Enhanced Thermal Conductivity for Advanced Manufacturing Applications," *SN Applied Sciences*, vol. 5, no. 989, 2023.

[13] J. Roberts and e. al., "Wear and Thermal Performance of H13 Tool Steel for Mold Applications," *Surface and Coatings Technology*, vol. 154, no. 2–3, pp. 207–213, 2002.

[14] H. Giberti and e. al., "Performance of 3D Printed Polymer Tooling in Injection Molding," *International Journal of Advanced Manufacturing Technology*, vol. 102, 2019.

[15] A. Greco and e. al., "Selective Laser Sintering and Stereolithography for the Production of Polymer Tooling in Injection Molding," *Composites Part A: Applied Science and Manufacturing*, vol. 125, 2019.

[16] "Injection Molding with 3D Printed Molds," Formlabs, 2025. [Online]. Available: https://3d.formlabs.com/injection-molding/. [Accessed 2025].

[17] T. e. a. Wu, "A review: From the whole process of making thermal conductive polymer to application," *Journal of Polymer Science*, 2024.

[18] C. D. Y. Park, "In: Data Science for Nano Image Analysis. International Series in Operations Research & Management Science, vol 308," in *Location and Dispersion Analysis*, Springer, Cham.

[19] FILOALFA, "PLA – Technical Information," Ciceri de Mondel Srl. [Online]. Available: https://www.filoalfa3d.com/gb/content/9-pla.

[20] Proto-Pasta, "Copper Metal Composite HTPLA," ProtoPlant, Inc. [Online]. Available: https://proto-pasta.com/products/copper-metal-composite-htpla.

[21] Roboze, "Carbon PA," Roboze S.p.A. [Online]. Available: https://www.roboze.com/en/technology/materials/carbon-pa-pro.

[22] The Virtual Foundry, "Copper Filamet," The Virtual Foundry, LLC. [Online]. Available: https://shop.thevirtualfoundry.com/en-it/products/copper-filamet.

[23] LUCEFIN, "Famiglie Acciai – Inossidabili," LUCEFIN S.p.A., Oct. 2023. [Online]. Available: https://lucefin.com/famiglie-acciai-inossidabili/.

[24] LyondellBasell, "Moplen HP500N-B," LyondellBasell Industries Holdings B.V. [Online]. Available: https://www.lyondellbasell.com/en

[25] FlashForge, "Creator 3 Pro," FlashForge. [Online]. Available: https://www.FlashForge.com.hk/creator-3-pro.html.

[26] Piocreat, "Pellet 3D Printer – G5 PRO," Piocreat 3D. [Online]. Available: https://www.piocreat3d.com/pellet-3d-printer/.

[27] TA Instruments, "Dynamic Mechanical Analysis (DMA) – Q Series," TA Instruments. [Online]. Available: https://www.tainstruments.com/pdf/brochure/dma.pdf.

[28] Optris, "Infrared Camera PI 640i," Optris GmbH. [Online]. Available: https://optris.com/us/products/infrared-cameras/precision-line/pi-640i/.

[29] Phoenix Scientific Industries, "HERMIGA 100/10 VI Atomiser – Pilot-Scale Vacuum Inert Gas Atomisation System," Phoenix Scientific Industries Ltd. Available:

https://www.psiltd.co.uk/technology/hermiga-vacuum-inert-gas-atomisation-systems/the-hermiga-pilot/hermiga-100-10-vi/

[30] M.T. Takemori, Towards an Understanding of the Heat Distortion Temperature of Thermoplastics, Polym Eng Sci 19(15) (1979) 1104-1109.

APPENDIX

Operating guidelines for the Piocreat G5 Pro and Creality Print

The present appendix provides practical documentation on the setup and operation of the Piocreat G5 PRO pellet-based 3D printer, together with the use of the Creality Print slicing software. Its purpose is to consolidate technical instructions, recommended parameters, and maintenance guidelines into a single resource that can support future students and researchers working with the same system.

Figure 1. Overview of the Piocreat G5 PRO printer

The content presented here integrates information from official manuals, software documentation, and laboratory experience, with the aim of facilitating reproducibility of experimental work and reducing the learning curve for new users. The appendix is therefore intended as a hands-on reference rather than a theoretical discussion, complementing the scientific analyses in the main body of the thesis with practical knowledge essential for successful operation of the equipment.

1. Safety and lab readiness

The Piocreat G5 PRO pellet-based 3D printer integrates high-temperature extrusion zones, a screw-driven pellet feeder, and a heated build platform, as shown in Figure 2. Safe operation therefore requires strict adherence to laboratory practice and to the specific requirements of fused granular fabrication (FGF). The manufacturer recommends that the printer be installed in a well-ventilated, low-dust environment, away from heat sources or flammable materials, and always connected using the supplied grounded power cable. Users should not attempt to manually move the nozzle or platform when the machine is powered or operate the system with its protective cover open.

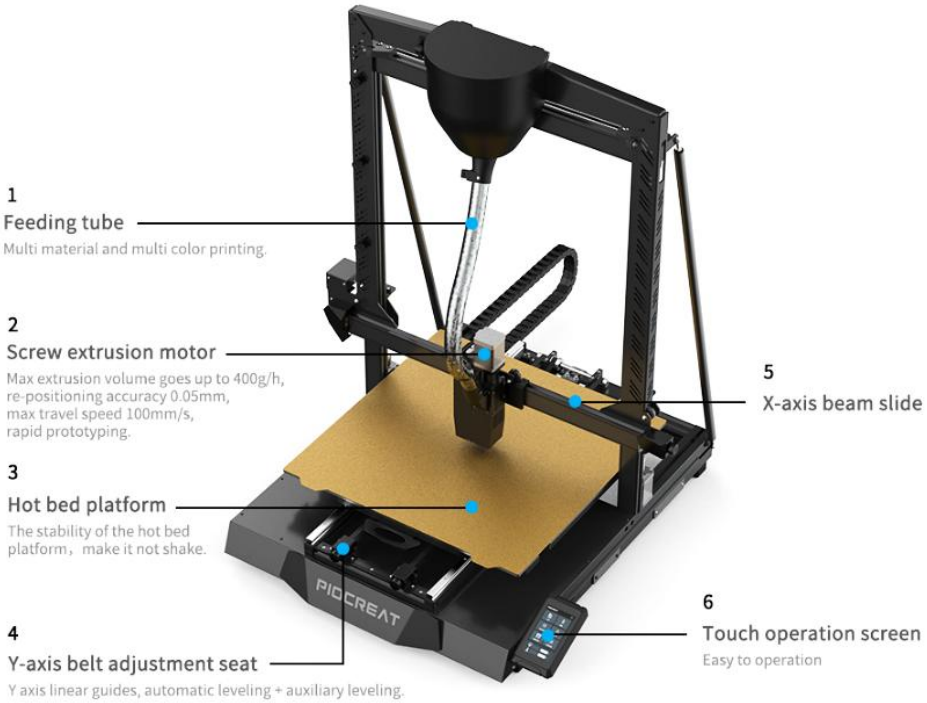

Figure 2. Piocreat G5 PRO pellet-based 3D printer

Additionally, the extrusion nozzle and heated bed can exceed 200 °C and may remain hot for several minutes after printing. Handling of printed parts must only be carried out once sufficient cooling has occurred, and always with protective gloves and suitable tools. Operators should avoid loose clothing and cotton gloves during operation, as these can become entangled in the printer's moving components, causing injury or print disruption.

It is important to consider operation with raw polymer pellets introduces additional safety concerns compared to filament-based extrusion. Pellets and the extruder throat area may

retain heat after printing and must only be accessed when cooled. All pellets must be thoroughly dried before use, as residual moisture can lead to steam bubbles, extrusion instability, or nozzle clogging. Furthermore, the extruder should be purged with waste material both before and after printing to prevent contamination and to stabilize the melt flow.

In this thesis, the printer was not operated with large material quantities, and the full hopper was therefore unnecessary. Instead, pellets were introduced through a small cavity (Figure 3) directly connected to the screw feeder (extruder throat). This adaptation facilitated easier manual feeding, ensuring a continuous supply of material to the melting zone without filling the entire hopper. While effective for laboratory-scale experiments, users must take particular care to avoid accidental contact with the heated throat during manual loading. To ensure safe and reliable operation, the following points should be verified before each print:

- Printer positioned on a stable, vibration-free surface
- Workspace clear of solvents, papers, and combustible materials
- Pellets dried according to recommended conditions
- Build plate leveled and Z-offset adjusted
- G-code prepared and verified in Creality Print
- Fire extinguisher and emergency stop access confirmed

Adhering to these measures minimizes the risk of burns, clogs, or operational failures while promoting reproducible results suitable for research applications.

Figure 3. Manual feeding cavity used instead of the hopper

2. System Overview – Piocreat G5 PRO (Pellet Extrusion)

The Piocreat G5 PRO is a pellet-based 3D printer equipped with a screw-driven extrusion system for processing polymer pellets. The machine is built on a rigid gantry architecture and integrates a heated build platform, a multi-zone extruder, and a touchscreen control interface. Main Components are listed as below:

- Pellet hopper and extruder throat – delivers raw material into the screw assembly
- Screw and barrel assembly – gradually melts and homogenizes pellets using segmented heating zones (Figure 4)
- Nozzle – capable of high-temperature extrusion for a wide range of polymers
- Heated build plate – ensures part adhesion and dimensional stability during printing
- Motion system – X–Y gantry and Z-axis lifting screw with limit switches and energy chains for precise positioning
- Control system – touchscreen panel with options for offline and network printing
- Auto-Leveling system – laser-based 64-point mapping for consistent first-layer calibration

Figure 4. Screw and barrel assembly

The G5 PRO is equipped with a nozzle capable of reaching 450 °C, with segmented heating of 360 °C in the upper zone and 420 °C in the lower zone. It supports print speeds of up to 100 mm/s and incorporates an intelligent 64-point laser auto-leveling system for precise bed calibration. These elements define the standard configuration of the G5 PRO

and provide the basis for correct installation, calibration, and operation in the laboratory. Before routine work, the printer should be commissioned using the touchscreen interface, as illustrated in Figure 5. By selecting Auto Leveling, the printer automatically performs a 64-point bed calibration. The Temp option allows the nozzle and heated bed to be preheated to their target values, while Move is used to manually adjust the x, y, and z axes. Once the nozzle and bed have reached the desired temperatures and sufficient material has melted, the extruder can be purged by selecting Load Pellet within the Move menu, confirming stable material flow. Finally, a short calibration print should be run to validate motion accuracy, extrusion consistency, and first-layer adhesion. Completing these steps ensures that the G5 PRO is properly prepared for operation and minimizes the risk of early printing errors.

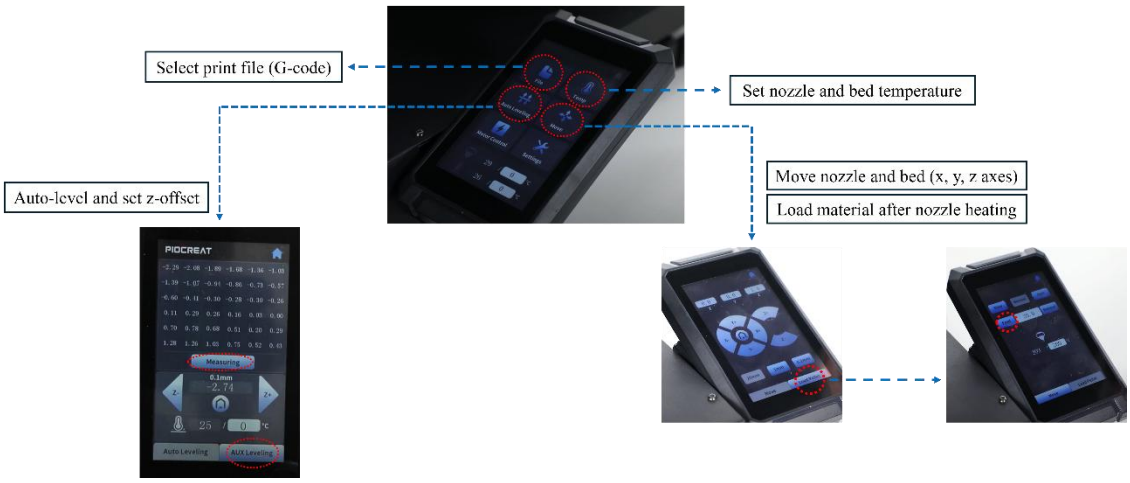

Figure 5. Touchscreen interface of the Piocreat G5 PRO showing the main functions

3. Creality Print

Creality Print is the slicing environment officially recommended for the Piocreat G5 PRO. It provides the necessary interface for preparing three-dimensional models, generating machine-readable G-code, and managing process parameters. The correct installation and initial configuration of this software are therefore essential prerequisites for reproducible printing outcomes. The installation package is distributed free of charge through the official Creality website, with current releases available for both Windows and macOS operating systems. It is advisable to install the most recent stable version, as this ensures

full compatibility with the firmware of the G5 PRO and incorporates the latest updates to the slicing engine.

At first launch, the user is prompted to define several initial settings. These include the choice of interface language, the confirmation of the workspace layout, and the registration of the connected printer. The G5 PRO must be selected from the printer library, after which its build volume, nozzle diameter, and default start- and end-code scripts are automatically applied, as shown in Figure 6.

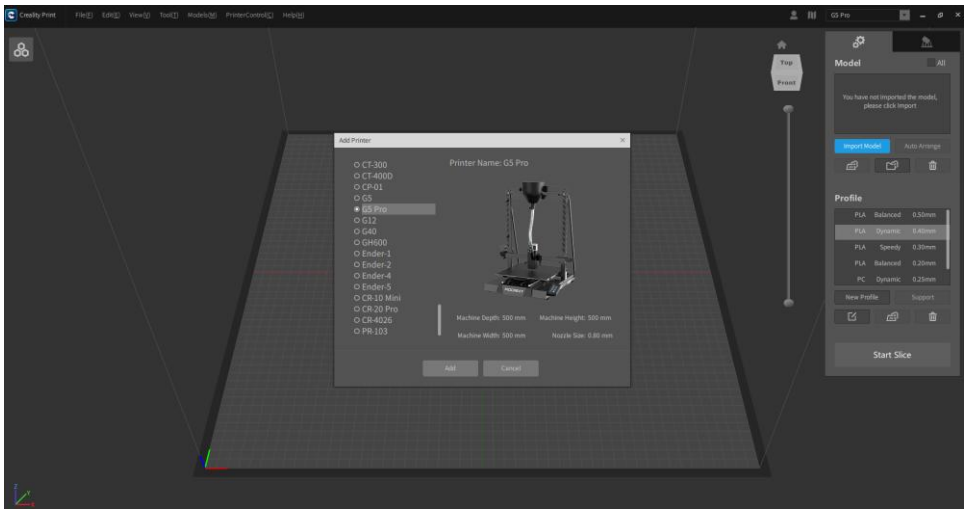

Figure 6. Registration of the connected printer (G5 PRO)

Creality Print accepts the most common file types used in additive manufacturing, namely STL, OBJ, and 3MF, and exports the prepared toolpath in standard G-code format. The software also supports its own project format (CX3D), which preserves both model placement and parameter configurations, thereby facilitating repeatability and collaboration between users. Configuration data, including printer profiles, material definitions, and slicing presets, are stored locally within the application directory but may additionally be synchronized with an online Creality Cloud account if cloud functionality is enabled. Within each printer profile, initialization and termination scripts expressed in G-code establish communication between the slicing environment and the hardware. The start sequence typically performs axis homing (G28), sets the target nozzle temperature (M104) and bed temperature (M140), waits until these values are reached (M109 and M190), and executes a controlled purge of the extruder (G1 E20 F200) to ensure a stable melt flow before printing begins. The end sequence disables heaters (M104 S0, M140 S0), retracts the material slightly to relieve pressure (G1 E-2 F200), and moves the print head to a defined rest position (G1 X0 Y200) to allow safe cooling and to prevent nozzle

blockages. The reliability of printed output depends directly on the correspondence between these digital instructions and the physical parameters of the machine. An accurately defined printer profile guarantees that the slicing environment reflects the true build volume, nozzle geometry, and thermal capacities of the G5 PRO, thereby ensuring that generated toolpaths are interpretable by the hardware and executed without error. Through these steps, the installation and first launch of Creality Print establish a slicing environment that is aligned with the hardware characteristics of the Piocreat G5 PRO. Ensuring this alignment at the outset is critical for subsequent process reliability, as it guarantees consistency between digital preparation and physical execution.

The workspace in Creality Print constitutes the environment in which digital models are prepared prior to slicing. A clear understanding of its structure and functions is essential, as model positioning, orientation, and transformation directly influence the quality of the toolpath and the success of subsequent printing operations. At the center of the interface lies the model display area, which represents the build plate of the configured printer. Imported models appear here and can be manipulated interactively. Surrounding this area are the primary toolbars and information panels, which provide access to geometric transformations, slicing parameters, and preview functions.

As shown in Figure 7, the menu bar in Creality Print provides access to the global functions required for managing models, projects, and system preferences. It consists of six primary categories: File, Edit, View, Tool, Model Library, and Help. Together, these menus establish the central framework for model import, visualization, slicing configuration, and software customization

- File – Used for importing and exporting models and projects. Supported formats include STL, OBJ, 3MF, images, Gerber files, and the proprietary CX3D project file. The File menu also provides access to recently opened projects and allows saving models or project states for later use.
- Edit – Contains the Undo and Redo functions, which allow stepwise navigation through modeling or parameter adjustments.
- View – Provides options for modifying the visual representation of the workspace. Models can be displayed in line, surface, or combined line-surface modes. Additional commands enable mirroring along the X, Y, and Z axes, resetting transformations, applying standard view orientations (front, back, left, right, top,

bottom, perspective, orthogonal), and realigning models to the origin or platform. These tools support accurate orientation and verification before slicing.

- Tool – Hosts global system settings. Functions include language selection, autosave preferences, log view, and theme customization. More advanced options include Repair (to fix mesh errors), Manage material (to define feedstock properties such as type, diameter, and processing temperature), and Manage printer (to configure machine dimensions, nozzle geometry, heated bed, and preview images). These tools ensure correspondence between digital parameters and hardware capabilities.
- Model Library – Provides access to the integrated online repository of 3D models. Users may browse, search, download, and import designs directly into the workspace, as well as manage collections for repeated use.
- Help – Offers software documentation, version information, update checks, and direct links to tutorials or feedback submission through Creality Cloud.

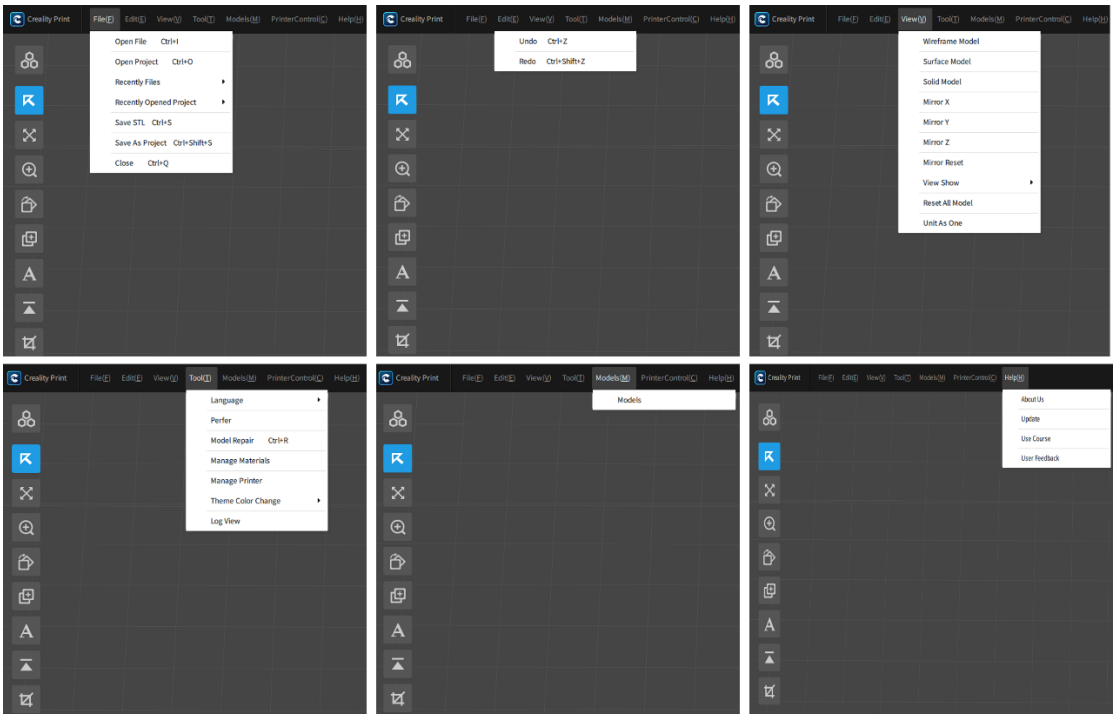

Figure 7. Overview of the Creality Print menu bar

In practice, users typically begin by importing geometry through the File menu, verify orientation and scale with View, define material and machine settings under Tool, and finally access online resources through the Model Library or Help. This structured layout

ensures that all aspects of the slicing workflow, from model preparation to machine communication, are logically centralized in a single interface.

Models can be imported in standard file formats (STL, OBJ, 3MF) through the Import function or by dragging files directly into the workspace. Once loaded, each model may be selected individually or as part of a group, with bounding boxes and coordinate axes displayed for reference. The right-click menu provides additional operations, including duplication, merging of multiple objects into a single part, splitting composite models, and clearing the build platform. The action bar (Figure 8) provides direct access to the basic tools for modifying model geometry within the workspace:

- Select – choose the model or return it to its default state
- Move – reposition the model along the X, Y, or Z axes, place it at the center or bottom of the build plate, or reset its location
- Scale – resize the model uniformly or along individual axes, with options to lock the ratio or reset to original size
- Rotate – rotate the model around the X, Y, or Z axes, with the option to reset orientation
- Clone – duplicate the model, with the number of copies defined before cloning
- Engrave – add text to the model, adjusting font, height, and thickness
- Cut – divide the model by setting the cutting position or angle along the X, Y, or Z axes, with options to start or reset the cut

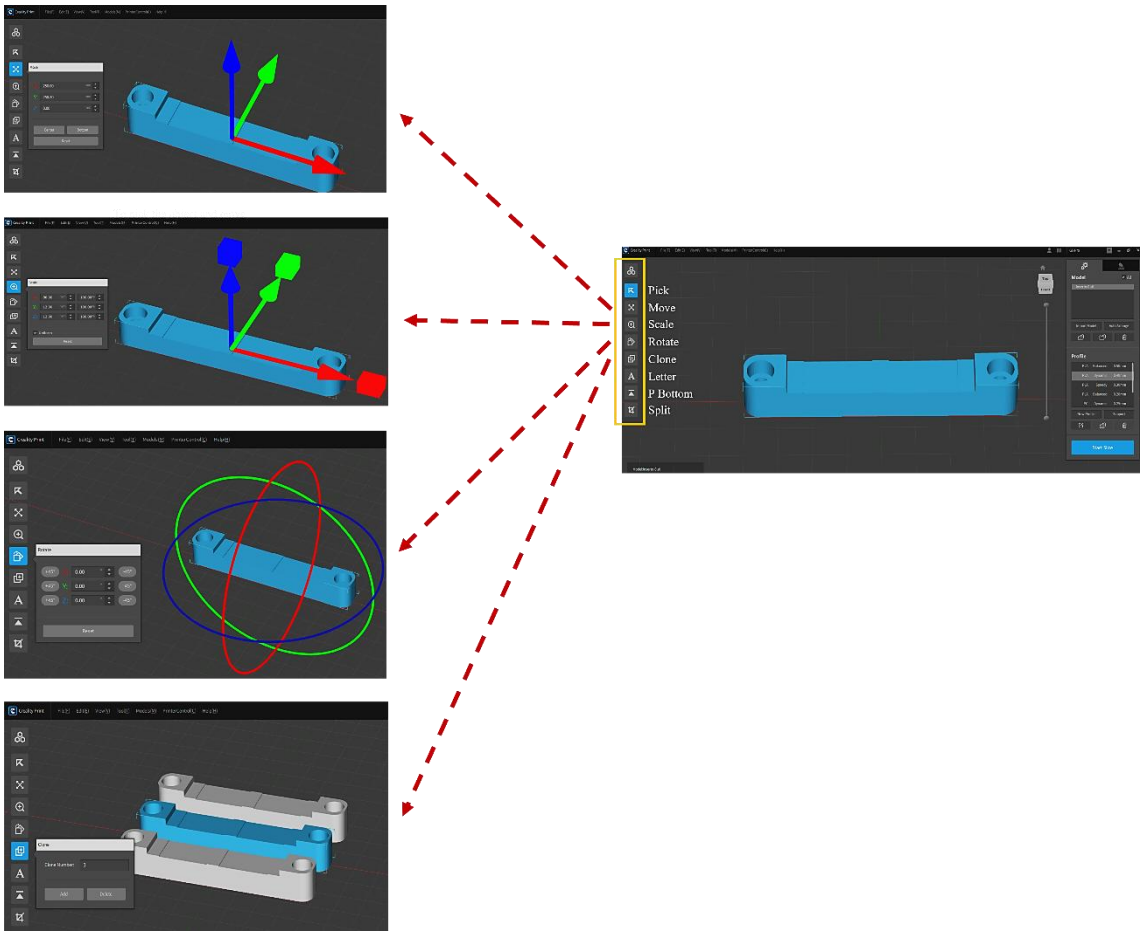

Figure 7. Action bar panel in Creality Print

Each transformation is numerically controlled through the parameter panel, ensuring precise adjustments in addition to interactive manipulation.

In Creality Print, model preparation and parameter definition are closely integrated. The workspace enables orbit, pan, and zoom operations, and once slicing is complete, a layer slider provides a layer-by-layer preview of the toolpath, including perimeters, infill, and supports. These visualization tools are complemented by the Manage Parameters interface, where complete sets of slicing variables can be created, duplicated, or imported. Clear labeling of parameter sets with information such as material type, nozzle diameter, and date of creation ensures traceability and reproducibility in laboratory environments.

Creality Print organizes settings into three levels of complexity:

- Basic mode exposes only the most essential parameters, such as layer height and infill density
- Advanced mode expands access to categories including shell thickness, print speed, and support generation

- Expert mode provides full control over all available slicing variables, enabling fine-tuning of cooling rates, movement sequences, and experimental functions

For research purposes, including in this thesis, expert mode is generally required, as it permits systematic adjustment of individual variables and the isolation of their effects on print quality. Within expert mode, parameters are grouped into functional categories:

- Quality – defines layer height and surface resolution
- Shell – controls wall thickness, top/bottom layers, and perimeter overlap
- Infill – specifies pattern, density, and structural orientation
- Material – sets nozzle and bed temperatures, flow rates, and cooling controls
- Speed – regulates print, travel, and extrusion speeds
- Movement – defines retraction distances, acceleration, and jerk limits
- Cooling – adjusts fan speeds and thermal management strategies
- Build plate adhesion – selects between skirt, brim, or raft for part stabilization
- Special and Experimental – provide access to advanced features such as adaptive layers or alternate infill strategies

Figure 9 illustrates the workflow in Creality Print, beginning with the creation and definition of a new profile, followed by the adjustment of slicing parameters according to the selected material and object requirements. The software provides different operating modes, enabling users to tailor settings for accuracy, strength, or speed, thereby ensuring optimized print conditions for diverse applications.

The structured arrangement of parameters in Creality Print enables users to maintain reproducibility while exploring the influence of specific variables on part quality and performance.

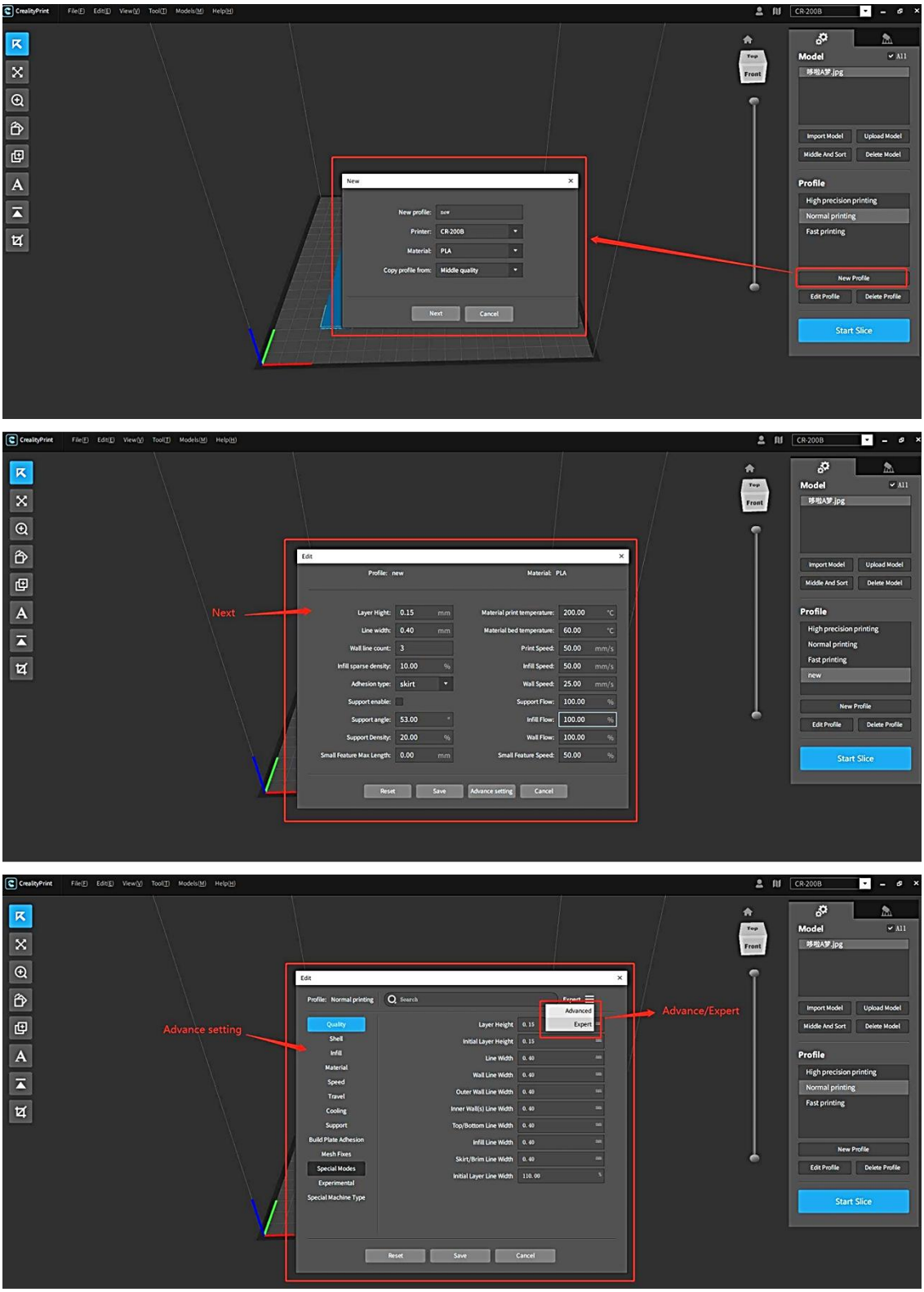

Figure 9. Defining a new profile and adjusting printing parameters in different modes

Once the model geometry and process parameters have been defined, the slicing stage converts the digital design into a sequence of machine-readable commands. In Creality Print, slicing is initiated by selecting Start Slicing, which processes the entire build

platform and generates the toolpath for all models present. Upon completion, the software automatically enters the preview environment, as illustrated in Figure 10.

The preview interface provides several visualization tools to evaluate the generated G-code before exporting it to the printer. At the upper part of the window, the Print report summarizes the estimated build time, material usage, and filament (or pellet) consumption required for the job, allowing the user to plan printing resources in advance. The model can then be examined layer by layer using the slider, enabling inspection of perimeters, infill structures, and support elements throughout the build height. Two types of preview are available: a color-coded display and a G-code view. The color display can be adjusted by speed, structure, or nozzle assignment, while the G-code mode allows inspection of the raw toolpath commands. Within the preview box, it is also possible to control how many layers are displayed, adjust visualization speed, or pause playback for closer examination. These functions represent an essential step in quality assurance, as they permit the detection of potential issues such as missing layers, unintended voids, or misaligned supports before the job is initiated on the printer.

Once verified, the prepared G-code may be exported. On the Piocreat G5 PRO, the standard procedure is to save the file locally and transfer it via SD card, since this model does not support direct USB transfer. Creality Print also allows WLAN-based transfer if the printer is network-connected, while USB online printing is available only for certain compatible machines. For long-term storage or sharing, G-code files may additionally be uploaded to a personal Creality Cloud account.

The slicing, preview, and export sequence forms the final link between digital preparation and physical manufacturing. Careful inspection of the toolpath, review of the print report, and the use of an appropriate transfer method ensure that printing begins with accurate data, thereby reducing the risk of build failures and improving reproducibility in experimental work.

After preparing the G-code and transferring it to the printer by SD card, calibration is the next prerequisite for achieving consistent print quality and reproducible experimental results with the Piocreat G5 PRO. Since pellet-based extrusion involves higher material flow rates and greater sensitivity to temperature stability compared to filament-driven systems, the accuracy of mechanical adjustments and preliminary test prints is of particular importance. The first step in calibration is the adjustment of the build plate level

and Z-offset. The G5 PRO incorporates a 64-point auto-leveling system that generates a digital map of the build surface (Figure 11). This is supplemented by fine manual adjustment of the Z-offset to define the precise distance between nozzle and plate during the first layer. A correct Z-offset ensures adequate adhesion without excessive compression of the extruded bead, both of which are critical to prevent part detachment or nozzle obstruction.

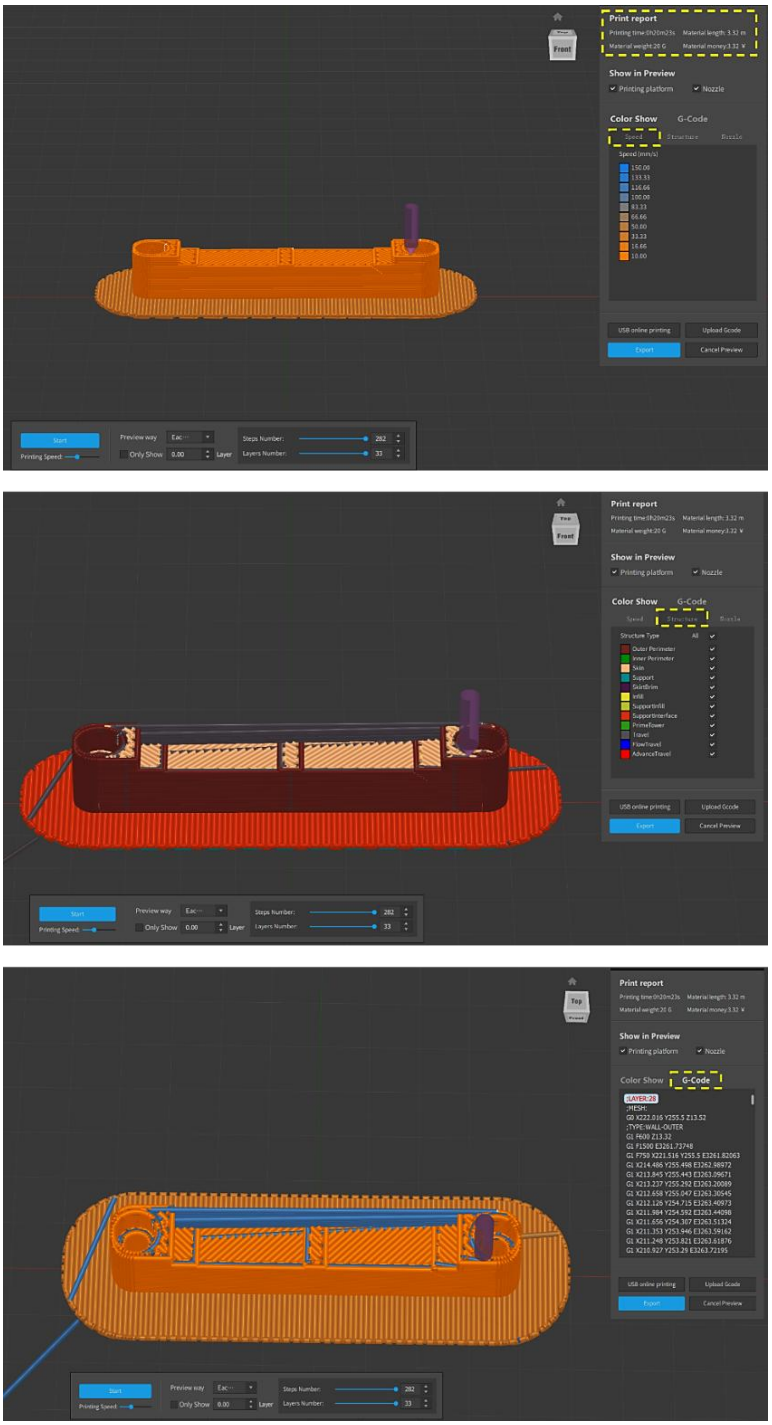

Figure 10. After setting parameters, the preview environment in Creality Print displays different menus

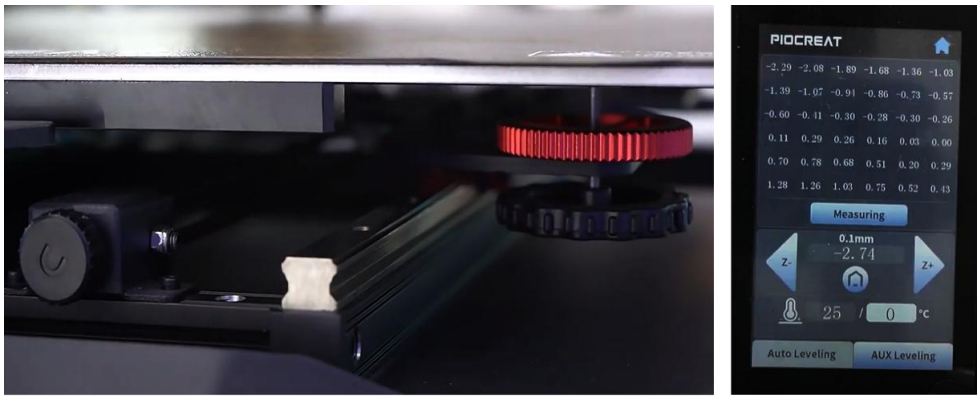

Figure 11. Manual calibration through the adjustment wheels located beneath the build plate, used to fine-tune leveling in addition to the automatic 64-point system

Flow calibration is equally important in pellet-based printing. The extruder must be purged until a steady stream of molten material is established, and the commanded extrusion volume must correspond to the actual delivered mass. This procedure stabilizes screw pressure and reduces variability in the deposition rate. Because pellet extrusion relies on continuous feeding rather than discrete retractions, flow calibration replaces conventional filament retraction tuning (Figure 12).

In practice, calibration and test prints are performed prior to every new experimental series. They serve to validate machine readiness, confirm parameter accuracy, and ensure that the extrusion system is free from residual material or partial obstructions. Only after these verifications are complete can experimental prints, such as polymer inserts or mechanical specimens, be initiated with confidence in their reproducibility.

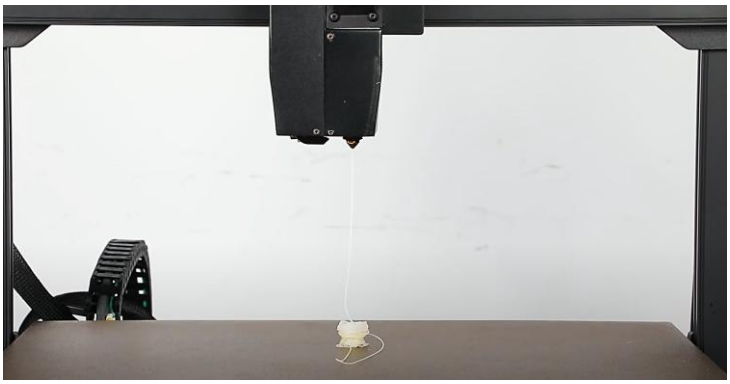

Figure 12. Purging and flow calibration carried out before initiating the print

For composite pellets, such as Copper–PLA or carbon-reinforced PA, several additional considerations must be taken into account. The presence of metallic or fibrous fillers increases the thermal conductivity and abrasiveness of the material compared to neat

polymers. As a result, higher nozzle temperatures are typically required to ensure full melting and dispersion of the polymer matrix, while extrusion through hardened steel or wear-resistant nozzles is recommended to minimize tool degradation. The increased thermal conductivity of metal-filled composites also accelerates heat loss, making bed adhesion strategies (e.g., higher build plate temperatures or the use of brims/rafts) more critical. In the case of carbon-filled polyamides, the hygroscopic nature of the polymer matrix further emphasizes the importance of thorough pre-drying to avoid void formation and nozzle clogging. Careful parameter adjustment is therefore necessary to achieve stable extrusion and reproducible mechanical performance when printing with composites.

Despite careful calibration and parameter control, issues may occasionally arise during operation of the Piocreat G5 PRO. In pellet-based extrusion, problems are often linked to material handling, thermal stability, or mechanical alignment, and their prompt identification is essential to avoid failed builds and equipment damage. The most frequent symptoms, their likely causes, and recommended corrective actions are outlined below.

- Under-extrusion is among the most common issues and is typically caused by residual moisture in pellets, partial clogging of the nozzle, or insufficient pressure within the screw. The recommended procedure is to ensure that all pellets are properly dried, purge the extruder to remove degraded material, and verify that the extruder throat is unobstructed.
- Nozzle clogging may result from polymer degradation at elevated residence times, contamination in the feedstock, or insufficient extrusion temperature. Corrective action involves performing a purge at a higher temperature, mechanically cleaning or replacing the nozzle, and checking that the selected thermal profile matches the material’s processing requirements.
- Inconsistent extrusion and surface defects, such as blobs or voids, often stem from pellet bridging in the feed throat or unstable heater performance. These issues can be mitigated by verifying that the pellets are dried to specification, ensuring smooth feeding, and recalibrating the heating zones for stable thermal conditions.
- Poor adhesion to the build plate generally occurs when the Z-offset is incorrectly calibrated, the build surface is contaminated, or the bed temperature is set too low. Preventive measures include recalibration of the first-layer height, cleaning the

build plate with isopropyl alcohol, and employing adhesion strategies such as a brim, raft, or surface coating.

- Layer shifting during a print is usually mechanical in origin, arising from loose belts, improper gantry alignment, or obstructions along the axes. Inspection and tightening of belts, cleaning of linear guides, and removal of any debris from the motion system are necessary corrective actions.
- Stringing and oozing are characteristic of pellet extrusion when the nozzle temperature is too high or cooling is insufficient. These defects may be reduced by lowering extrusion temperature, adjusting fan settings to improve solidification, and in some cases introducing a purge line or sacrificial wall to stabilize the melt flow before part deposition.

By systematically linking observable symptoms to probable causes, and by applying targeted corrective actions, most operational issues can be resolved without hardware replacement. A consistent troubleshooting approach not only reduces downtime but also contributes to reproducibility in experimental work, which is especially critical in the context of research-driven additive manufacturing.

The collected documentation provides practical guidance for safe operation, correct setup, and efficient use of the Piocreat G5 PRO together with Creality Print. By detailing system configuration, parameter management, calibration routines, and maintenance practices, the content serves as a structured reference to support future users.

ACKNOWLEDGMENTS

I would like to express my deepest gratitude to my supervisor, Professor Alberto Frache, from whom I have not only gained academic knowledge but also learned by example through his continuous support, kind guidance, and professional attitude. It has truly been an honor for me to work under his supervision.

My sincere thanks also go to my co-supervisor, Dr. Daniele Battegazzore, from whom I learned so much. He has been a constant source of practical knowledge and guidance, and his availability and willingness to help whenever needed have been invaluable throughout this work.

I also want to thank Professor Rossella Arrigo, who has always encouraged me and provided great motivation for my work and future, even though I did not have the honor of being directly her student.

I am also grateful to all the staff, researchers, and PhD students at Sede di Alessandria, in particular Giulia Bernagozzi, Fulvia Cravero, Chiara Paravidino, and Lorenza Abbà, for their kind support and collaboration.

Special thanks go to the colleagues working in the Metal Section, especially Professor Federico Simone Gobber for his time and assistance, and Dr. Antonio Pennacchio for his help and valuable input.

It has been a real pleasure to work in Alessandria, where I have always felt fully supported. This experience has made my thesis not only a scientific achievement but also an important moment of personal growth and an opportunity to meet many wonderful people.

Last but not least, I warmly thank my family and friends for their constant encouragement, patience, and unconditional support, which have been essential throughout this journey.